APPLICATION OF NUCLEAR MAGNETIC RESONANCE SPECTROSCOPY FOR THE DETECTION OF METABOLIC CHANGES IN NON-ALCOHOLIC FATTY LIVER DISEASE

by

RAQUEL TEIXEIRA SABORANO

A thesis submitted to the University of Birmingham for the degree of

DOCTOR OF PHILOSOPHY

The Institute of Cancer and Genomic Sciences

College of Medical and Dental Sciences

University of Birmingham

July 2019

ABSTRACT

The increasing rates of NAFLD worldwide are a major concern to healthcare providers leading to an arising need to study liver metabolism in health and disease. Metabolic analysis of specific biochemical processes by NMR spectroscopy allows detailed study of carbohydrate and lipid metabolism dysregulation in liver disease.

In order to identify the hepatic metabolic fingerprint at different stages of NAFLD I used *in vitro*, murine *in vivo* and human *ex vivo* models. Optimisation of NMR metabolic profiling and tracer-based studies using ^{13}C-labelled precursors were performed using cell lines and primary cells. Furthermore, metabolic alterations that occur during disease progression were compared between an *in vitro* model of steatosis and human *ex vivo* liver samples. Flow cytometry, immunohistochemistry, qPCR and biochemical analysis were also used to confirm the extent of the liver injury during NAFLD progression.

Fructose supplementation led to accelerated obesity, hepatic steatosis and insulin resistance, as well as increased inflammation in my murine model. The use of 1D NMR-based metabolomics and 2D HSQC spectra to follow [U-^{13}C] fructose confirmed selective enhancement of the glycolytic pathway and TCA cycle intermediates together with nucleotide production. Moreover, increase in the production of glycerol intermediates was observed, which drives *de novo* lipogenesis. Lastly, the inhibition of ketohexokinase activity in both the animal model and the *ex vivo* human perfusion system highlighted its potential as a therapeutic approach in NAFLD.

Hence, these findings demonstrate the relevance of using NMR metabolomics and tracer-based approaches to study metabolic changes in the context of human disease and provided detailed mechanistic information that can lead to the identification of novel diagnostic, prognostic and therapeutic tools.

ACKNOWLEDGMENTS

Who would have thought that a PhD journey would be so similar to a rollercoaster ride? It had its ups and downs, it seemed never-ending at times and so short in others. At this time, I can only thank everyone who accompanied me, who watched me grow as a person but also who helped me improve at a professional level, and finally, who stayed by my side showing what friendship has best to offer.

First, I would like to thank my supervisors, Prof. Ulrich Günther and Dr. Patricia Lalor, for allowing me to enter this adventure, for giving me the freedom to explore so many different options and for allowing me to grow as a research scientist. To Dr. Patricia Lalor, I would also like to thank for all the times exchanging ideas, all the support you gave me and, above all, the sympathy with which you always welcomed me.

Being part of the Marie Curie project EUROPOL was also a great privilege and I would like to thank everyone in the network that made this possible. A special thank you for my secondment supervisors Prof. Jan Ardenkjær-Larsen and Prof. Pernille Jensen for your prompt availability, all the hours teaching and supporting me throughout a great time in Denmark. To Signe Holm, Demet, Elisa and everyone I crossed paths during my time in DTU, thank you for making those weeks so special.

Back in Birmingham, I would like to warmly acknowledge Christian, Michelle, Mark, Sue and Karen in the HWB-NMR facility who ensured all the work was always running as easily as possible. To Sara, thank you for always being available to help, even if it wasn't related to work.

In the liver labs, a big thank you to Dr. Emma Shepherd, Dr. Lozan Sheriff, Dr. Yung-Yi and Dr. Thin-Luu, as you helped made this project possible by keeping the morale up, supporting my crazy experiments and allowing me to shine in exciting new fields of

biology. To Janine, thank you for keeping things running smoothly even when no one notices.

Now, to all the warriors who shared this path with me and always had a friendly word to offer, a dinner to organise or just a coffee in the afternoon, thank you: Zuhal, Nuria, Gaelle, Greg, Catarina and Ana. Thank you too Bannay, it was such a pleasure having you on my side for this PhD journey. Also, to those who never left and made the distance so insignificant at times, thank you Mélanie and Diana, you kept me sane.

In particular, a special thank you to the best trio Birmingham has presented me with: Dan and Kostas. I will never forget our times in the lab or our times at the Cherry Reds. For some reason, I always felt so comfortable with you two that all moments we have shared were special to me. You showed me how to enjoy life with a full smile even if life doesn't go as planned.

Jennie, you were one of the best things Birmingham has given me. Such a pleasure sharing this learning process with you, the discovery of new places and new foods, but most importantly, thank you for the strength and support you always gave me, and for believing in me even when I couldn't. Bebiana, a simple thank you wouldn't be enough. Who would have thought that 8 years later we would still be laughing together over good coffee and beer? Me neither, but I couldn't be happier. Thank you for always being there.

To you Vasco, a special thank you for being strong for me and for us, for making me happy every day, for believing in me, for helping me enter adulthood without losing my smile. You supported me like no one else over these last few years, you brought me peace when I most needed. You are really special to me, never forget that.

At last, a massive thank you to my parents, António and Fernanda, you are the light in this path we call life. Thank you for always being there and for the endless unconditional support. Without you, this would not be possible.

SCIENTIFIC CONTRIBUTIONS

Publications

1. **Saborano, R.**, *et al*. Hepatic metabolism does not stand a chance against NAFLD while sugar and fat collaborate. *In preparation*
2. Shepherd, E.L. and **Saborano, R.**, *et al.* Ketohexokinase inhibition: a validated paradigm for treating non-alcoholic steatohepatitis through reduction in fructose-induced steatosis and fibrogenesis. *Submitted to Gastroenterology*
3. Harrison, M.J., **Saborano, R.**, *et al*. Stimulation of hepatic LTBR primes hepatocyte nucleotide production and de novo lipogenesis leading to circulating hyperlipidaemia and atheroma formation. *Submitted to Scientific Reports*
4. **Saborano, R.** and Eraslan, Z., *et al*. (2019) A Framework for Tracer-Based Metabolism in Mammalian Cells by NMR. *Sci. Rep. DOI:10.1038/s41598-018-37525-3*.

All material taken from these publications to be used in this thesis is my own work.

Presentations

1. Short talk and poster presentation: **Raquel Saborano**, Emma L. Shepherd, Patricia F. Lalor, Ulrich L. Günther, 2019. *How can stable isotopic tracer studies elucidate metabolism in liver disease?*. Keystone symposium: Integrated Pathways of Disease in NASH and NAFLD (A4), Santa Fe, New Mexico, USA
2. Short talk: **Raquel Saborano,** Patricia F. Lalor, Ulrich L. Günther, 2018. *Could the suppression of LTBR signalling in hepatocytes lead to design of new therapeutics for NAFLD?.* VIII Ibero-American NMR Meeting, Lisbon, Portugal

3. Poster presentation: **Raquel Saborano**, Patricia F. Lalor, Michelle AC Reed, Ulrich L. Günther, 2017. *Metabolism in liver disease.* EUROMAR European Congress on Magnetic Resonance, Warsaw, Poland
4. Poster presentation: **Raquel Saborano**, Patricia F. Lalor, Michelle AC Reed, Ulrich L. Günther, 2017. *Metabolism in liver disease.* AMPERE NMR School, Zakopane, Poland
5. Short talk: Zoe Schofield, **Raquel Saborano**, *et al*, 2016. *Metabolic profiles of alcoholic and non-alcoholic steatohepatitis*. ECLCB-7, Ascot, London, United Kingdom

CONTENTS LISTINGS

Table of Contents

LIST OF ABBREVIATIONS

ACACA	Acetyl-CoA carboxylase alpha
aLMF	activated Liver Myofibroblasts
ADP	Adenosine di-phosphate
AMP	Adenosine mono-phosphate
ATP	Adenosine tri-phosphate
ALT	Alanine transaminase
ALD	Alcoholic Liver Disease
AldoB	Aldolase B
ALP	Alkaline Phosphatase
AST	Aspartate transaminase
BD	Bile Ducts
BEC	Biliary Epithelial Cells
BBI	Broadband inverse
ChREBP	Carbohydrate-Responsive Element-Binding Protein
Chol	Cholesterol
CholE	Cholesterol ester
CLD	Chronic Liver Disease
CD	Cluster of differentiation
CoA	Coenzyme - A
cDNA	Complementary Deoxyribonucleic Acid
COSY	Correlation Spectroscopy
DNL	*de novo* lipogenesis

DMEM	Dulbecco's Modified Eagle Medium
DNP	Dynamic Nuclear Polarisation
FA	Fatty Acid
FASN	Fatty Acid Synthase
FBS	Fetal Bovine Serum
FID	Free Induction Decay
Fru	Fructose
FBP	Fructose 1,6-biphosphate
F6P	Fructose 6-phosphate
GGT	gama-Glutamyl Transferase
GC	Gas phase Chromatography
GI	Gastrointestinal
GK/HK	Glucokinase/Hexokinase
Glc	Glucose
G1P	Glucose 1-phosphate
G6P	Glucose 6-phosphate
GLUT	Glucose Transporter
GPC	Glycerophosphocholine
GTP	Guanosine tri-Phosphate
H&E	Haematoxylin and Eosin
HICs	Hepatic Immune Cells
HSC	Hepatic Stellate Cells
HCC	Hepatocellular Carcinoma
HCC	Hepatocyte Cytoplasm
HN	Hepatocyte Nuclei

Heps	Hepatocytes
HMQC	Heteronuclear Multiple Quantum Correlation Spectroscopy
HSQC	Heteronuclear Single Quantum Correlation Spectroscopy
HFD	High Fat Diet
HDL	High-Density Lipoprotein
HMDB	Human Metabolome Database
IMP	Inosine Mono-Phosphate
INEPT	Insensitive Nuclei Enhancement by Polarization Transfer
IFN	Interferon
IL	Interleukin
IMC	isotype matched control
J-Res	*J*-Resolved Spectroscopy
KHK	Ketohexokinase
LC	Liquid phase Chromatography
LFD	Low Fat Diet
LDL	Low-Density Lipoprotein
MRI	Magnetic Resonance Imaging
MS	Mass Spectrometry
NK	Natural Killer
NKT	Natural Killer cells expressing T-cell receptor
NC	Negative Control
NADH	Nicotinamide adenine dinucleotide

NAFLD	Non-Alcoholic Fatty Liver Disease
NASH	Non-Alcoholic Steatohepatitis
NUS	Non-Uniform Sampling
NMR	Nuclear Magnetic Resonance
NOESY	Nuclear Overhauser Effect SpectroscopY
OA	Oleic Acid
1D	One Dimensional
ANOVA	One-way Analysis of Variance
Ilab	Peak intensity from 13C-labelled sample
Ict	Peak intensity from matched unlabelled sample
PBS	Phosphate-buffered saline
PTC	Phosphatidylcholine
PTE	Phosphatidylethanolamine
PC	Phosphocholine
PEP	Phosphoenolpyruvate
PFK-1	Phosphofructokinase 1
presat	pre-saturation
PBC	Primary Biliary Cholangitis
PFG	Pulsed Field Gradients
PC	Pyruvate Carboxylase
PDH	Pyruvate Dehydrogenase
PK	Pyruvate Kinase
qPCR	Quantitative Polymerase Chain Reaction
RF	Radiofrequency
ROS	Reactive Oxygen Species

RPM	Revolutions per minute
RNA	Ribonucleic Acid
RT	Room Temperature
RPMI	Roswell Park Memorial Institute
S/N	Signal to Noise
SM	Sphingomyelin
SD	Standard Deviation
SREBP1c	Sterol Response Element Binding Protein 1c
TCR	T-Cell Receptor
TMS	Tetramethylsilane
C_T	Threshold cycle
TOCSY	Total Correlation Spectroscopy
TSA	Total Spectral Area
TCA	Tricarboxylic Acid
TG	Triglyceride
TMSP	Trimethylsilylpropanoic acid
TCI	Triple resonance NMR “inverse”
TNF	Tumour Necrosis Factor
2D	Two Dimensional
UMP	Uridine Mono-Phosphate
VLDL	Very Low-Density Lipoprotein
WATERGATE	WATER suppression by GrAdient Tailored Excitation

CHAPTER 1

GENERAL INTRODUCTION

1. General introduction

1.1. How does the liver work?

1.1.1. Liver anatomy and physiology

The human liver is a large essential metabolic organ that weighs 1.2-1.5 kg and is located in the right upper abdominal quadrant, below the diaphragm. The liver is usually subdivided into left and right lobes, separated by the falciform ligament, and has its own blood supply and segmental bile ducts. Blood enters the liver through the hepatic artery, carrying oxygen-rich blood from the arterial circulation and the portal vein carries blood rich in nutrients coming from the gastrointestinal (GI) tract, pancreas and spleen. Blood from these two routes mixes in the smaller capillaries, or liver sinusoids, within the liver lobules, which make up the functional units of the liver. Hepatic lobules consist of liver cells and associated vascular and biliary structures within the parenchyma and portal tracts, which include branches of the portal vein, hepatic artery and bile ducts, surrounded by connective tissue [1–3].

The main cell type of the liver is the hepatocyte, which constitutes around 80% of the parenchymal tissue and is responsible for protein synthesis and storage, transformation of carbohydrates, detoxification and modification of potential damaging substances, and the formation and secretion of bile. The hepatocytes within the lobules, provide a structural but also secretory and microcirculatory unit. This functional unit consists of hepatocytes radiating outward from a central vein, along with the hepatic artery and bile duct (the portal triad). The blood reaches the central vein through liver sinusoids, which are separated from hepatocytes by the space of Disse, which drains lymph into the lymphatic capillaries. Within the sinusoids, we can also find the non-parenchymal cells, including endothelial cells, Kupffer cells, lymphocytes and stellate cells (see Figure 1. 1) [3–5].

Endothelial cells that line the sinusoids are fenestrated, allowing direct cell-to-cell contact, and are characterised by an absence of tight junctions and minimal basement membrane. Adherent to the endothelial cells, Kupffer cells play a role in defence against foreign endotoxins, bacteria and microbial debris derived from the gastrointestinal tract that reach the liver through the portal vein. Kupffer cells are resident liver macrophages that act as one of the first lines of defence against blood-borne pathogens, being essential for phagocytosis and also for the release of mediators and cytotoxic agents [6].

Lymphocytes also play a role in defence against tumours and viruses and help resist infection, being recruited to the liver and binding to hepatic endothelial cells under different conditions. Distribution and composition of these immune-competent cells varies according to the inflammatory status of the liver. Under basal condition, intrahepatic lymphocytes are present in the sinusoidal lumen and include natural killer (NK) and NK-T cells that modulate the immune response of this organ. Under conditions of injury, increased numbers of CD4 and CD8 positive lymphocytes are recruited and retained in the liver along with other myeloid cells in order to remove damaging pathogens and aid resolution of injury [7–9].

Lastly, hepatic stellate cells have unique features, playing vital roles in the regulation of retinoid (vitamin A and its metabolites) homeostasis. In normal conditions, these cells are responsible for the storage and regulation of 80% of the total retinoids in the whole body, as lipid droplets in the cytoplasm. Moreover, they can contribute to fibrosis by undergoing changes in their morphology, proliferation and secretory functions leading to enhanced extracellular matrix synthesis and remodelling [10,11].

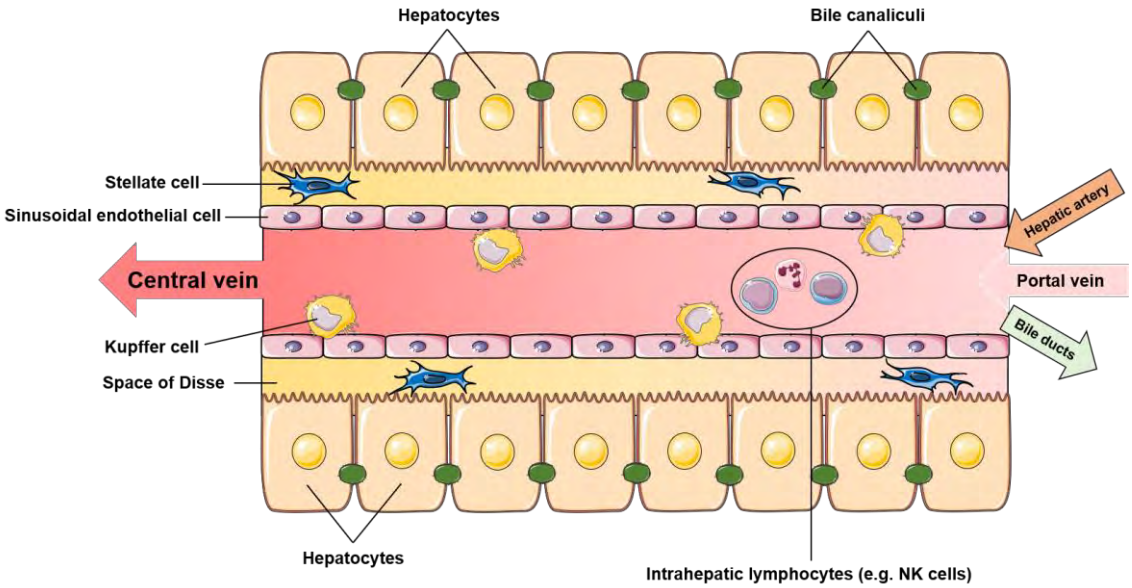

Figure 1. 1 – Diagram of the cellular components of the hepatic lobule. Each hepatic lobule consists of an arrangement of hepatocytes in cords separated by adjacent sinusoids lined with endothelial cells. The sinusoids receive blood from terminal branches of the hepatic artery and portal vein and deliver it to the central veins, while bile is secreted by hepatocytes into the bile canaliculi and drains towards the bile ducts. Resident Kupffer cells can be found along the hepatic sinusoids, as well as stellate cell and intrahepatic lymphocytes. Image designed with cellular components from Servier Medical Art [12] (Creative Commons Attribution 3.0 Unported License).

1.1.2. The liver as a metabolic organ

1.1.2.1. Hepatic carbohydrate metabolism

The liver plays a central role in the control of carbohydrate metabolism by maintaining circulating glucose concentrations within a narrow, normal range. Accordingly, its metabolic functions that preserve blood glucose homeostasis are under hormonal control, particularly by the release of pancreatic hormones, like glucagon and insulin [13,14].

The maintenance of normal blood glucose levels is kept during the absorptive (feeding) state, when the liver stores glucose as glycogen (via glycogenesis), or the post-absorptive (fasting) state when the liver releases glucose (via glycogenolysis) or synthesizes glucose from non-carbohydrate sources (via gluconeogenesis). Therefore, the liver possesses tightly regulated systems that control either glucose breakdown or synthesis in hepatocytes [15,16].

After a meal, in the fed state, glucose is carried by the hepatic portal vein to the liver and is taken up into hepatocytes via glucose transporter 2 (GLUT2). Hence, this transporter is responsible for the equilibrium of glucose concentration between the cell and the blood [17]. The excess of glucose taken up by the hepatocytes is phosphorylated by glucokinase to glucose-6-phosphate (G6P), which lowers intracellular glucose levels and increases its uptake, under the influence of insulin. Depending on the systemic metabolic state, G6P can be further metabolized as a precursor for glycogen synthesis, by glycogen synthase, to increase liver glycogen storage. Alternatively, it can be processed through glycolysis, generating adenosine triphosphate (ATP) and nicotinamide adenine dinucleotide (NADH). In glycolysis, two molecules of pyruvate are obtained from each glucose molecule, which can either be converted to lactate (in anaerobic conditions) or decarboxylated to acetyl-CoA (in aerobic conditions). Acetyl-CoA can be further

processed into the tricarboxylic acid (TCA) cycle to produce energy in the mitochondria, or be used for *de novo* lipogenesis in the cytosol [14,18,19].

During sleep or in between meals, the fasting state, the α-pancreatic cells start secreting glucagon leading to a rise in plasma glucose levels through the inhibition of glycogen synthase and activation of glycogen phosphorylase. When blood glucose concentrations begin to decline, the depolymerisation of glycogen (glycogenolysis) occurs in the liver in order to export glucose back into the blood, for transport to other tissues. Through glycogenolysis, glycogen is cleaved into glucose-1-phosphate (G1P) that will be converted into G6P and, eventually resulting in free glucose [1,14,20].

In periods of prolonged fasting or starvation, the glycogen store is depleted, and hepatocytes can synthesize glucose through gluconeogenesis. Moreover, there are several gluconeogenic precursors that can be used, including lactate, pyruvate, glycerol, and amino acids, which are generated either in the liver or delivered into the liver through the portal vessels. Gluconeogenesis is not the direct opposite of glycolysis though they share seven out of the ten steps. Indeed, there are three irreversible reactions in glycolysis that cannot be used in gluconeogenesis. Although energetically expensive, these three steps are essential and by-passed by another set of enzymes, including the conversion of pyruvate to phosphoenolpyruvate (PEP), the conversion of fructose 1,6-biphosphate (FBP) to fructose-6-phosphate (F6P), and the conversion of G6P to glucose. Therefore, the release of glucose into the bloodstream occurs through the contribution of glycogenolysis and gluconeogenesis, restoring the normal levels of glucose in the blood [1,20].

Although glucose is the main source of energy, fructose is another simple sugar that can be used for energetic and biosynthetic needs. Fructose is naturally found in dietary constituents such as fruit, honey and most root vegetables, but it has also become one of

the most supplemented sources of sugar in diets worldwide, especially in sweetened beverages such as sodas, soft and sport drinks [21,22].

Dietary glucose and fructose absorption and distribution is quite different. There are fourteen glucose transporters (GLUTs) that can facilitate glucose transport across the plasma membrane, nevertheless glucose uptake is regulated by insulin action and energy needs. When glucose enters the cells, it is metabolised by glucokinase/hexokinase (GK/HK) to form glucose 6-phosphate and can be further used to produce energy [17,23]. Fructose on the other hand, enters the cells through two major GLUT transporters, namely GLUT5 and GLUT2, independent of hormonal regulation. While GLUT5 is an exclusive fructose transporter, mostly expressed in the small intestine, GLUT2 is a low-affinity transporter, also capable of recognizing glucose and galactose, and located in the liver and pancreas. Following uptake, most of the dietary fructose passes via the portal circulation to the liver, where it can be rapidly cleared. Intracellular hepatic fructose metabolism also differs from glucose, as the first phosphorylation reaction is mediated by ketohexokinase (KHK) forming fructose 1-phosphate [21,24,25].

Next, fructose 1-phosphate will be cleaved by aldolase B (AldoB) to generate D-glyceraldehyde and dihydroxyacetone phosphate. From this step forward, the trioses can enter glycolysis and share the same pathway as glucose or generate glycerol intermediates to enter *de novo* lipogenesis (DNL). Worthy of note, fructose is able to bypass the main regulatory step of glycolysis controlled by phosphofructokinase, where glucose 6-phosphate is converted to fructose 1,6-biphosphate. Therefore, while glucose would be negatively regulated by this enzyme, fructose can enter glycolysis freely to generate pyruvate, lactate, glucose, glycogen, glycerol and acylated molecules that will promote excess energy flux and production of triglycerides [26,27].

A representation of carbohydrate metabolism in the liver can be seen in Figure 1. 2.

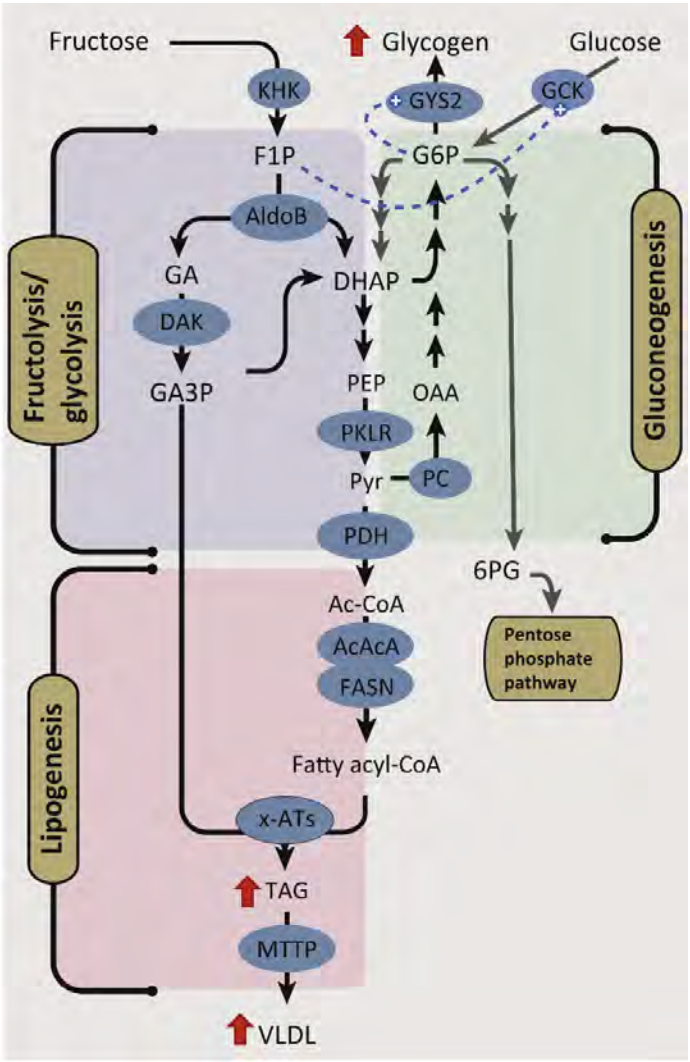

Figure 1. 2 – Overview of carbohydrate metabolism. Glucose and fructose are the main carbohydrate sources for energy supply obtained through glycolysis, gluconeogenesis, lipogenesis and the electron transport chain. While glucose is phosphorylated into glucose 6-phosphate (G6P) by glucokinase activity (GK), fructose enters the cells to be phosphorylated in the position 1 by ketohexokinase activity (KHK). Later, they share some metabolic steps involving the activity of aldolase B (AldoB) to produce intermediates of glycolysis dihydroxyacetone phosphate (DHAP) and glyceraldehyde (GA). When there is an excess of energy substrates, intermediates of lipogenesis can be obtained directly via fructolysis (GA3P) or via acetyl-CoA (Ac-CoA), feeding lipid metabolism. Moreover, glucose can also be stored in the form of glycogen to be later used during periods of prolonged fasting. From Herman *et al* [28].

1.1.2.2. Hepatic lipid metabolism

Lipids such as fatty acids and glycerol constitute the largest energy reserve in mammals, and homeostasis is maintained by co-operation between skeletal muscle, adipose tissue and the liver. The liver plays a key role in lipid metabolism as it is capable of both synthesizing and oxidizing fatty acids, but also of transporting and making them available to the rest of the body (see Figure 1. 3) [29–31].

The importance of dietary regulation of hepatic lipid metabolism is well recognized, since it can influence several metabolic pathways, depending on the action of hormones (insulin and glucagon) and the nutritional state. After a meal, dietary fat is digested in the small intestine and converted into chylomicrons, lipoprotein particles that consist mainly of triglycerides, phospholipids, cholesterol, and proteins. This solubilisation occurs to aid intestinal lipid absorption, where lipid droplets are emulsified by bile acids, synthesized within the hepatocytes. In this way, lipid molecules become accessible to lipase hydrolysis, facilitating the digestion of the chylomicron triglycerides (TGs) into fatty acids and glycerol. Also, non-esterified fatty acids arise from this hydrolysis, being secreted into the lymphatic system, and transported, via the blood to the liver and adipose tissues [19,20,31].

Circulating fatty acids, bound to albumin, can enter the hepatocytes through endocytosis or passive diffusion. Once inside the cell, a CoA group is added to the fatty acid so it can be broken down by β-oxidation. In the human liver, β-oxidation occurs in the mitochondria and it is responsible for the oxidation of short-chain (<4 carbons), medium chain (4-12 carbons) and long chain (10-20 carbons) fatty acids. Oxidation can also occur in peroxisomes during periods of increased influx of fatty acids to the liver. In each cycle of this pathway, one acetyl-CoA molecule is produced, that enters the TCA cycle in the mitochondria and produces ATP. However, when fatty acids are abundant,

the acetyl-CoA is converted to ketone bodies (via ketogenesis) which are important energy sources for certain extrahepatic tissues, including the brain [20,32].

Fatty acids taken up by the liver can also be converted via esterification to triglycerides (TG) and stored as cytosolic lipid droplets or incorporated in the membrane of the hepatocytes. Afterwards, TG can be used by the liver to synthesize very low-density lipoproteins (VLDL) and release them into the bloodstream [29]. The extraction of lipids from VLDL and the loss of some apolipoproteins, progressively converts some of it to low-density lipoproteins (LDL), delivering cholesterol to extrahepatic tissues or the liver. In the hepatocytes, cholesterol is an essential component of cell membranes, regulating their structure and function and is present as unesterified (free) cholesterol, and cholesteryl ester. The esterification of free cholesterol is tightly regulated in order to protect the hepatocytes from cholesterol accumulation. Nonetheless, the excess of cholesterol in other tissues can be transported back to the liver as high-density lipoproteins (HDL) and excreted in bile after its conversion to bile acids [20,33,34].

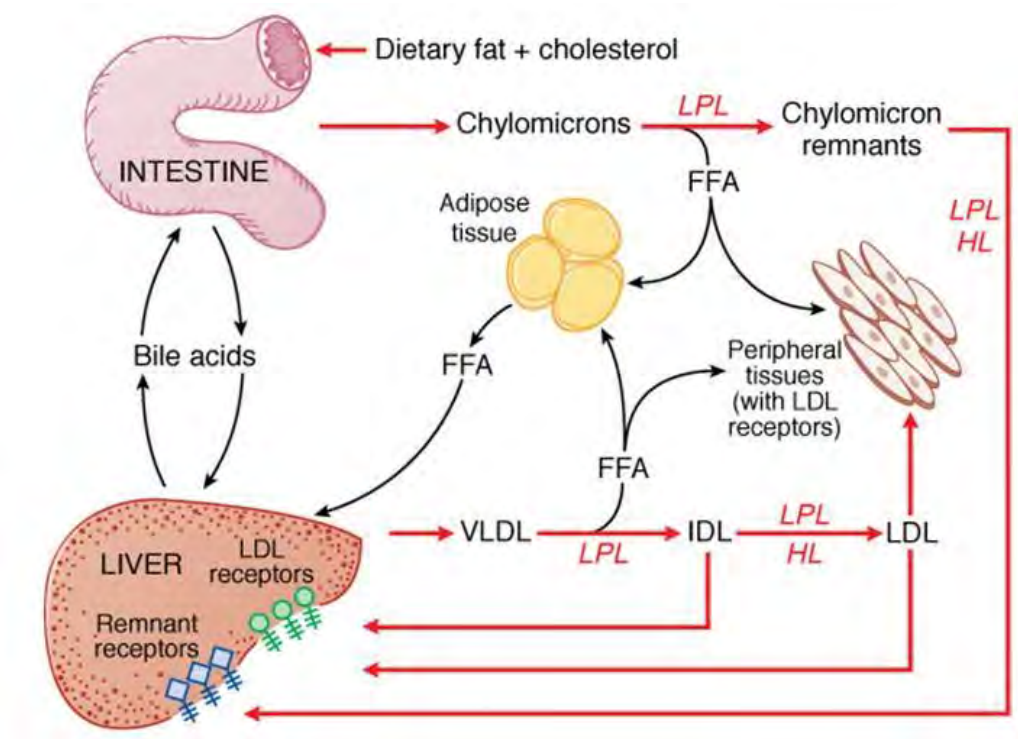

Figure 1. 3 – Overview of lipid metabolism. The main pathways of lipid metabolism and homeostasis are maintained due to the collaboration between skeletal muscle, adipose tissue and the liver. After the ingestion of dietary fat and cholesterol, the small intestine converts them into chylomicrons with the aid of bile acids produced within the hepatocytes. Later they can be hydrolysed and made available for the rest of the body. Moreover, the liver is also able to synthesize and oxidise fatty acids, transport them in the form of VLDL and making lipids available for extra-hepatic tissues. From Goodman & Gilman's The Pharmaceutical Basis of Therapeutics [35].

1.1.2.3. Hepatic amino acid metabolism

Similar to glucose and fatty acids, amino acids represent a large source of energy in the body. Almost all amino acid catabolism takes place in the liver, with the exception of branched chain amino acids that are preferentially taken up by the skeletal muscle [36]. However, amino acids are not stored just for energy production, as they are also needed for protein synthesis which have important biological functions. Amino acids can either be obtained from proteins in food, through the hepatic portal vein and metabolized in the hepatocytes, or through hepatic protein degradation [19,37].

One of the most important amino acid reactions is characterised by the transfer of the amino group to an α-keto acid, termed the transamination reaction. Transaminases activity in hepatocytes involves alanine (ALT) and aspartate (AST) transaminases that convert L-alanine and L-aspartate into α-ketoglutarate and pyruvate or oxaloacetate, respectively. Subsequently, the keto acids can undergo oxidation and provide substrates that can either enter gluconeogenesis to generate glucose and feed other tissues or be catabolised into the TCA cycle to produce energy. These reactions are reversible and therefore dependent on the substrate concentration and availability. Consequently, these transaminases activities are a great indicator of hepatocyte status, providing information about the metabolic processes of cells during health and disease states [38–40].

In order to maintain energy homeostasis in situations of prolonged fast or starvation, amino acids such as alanine and glutamine can be released from muscles into circulation. Usually, alanine is taken up by the liver and ALT converts it into pyruvate, so it can enter gluconeogenesis and produce glucose. Afterwards, the glucose can be released by the liver into circulation and can in turn be used by the skeletal muscles as an energy source. This links the liver and the skeletal muscle, and can occur with other gluconeogenic amino acids, such as aspartate, glutamate and others [19,20,39].

Amino acid catabolism generates a supply of amino nitrogen resulting from amino acid oxidation, which will be excreted in the form of urea and some ammonia. The liver is responsible for urea synthesis, and this relatively non-toxic compound is excreted by the kidneys. Ammonia generated in extrahepatic tissues also travels to the liver, in the form of amino groups such as glutamine and glutamate, for conversion to the excretory form [20,41].

Substrate supply is the main restraint of short-term amino acid catabolism and urea synthesis which depends only on the availability of dietary amino acids. However, in a long-term starved state, these metabolic pathways are dependent on glucagon and cortisol signalling as they rely on body protein breakdown [38,41]. Therefore, the liver is able to regulate overall amino acid metabolism in the organism, as represented in Figure 1. 4.

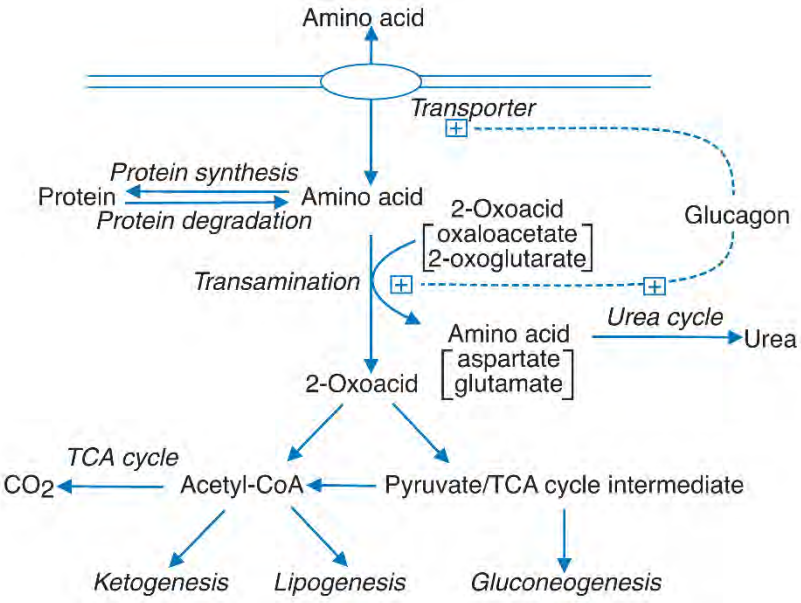

Figure 1. 4 – Overview of hepatic amino acid catabolism. The main pathways of amino acid metabolism occur in the liver. The main metabolic events involve protein turnover, which includes the continuous degradation and synthesis of proteins; catabolism of surplus amino acids, since they cannot be stored; and production of metabolites for other synthetic pathways. A key step in amino acid metabolism includes the transamination reaction where the α-amino group is separated from the carbon skeleton and shunted into the pathways of amino group metabolism. While the α-oxoacids can enter the main metabolic pathways as precursors of glucose or TCA cycle intermediates, the excess nitrogen will be excreted as ammonia, uric acid or urea. From Frayn *et al* [38].

1.1.3. The liver as an immunological organ

As well as being an essential player in metabolic, nutrient storage and drug metabolism, the liver is also responsible for modulating immune responses. The liver is continuously exposed to pathogens, toxins, dietary and microbial products from the systemic circulation, and thus must maintain good equilibrium between tolerance to harmless material and appropriate inflammatory responses to pathogenic or damaging molecules [42–44].

In a healthy liver, immune homeostasis depends on the cooperation between innate and adaptive immunity. This is achieved by the production of cytokines, chemokines and acute phase proteins by a diverse range of resident immune cells, which include lymphocytes, Kupffer cells, natural killer cells, stellate cells, and dendritic cells [45,46].

1.1.3.1. Lymphoid cells

Lymphocyte populations usually reside in the portal tract in homeostatic conditions but can also be found through the parenchyma. Hepatic adaptive lymphocytes comprise T and B cells, and innate lymphocytes include natural killer (NK) cells and natural killer cells expressing T-cell receptor (NKT) [7,46].

T cells get their name due to the presence of a cell surface αβ-chain T cell receptor (TCR) that can be identified using CD3, a pan T-cell marker. Cells positive for this antigen receptor also express either CD8 glycoprotein, denominated $CD8^+$ T cytotoxic cells, or CD4 glycoprotein and are called $CD4^+$ T helper cells. Depending on their physiological function and cytokine secretion, T cells can differentiate into different subsets and regulate either pro- or anti-inflammatory immune processes. $CD4^+$ T helper cells, play an important role in cytokine secretion and supporting the adaptive immune

system against intracellular pathogens. On the other hand, $CD8^+$ cytotoxic T cells are responsible for the secretion of cytokines such as tumour necrosis factor (TNF)- α and interferon (IFN)-γ, which will induce elimination of infected or malignant cells [7,9,47].

The most abundant constituents of the innate immune system in the liver are NK and NKT cells and they are quick responders to numerous pathological signals. NK and NKT cells act as pro-inflammatory cells that can kill other cells following exposure of pathogens and toxins from the gut, virus infection or tumours. NK cells are able to modulate inflammation through the release of cytokines and chemokines, enhancing macrophage activation. Inflammation mediated by lipids can also be facilitated by NKT cells, as these cells have a T cell receptor able to recognise lipid antigens presented by the molecule CD1d. CD1d can recognize antigens of dietary fatty acids, which ultimately will lead to NKT activation and increased influx of NKT cells in the liver [48,49].

1.1.3.2. Myeloid cells

Immune homeostasis in the liver is also dependent on the myeloid populations acting as the first line of defence against bacteria, toxins and injury of the tissue. This is achieved by resident liver cells such as macrophages, and recruited monocytes and neutrophils [5,48].

The liver innate immune system hosts the majority of tissue macrophages in the body, the Kupffer cells and monocyte-derived macrophages. Macrophages are involved in removing gut-derived foreign and toxic substances via phagocytosis and lysosomal activity [50–52]. In addition to phagocytosis of pathogens, macrophage activation leads to the production of cytokines, chemotactic and immunosuppressive factors, such as interleukin (IL)-1, IL-6, IL-10 and TNF-α. These mechanisms promote the generation of

regulatory T cells, and recruitment of monocytes which will ultimately modulate the inflammatory response and fibrogenesis [53,54].

In response to infection there is a rapid neutrophil infiltration followed by the recruitment of monocytes, and together they are able to regulate bacterial infection and stimulate liver regeneration. Their presence in the liver reflects the hepatic inflammatory status, as the flux of these cells is promoted by hepatocyte damage due to carbohydrate and cholesterol stimulus, production of reactive oxygen species (ROS) and intestinal bacteria delivered through the portal vein [55,56]. Neutrophils are also able to enhance the activity of macrophages, influencing macrophage polarisation and heterogeneity, which will determine their function. More importantly, the balance between neutrophils and monocyte-derived macrophages is tightly regulated as they can easily switch between a pro-fibrotic and pro-inflammatory functional phenotype to an anti-inflammatory pro-resolution state [57].

Therefore, the recruitment, activation and action of lymphocytes and myeloid cells play an important role in liver homeostasis, and these cells are notably essential in understanding the initiation and progression of liver diseases.

1.2. The evolving landscape of Non-Alcoholic Fatty Liver Disease

As described in the previous section, the dynamic regulation of carbohydrate, lipid and protein metabolism is essential for metabolic homeostasis and adaptation to nutrient availability and deficiency. Despite the complexity and organisation of the liver machinery, when any alteration at cellular or molecular level occurs, it can lead to organ function impairment and subsequent pathologies [31,58,59].

Nowadays, the increasing rates of obesity, alcohol consumption and environmental pollution all over the world, are related to an increased occurrence of the metabolic syndrome. The hepatic manifestation of the metabolic syndrome is reflected by the increase in incidence and prevalence of non-alcoholic fatty liver disease (NAFLD). NAFLD is characterized as a spectrum of liver diseases from simple steatosis (intrahepatic lipid accumulation) through inflammation (non-alcoholic steatohepatitis – NASH), to cirrhosis and hepatocellular carcinoma (HCC). These liver histological alterations occur in the absence of significant alcohol consumption or other causes of chronic hepatic liver disease [60,61].

NAFLD affects around 25% of the world population, and the progression of disease is usually associated with several co-existing risk factors. These include weight gain, obesity and diabetes, associated with high-calorie diets in the Western world, and genetic factors, such as race and ethnicity. Among patients with NAFLD, mortality can also be related to non-hepatic causes, such as cardiovascular events, kidney disease, hypertension, hyperlipidaemia and others [61–63].

1.2.1. Pathophysiology of NAFLD

Fatty liver is the earliest manifestation of NAFLD, and it is characterised by excessive intrahepatic lipid accumulation affecting more than 5% of hepatocytes. The progression of liver disease depends on the interaction of multiple variables, including hormonal, nutritional and genetic factors, and has been explained based on the "two-hit" model, proposed by Day *et al* in 1998 [64].

The first hit is characterized by the accumulation of triglycerides and fatty acids in the hepatocytes which is a consequence of insulin resistance, obesity and increased hepatic lipogenesis. As a result of this lipid metabolism dysregulation, insulin signalling is inhibited, glycogen synthesis decreases and gluconeogenesis is induced, thus further damaging glucose metabolism. Nevertheless, liver disease does not usually progress unless additional cellular events occur, known as the second hit. If the liver is continuously exposed to some of the factors that induce the first hit, the liver will trigger immune cells infiltration and inflammation, lipid peroxidation and mitochondrial dysfunction leading to hepatocyte damage and inflammation. Mechanisms driving lipotoxicity and cellular disfunction will ultimately lead to the development of fibrosis and subsequent progression to NASH [65–67].

Emerging evidence suggests that nutrient intake and energy expenditure have major impact on the severity of NAFLD outcome. Increased calorific intake derived from a high fat feeding and carbohydrate consumption play an important role in the initial process of fat deposition. Excessive fructose consumption in particular has been suggested to induce adverse metabolic effects associated with lipogenic processes in the liver, favouring NAFLD progression [62,68].

Bearing in mind that fructose consumption has increased in parallel with the global rise in NAFLD, there have been several investigations conducted in animals and humans to understand the causal relationship between them [69–74]. Dietary fructose has a distinct absorptive and metabolic process from glucose, being mainly absorbed in the small intestine. Subsequently, fructose is transported to the liver via the portal vein, where it will be metabolised by the ketohexokinase into fructose 1-phosphate. Fructose clearance in the liver occurs rapidly and efficiently, as the KHK activity is not dependent on the cellular energy status or hormonal feedback regulation. From here, aldolase B will cleave the molecule to produce dihydroxyacetone phosphate and D-glyceraldehyde, which can either enter the glycolytic pathway or be directed towards triglyceride synthesis [22,25].

In murine studies, fructose supplemented diets lead to accelerated obesity, hepatic steatosis and insulin resistance, by upregulating key lipogenic transcription factors such as Sterol Response Element Binding Protein 1c (SREBP1c) and Carbohydrate-Responsive Element-Binding Protein (ChREBP). These will increase lipogenic enzyme expression. Consequently, fructose intake seems to stimulate *de novo* lipogenesis, increase in triglyceride and fatty acids and mitochondrial function impairment [71,74,75].

In humans, the biological effects of fructose as a pivotal driver of NAFLD are still not fully understood, and additional studies are necessary [76]. Stanhope *et al* [69] studied the effects of sugar-sweetened beverages providing 25% of the energy requirements with ad libitum diets, during 10 weeks for 32 adults. They have found that fructose consumption promotes higher total and visceral adipose tissue deposition than glucose. Furthermore, this study demonstrated that long-term fructose but not glucose consumption increases hepatic DNL and limits fatty acid oxidation in the liver via production of malonyl-CoA. This leads to mitochondrial dysregulation, but also increased availability of fatty acids in circulation.

In a different approach, Abdelmalek *et al* [77] have used cross-sectional analysis with data from 427 adults registered in the NASH Clinical Research Network. Dietary information collected within 3 months of liver biopsy was used together with histological analysis and other study variables, such as age, sex, ethnicity and race. This revealed that a link between fructose consumption and metabolic abnormalities exists but is dependent on multiple factors. Worse outcomes were seen for older patients with high fructose intake, exhibiting exacerbated liver injury with increased fibrosis, which is seen at the histological level with lobular inflammation and ballooned hepatocytes. A few years later, the same team was able to link hepatic oxidative damage and lipid peroxidation with ATP depletion and uric acid generation due to fructose consumption [78]. A cohort of 25 diabetic adults was subjected to an intravenous fructose challenge to evaluate the relationship between dietary fructose, uric acid levels and hepatic adenosine triphosphate (ATP) depletion. Their study showed that, the higher the fructose consumption levels the less ATP would be found in the liver. ATP depletion during fructose metabolism generates adenine di- and mono-phosphate (ADP and AMP), which can either regenerate ATP or lead to uric acid accumulation. In more severe ATP depletion scenarios, hyperuricemia can occur which will lead to worse NAFLD prognosis.

More recently, Berneis and co-workers [79] have performed a crossover study in 34 healthy men, measuring the effects of adding different types of sugar in sweetened beverages on fatty acid metabolism, during a three-week intervention. Results were obtained after each intervention from a fasting total plasma fatty acid composition measurement. The study showed that only fructose was able to increase fatty acid synthesis, showing increased palmitate abundance, whereas both fructose and sucrose were able to increase fasting long-chain acyl-carnitines impairing β-oxidation flux.

In summary, even though the impact of fructose in NAFLD development and progression has been suggested to affect lipid metabolism and insulin sensitivity, further and more complete clinical studies are necessary. The precise mechanisms by which fructose impacts liver metabolism are still unknown. Most studies using animal models do not accurately represent specific properties and hepatic consequences that occur during human disease progression as the diet choices are still lacking consistency in terms of nutrient sources and feeding formulations. Furthermore, experimental times and length of exposure to high fat diets and sugar consumption have been quite short, which ultimately are inadequate when trying to understand long-term effects of fructose consumption. In human studies, even though improvements have been made in the past years to understand the relationship between fructose and NAFLD development, a high number of variables has still not been addressed. Genetics, gender, diet and environmental factors should also be accounted when trying to understand the metabolic alterations. Therefore, specific metabolic pathway analysis can be extremely valuable when performing new clinical studies, trying to investigate the efficacy of new diagnostic methods and therapies.

1.3.Diagnostic approaches and current therapies for NAFLD

Livers of patients with steatosis, usually contain large and small lipid droplets within the hepatocytes. Sometimes, localised inflammation can also be present (steatohepatitis) and this distinguishes the progressive form of NASH from the non-progressive form. However, diagnosis and staging of fatty liver disease still represents a major challenge, as there is much overlap in biochemical and serological characteristics with other chronic liver conditions. Similarly it is important to measure where a person lies on the NAFLD spectrum as mortality and outcome, as well as likely clinical management strategies vary depending on disease stage [37].

Diagnosing NAFLD appearance and progression poses a challenge to clinicians because the occurrent metabolic disturbances are both multifactorial and complex. Most commonly used techniques are based on serum and imaging tests as well as the interpretation of liver specimens after a biopsy [80]. Initial monitoring and diagnosis of liver injury and disease is performed by investigating multiple serum markers including transaminases (alanine and aspartate transaminases, ALT and AST), γ-glutamyl transferase (GGT), alkaline phosphatase (ALP), bilirubin and albumin [81]. Briefly, their value as diagnostic tools is associated with maintenance of liver functions such as synthesis, excretion and detoxification. While elevated serum ALT or AST are associated with hepatocyte damage and inflammation, increased ALP levels are indicators of biliary obstruction [39,82]. Albumin is a protein synthesised by the liver only, so reduced levels in serum are usually an indicator of impaired hepatic synthetic function. Thus alterations in albumin concentration are seen during sepsis, inflammatory disorders or fibrosis [83]. Bilirubin on the other hand, is a product of haemolysis that is transported to the liver to be excreted. Hyperbilirubinemia is usually associated with parenchymal liver disease or

obstruction of the biliary system, and patients exhibit signs of jaundice [84] when levels in blood exceed 2-3 mg/dl.

Nevertheless, although initial abnormal liver blood tests provide valuable information on the liver status, their fluctuations can be influenced by other mechanisms such as cardiovascular disease and diabetes. They are also non-specific signs of injury rather than pointers to a specific aetiology. Therefore, they should be interpreted together with past medical information (BMI, comorbidities, family history). A clear diagnosis should be obtained together with further clinical testing, either with non-invasive techniques such as ultrasound and computed tomography to detect hepatic fat, or by following a more invasive approach like a liver biopsy [85].

Considering that NAFLD encompasses a spectrum of liver diseases, it is difficult to assess in which stage patients find themselves using non-invasive methods. Thus, the liver biopsy is still the "gold standard" practice to stratify and separate patients with only steatotic features from those who demonstrate inflammatory infiltration and fibrosis. Even though performing a liver biopsy permits direct histological evaluation of the tissue, allowing for grading and staging, it is too expensive and invasive to use widely as a screening tool [86,87]. Any new non-invasive clinical test should meet the requirement for diagnostic sensitivity and specificity and ability to follow-up progression of disease for treatment and prognosis. Therefore, the aforementioned methods still have limitations, variable diagnostic accuracy and lack of validation. This has led to significant advances in other techniques such as nuclear magnetic resonance (NMR) spectroscopy, and magnetic resonance imaging (MRI) and elastography [65,87–89].

Accurate prediction of disease progression based on unique drivers of disease, such as genetic and metabolic factors is still missing. There is also as yet, no licenced therapy

for NAFLD [90]. To improve metabolic factors driving hepatic steatosis, involving glucose and lipid metabolism, the first-line therapeutic option still relies on lifestyle intervention measures. Modification of diet and exercise leading to weight loss have been shown to improve liver function tests, degree of steatosis and even histological resolution of steatohepatitis [91–93].

Regardless of the benefits from lifestyle measures, resolution of NAFLD with long-term intervention still faces challenges and motivation limitations. Additional pharmacological intervention is recommended for the management of disease as there are multiple conditions co-occurring with liver disease, such as insulin resistance, hypertension and hyperlipidaemia. Therefore, many therapeutic approaches and clinical trials have been developed based on new molecular targets, including insulin sensitizers (metformin, thiazolidinediones), lipid lowering drugs (statins, polyunsaturated fatty acids), anti-oxidants (vitamin E, betaine) and probiotics [80,94,95].

Efforts have been made to address the knowledge gap regarding NAFLD diagnosis and prognosis with clinical trials outcomes. The application of metabolomics can provide a better understanding of the safety, robustness and durability of new treatment options [65]. The detection of essential non-invasive biomarkers is relevant for disease phenotyping, to identify metabolic pathways variations and linking to risk factors in the general population. Thus, novel clinical approaches involving the integration of metabolomics in liver disease diagnosis and treatment efficiency are promising for patients in the future [89,96,97].

1.4. Metabolic studies using NMR spectroscopy

Biological systems can be defined as a complex network of cellular metabolites that exist and interact in a dynamic steady state with their surroundings. These metabolites are endogenous small molecules (<1000 Da) that participate in the major metabolic pathways in nearly every cell and compose the metabolome. They include the building blocks for macromolecules such as amino acids, lipids, nucleic acids and carbohydrates. Therefore, the determination and quantification of metabolites that compose the cellular metabolism allows to estimate cellular function and the overall physiological status of an organism [98–100].

The field of metabolomics refers to the analysis of metabolite concentrations and fluctuations in biological systems and may be used to characterise metabolic disturbances in response to stimuli, including disease, genetic modifications or even drugs. Assessment of metabolic profiles and understanding pathway activity can provide valuable biological insights about human health and also determine the efficacy of new therapies [101,102].

The most commonly used analytical techniques in metabolomics studies are mass spectrometry (MS) and nuclear magnetic resonance (NMR) spectroscopy as they enable the detection of numerous metabolites in a single measurement. Both techniques have different strengths and limitations, hence the choice of the analytical platform will depend on the study purpose. Despite the lower sensitivity, NMR-based metabolomics has significant advantages that are beneficial to biomedical research. NMR spectroscopy has excellent reproducibility and quantitative accuracy, it enables unambiguous identification of unknown molecules (important when analysing complex mixtures) and samples remain intact after analysis, allowing the combination with other methods such as MS [103–105].

1.4.1. Basic principles

NMR spectroscopy is an analytical technique based on the physical properties of atomic nuclei that can be used to determine molecular structures. An atomic nucleus can be seen as a charged particle in motion; therefore, it has an angular momentum (P) which can be quantified as a nuclear spin quantum number (I). The overall spin of an atom depends on its nucleon content and when $I > 0$ it generates a magnetic moment (μ) which is detectable by NMR [106,107]. The relationship between magnetic moment and angular momentum can be obtained by the following equation (Equation 1.1):

Equation 1.1 $\mu = \gamma P$

where, μ is the magnetic moment, γ is the gyromagnetic ratio (a characteristic constant of a specific nucleus) and P the angular momentum. The magnetic quantum number is dependent on spin orientations (nuclear spin states) in relation to the spinning axis of the nucleus, and can them be defined as follows (Equation 1.2 and 1.3):

Equation 1.2 $P = \hbar m_I$

Equation 1.3 $\mu = \gamma \hbar m_I$

Where m_I is the magnetic quantum number, ħ=h/2π being h is Planck's constant. The magnetic quantum number for detectable nuclei by NMR can have $2I + 1$ orientations relative to an axis. For an I = ½ nucleus this allows for two possible states, α and β with m_I = +½ (α state) or -½ (β state).

The most commonly observed spin ½ nuclei in NMR include protons (^{1}H) (99.08% natural abundance), the carbon isotope ^{13}C (1.11% n. abundance), phosphorus (^{31}P)

(100% n. abundance) and the nitrogen isotope ^{15}N (0.37% n. abundance). These atoms have opened avenues for NMR to be used to characterise biological molecules due to their ubiquity in proteins and metabolites. When spin ½ nuclei are placed in an external static and homogeneous magnetic field (B_0) these spins are observed in two different energy levels, with an energy difference of $\Delta E = \gamma \hbar B_0$, as depicted in Figure 1. 5 [106,108].

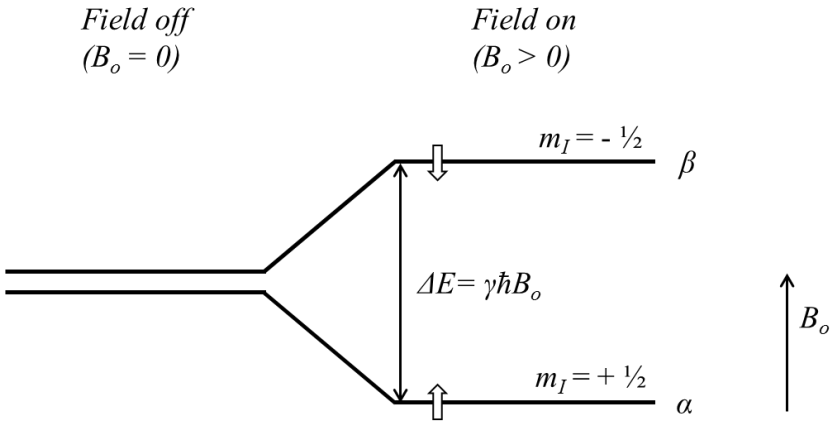

Figure 1. 5 – Schematic representation of the nuclear spin energy levels of a spin- ½ nucleus in a magnetic field. The energy difference between the two states is given by $\Delta E = \gamma \hbar B_0$, where ΔE is the energy difference between the two states, m_I the magnetic quantum number, $\hbar = h/2\pi$ (where h is Planck's constant 6.6260693(11) x 10^{-34} J.s) and B_0 the magnetic field.

After polarisation builds up in a magnetic field, detectable transverse magnetisation can be generated by a radio frequency (RF) pulse at a frequency that matches ΔE. As a consequence, the spins start to precess around the z-axis with the Larmor frequency. This precession gives rise to an alternating magnetic field in the x,y-axis that can be observed by a receiver coil. The simplest NMR experiment would therefore consist of an RF pulse applied to spin ½ nuclei in a magnetic field, followed by acquiring the signal arising from the resonance that was induced by the initial pulse. After the RF pulse is turned off, the magnetisation is re-established along the z-axis (longitudinal relaxation process, T_1), and

nuclei return to the low-energy state. In addition, transverse relaxation (T_2) causes loss of coherence in transverse plane, leading to a decaying signal, termed free induction decay (FID).

The longitudinal relaxation, T_1, refers to the time that a sample needs to recover the magnetisation in the z-axis, approaching a thermal equilibrium state (equation 1.4). Therefore, T_1 determines the interscan delay (recycle time) that needs to be sufficiently long to avoid saturation. Full relaxation between scans is required if one wants to interpret intensities quantitatively. On the other hand, transverse magnetisation, T_2, is defined by spins interactions, where they can modify their precession rate causing a loss of phase coherence in the x,y-direction. Thus, as the signal is under the influence of T_2 relaxation observed in the form of an FID it can determine the signal line width (equation 1.5). The superimposition of the frequency of nuclei in the sample subject to exponential T_2 relaxation can be converted into a frequency domain spectrum using a Fourier transformation [109,110].

Equation 1.4 $$M_z(t) = M_0(1 - e^{\frac{t}{T_1}})$$

Equation 1.5 $$M_{x,y}(t) = M_0\, e^{-\frac{t}{T_2}}$$

Where M_z is the magnetisation of the sample in the z-axis over time (t), $M_{x,y}$ is the magnetisation in the x,y-axis over time (t), and M_0 refers to the thermal equilibrium magnetisation of the sample.

In order to obtain an NMR signal, the number of nuclei populating the two energy levels must be different, and the detected signal will be proportional to the total magnetic moment of the sample. The population difference which determines the signal intensity of the total number of spins (N) that are aligned in parallel with the B_0 field and those that are anti-parallel, is dependent on the magnetic field strength. When the B_0 field strength is increased this will lead to a larger energy gap between the spin energy states, which will ultimately lead to a more intense signal.

Other important factors that influence the sensitivity of the NMR signal are the gyromagnetic ratio of a specific nuclei and the temperature of the NMR measurements [111]. Lower temperatures reduce the noise levels by cooling the wires of the detection coil and the preamplifier. Factors that influence the sensitivity of the NMR detection are summarised in equation 1.6 and equation 1.7 allows to calculate the percentage of polarisation [109,112,113].

Equation 1.6

$$\frac{N_\alpha}{N_\beta} = e^{-\frac{\Delta E}{kT}} \rightarrow \frac{N_\alpha}{N_\beta} = e^{-\frac{\gamma \hbar B_0}{kT}} \rightarrow N_\alpha = N_\beta \times e^{-\frac{\gamma \hbar B_0}{kT}}$$

Equation 1.7

$$\frac{N_\alpha - N_\beta}{N_\alpha + N_\beta} = \frac{N_\beta \times e^{-\frac{\gamma \hbar B_0}{kT}} - N_\beta}{N_\beta \times e^{-\frac{\gamma \hbar B_0}{kT}} + N_\beta} = \frac{e^{-\frac{\gamma \hbar B_0}{kT}} - 1}{e^{-\frac{\gamma \hbar B_0}{kT}} + 1} = \tanh\left(\frac{\gamma \hbar B_0}{kT}\right)$$

Where N_α and N_β represent the population of nuclei in α and β energy states, ΔE is the energy difference between them, k is the Boltzmann constant (1.3807×10^{-23} joules per Kelvin), γ is the gyromagnetic ratio of a specific nucleus, B_0 is the external magnetic field, $\hbar = h/2\pi$ where h is Planck's constant, and T is the temperature in Kelvin.

1.4.2. Significant features of NMR instrumentation

The acquisition of NMR spectra is performed by NMR systems that are composed of a magnet, a probe, a RF transmitter, a receiver and a signal-recording device. In the past decades, the sensitivity of NMR spectroscopy has been improved with the introduction of stronger magnets, more sensitive receivers to amplify the NMR signals, and in particular with improved probes [114,115]

If we consider equation 1.7, we can see that the sensitivity of NMR is proportional to the B_0 field strength and the distribution of energy states of specific nuclei. Superconducting magnets with higher field strengths have improved the signal to noise (S/N) ratio of the NMR signal and spectral resolution due to larger signal dispersion. Nowadays, design of new magnets has led to the significant increase in magnetic field strengths, ranging from 40 MHz to 1.2 GHz for proton resonance frequencies. However, these high fields are not necessarily practical for small molecule NMR spectroscopy as strong couplings increase with field strength yielding more complex spectra that require simulations for interpretation. [105,116,117]

Another significant improvement for the field of metabolomics is related to probe performance. NMR probes are placed in the centre of the magnetic field, containing RF coils that can be tuned at specific frequencies to excite specific nuclear spins and detect the NMR signal. Besides the probe diameter reductions, primarily associated with the NMR tubes used (10 mm to 1.7mm in diameter) allowing smaller sample size, the major contributor to sensitivity rise is related to the introduction of cryogenic probes. Initially demonstrated by Styles *et al* in 1984 [115], the sensitivity enhancement in the cryogen probe is accomplished by keeping the RF receiver coils at low temperature, reducing their resistance [114,117,118]. Modern probes also keep the preamplifiers at 20 K in order to minimise thermal noise impairing the small amplitude of the NMR signal. By using

cryogenic probes the S/N ratio gain obtained is between 4 and 10, as it was demonstrated in 2001 by Serber *et al* [119] and more recently by our group [120], offering great advantages for the field of metabolomics. Cryoprobes have a disadvantage for salty samples [119], mainly owing to losses caused by the electric field, although modern probes have coil designs that minimise such losses, as well as the use of lower volume and specially shaped NMR tubes [121]. Moreover, the 1.7mm cryoprobes now available offer much improved mass sensitivity yielding a significant S/N advantage specifically for mass limited samples.

Although not explored in this thesis, other approaches offered significant sensitivity enhancements in NMR spectroscopy, including hyperpolarisation techniques such as dynamic nuclear polarisation (DNP) [122,123], optimisation of sample volume and solubility [124,125], as well as pulse sequence refinements [104,119,126,127]. While hyperpolarisation has great potential in conjunction with MRI [128], its potential is currently too limiting in resolving signals from a wide range of metabolites. The main constraint is that the dissolution DNP approach is massively limited by the *T1* relaxation time of the observed metabolites. Efforts have been made to use probes with longer relaxation times, as Wilson *et al* [129] demonstrated using [1,1-^{13}C] acetic anhydride with amino acid mixtures in order to hyperpolarize biomolecules of interest. Nevertheless, these approaches are not ready to be used to determine label incorporations in a wide range of metabolites.

1.4.3. Fundamentals of NMR acquisition and interpretation

1.4.3.1. Chemical shifts and spin-spin interactions

In the previous section, the physical principles on which NMR spectroscopy is based were briefly described to show how an NMR spectrum can be obtained. An NMR signal from a given molecule depends on ratio and distribution of nuclei populating the different energy levels when placed in an external homogeneous magnetic field. Also, the different chemical environments of the nuclei give rise to NMR signals at different frequencies as a result of the nuclear shielding effect. The magnetisation experienced by each nucleus depends on the interactions occurring between the nuclear spins and the effect of the electrons surrounding them, giving rise to signals at different positions of the NMR scale [106].

To set the NMR scale, reference compounds such as tetramethylsilane (TMS) are used to define the zero in the chemical shift scale. The chemical shift of a specific nucleus is measured as the distance between the TMS signal and the sample signal. Chemical shifts of a nucleus (< 6000 Hz) are much smaller than the total field strength (600 MHz, for example) and can be presented in parts per million (ppm), which is a constant unit independent of the frequency of the operating spectrometer [106,110]. Frequency values are converted to as follows:

Equation 1.8 $$\delta = \frac{\nu_{sample} - \nu_{standard}}{\nu_{spectrometer}} \times 10^6 \rightarrow \delta = \frac{\Delta\nu}{\nu_{spectrometer}} \times 10^6$$

where δ is the chemical shift in ppm, ν_{sample} is the resonance frequency of the sample, $\nu_{standard}$ is the resonance frequency of the standard (TMS), and $\nu_{spectrometer}$ is the spectrometer frequency in Hz. As the standard is set to zero by definition, the equation can be simplified as the second form.

For a proton spectrum, the absorption regions of functional groups generally fall within a range of δ 0 – 12 ppm. The shift of resonances is dependent on the degree of shielding from the surrounding electrons, where more shielded nuclei resonate at lower frequencies (lower chemical shifts), whereas less shielded nuclei, such as those with electronegative neighbours (e.g., N, O, Cl), resonate at higher frequencies (higher chemical shift). The characteristic functional groups in organic compounds and their chemical shifts in a ^{1}H spectrum are presented in Figure 1. 6 [108,113].

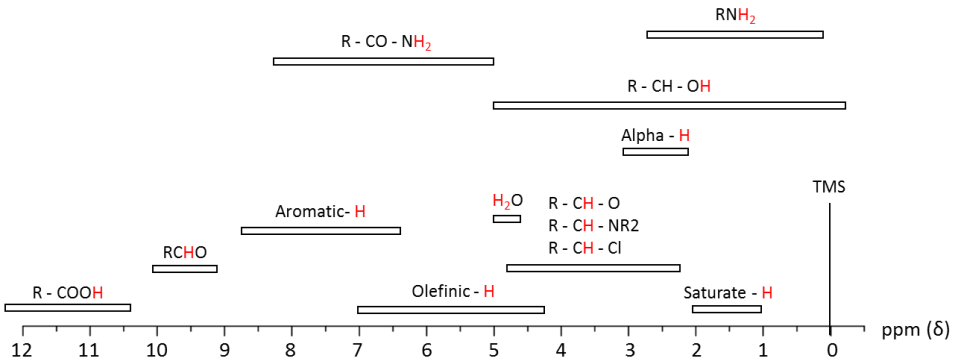

Figure 1. 6 – Typical ^{1}H chemical shift ranges (in ppm) of some functional groups. Based on Metin Balci's book [113].

Interactions between neighbouring spins in the same molecule that are linked via chemical bonds give rise to scalar or *J*-couplings. The coupling between spins is usually observed if they are separated by less than 5 chemical bonds and can occur as homonuclear scalar couplings (e.g. ^{1}H-^{1}H) or as a heteronuclear coupling (e.g. ^{1}H-^{13}C). Nuclei under the influence of a scalar coupling will experience the external magnetic field B_0 differently and will resonate at different values creating coupling patterns. The distance between the nuclei under consideration, in Hertz, corresponds to the coupling constant, *J*. These couplings will distribute the signal intensity over smaller peaks, hence

the multiplicity and magnitude of the couplings will provide information about the number of neighbouring protons and the molecular structure [109,130].

1.4.3.2. 1D and 2D NMR experiments

Analysis and characterisation of multiple metabolites in biological samples (cells, tissues, biofluids) is usually performed by acquiring one-dimensional (1D) ^{1}H NMR spectra. Structural and quantitative information can be obtained, as the signal in a spectrum is proportional to the number of protons from which the resonance arises. Therefore, metabolite concentrations can be obtained, providing information about the intra- and extracellular environment. Metabolite variations can then be associated with changes in particular metabolic pathways, overall cellular metabolism in response to external stimuli, availability of substrates, pH changes and temperature [103,131].

NMR-based metabolomic analysis of biological samples is usually carried out in aqueous solutions (which can be deuterated), thus the spectrum will be dominated by a strong water signal which, if unsuppressed, would saturate the dynamic range of the receiver. To improve the overall quality of the spectrum, solvent suppression schemes need to be employed [132]. The effective use of pre-saturation pulses to selectively saturate the water signal and improve the information content of the spectra was already reported in 1983 by Haasnoot and Hilbers [133]. Since then, several pulse sequences have been developed to improve water suppression, including WATERGATE [134], 1D diffusion-edited spectra [135] and 1D NOESY (nuclear Overhauser effect spectroscopy) pre-saturation (NOESYpresat) [136].

The most widely used pulse sequence in metabolomics studies has been the 1D NOESYpresat, as stated by Beckonert *et al* [137] and explained by McKay *et al* [126]. The

water suppression in a 1D NOESYpresat is achieved by adding a pre-saturation preparation block at the water frequency during relaxation delay and mixing time (see Figure 1. 7) [138].

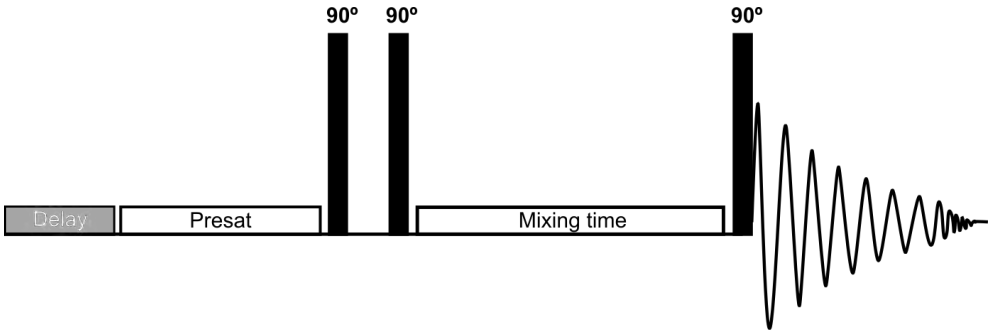

Figure 1. 7 – Schematic illustration of the 1D NOESYpresat pulse sequence. The sequence begins with a long, lower power saturation period during the relaxation delay allowing for the selectivity of the solvent resonance. After the delay (for equilibrium recovery) and pre-saturation period, there are two 90 º pulses followed by a mixing period (specific delay) and to finish another 90 º pulse and acquisition. (Based on noesypr1d sequence from Bruker topspin pulse sequences library)

Following improvements in solvent suppression and improved quality spectra, analysis of 1D ^{1}H spectra can provide information regarding chemical shifts, signal multiplicities, coupling constants and relaxation times. However, complex biological samples comprise many overlapping signals due to the narrow range of metabolic shifts, thus metabolite assignment becomes very difficult and ambiguous. For better spectral resolution, the acquisition of 1D ^{13}C NMR spectra can be useful, as the chemical shift range for ^{13}C is much higher than for protons. Still, the ^{13}C nuclei have a long T_1 relaxation delay, which requires long repetition delays and as a consequence long acquisition times. This approach would not be suitable for large sample numbers as acquisition of spectra with acceptable S/N would be very time consuming (compared with ^{1}H) [130,139].

Two-dimensional (2D) NMR spectroscopy is usually employed to aid spectral interpretation of complex samples and overcome chemical shift overlap. The 1D NMR spectrum is obtained as a single time variable in a FID and is represented as a function of one frequency variable. On the other hand, the 2D NMR spectrum is a result of the FID signals collected from multiple experients with two evolution times (t_1 and t_2) in a constant time interval, plotted as a function of two frequency dimensions [109,130].

Any 2D experiment will be composed of four building blocks, including preparation, evolution, mixing and detection. During the preparation time, the spins of the first nucleus are excited by one or more pulses, and the resulting magnetisation will evolve during the inter-pulse delay t_1 (evolution). During the evolution time, a further pulse or sequence of pulses are applied, and a transfer of magnetisation will occur within an interacting pair of spins (scalar coupling – bonds, or dipolar interaction through space – NOE). Finally, the signal will be recorded as a function of t_2 acquisition time. The experiment is repeated using increasing t_1 values until sufficient data is recorded, and an FID as a function of t_2 for each value of t_1 can be obtained. After applying a Fourier transformation, the resulting plots allow to investigate interactions between pairs of spins that create cross-signals depending on the transfer of magnetisation that occurred during the pulse sequence [109,110].

Most commonly applied metabolomics experiments include homonuclear experiments, revealing information on ^{1}H-^{1}H spin connectivities, such as correlation spectroscopy (COSY) and total correlation spectroscopy (TOCSY). For tracer-based metabolism experiments, these are particularly important as the gyromagnetic ratio of protons is about four times higher than the ^{13}C gyromagnetic ratio ($\gamma_{1H} = 4 \times \gamma_{13C}$). Therefore, ^{1}H-observed experiments are more sensitive than their ^{13}C-observed

counterparts. Nevertheless, the use of heteronuclear experiments to investigate the interaction between two different nuclei offers improved information for assignment purposes as it resolves peaks that are still overlapped in homonuclear 2D spectra.

The application of heteronuclear single-quantum correlation spectroscopy (HSQC) is particularly important as it permits to study the scalar coupling between two different types of nuclei, usually ^{1}H with ^{13}C or ^{15}N. This becomes particularly significant for tracer-based metabolic approaches, using ^{13}C-labelled precursors to follow ^{13}C-enrichments in metabolites of specific metabolic pathways. When acquired with high resolution, signal intensity increases, multiplicity and ^{13}C-^{13}C coupling (J_{CC}) information can be obtained providing valuable details about metabolic features. For example, the use of ^{13}C-glucose tracers allows to follow glycolysis by observing ^{13}C-isotopomers of pyruvate, lactate and alanine and, if ^{13}C-labelled carbons are transferred through the TCA cycle, ^{13}C-isotopomers of glutamate, malate and aspartate are also commonly identified. Therefore, 2D ^{1}H-^{13}C HSQC experiments can provide information related to metabolite transformations through glycolysis and the TCA cycle, by analysing the specific position of ^{13}C in key metabolites [99,137,139,140].

In a 2D ^{1}H-^{13}C HSQC experiment, as the natural abundance and gyromagnetic ratio of protons is much higher than the heteronucleus (^{13}C), the sequence starts with proton magnetisation, and is later transferred to the ^{13}C using an INEPT (insensitive nuclei enhancement by polarization transfer) block to allow for evolution under the influence of ^{13}C chemical shifts and ^{13}C-related couplings during t_1. After the evolution period (t_1), the magnetisation is transferred back to the proton for acquisition (inverse experiment), for acquisition at the sensitivity of the proton [109,141].

The pulse sequence of an HSQC can be better understood by describing its building blocks, as represented in Figure 1. 8. As said before, the sequence starts with an INEPT pulse train, which permits the polarisation transfer between the ^{1}H to the ^{13}C if they are directly bonded (J_{CH}). Next, the ^{13}C magnetisation evolves during the evolution period t_1, and a 180 º pulse in the proton sequence is applied in the middle of this period to refocus ^{1}H-^{13}C coupling constants. Then, another INEPT-like pulse train is applied to convert the ^{13}C magnetisation to in-phase ^{1}H magnetisation to be observed. In the end, proton acquisition is performed while ^{13}C are continuously decoupled [109,127,142].

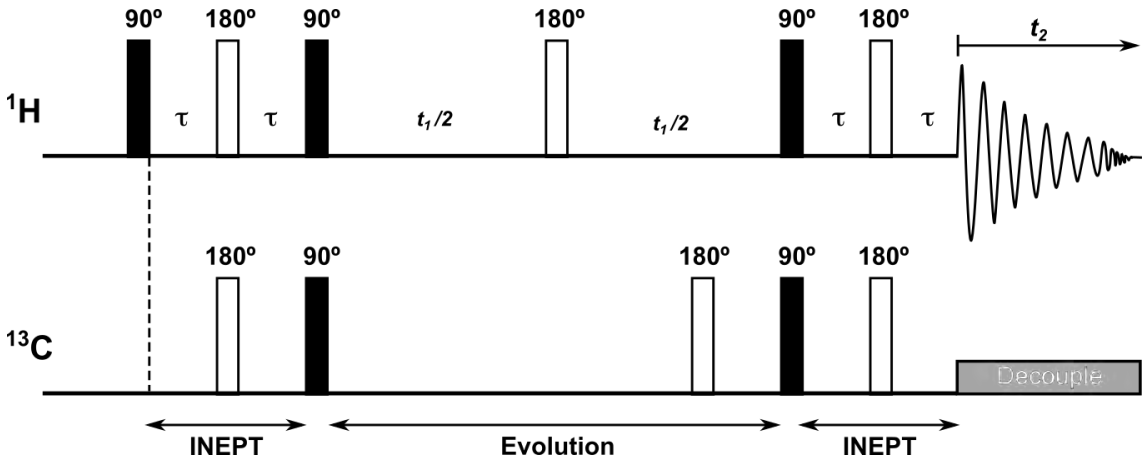

Figure 1. 8 – Schematic illustration of the ^{1}H-^{13}C HSQC pulse sequence. (Based on hsqcph sequence from Bruker topspin pulse sequences library).

1.5. Scope of this work

The increasing rates of non-alcoholic fatty liver disease worldwide have become a major concern in health care leading to a rising need to study and understand liver metabolism in healthy and diseased contexts. The influence of dietary constituents on the severity of NAFLD outcome has gained special attention over the past few years, where fructose has been considered particularly harmful [61,143,144]. In order to understand the hepatic response to fructose and high fat diet feeding, and its pathological consequences, new models able to recreate the human disease have been developed and extensively reviewed [145–147]. However, further research is necessary to develop more accurate and robust models to provide increased clinical significance when testing new therapeutic approaches.

Therefore, the overall aim of this thesis was '*to study the metabolic fingerprint of the liver at different stages of NAFLD pathogenesis and progression'*. This was achieved by employing a variety of immunological and analytical techniques, including flow cytometry, histological examination and NMR spectroscopy in both human and animal models. To do this I focused on a series of specific experimental objectives:

First, I needed to characterise and optimise the best method for NMR metabolic profiling and disease characterisation using mammalian cells lines and primary cells (chapter 3).

Then I wanted to validate my optimised methodology using an *in vitro* model of steatosis where the metabolic effects of lipid accumulation on the cellular metabolome could be assessed. Subsequently, I compared these *in vitro* metabolic adaptations to human *ex vivo* samples to understand how liver metabolism adapts during NAFLD

progression, and whether in vitro models recreate the physiological picture in humans (chapter 4).

Next, I sought to develop a mechanistic understanding of the weight gain and hepatic metabolic changes in carbohydrate and lipid metabolism, inflammation and liver enzymes alterations following external stimuli such as a high fat diet and sugars using a murine model. This meant I had to characterise a murine NASH model (chapter 5).

Finally, to validate my findings and test whether my methodology could be applied to a potential therapeutic situation in humans, the potential of a ketohexokinase inhibitor as a novel therapeutic target in NAFLD was investigated. Here I used both the animal model and a human perfusion model that I developed during this project (chapter 6).

CHAPTER 2

MATERIALS AND METHODS

2. Methodology

2.1. Isotopes and antibodies used in this study

Table I – Cortecnet isotopes used for metabolic tracer-based studies

Catalog #	Description
CC790P10	D-Fructose-[U-13C], 99% 13C
CC858P1	D-Glucose-[1,2-13C], 99% 13C
CC860P1	D-Glucose-[U-13C], 99% 13C

Table II – Antibodies for Flow Cytometry

Company (Ref #)	Description	Species/Clone	Format	Size
BD Biosciences (553164)	NK-1.1 (NKR-P1B and NKR-P1C)	Mouse, PK136	FITC	0.5 mg
BD Biosciences (553048)	CD4(L3T4)	Mouse, RM4-5	PE	100 µg
BD Biosciences (550994)	CD45 (Leukocyte Common Antigen)	Mouse, 30-F11	PerCP-Cy5.5	100 µg
BD Biosciences (553035)	CD8a (Ly-2)	Mouse, 53-6.7	APC	100 µg
BD Biosciences (553311)	CD11b (Integrin αM chain, MAC-1a)	Mouse, M1/70	PE	200 µg
Biolegend (108412)	Ly-6G/Ly-6C(Gr-1)	Mouse, RB6-8C5	APC	100 µg
Biolegend (100233)	CD3 (T3)	Mouse, 17A2	BV510	125 µl
Biolegend (115538)	CD19 (B4)	Mouse, 6D5	BV421	500 µl
Biolegend (123108)	F4/80 (EMR1, Ly71)	Mouse, BM8	FITC	500 µg
Biolegend (100214)	CD3 (T3)	Mouse, 17A2	PB	100 µg
Biolegend (423105)	Zombie NIR™ Fixable Viability	Mammalian cells	APC/Cy7	100 tests

Table III – Ketohexokinase (KHK) study (antibodies and inhibitors)

Company (Ref #)	Description	Species/Clone
ATLAS Ab Anti-KHK HPA007040 (0.05 mg/ml)	KHK total	Rabbit polyclonal
Insight Biotechnology KHK-A #21708-2 (1 mg/ml)	KHK A	Rabbit polyclonal
Insight Biotechnology KHK-C #21709-2 (1mg/ml)	KHK C	Rabbit polyclonal
Thermo Fisher β-actin # PA1-46296 (1mg/ml)	β-actin	Rabbit polyclonal
Dako (P0448) Goat Anti-Rabbit Immunoglobulins/HRP	Horseradish peroxidase-conjugated antibody	Rabbit polyclonal
TAKEDA (confidential)	KHK inhibitor	–

2.2. Human cell-based model systems

2.2.1.1. Cell culture methods

The hepatocellular carcinoma cell line, HuH7, was available in house. Cells were grown as monolayer cultures in Dulbecco's Modified Eagle Medium (DMEM, Invitrogen) supplemented with 1% penicillin-streptomycin, and 10% (v/v) heat inactivated fetal bovine serum (FBS, both Invitrogen), in a humidified atmosphere of 5% CO_2 at 37ºC in 75 cm^2 Corning flasks. The cultures were routinely subcultured every 3 days (when they reached 80% confluency) using trypsin to detach the cells from the flask. Briefly, the spent media was discarded, the flask was washed with 10ml phosphate-buffered saline (PBS) and the PBS was discarded. Then, 2 ml of trypsin was added to the flask and incubated for 5 minutes. After microscopic assessment to confirm the cells were detached, 5 ml of media was added to the flask to inactivate the trypsin. In triplicate, 1ml of this mixture was then inoculated into 9 ml of media and the flasks were incubated again at 37ºC.

2.2.1.2. *In vitro* model of hepatocyte steatosis

To generate an *in vitro* model of hepatocyte steatosis, HuH7 cells were grown as explained above (2.2.1.1). To induce fat-overloading of cells, they were exposed to oleic acid for 24 hours at a concentration of 2 mM when they reached around 70% confluency.

2.2.1.3. Isotopic labelling of cells

For tracer-based metabolic analysis, cultured cells were transferred to a glucose-free DMEM (Thermo Fischer, UK) and then supplemented with labelled precursors. Pilot experiments indicated that sufficient time should be given before metabolite extraction

in order to obtain an average cell yield of 10-15 x 10^6 cells per sample, the required cell density to provide a strong signal for NMR analysis. Cells were cultured with tracers for varying time points (0.5 - 24 hours) prior to intracellular metabolite extraction.

2.3. Studies using whole tissue samples from human and mouse livers

Human liver samples used for analysis were taken from explanted organs collected during transplantation or tumour resections performed at the Queen Elizabeth Hospital (Birmingham, UK) after written, informed consent was gained from patients and under local ethics committee approval (Local Research Ethics Committee: reference number 06/Q2702/61). Samples were collected from patients with Alcoholic Liver Disease (ALD), Non-Alcoholic Steatohepatitis (NASH), hepatocellular carcinoma (HCC) Primary Biliary Cholangitis (PBC) and donor material was collected from livers surplus to requirements for transplantation. These donor tissues typically exhibited signs of steatosis. Slices from human tissue explants approximately 8 cm^3 were stored in DMEM at 4 °C before processing, and material was used within 6 hours of collection.

For mouse studies, all procedures were performed under Dr Patricia Lalor's Home Office Project License number P2DF9DB6E and my Personal License number I3879CBCA. All procedures had been reviewed and approved by the local research ethics committee. Upon sacrifice, mouse livers were collected and divided into three blocks: one for formalin fixation and histological analysis; a second one for liquid nitrogen snap freezing and storage at -80 ºC; and a third one was placed in cold Roswell Park Memorial Institute (RPMI) 1640 Medium for isolation of resident hepatic immune cells and staining using flow cytometric analysis.

2.3.1.1. Histology

2.3.1.1.1. Haematoxylin and Eosin (H&E)

Haematoxylin and Eosin (H&E) staining of human and mouse liver tissue was performed in order to assess the tissue morphology, and presence of steatosis and fibrosis.

For the staining procedure, 5 µm sections of human and mouse liver tissue were stained with Haematoxylin and Eosin, according to in house protocols with sequential baths in the reagent series indicated in Figure 2. 1 for various time points as indicated. Following completion of the staining protocols, sections were then mounted in DPX mountant (Leica, UK) and covered with a 24x40 mm coverslip according to standard protocols. Sections were allowed to dry for 24 hours before representative bright field images were collected using a Zeiss Axioscope microscope and Axiovision software.

HE staining	Xylene 2 min (3x)
	Alcohol 2 min (2x)
	Water 2 min (2x)
	Haematoxylin Harris 4 min
	Water 2 min
	Acid Alcohol 30s
	Water 2 min
	Scott's Tap Water Substitute 30s
	Water 2 min
	Eosin 1 min
	Water 2 min (2x)
	Alcohol 2 min (4x)
	Xylene 2 min (3x)
	Mount in DPX

Figure 2. 1 – Protocol for histological staining using H&E.

2.3.1.2. Immunohistochemical analysis of KHK expression in human tissue

To assess the cellular expression of KHK in human tissue samples I performed an indirect immunochemical detection on 6 µm paraffin-embedded tissue sections. Staining was performed on material from normal (from deceased patients of non-hepatic causes and from livers surplus to requirements for transplantation), steatotic, non-alcoholic steatohepatitis (NASH), alcoholic liver disease (ALD), hepatocellular carcinoma (HCC) and primary biliary cholangitis (PBC) patients. Sections were immersed in xylene and alcohol wells for dewaxing, followed by rehydration in water. A heat-induced antigen retrieval step was performed to improve antibody-epitope binding using an antigen unmasking solution (pH 6) and microwaving the sections for 30 minutes in this solution. Sections were allowed to cool down and then were transferred into a buffer solution (Tris Buffered Saline with 0.1% Tween 20– TBS-T, pH 7.6) for 5 minutes to permeabilize the tissue.

Using a hydrophobic barrier pen, circles were drawn around the tissue. Next, 2-3 drops of BLOXALL blocking solution (SP-6000) was used to cover the tissue for 5 minutes and to block endogenous peroxidase activity. After, sections were incubated with a casein 2x working solution to block any non-specific binding for 20 minutes in a humidified chamber. Subsequently, sections were incubated for 20 minutes at room temperature with diluted normal blocking serum (2.5% horse serum in TBS-T).

For the antibody staining, primary antibody solutions and isotype matched control antibodies (IMC) were prepared in diluted horse serum (1 µl of primary + 100 µl of diluted horse serum). Sections were incubated for 1 hour at room temperature (or overnight at 4 ºC) in a humidified chamber. Sections were washed in buffer and incubated for 30 minutes with ImmPRESS secondary reagent anti-rabbit Immunoglobulin G. The

immunoreaction was then visualised with ImmPACT NovaRED peroxidase (HRP) after 4 minutes incubation. Sections were rinsed with tap water, counterstained with filtered Mayers haematoxylin, dehydrated and mounted in DPX. After each step, the sections were washed for 5 minutes with TBS-T.

Representative images were obtained using Zeiss Axioscope microscope and Axiovision software.

2.3.1.3. Western blot for KHK

Frozen liver tissue (70-90 mg) or cell pellets (10^6-10^7 cells) were lysed in CelLytic MT lysis buffer (Sigma) supplemented with proteinase inhibitor (Roche) and DNaseI (Sigma). Next, they were placed in gentleMACS M-Tubes (Miltenyi Biotec) prior to homogenization using a gentleMACS Dissociator with the program "protein_01". Protein concentrations were determined by Pierce™ BCA Protein Assay Kit (ThermoFisher Scientific) and lysates (20-40 μg/lane) were separated on a 10% sodium sulphate polyacrylamide gel, blotted onto Hybond ECL membrane (GE Healthcare) and membranes were blocked in PBS/5% milk/0.1% Tween 20 with constant agitation (1 hour, room temperature). The membrane was then immunoblotted with primary antibodies KHK, KHK-A, KHK-C or β-actin at a working dilution of 1:1000 (Table III) with constant agitation (1 hour, room temperature). Membranes were washed with PBS/0.1% Tween three times for 5 minutes and incubated with horseradish peroxidase-conjugated secondary antibody diluted in PBS/5% milk/0.1% Tween 20 for 1 hour at room temperature, and then washed as described for 30 minutes. Detection of the bound antibody was performed using enhanced chemiluminescence Western blotting substrate (ThermoFisher Scientific). ImageJ software v.1.70_75 was used to analyse western blot images.

2.3.1.4. Isolation of primary hepatocytes

Hepatocytes were isolated from marginal human donor liver. An encapsulated wedge of tissue was flushed with PBS to remove blood and initial dissociation buffer was used to loosen cell junctions (10 mM HEPES, 0.5 mM EGTA, Sigma). After another wash with PBS, tissue was dissociated using a combined enzymatic digestion buffer (0.5% w/v Collagenase A (from Clostridium Histolyticum, Roche, Hertford, UK, Lot number 70273822), 0.25% w/v Protease (Type XIV from Streptomyces Griseus, Sigma, Lot number 076K1177, 4.5 units/ mg), 0.125% w/v Hyaluronidase (from bovine testes, Sigma, Lot number 025K7015, 451 units/mg) and 0.05% w/v Deoxyribonuclease (from bovine pancreas, Sigma, Lot number 107K7013, 552 units/mg) as previously described [148]. Following this the liver was mechanically disaggregated in media (DMEM + 10% FCS). The cell suspension was sieved and centrifuged at 50 x g to pellet hepatocytes. These were counted using trypan blue and plated out onto collagen-coated plastic.

2.3.1.5. Digestion of mouse liver for flow cytometric analysis

In order to isolate hepatic immune cells (HICs), livers were collected and weighed upon termination of experiment. For flow cytometry, the left liver lobe was used, and samples were kept on ice in a six well plate containing RPMI medium before processing. The tissue was mechanically disrupted using a 5 ml syringe plunger and passed through a 70 µm strainer, using cold RPMI to facilitate the digestion. The homogenates were transferred into 15 ml falcon tubes and centrifuged for 5 minutes at 430 x g. The supernatant was discarded, and the pellets were rewashed in 10 ml of cold RPMI. To obtain the HICs cell populations, the previous suspension was divided into two 15 ml tubes and layered over 7 ml Optiprep^{TM} Density Gradient Medium (Sigma) diluted with PBS in a 4:11 ratio. These samples were subjected to density gradient centrifugation at 1000x g, for 25 minutes at brake 3.

To isolate the immune cells from the gradient interface, the middle layer was collected using a sterile plastic pipette, pooling cells from the same liver sample (see Figure 2. 2). The new 15 ml tube was topped up with cold RMPI and cells were subjected to another 5 minutes centrifugation at 800 x g. This was then followed by a new wash with MACS buffer (PBS + 2% FBS + 1 mM EDTA) and another centrifugation at 800 x g for 5 minutes.

Next, the supernatant was discarded, and cells were resuspended in 500 µl of cold PBS. 200 µl of each sample were added to the respective lymphoid (L) and myeloid (M) wells of a 96 well plate, to test for both populations. The remaining volume of different samples was combined in a bijoux tube to use in the single colour (S), Zombie NIR™ Fixable Viability (Z) and negative control (NC) wells to test for cell viability and have gating controls. At this point, 100 µl of Zombie stain were added in darkness in the L, M and Z wells to assess live vs. dead status, using a dilution of 1:1000 in PBS. Samples

were mixed using a multichannel pipette and left to incubate for 30 minutes, covered in foil.

Whilst samples were incubating, the antibody master mix for lymphoid and myeloid panels were prepared as stated in Table IV. Supplier information for each reagent was described earlier in section 2.1.

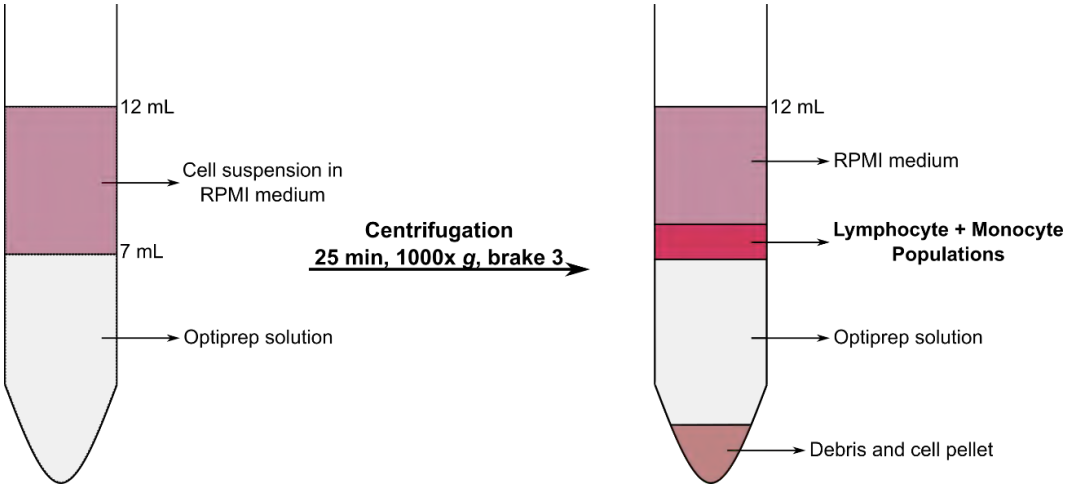

Figure 2. 2 – Isolation of lymphocyte and monocyte populations using an Optiprep™ Density Gradient Medium and centrifugation step.

After the Zombie stain incubation, samples were washed twice as before, and the supernatant was discarded. All samples were reconstituted in 100µl of MACS buffer. 30µl per well of the lymphoid master mix was added to the lymphoid samples, while 22µl per well of the myeloid master mix was used in the myeloid samples. In the single colour wells, the relevant antibody was added, as described in Table IV. Cells were left incubating in the dark for 30 minutes, followed by washing as described previously.

Samples were acquired with a 9-colour CyAn ADP flow cytometer running Summit v4.3 software (both Beckmann Coulter, UK). Offline analyses (compensation, gating, generation of plots and population statistics) were carried out with FlowJo v.10 (FlowJo, LLC, USA).

Table IV – Antibody master mix for lymphoid and myeloid combinations

Mixtures	Singles no.	Antibody	Fluorochrome	Volume per sample
T-cell/Lymphoid combination	S1	anti-CD3	BV 510	5 µl
	S2	anti-NK1.1	FITC	5 µl
	S3	anti-CD4	PE	5 µl
	S4	anti-CD45	PerCPCy5.5	5 µl
	S5	anti-CD8a	APC	5 µl
	S6	anti-CD19	BV 421	5 µl
Myeloid Combination	S7	anti-CD3	PB	5 µl
	S8	anti-F4/80	FITC	2 µl
	S9	anti-CD11b	PE	5 µl
	-	anti-CD45	PerCPCy5.5	5 µl
	S10	anti-Gr-1	APC	5 µl

Note 1 – All volumes were sampled directly from manufacturers stock (See Table II).

2.3.1.6. Metabolic assessment of human liver tissue by perfusion *ex vivo*

Ex vivo liver perfusion was used to assess human livers after surgical removal. This protocol was developed and refined during the course of my project to allow me to evaluate human liver metabolism, to study responses to substrates, and to test the efficacy of novel therapeutic targets. DMEM (glucose and glutamine free) was supplemented with 1% penicillin-streptomycin, and 10% (v/v) heat inactivated FBS and placed in the incubator to warm up to 37 ºC in advance of the fresh tissue being received in the laboratory. Depending on the experiment, glucose or fructose were also added to DMEM at a concentration of 4 g/l. For experiments using KHK inhibitor, a solution of 1 mM inhibitor (2.4 mg) was prepared in 5 ml of DMEM for a further dilution to 10 µM when used in the perfusion system. Samples of 1 ml of each media were saved before perfusion started as a time zero control.

As soon as fresh liver tissue was received in the lab, a small amount of tissue was immediately snap frozen by immersion into liquid nitrogen and was subsequently stored at -80 ºC. Another piece of tissue was placed into formalin for histological analysis. Before starting the perfusion, the liver wedges were weighed, and clean and sterile catheters was stitched into the bigger vessels to facilitate infusion of media. If necessary, the other superficial vessels were stitched to minimise loss of media from the cut face of the tissue. The catheters were connected to independent tubes all connected to the perfusion pump (Watson Marlow 505S system, 0.88 mm bore size, flow rate of 1.62 ml/min) and an initial flush with DMEM was performed to clear any remaining blood and clots inside the tissue (see Figure 2. 3).

When performing KHK inhibition, a pre-treatment was performed for 30 minutes prior to exposure to media containing sugars. For this, one wedge was perfused with

KHK inhibitor (10 μM) in unlabelled DMEM whilst a matched control wedge was perfused with unlabelled DMEM only. After this, used media was aspirated and a new perfusion started using 15-20 ml of ^{13}C-labelled media through both wedges.

The labelled DMEM was re-perfused through the tissue for the total duration of the experiment: the medium entered through the larger vessel which had the attached catheter and leaked through smaller ones across the cut face of the tissue. The other end of the tube connected to the catheter was collecting the same medium outside the wedge (that eventually filled the cup), which was perfusing the tissue. The perfusion was maintained for 3 hours, and media and pieces of 100-150 mg tissue were collected for both histology (in fixative) and NMR (snap freezing), at intervals varying between 0.5 and 3 hours. During collection of tissue, the wedge was cut as close as possible to the catheter without compromising tissue integrity and perfusion routes.

Figure 2. 3 – Workflow of perfusion system setup. From left to right: 1. fresh human liver after surgical removal; 2. liver wedge with visible vessels to insert catheter for perfusion; 3. perfusion setup of *ex vivo* liver wedges, while being perfused. Each condition was tested using individual liver wedges, from the same liver, to compare perfusion of unlabelled substrates with ^{13}C-labelled substrates in DMEM.

2.3.1.7. Gene expression analysis using RT² Profiler™ PCR Array

A RT² Profiler™ PCR array (Mouse fatty liver: PAMM-157Z, Qiagen) was used to investigate the expression of 84 key genes involved in the mechanisms of NAFLD in our murine liver samples. These genes are involved in hepatic insulin and adipokine signalling, metabolic enzymes and transporters, genes related with non-insulin dependent diabetes mellitus as well as genes involved in inflammatory response and apoptosis. The gene list can be found in Table V.

Table V- Gene list from RT² Profiler™ PCR Array Mouse Fatty Liver

Insulin Signalling	Akt1, Foxa2 (Hnf3b), Gsk3b, Igf1, Igfbp1, Insr, Irs1, Mapk1 (Erk2), Mapk8 (JNK1), Mtor, Pik3ca (p110alpha), Pik3r1 (p85alpha), Pklr, Ppargc1a (Pgc-1alpha), Prkaa1 (Ampk), Ptpn1 (PTP1B), Slc2a4 (Glut4), Socs3, Srebf1.
Adipokine Signalling	Adipor1, Adipor2, Akt1, Cd36, Irs1, Lepr, Mapk8 (JNK1), Mtor, Nfkb1, Ppara, Ppargc1a (Pgc-1alpha), Prkaa1 (Ampk), Rxra, Serpine1 (PAI-1), Slc2a1, Slc2a4 (Glut4), Socs3, Stat3, Tnf.
Non-Insulin Dependent Diabetes Mellitus	Gck, Insr, Irs1, Mapk1 (Erk2), Mapk8 (JNK1), Mtor, Pik3ca (p110alpha), Pik3r1 (p85alpha), Pklr, Slc2a2, Slc2a4 (Glut4), Socs3, Tnf, Xbp1.
Metabolic Pathways	**Carbohydrate Metabolism**: Acly, G6pc, G6pdx, Gck, Gsk3b, Mlxipl, Pck2, Pdk4, Pklr, Rbp4. **Beta-Oxidation:** Acadl, Acox1, Akt1, Cpt1a, Cpt2, Fabp1, Irs1, Mtor, Ppara. **Cholesterol Metabolism & Transport:** Abca1, Abcg1, Apoa1, Apob, Apoc3, Apoe, Cd36, Cnbp, Cyp2e1, Cyp7a1, Hmgcr, Ldlr, Lepr, Nr1h2, Nr1h3, Nr1h4, Ppara, Ppard, Pparg, Prkaa1 (Ampk), Rxra, Srebf1, Srebf2. **Other Lipid Metabolism & Transport Genes:** Acaca, Acsl5, Acsm3, Dgat2, Fabp3, Fabp5, Fasn, Gk, Hnf4a, Lpl, Ppa1, Scd1, Slc27a5. **Oxidative Phosphorylation:** Atp5c1, Ndufb6, Ppa1.
Inflammatory Response	Cebpb, Fas (Tnfrsf6), Ifng, Il10, Il1b, Il6, Nfkb1, Rxra, Tnf.
Apoptosis	Akt1, Casp3, Cebpb, Fas (Tnfrsf6), Mapk1 (Erk2), Mapk8 (JNK1), Nfkb1, Pik3ca (p110alpha), Pparg, Prkaa1 (Ampk), Rxra, Serpine1 (PAI-1), Socs3, Tnf.

2.3.1.8. RNA extraction

For the ribonucleic acid (RNA) extraction, the following solutions were prepared before the experiment:

- Buffer RLT Plus: adding 10 µl of 2-mercaptoethanol per 1 ml of buffer.
- Buffer RPE: adding 44 mL of 100% ethanol to 11 mL of buffer.
- 70% ethanol: diluting 100 % stock with RNase-free water.

RNA was isolated from approximately 30 mg of frozen mouse liver tissue using the RNeasy® Plus Mini Kit from QIAGEN as per manufacturer's instructions. Briefly, the tissue was disrupted using gentleMACS M tubes and homogenized in 600 µl of buffer RLT Plus. The lysate was centrifuged for 3 minutes at 800 x g and the supernatant was transferred into a gDNA eliminator spin column placed in a 2 ml collection tube. After a new 30 s centrifugation at 8000 x g, the column was discarded and the flow-through was saved. 600 µl of 70% ethanol were added and mixed immediately by pipetting. Up to 700 µl of the sample were then transferred to a RNeasy spin column placed in a 2 ml collection tube, a quick 15 s centrifugation at 8000 x g was done and flow-through discarded. The next two steps were similar, either adding 700 µl of buffer RW1 (as provided) or 500 µl of buffer RPE. One last addition of 500 µl buffer RPE was used in the RNeasy spin column and centrifuged for 2 minutes at the same speed. Then, the RNeasy spin column was placed in a new 1.5 ml collection tube and 30-50 µl of RNAse-free water were added directly to the spin column membrane. One last centrifugation was carried out at 8000 x g for 1 minute to elute the RNA.

The concentration of the eluted RNA from all samples was assessed, as well as the purity and integrity using a NanoPhotometer (Implen). Purity was estimated based on the 260/280nm and 260/230nm ratios, where a value of 2 is indicative of relatively pure RNA. Samples were then stored at -80ºC until needed.

2.3.1.9. cDNA synthesis

Complementary deoxyribonucleic acid (cDNA) was synthesised from an RNA template to further use in the Polymerase Chain Reaction (PCR). Sample preparation was carried out using the cDNA synthesis RT^2 First Strand Kit from Qiagen.

Briefly, the genomic DNA elimination mix was prepared for each RNA sample, using the same concentration of total RNA. For this mix, each sample was prepared in a total volume of 10 µl, using 2.5 µg of RNA, 2 µl of buffer GE together with variable volumes of RNase-free water. Each sample was gently mixed by pipetting and then centrifuged for 30 seconds. Next, the genomic DNA elimination mix was incubated for 5 minutes at 42 ºC, then placed on ice for at least 1 minute.

A reverse-transcription mix was prepared using 4 µl of 5x buffer BC3, 1 µl of control P2, 2 µl of RE3 Reverse Transcriptase Mix, 3 µl of RNase-free water for a final volume of 10 µl per sample. Then, 10 µl of this mix was added to each tube containing 10 µl genomic DNA elimination mix, and gently mixed. Samples were further incubated at 42 ºC for exactly 15 minutes, immediately followed by an incubation of 5 minutes at 95 ºC to stop the reaction. 91 µl of RNase-free water was added to each reaction and gently mixed. Samples are then ready for real-time PCR and were stored in a -20 ºC until further analysis.

2.3.1.10. Real-Time PCR for RT^2 Profiler PCR Array

Real-time PCR using RT^2 Profiler PCR array was used in combination with a SYBR Green Mastermix.

After a brief centrifugation, the PCR component mix was prepared in a loading reservoir using 650 µl of RT^2 SYBR Green Mastermix, 548 µl of RNase-free water and 102 µl of the cDNA synthesis reaction for each sample. Next, the PCR components mix

was added to the RT^2 Profiler PCR Array according to the manufacturer's instructions, using one plate for each four samples. 10 µl of the PCR components mix was added to each well and in the end the array was tightly sealed with optical adhesive film. Lastly, the plate was centrifuged for 1 minute at 1000 x g at room temperature to remove bubbles.

Next, the RT^2 Profiler PCR array was placed in the real-time cycler Roche LightCycler 480 to start the run. The threshold cycle (C_T) was calculated for each well using the real-time cycler software for data analysis. A melting curve analysis was also carried out to verify PCR specificity.

2.4. *In vivo* model of NAFLD

2.4.1.1. Mouse husbandry

Six to eight-week old C57BL/6 male mice (Charles River, UK) were group housed in temperature and humidity-controlled specific pathogen–free rooms on a 12-hour light-dark cycle with ad libitum access to water and food in accordance with the Animals (Scientific Procedures) Act (1986). Four mice were kept per individually ventilated cage.

2.4.1.2. Mouse diets

Mice were maintained either on a low-fat control diet (D12450Ji, Research Diets, Inc) or in a high fat diet (D12492i, Research Diets, Inc) for up to 21 weeks. While mice on the low-fat diet were given ad libitum access to regular water, mice on the high fat diet were also given ad libitum access to water, either regular or sweetened with 20% fructose or 20% glucose. Both diets were acquired from the same company, to properly match control low fat diet with the high fat experimental diet [149]. Information relating to dietary composition and comparison with a "standard chow" diet can be found in Table VI.

Table VI – Diet composition of low fat diet (LFD) D12450Ji, high fat diet (HFD) D12492i and Standard Chow diet D10001i (AIN-76A Rodent Diet)

	LFD		HFD		Chow	
Product #	**D12450Ji [a]**		**D12492i [a]**		**D10001i [b]**	
	g%	**kcal%**	**g %**	**kcal %**	**g %**	**kcal %**
Protein	19.2	20	26	20	20	21
Carbohydrate	67.3	70	26	20	66	67
Fat	4.3	10	35	60	5	12
kcal/gm - Total	**3.85**	**100**	**5.24**	**100**	**3.86**	**100**
Ingredient	**g**	**kcal**	**g**	**kcal**	**g**	**kcal**
Casein, 80 Mesh (LFD and HFD), 30 MESH (Chow)	200	800	200	800	200	800
L-Cystine (LFD and HFD), DL-Methionine (Chow)	3	12	3	12	3	12
Corn Starch	506.2	2024.8	0	0	150	600
Maltodextrin 10 (LFD and HFD), Cellulose, BW200 (Chow)	125	500	125	500	50	0
Sucrose	68.8	275.2	68.8	275	500	2000
Cellulose, BW200	50	0	50	0	50	0
Soybean Oil (LFD and HFD), Corn Oil (Chow)	25	225	25	225	50	450
Lard	20	180	245	2205		
Mineral Mix S10026 (LFD and HFD), S10001 (Chow)	10	0	10	0	35	0
DiCalcium Phosphate	13	0	13	0		
Calcium Carbonate	5.5	0	5.5	0		
Potassium Citrate, 1 H_2O	16.5	0	16.5	0		
Vitamin Mix V10001	10	40	10	40	10	40
Choline Bitartrate	2	0	2	0	2	0
FD&C Dye	0.05	0	0.05	0	-	-
Total	**1055.05**	**4057**	**773.85**	**4057**	**1000**	**3902**

Note 2 – Values obtained on April 2018 from the website of the company supplying the diet:

a) https://researchdiets.com/opensource-diets/dio-series-diets;

b)https://www.researchdiets.com/formulas/D10001i.

2.4.1.3. Dosing with KHK inhibitor by intraperitoneal injection

As the ketohexokinase (KHK) inhibitor was not easily soluble in phosphate-buffered saline, a low concentration solution of 0.5 mg/ml was prepared. This was carried out on the same day that the injections were performed so that the inhibitor would remain dissolved before the injections. The KHK inhibitor was administered via intraperitoneal injection (i.p.) to minimize stress to the animal and avoid any need for anaesthesia. For the greatest accuracy in dosing, each individual animal was weighed, and the dose was calculated as follows:

$$Injection\ volume\ (ml) = \frac{mouse\ weight\ (Kg)\ \times Dose\ required\ \left(\frac{mg}{kg}\right)}{Concentration\ of\ KHK\ inhibitor\ \left(\frac{mg}{ml}\right)}$$

As an example, for a 50 g mouse, the injected volume would be:

$$Injection\ volume\ (ml) = \frac{0.05\ (Kg)\ \times 15\ \left(\frac{mg}{kg}\right)}{0.5\ \left(\frac{mg}{ml}\right)} = 1.5\ ml$$

The administration volume represents an i.p. injection of 30 ml/kg, following good practice guidelines [150], without compromising animal welfare.

Individual mice were weighed and dosed with KHK inhibitor at 15 mg/kg, 4 hours prior to culling. Records of all dosings were kept in the laboratory notebook.

2.4.1.4. Intraperitoneal injection of [U-^{13}C] fructose

In order to assess *in vivo* metabolic changes of mice with fatty liver disease, [U-^{13}C] fructose was used. Similar to the KHK inhibitor, fructose was dissolved in PBS and administered to animals by i.p. injection at 1M (volume of 0.1 ml, mass of 0.2 g) - optimised by Dr. Volpari for her PhD thesis in November 2015, University of Birmingham. Animals were euthanised 30 minutes after administration of the tracer to

allow for absorption, metabolization in the liver and accumulation of downstream labelled metabolites.

2.4.1.5. Blood samples

During the course of the experiment, blood was collected from mice at pre-determined time points by tail vein bleeding. For tail vein blood sampling, the animals had to be kept in a warming cabinet, for no more than 10 minutes, in order to dilate the blood vessels. One blood sample up to 200 µl of blood was collected from each mouse and was stored in a 1.5 ml Eppendorf, using a 25-gauge needle while the mouse was in a restraint tube.

The last blood collection was performed at the end of the experiment, while animals underwent general anaesthesia with isoflurane. Induction of anaesthesia was undertaken with 4% isoflurane using pure oxygen as a carrier gas. Maintenance of anaesthesia was carried out with 2% isoflurane with oxygen. Pedal reflex testing was performed in order to confirm the effectiveness of anaesthesia. Cardiac puncture was done with a 25-gauge needle under anaesthesia and blood samples were placed in 1.5 ml Eppendorfs.

In order to obtain serum of high quality, blood samples were allowed to form a clot at room temperature for 60 minutes. To remove the clot, blood was centrifuged twice for 10 minutes at 13 400 x g (MSE MicroCentaur). Serum was collected and transferred to a clean Eppendorf. The serum was then transferred into 0.5 ml Eppendorfs to further storage at -80 ºC. For biochemical analysis, 100 µl of serum was diluted in a saline solution (1:2) in a clean polypropylene tube. Samples were taken to the chemistry lab in the Women's Hospital in Birmingham to determine of serum enzymes activity and urea concentration using standard clinical analysers.

2.5.NMR spectroscopy of biological samples

2.5.1.1. MeOH/$CHCl_3$ extraction protocols for NMR samples from cells

PBS and purified water were kept at 4 ºC, and the methanol and chloroform at -20 ºC prior to use. For the quenching process, the spent medium was collected, and each flask was washed twice with cold PBS. Then, intracellular aqueous metabolites and lipids were extracted using a dual phase extraction procedure adapted from Teng *et al*. [151]. Briefly, 600 µl of cold methanol (HPLC grade) was added to stop metabolic activity, and the cells were scraped off the flask. Afterwards, the suspension was transferred into a labelled glass vial and vortexed for 30 s. Chloroform (200 µl + 200 µl) and purified water (300 µl) were then added to each sample, each addition was followed by vortexing for 30 s. Samples were left to rest on ice for 10 min. After centrifuging at 1720 x g for 10 min, in a swinging-bucket rotor centrifuge, the upper aqueous phase (~ 500 µl) and the lower organic phase (~ 200 µl) were then carefully transferred into new vials using a 500 µl Hamilton Syringe. The upper (polar) phase was dried under vacuum while the lower organic phase was left to dry overnight in the fume hood.

2.5.1.2. Extraction protocols for NMR samples from tissue

Liver samples (approximately 150 mg) were added to gentleMACS M-Tubes in cold (-20 ºC) methanol (8 µl/mg) and purified water (2 µl/mg). They were homogenised using a gentleMACS Dissociator (Miltenyi, UK), using the program “m_spleen_01” for two minutes. The resultant suspension was decanted into a 15 ml glass vials. Cold (-20 ºC) chloroform (8 µl /mg) and water (4 µl/mg) were added and samples vortexed for 30 seconds. The mixture was left to stand on ice, around 10 minutes, before centrifugation (5 mins at 670 x g followed by another 5 mins at 970 x g). The upper layer of the resultant

multiphasic solution was carefully pipetted into a sterile Eppendorf tube (~ 400 µl) and dried using a speed vacuum dryer for 4 hours. The lower layer containing lipids (~ 200 µl) was carefully transferred into new vials using a 500 µl Hamilton Syringe and left to dry overnight in a fume hood.

2.5.1.3. NMR sample preparation from cells and tissue

Aqueous extracts were reconstituted in 50 µl of deuterated sodium phosphate buffer (100 mM, pH 7.0) containing 0.5 mM TMSP, 3 mM sodium azide and 10% D_2O or 100% D_2O, while organic phase extracts were reconstituted in deuterated chloroform ($dCHCl_3$) containing 0.5 mM TMSP. Each sample was sonicated for 10 minutes and vortexed briefly, before a volume of 35 µl was transferred into 1.7 mm NMR tubes, either using a GILSON Sample preparation unit (10% D_2O buffer) or manually for samples in 100% D_2O buffer and samples in $dCHCl_3$. Media samples were prepared by dissolving 162 µl of media in 18 µl of 10% D_2O buffer, vortexed and transferred into 3.0 mm NMR tubes. All samples were kept at 4°C prior to NMR acquisition.

2.5.1.4. NMR acquisition

All spectra were acquired at 300 K on a 600 MHz Bruker Avance III spectrometer with a proton-optimised triple resonance NMR "inverse" (TCI) 1.7mm z-axis pulsed field gradients (PFG) cryogenic probe using a cooled Bruker SampleJet autosampler, except for the spectra acquired for the probe comparison study. For this, additional probes were tested including a TCI 5mm z-PFG cryogenic probe and a 5mm double resonance broadband inverse (BBI) z-PFG room temperature probe, all using 600 MHz Bruker Avance III spectrometers. In all experiments, the ^{1}H carrier was set on the water frequency and the ^{1}H 90° pulse was calibrated at a power of 0.256 W. Typically pulse widths of 9.5 µs were achieved.

For the ^{1}H 1D spectra, the standard Bruker pulse sequence noesygppr1d for a 1D NOESY with water pre-saturation was used. Key parameters were as follows: spectral width 11.97 ppm/7183.9 Hz; complex points, TD 32768; interscan delay, d1 4 s; short NOE mixing time, d8 10 ms; number of scans, ns= 128; dummy scans, ds= 8. The grad_blk option was used as this extra lock blanking gave a better signal line shape. Total experiment time was 14 minutes.

For ^{1}H-^{13}C HSQC spectra in water, the pulse sequence used was based on the Bruker standard pulse program hsqcetgpsp, which uses echo/anti-echo TPPI gradient selection, with added gradients during the INEPT periods. For the ^{1}H-^{13}C HSQC spectra in D_2O, the pulse sequence used was a modified version of the Bruker standard pulse program, hsqcgphprsp. In both cases additional gradient pulses were added during INEPT echo periods to improve signals and to help suppress T_1 noise in D_2O and soft 180˚-pulses were used for ^{13}C. For the ^{1}H observe dimension, a spectral width of 7812.5 Hz/13.02 ppm with 1024 complex points (i.e. 2048 total points) was used. For the ^{13}C indirect dimension, 2048 complex points (4096 increments) were acquired with a spectral width

of 24154.6 Hz/160.1 ppm. Spectra were acquired with 2 scans and an interscan delay of 1.5 s giving a total experiment time of *ca.* 16h. For all NUS-HSQC spectra, a 25% non-uniform sampling (NUS) schedule with 4096 increments was used to yield 8192 complex points after processing, using Wagner's schedule generator (http://gwagner.med.harvard.edu/intranet/hmsIST/gensched_new.html) with a tolerance of 0.01 and other parameters with default values, reducing the total experiment time to *ca*. 4 hours.

2.5.1.5. NMR data processing

2.5.1.6. One-dimensional NMR spectra

1D ^{1}H NMR spectra were processed using Metabolab program [152] within Matlab, version R2017a (MathWorks, Massachusetts, USA). The free induction decay (FID) signals were multiplied by a 0.3Hz exponential window function and zero-filled to 65536 points prior to Fourier transformation. Spectra were phased, referenced to TMSP at δ 0.00 ppm, baseline corrected and the water region and regions devoid of signal at the edges of the spectrum were excluded. Furthermore, segmental alignment using the icoshift software[153] was performed in several metabolites aligning resonances that could be slightly shifted by small differences, for example, in sample pH. Finally, the spectra were scaled to a constant total spectral area (TSA-scaling). Resonances were assigned using Chenomx (Alberta, Canada, 2015), and by consulting the NMR metabolic profiling human metabolome database (HMDB) [154].

2.5.1.7. Two-dimensional NMR spectra

2D HSQC spectra were processed using Metabolab within Matlab, version R2017a (MathWorks, Massachusetts, USA). Cosine-squared window functions were applied to both dimensions and spectra were phased manually. Calibration was carried out manually using the L-lactic acid methyl signal as a reference (δ 1.31/22.9 ppm). Metabolite identification used the MetaboLab[152] library with reference to HMDB. For 2D NUS-HSQC spectra, data processing was initially performed using NMRPipe[155] with the Hyberts extension for processing NUS spectra[156] and subsequent analysis was then performed with Metabolab as described above for regular HSQC spectra.

2.5.1.8. Scaling of HSQC spectra

1D ^{1}H NMR spectra allow the identification and accurate quantification of metabolites, since the integrated signal of a specific metabolite is directly proportional to the number of protons in the mixture. However, in 2D NMR spectra, metabolite quantification is more complex since it is dependent on additional factors such as peak multiplicity, non-uniform relaxation, evolution times and homonuclear coupling constants [157–159]. Determining exact metabolite concentrations from 2D peak intensities is a challenge, which would require longer experimental times and complex calibration data, so relative intensities were obtained for this thesis.

In theory, the ratio for ^{13}C incorporation could be calculated as follows:

$$Ratio\ ^{13}C = \frac{Peak\ intensity\ from\ 13C\ labelled\ sample\ (Ilab)}{Peak\ intensity\ from\ matched\ unlabelled\ sample\ (Ict)}$$

However, inter- and intra-variability of biological samples makes it almost impossible to prepare appropriate matched unlabelled samples as a reference for natural abundant ^{13}C. Besides, signal intensities in HSQC spectra depend on metabolite concentration as well as on label incorporation. Therefore, a normalisation step needs to be employed to obtain true peak intensities. One recurring option has been the use of a chemical shift referencing standards (usually TMS, TMSP or DSS) with a known concentration, but this is unsuitable for intensity referencing since it is added after the sample has been prepared so it cannot be used to identify changes arising from varying cell numbers.

In this work, corresponding 1D ^{1}H spectra of the same sample were used to determine total metabolite concentration, by calculating the total spectral area (TSA) and using this as a scaling factor for the 2D HSQC spectrum. This is based on the assumption that the

total concentration of all observed metabolites should be the same for similar samples. These scaling factors were then applied to scale the associated HSQCs for both labelled and unlabelled samples, and ratio of ^{13}C incorporation in specific metabolites was obtained as follows:

$$Ratio\ ^{13}C = \frac{Ilab\ \times TSA\ scaling\ factor\ from\ labelled\ sample\ (Slab)}{Ict\ \times\ TSA\ scaling\ factor\ from\ matched\ unlabelled\ sample\ (Sct)}$$

With this approach, metabolite intensities are normalised according to total metabolite concentration in each sample instead of relying in one reference metabolite. Hence, intensities between HSQC spectra were compared using this method.

2.6.Statistical analysis

Statistical analysis was carried out using GraphPad Prism version 7.0 (Graphpad, US). For multiple group comparison ordinary one-way analysis of variance (ANOVA) was used. Data was considered significant when *p*-values were below 0.5 and were represented in figures following the standard convention: * $p<0.05$, ** $p<0.01$, *** $p<0.001$, **** $p<0.0001$. Statistical hypothesis testing was performed, followed by Bonferroni's correction when data had different sample size and Tukey's correction when equal samples sizes were tested. Figure legends contain information about the number of samples for each experiment and all data was represented as mean ± standard deviation unless otherwise specified.

For 2D ^{1}H-^{13}C HSQC data, to find the ^{13}C ratios standard error of the mean ($Ratio_{error}$), additional calculations were carried out using Microsoft Excel (Microsoft, US). Average and standard deviation (SD) of each mean (unlabelled control – ct, and ^{13}C-labelled spectra – lab) were used to obtain the error associated with the ratio calculation as follows:

$$Ratio\ ^{13}C(multiple\ samples) = \frac{Average\ Ilab}{Average\ Ict}$$

$$Ratio_{error} = Ratio\ ^{13}C \times \sqrt{\left(\frac{SDct}{Average\ Ict}\right)^2 + \left(\frac{SDlab}{Average\ Ilab}\right)^2}$$

CHAPTER 3

WHEN BEING GOOD IS NOT ENOUGH

3. Refinement of techniques towards sample preparation for metabolomics investigation

3.1. Overview

In this chapter I will describe techniques optimised in our laboratory in order to establish a protocol for NMR metabolic profiling and liver disease characterisation [120]. Thus, I begin by exploring the growth characteristics of hepatic cells prior to sample preparation for metabolomics applications. Quenching methods to extract the largest number of metabolites with regards to differing physical and chemical properties of the cellular metabolome were also tested. In light of recent technological developments, NMR probe performance was verified for the analysis of limited mass biological samples, for routine 1D and 2D NMR measurements. Once suitable sample preparation and NMR methodology were defined, a comprehensive characterisation of human hepatocytes metabolome was performed by 1D and 2D NMR spectroscopy when using ^{13}C-labelled precursors. The tracer-based metabolism data was evaluated to assess best culture time, optimal precursor use and how labelled compounds are integrated into hepatic metabolism.

The work described in this chapter establishes the ground for NMR metabolic profiling and tracer-based metabolism of Non-Alcoholic Liver Disease (NAFLD) studies which are described in the next chapters 4, 5 and 6.

3.2. Optimal cellular performance for metabolomic studies

In order to assess the growth characteristics of the HuH7 cell line and determine the best time range for evaluating their metabolic activity, a growth curve was been established (Figure 3. 1). The initial cell density plated on each T75 cm^2 flasks (approximately 3 x 10^6 cells) was chosen in order to have sufficient cells for metabolomics every two days, while splitting them at a ratio 1:3. Cells were found to reach confluence about day 3 (Figure 3. 2) and to be in the exponential growth phase from 24 to 72 hours, after attachment to the new growth surface and initiation of proliferation. From 72 hours onwards, cells were very confluent, and medium was found to be extremely yellow, which reflects a pH lower than 7 by the indicator phenol red present in the DMEM, which is less than ideal conditions. Thus, the time range selected for the HuH7 cells used in metabolomics studies was between 24 and 72 hours, as during this phase the cells should be most responsive to external stimuli. Hence, to investigate cellular responses using enough cells to obtain a good signal in the NMR spectrometer, my experiments were performed within the first 72 hours of plating them, minimizing assay artefacts due to confluence.

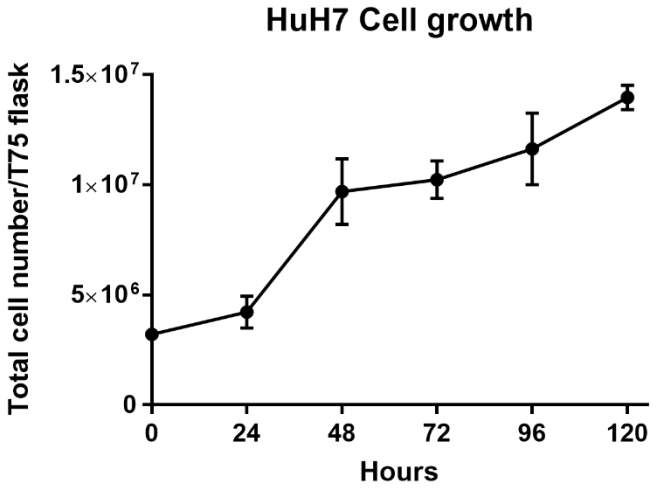

Figure 3. 1 – Growth curve of HuH7 cells. Approximately 3x10^6 cells were plated on a T75 cm^2 flask and cell growth was monitored daily. (n=3 independent experiments. Error bars represent standard deviation).

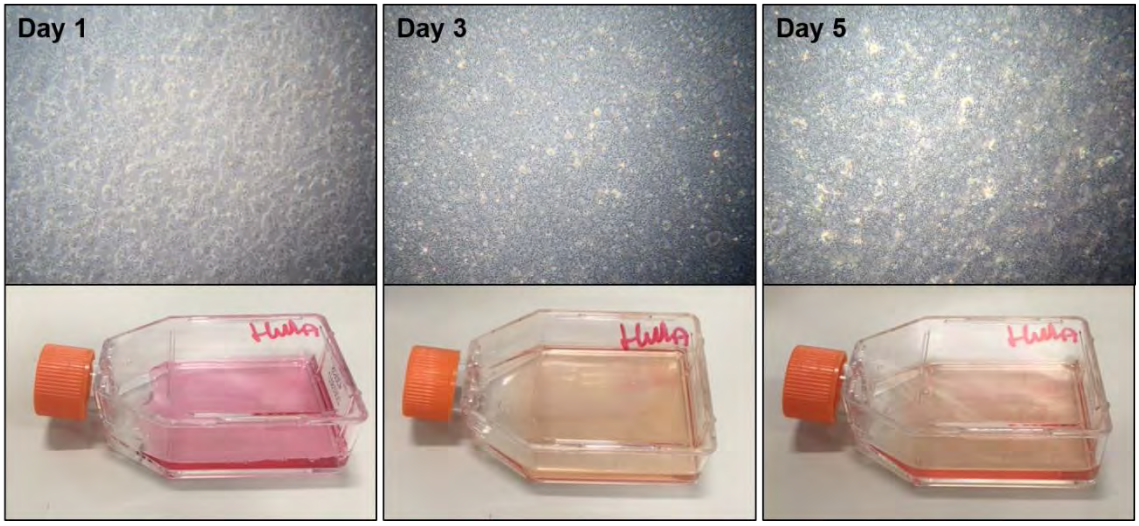

Figure 3. 2 – Examination of the culture for general cellular morphology and confluency using an inverted microscope and macroscopic evaluation of the medium pH shifts, indicated by the colour change.

3.3.Metabolite extraction using methanol, water and chloroform

The metabolic analysis of biological systems, such as cells or tissues, requires the acquisition of reproducible and reliable data sets. Also, high spectral resolution, global detection capability and ease of sample preparation are desired. Therefore, metabolite extraction is a crucial step for NMR-based applications of metabolomics [124,125,160]. For biochemical analysis and quantification of metabolites profiles through NMR spectroscopy, the extraction procedures most commonly used are the liquid-liquid extractions. Liquid-liquid extraction, also known as solvent extraction, is a separation process based on different solubilities of components in two immiscible, or partially miscible, liquids [161,162]. For my studies, in order to detect the entire cell metabolome, intracellular metabolites were extracted using a methanol, chloroform and water system, described elsewhere [125,137,163]. Whereas methanol is miscible with water and may be used to enhance solubility of less-polar metabolites during the extraction process, chloroform is volatile, immiscible with and denser than water. This system then allows the simultaneous extraction of hydrophilic compounds, such as lactate, amino acids, tricarboxylic acid cycle intermediates, and hydrophobic metabolites like fatty acids, from the same sample [124,162,163].

This two-phase liquid system was further optimised to improve the yield of metabolites by changing the ratio of solvents used. Hence, several volumes of chloroform were tested (see Figure 3. 3) in order to investigate which ratio would enhance aqueous metabolite extraction. Using 600 µl of methanol and 300 µl of distilled water, the volume of chloroform tested ranged from 350 µl to 600 µl, in 50 µl intervals.

Changing the volume of chloroform used caused the intensities of some metabolites to change, although the number of metabolites observed was virtually the same.

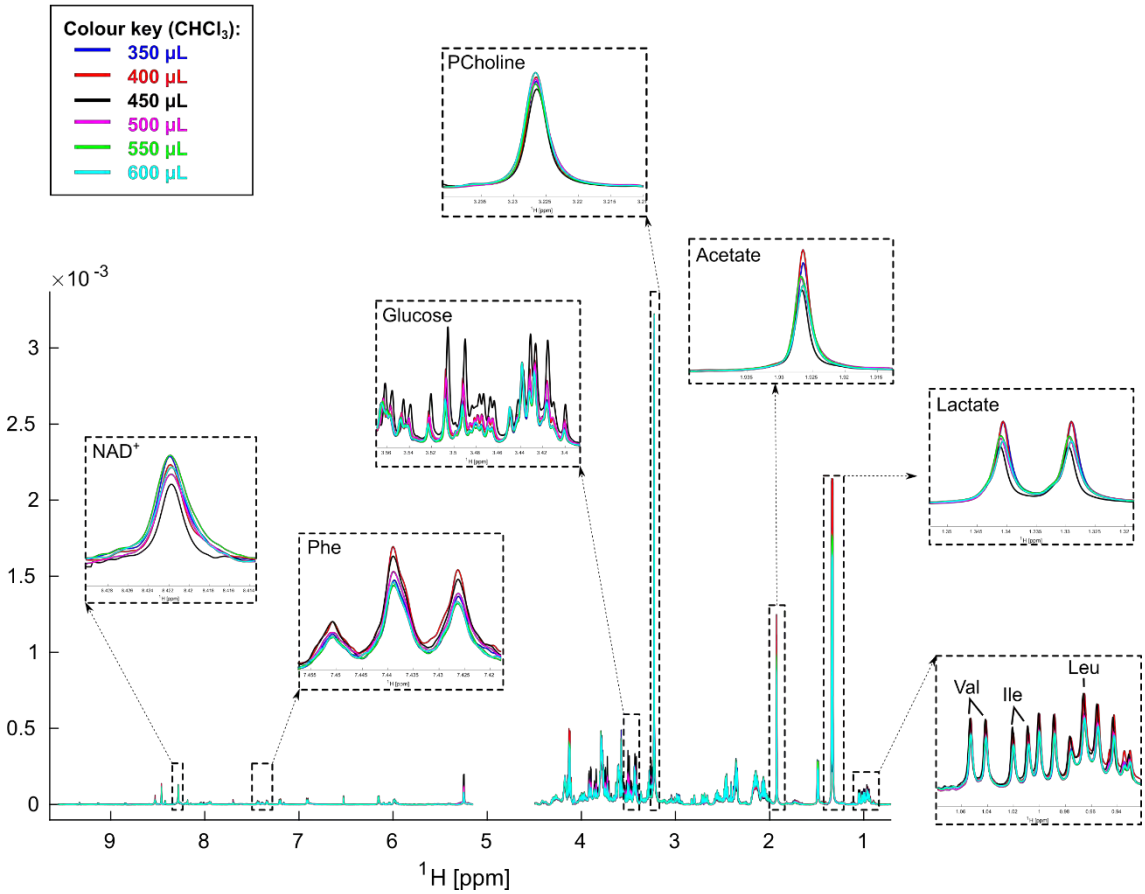

Figure 3. 3 – The effect of different solvent extraction ratios on 600 MHz ^{1}H NMR spectra from HuH7 cells. The volume of methanol (600 µL) and water (300 µL) was maintained equal in all extractions; however, the volume of chloroform was used within a range of 350-600 µL, as shown in the colour key. Dashed boxes highlight specific metabolites within the spectra: Val valine, Ile isoleucine, Leu leucine, Lactate, Acetate, Glucose, Phe phenylalanine, NAD^{+} nicotinamide adenosine dinucleotide and PCholine phosphocholine.

The solubility of metabolites is related with their polarity, thus the more polar extraction solution (350 µl chloroform) will dissolve more polar compounds and conversely, the least polar solution (600 µl chloroform) will dissolve less polar compounds. In agreement with this, the results show metabolite yields with substantial differences in branched chain amino acids, aromatic amino acids, lactate, formate, acetate, serine and choline compounds levels depending on solvent used.

Most of these metabolites are organic acids, such as amino acids and lactate, which have acidic properties. This acidity is usually related with their carboxylic group -COOH, which is strongly hydrophilic, therefore it is natural that their intensity changes according to polarity of the extraction solution. A quantification of these individual metabolites was performed from the ^{1}H NMR spectra to support these findings. In Figure 3. 4 we can see that most organic acids are more concentrated (have a higher signal intensity) when the volume of chloroform used is 400 µl. Therefore, as organic acids are the end products and intermediates of a wide range of metabolic pathways that I am interested in studying, the selected methanol/$CHCl_3$/H_2O ratio was of 2.0:1.3:1.0, using 400 µl of chloroform.

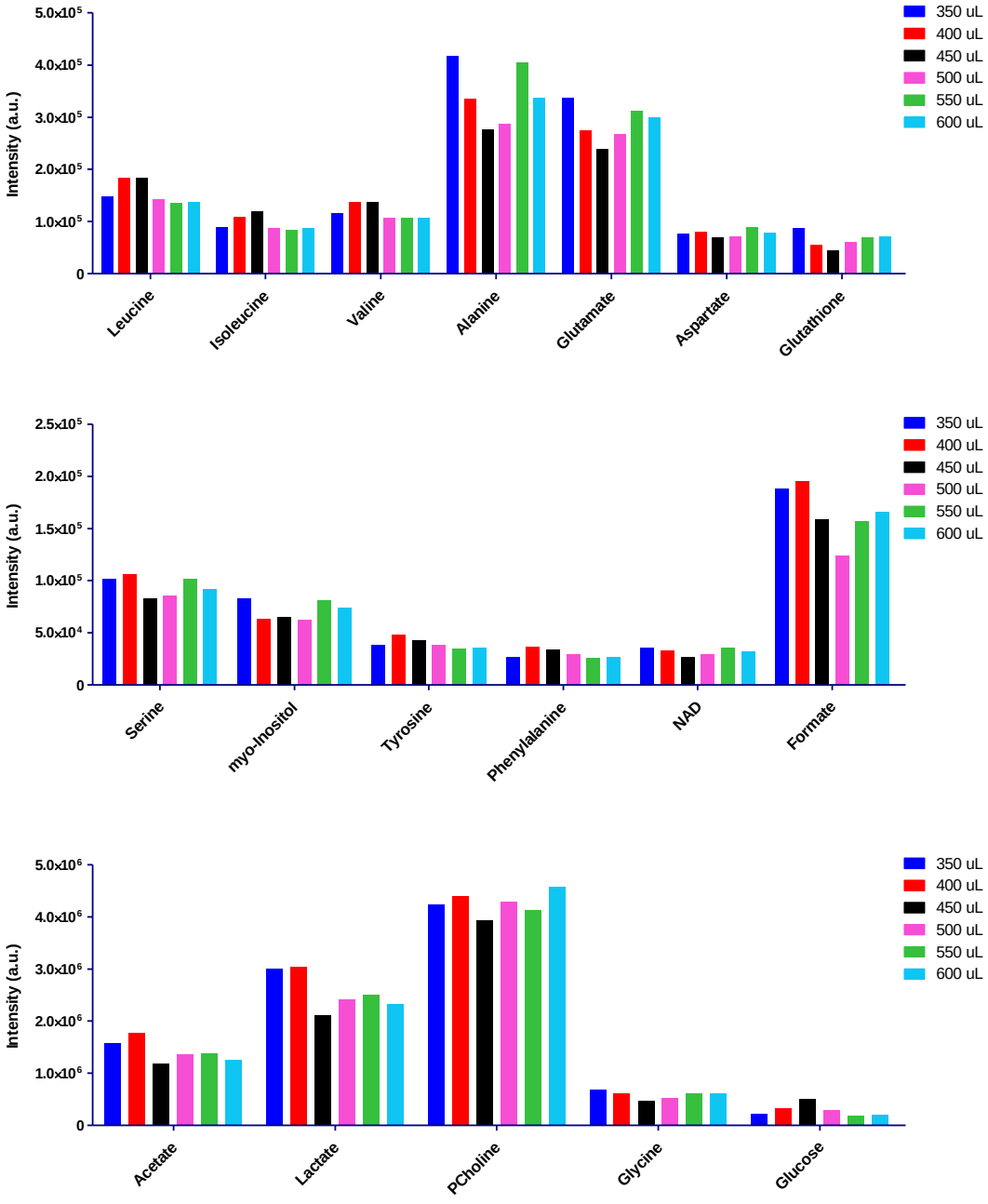

Figure 3. 4 – Individual metabolite intensities change depending on the chloroform volume used for extractions. HuH7 cells from 6 individual T75 flasks were extracted at the same time, using a methanol water and chloroform extractions, with varying volumes of chloroform, ranging from 350-600 µL, as shown in the colour key.

3.4. Use of a smaller cryoprobe permits reduced sample size

Modern cryoprobes have driven advances in NMR spectroscopy for the study of biomolecules, by increasing the sensitivity by a factor of two or three-fold and allowing better quality spectra to be generated. However, the performance of these cryoprobes is always dependent on the sample concentration, viscosity and salt interactions, which might affect line shape and chemical shifts [115,164].

In this study, spectra from equal mass samples were acquired with a 5.0mm room temperature (RT) probe, a 5.0mm cryoprobe and a 1.7mm micro-cryoprobe. The sensitivity discrepancy between different probes can be seen in Figure 3. 5. For this comparison, two sucrose samples were prepared from a solution of sucrose with a concentration of 0.1 M, one diluted in 35 µl for the 1.7 mm micro-cryoprobe and another one diluted in 600 µl for the 5.0 mm probes. Using 32 scans, almost no signal was observed in the RT probe and a signal to noise (S/N) ratio gain of at least 10 was seen from using the 1.7mm cryoprobe instead of the 5mm cryoprobe (Figure 3. 5. A).

When analysing intracellular polar extracts from the HuH7 cell line, similar results were obtained (Figure 3. 5.B). For this, two matched samples of the same mass were prepared from the same flask, and equal volumes from the polar layer of the methanol/chloroform/water extraction were dried under vacuum. They were then resuspended in different volumes, as for the sucrose experiment. The NMR analysis was carried out using 128 scans, and whilst the RT probe showed very low-intensity signals, the cryoprobes generated a huge improvement with a further signal enhancement factor of 4-5 for the micro-cryoprobe. Overall sensitivity improved by a factor of at least 40 with this probe technology for both samples (Table VII). Importantly, the salt tolerance of the micro-cryoprobe (1.7 mm) is much better than that of conventional cryoprobes but

shimming becomes more challenging due to the large length/width ratio and the temperature gradient along the sample length of the NMR tube.

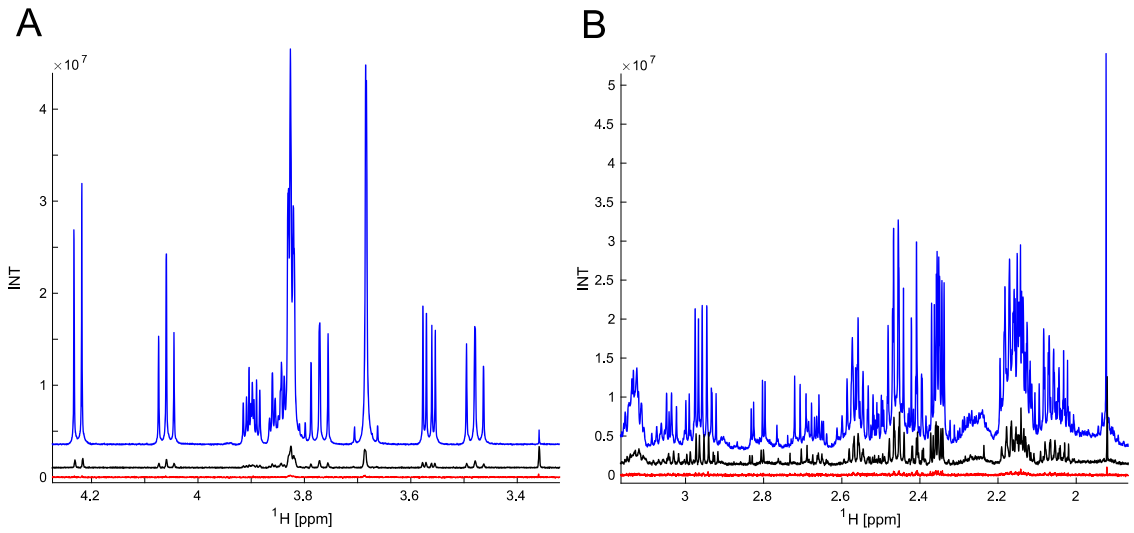

Figure 3. 5 – Modern probe technology improves sensitivity for NMR metabolomics analysis. Comparison of 1D spectra obtained from two equal mass samples, either sucrose (A) or hepatocarcinoma cell line extracts (B) using a 1.7mm micro-cryoprobe (blue), a 5 mm cryoprobe (black) and a 5 mm room temperature (RT) probe (red).

This figure is published in [120], but it is my own work.

Table VII – Comparison of peak intensities from sucrose and cell extract equal mass samples acquired with a 5.0mm room temperature (RT) probe, a 5.0mm cryoprobe and a 1.7mm micro-cryoprobe

A. Sucrose			
Intensity	**1.7mm cryoprobe**	**5mm cryoprobe**	**5mm RT probe**
Peak @ 3.479 ppm	1.28E+07	7.40E+05	6.10E+04
Peak @ 3.684 ppm	4.12E+07	1.88E+06	2.33E+05
Peak @ 3.770 ppm	1.32E+07	7.53E+05	2.73E+04
Fold change	**1.7mm cryo/5mm cryo**	**5mm cryo/ 5 mm RT**	**1.7mm cryo/5mm RT**
Peak @ 3.479 ppm	17.3	12.1	209.5
Peak @ 3.684 ppm	21.9	8.1	177.0
Peak @ 3.770 ppm	17.5	27.6	482.7
B. HuH7 cells			
Intensity	**1.7mm cryoprobe**	**5mm cryoprobe**	**5mm RT probe**
Acetate @ 1.923 ppm	5.03E+07	1.12E+07	1.03E+06
Glutamate @ 2.338 ppm	2.10E+07	4.56E+06	5.63E+05
Aspartate @ 2.796 ppm	8.28E+06	1.82E+06	2.32E+05
Fold change	**1.7mm cryo/5mm cryo**	**5mm cryo/ 5 mm RT**	**1.7mm cryo/5mm RT**
Acetate @ 1.923 ppm	4.5	10.9	48.8
Glutamate @ 2.338 ppm	4.6	8.1	37.2
Aspartate @ 2.796 ppm	4.5	7.8	35.7

Note 3 – Intensity values were obtained from the integration of the ^{1}H 1D NMR spectra at the defined spectral region (in ppm) for all tested probes. Fold change is the ratio obtained by dividing the intensity of a specific peak from two different probes.

3.4.1. Increased sensitivity of cryogenic probes benefits 2D NMR

Improvements in technology have opened new avenues for NMR metabolomics, enabling data from 2D NMR experiments to be acquired in a reasonable time without compromising resolution. 2D NMR spectroscopy has advantages over 1D NMR since it reduces spectral overlap due to increased spectral dispersion. Commonly used 2D NMR experiments in metabolomics include proton homonuclear (^{1}H-^{1}H) experiments such as Correlation Spectroscopy (COSY), Total Correlation Spectroscopy (TOCSY) and J-resolved NMR spectroscopy (*J*-Res), as well as heteronuclear (^{1}H-^{13}C/^{1}H-^{15}N) experiments like Single Quantum Coherence (HSQC) and Multiple Quantum Correlation (HMQC). Although all these experiments are valuable to determine stable isotopic labelling at specific atomic positions, HSQC experiments provide straightforward information and offer a sufficiently high resolution to identify ^{13}C-enriched isotopomers by correlating ^{1}H and ^{13}C (or ^{15}N) chemical shifts. In order to achieve this, HSQCs were employed to obtain signal intensities, ^{13}C chemical shifts and coupling patterns [105,165].

In HSQC spectra, signals arise only from protons attached to ^{13}C, therefore, levels of label incorporation can be estimated comparing labelled samples with matched unlabelled controls. In both samples there will be signal intensities arising from the 1.1% natural abundance of ^{13}C, therefore ^{13}C-incorporation in specific positions can be determined by measuring intensities from unlabelled and labelled HSQC samples. However, correction for sample variability affecting the overall concentration is required, as described in section 2.5.1.8. Briefly, the overall intensity of HSQC signals is a product of concentration and label incorporation, and the relative concentration can be estimated from the total spectral area of the corresponding 1D spectrum, which does not depend on label incorporation.

Another advantage of the HSQC spectra for isotopomer analysis arises from the quantitative information in the multiplet structure in the incremented ^{13}C-dimension, as originally suggested by Szyperski [166]. For example, in a mixture of isotopomers for the central carbon of a 3-carbon fragment, there is a superimposition of resonances arising from isolated ^{13}C singlets, two possible ^{13}C-^{13}C doublets, and the possibility of doublets of doublets when all three carbons are labelled as shown in Figure 3. 6:

(1) the observed carbon position is a terminal C3 fragment which gives rise to a singlet, symbolised in black, and a doublet indicated in blue, as the coupling pattern from one-bond scalar coupling constant $^{1}J_{CC}$. This is observed for carbon-3 of alanine.

(2) the observed carbon is in a C3 fragment and the scalar coupling constants to the adjacent carbons are identical within the HSQC resolution. This yields a singlet (black), a doublet (blue) and a triplet (black and blue combined), which can be found in the spectral region of carbon-5 of glucose.

(3) finally, the observed carbon is embedded in a C3 fragment with different scalar coupling constants since the chemical environment of the neighbouring carbons is different. In a situation where $^{1}J_{CC}<^{1}J_{*CC}$ we can see a singlet (in black), two different doublets (one from $^{1}J_{CC}$ and other from $^{1}J_{*CC}$,), and a double of doublets in the final spectrum (all in blue). This is seen in carbon-2 of alanine.

Nevertheless, to obtain information regarding J_{CC} values involving the labelled carbons, high-resolution HSQC spectra are needed. For this, high-resolution HSQC spectra need to be acquired with 16384 real points, leading to long acquisition times (around 16 hours) even when using 2 scans. Due to advancements in software and technology, HSQC spectra can now be acquired with non-uniform sampling (NUS),

leading to overall decrease in acquisition time without compromising resolution. Hence, for my experiments, NUS HSQC spectra were acquired with 512 complex data points for ^{1}H and 8192 complex data points for ^{13}C with 25% sampling rate (2048 complex points, 4096 increments), taking approximately 4.5 hours of acquisition time. Using the IST algorithm from Wagner and co-workers [156], NMR data was reconstructed with zero filling and applying a Fourier transformation, ultimately doing a convolution of the zeros with the data and increasing final resolution.

To test the performance of the NUS HSQC spectra reconstruction, a sample from HuH7 cells was acquired with regular sampling and with 25% NUS sampling. Figure 3. 7 displays both the HSQC spectra acquired and the multiplet patterns from glutamate. The NUS-HSQC spectrum is virtually indistinguishable from the one with regular sampling, where all metabolites are visible without the presence of artefacts from the NUS scheduling. Moreover, multiplet patterns arising from the $^{1}J_{CC}$ scalar coupling are observable at the same level with little or no differences in resolution.

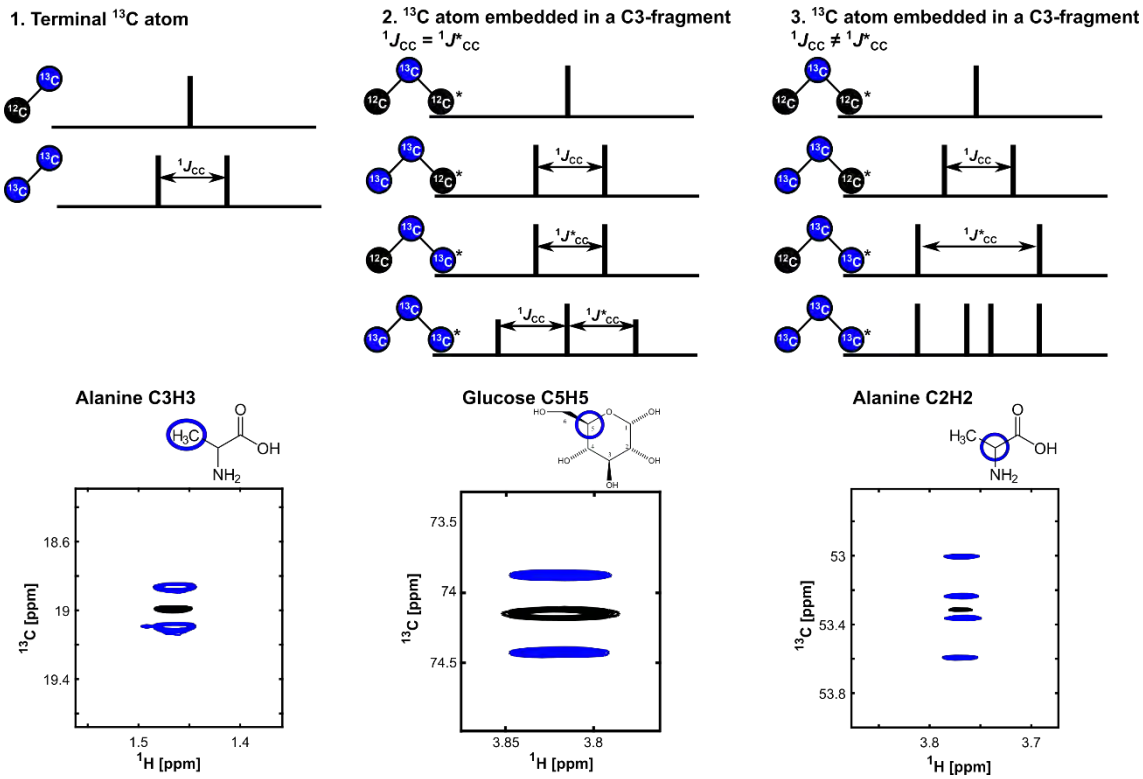

Figure 3. 6 – Labelling patterns and corresponding multiplets as observed in ^{1}H-^{13}C HSQC spectral regions of typical metabolites after ^{13}C-enrichment (adapted from [166]).

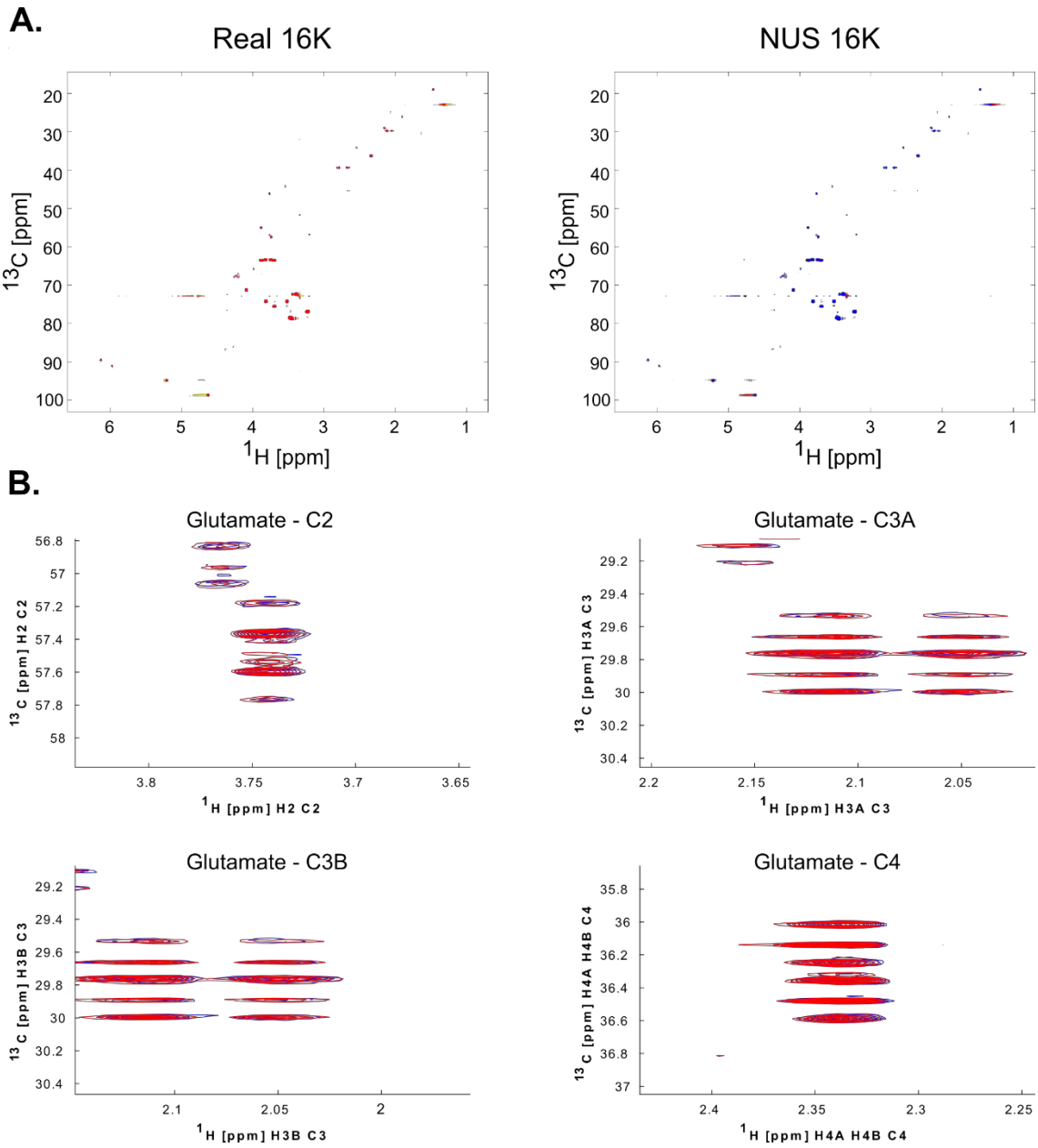

Figure 3. 7 – HSQC data for ^{1}H-^{13}C-HSQC spectrum acquired with regular sampling (red) vs a spectrum with a 25% non-uniformly incremented schedule (blue), using 16384 (16k) data points. Panel A shows an overview of the HSQC from HuH7 cells exposed to [U-^{13}C] glucose for 12 hours and panel B shows spectral regions of glutamate from both spectra. The resulting spectra are virtually indistinguishable, and the main difference is related with the noise. NUS-HSQC spectra were processed using Hyberts' hmsIST[156] module in nmrPipe[155].

This figure is published in [120], but it is my own work.

3.5. Tracer based metabolism in hepatic cells

3.5.1. How to choose a time point?

Cells are complex dynamic living systems, it is therefore important to understand how they behave in changing culture conditions and assess what influence sampling time has on the metabolic profile. As an open system, some metabolites are exchanged between the intracellular and extracellular environment in order to sustain cell growth needs and maintain homeostasis. Therefore, by characterizing cellular metabolism parameters, such as substrate uptake and metabolite secretion rates (fluxes), intracellular metabolite levels and pathway activities, it will be possible to understand the biochemical reaction network [167,168].

To investigate the metabolic regulation that occurs during cellular growth and proliferation, HuH7 cells were plated in 75 cm^2 Corning flasks and nutrient availability and consumption was determined by 1D ^1H NMR spectroscopy. For this, analysis of the intracellular and extracellular metabolic profile was performed, reflecting metabolite variations. Medium and intracellular polar extracts were collected at different times, ranging from 30 minutes to 12 hours after the beginning of the exponential growth phase (Figure 3. 8 to Figure 3. 11).

Figure 3. 8 shows representative ^1H NMR spectra for the intracellular variations in HuH7 over culture time, reflecting the metabolic adaptation during growth. Selected metabolites are shown in Figure 3. 8B to aid visualisation. Figure 3. 9 shows quantitative analysis of the intracellular metabolites within these samples and includes integration of the metabolites that participate in the main metabolic pathways. It is clear that glucose and branched chain and aromatic amino acids are consumed with increasing culture time while glycolysis and TCA cycle intermediates such as lactate, alanine, acetate, glutamate and succinate are being produced. This reflects anabolic metabolism characteristic of cell

growth and proliferation; however, these trends shift slightly after the 9 hours' time-point. During cell growth, the accumulation of several acidic metabolites, such as lactate, pyruvate, acetate and malate is clearly visible, which will decrease the pH in the cell.

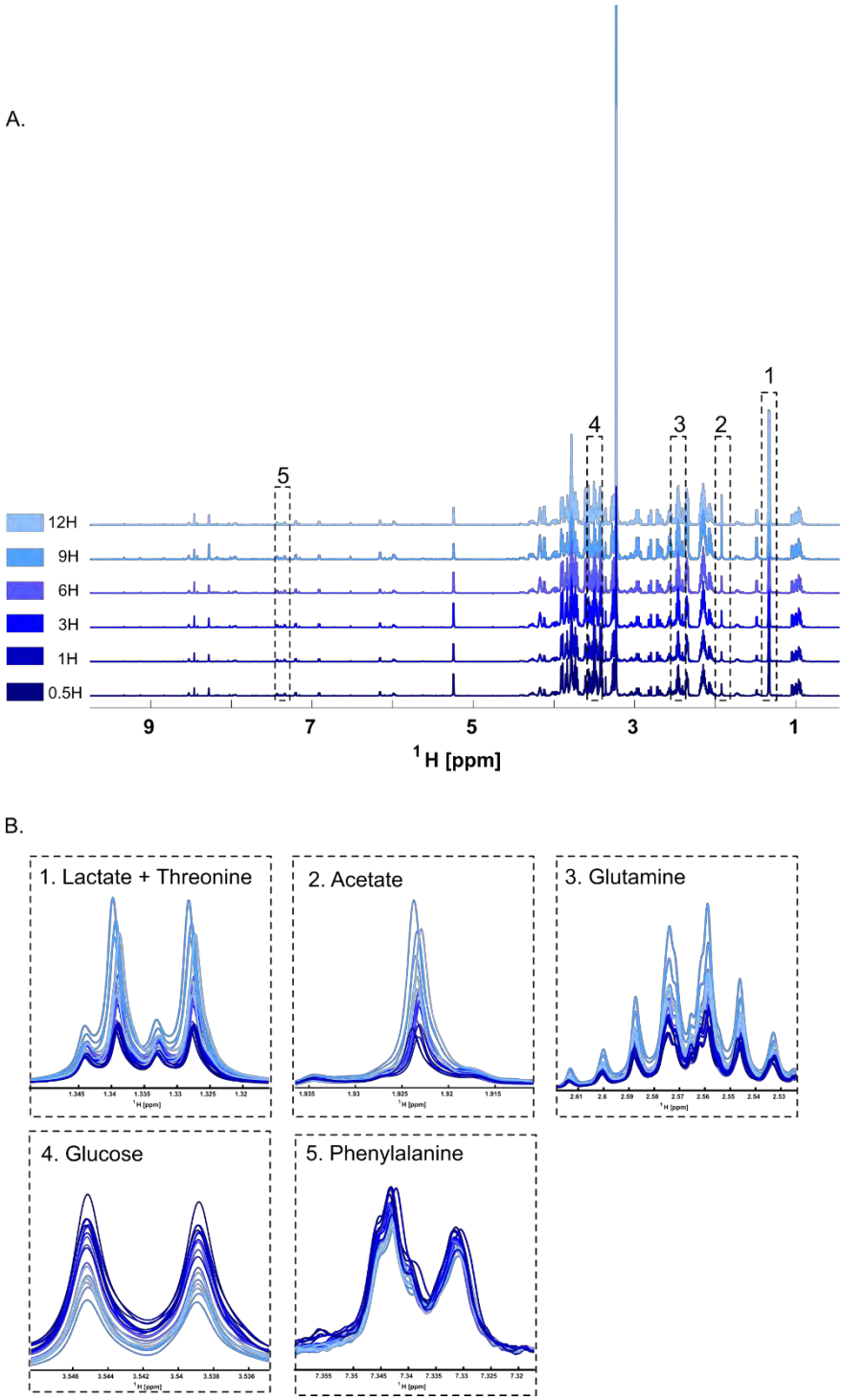

Figure 3. 8 – Representation of 1D ^{1}H NMR spectra obtained in a 600 MHz spectrometer of aqueous extracts from the hepatocellular carcinoma cell line (HuH7) over culture time. Section A. shows the superimposition of all representative spectra of the HuH7 cell aqueous extracts at each time point (n=3). Section B. shows expansions of the ^{1}H NMR spectra containing the resonances from lactate, threonine, acetate, glutamine, glucose and phenylalanine.

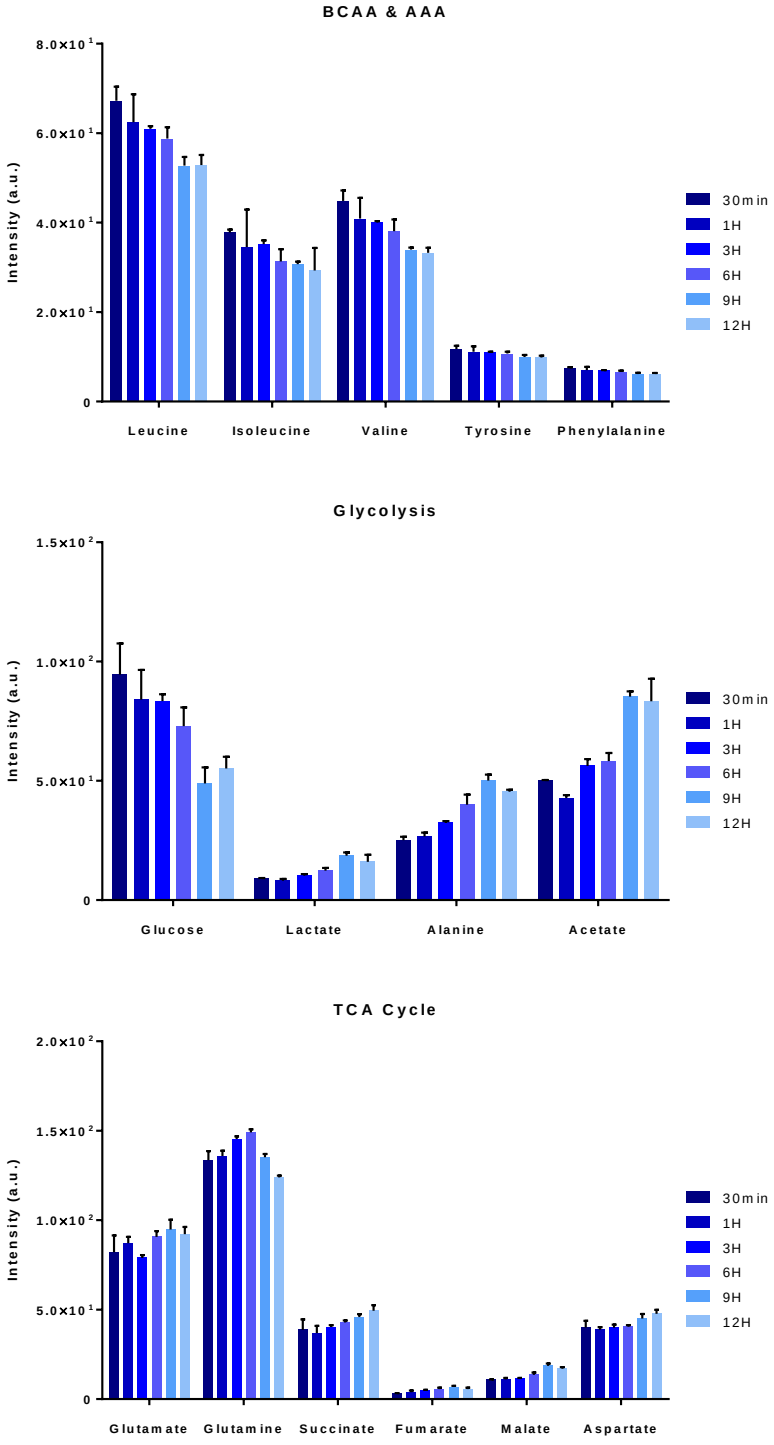

Figure 3. 9 -Graphical representation of the quantification of metabolites from intracellular polar extracts of HuH7 cells. Graphs are a representation of peak intensity ± standard deviation, with n=3 independent samples. This graph includes metabolites involved in amino acid metabolism, glycolysis and TCA cycle to help derive metabolic pathways contribution over culture time.

Figure 3. 10 displays the standard ^{1}H NMR spectra of the variations in HuH7 culture medium over culture time, as well as spectral regions for specific metabolites. Graphical representation of the metabolite intensities is shown in Figure 3. 11 which illustrates the dynamic exchanges that occur between the culture medium and the cells. Analysis of overall metabolite fluctuations shows that glucose is rapidly taken up from the medium to supply the cell with precursors for synthetic pathways. The up-regulation of glycolysis seems to be producing enough energy to meet the demand of the proliferating cells since the concentration of amino acids in the medium barely changes. Moreover, the increase in the glycolytic flux is also reflected by the excretion of acidic metabolites in the medium, such as pyruvate, lactate, acetate and glutamate.

To further investigate hepatocyte function and preferred metabolic pathways, changes in metabolism were followed using ^{13}C-labelled precursors.

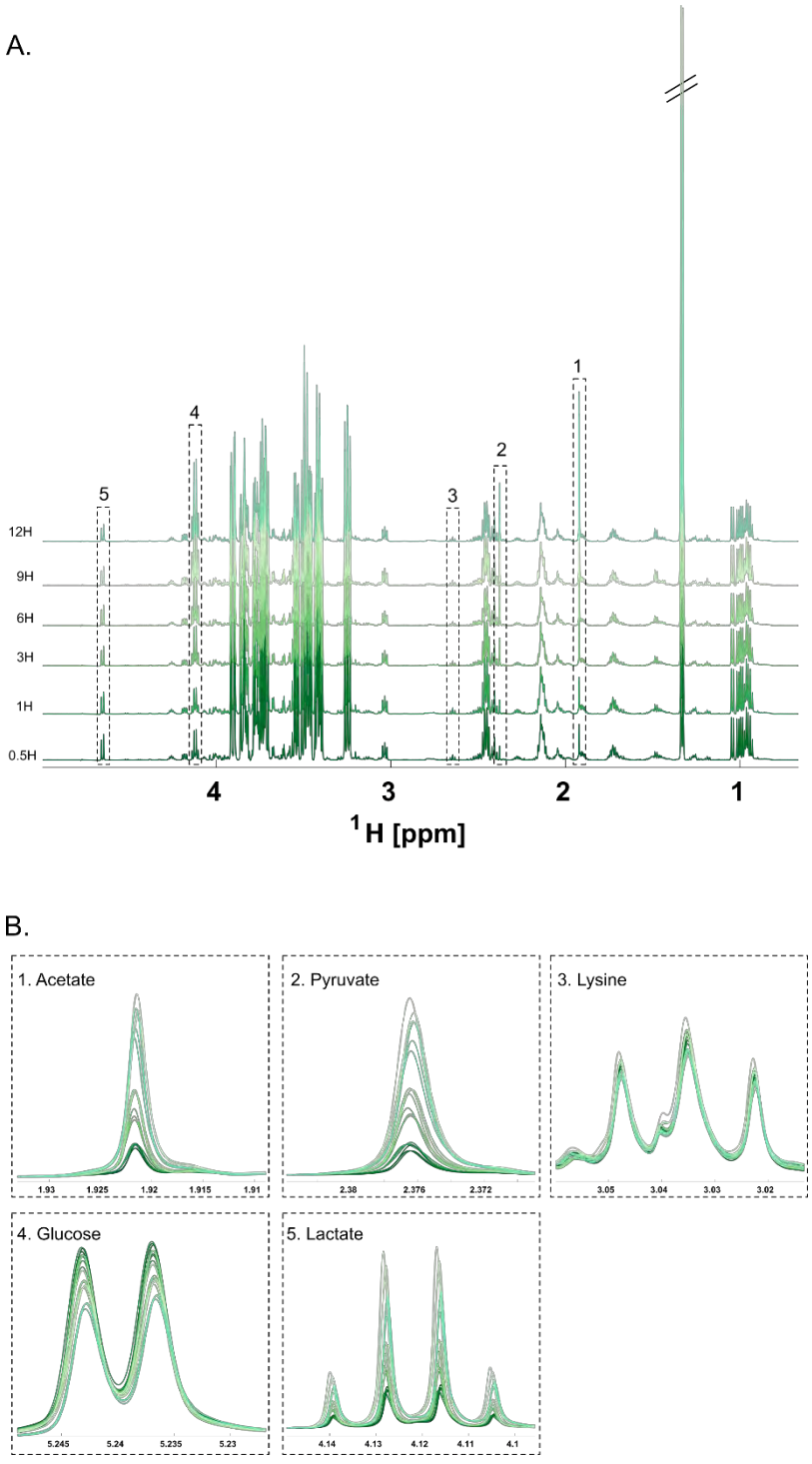

Figure 3. 10 – Representation of 1D ^{1}H NMR spectra obtained in a 600 MHz spectrometer of medium samples over culture time. Section A. shows the superimposition of all representative spectra of the medium samples at each time point (n=3). Section B. shows expansions of the ^{1}H NMR spectra containing the resonances from acetate, pyruvate, lysine, glucose and lactate.

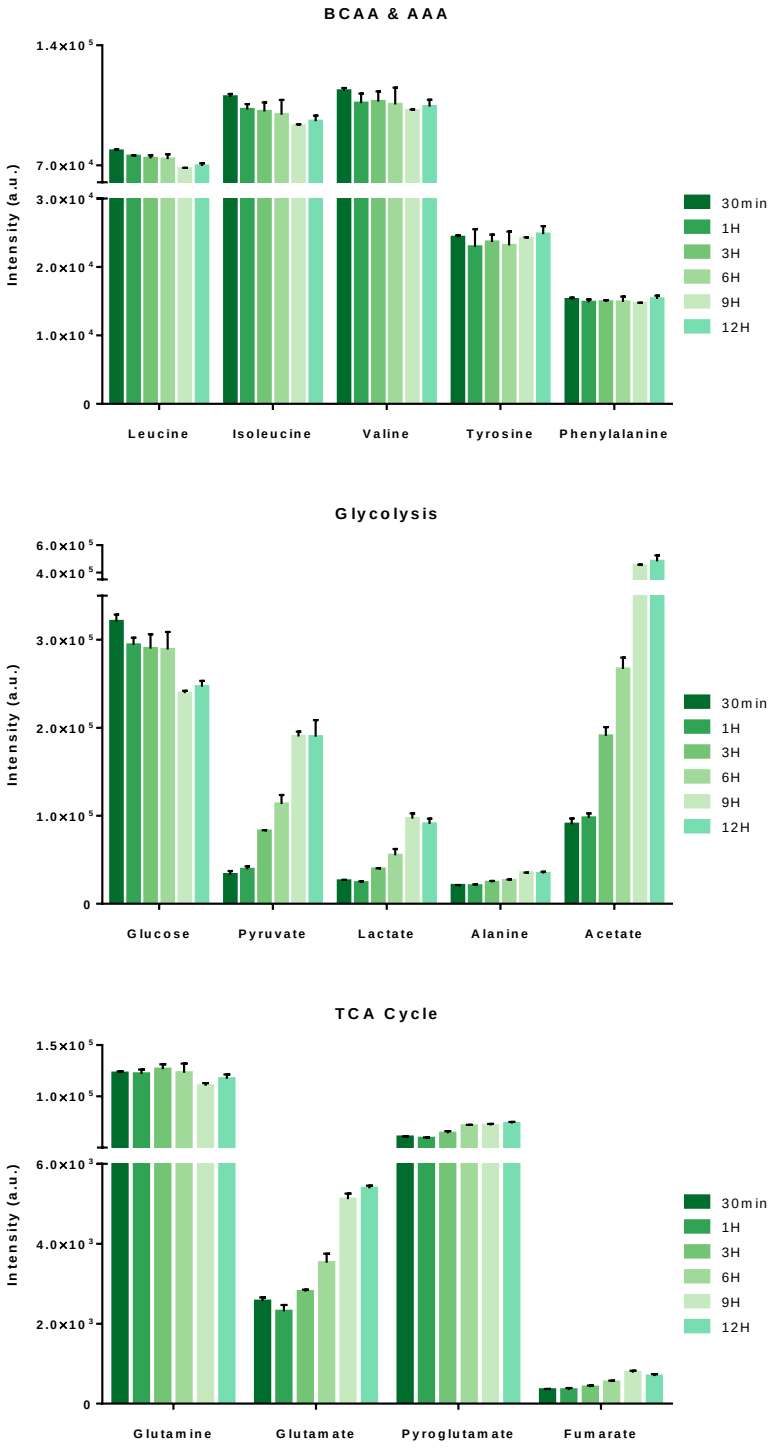

Figure 3. 11 – Graphical representation of the quantification of metabolites from extracellular samples of HuH7 cells. Graphs are a representation of peak intensity ± standard deviation, with n=3 independent samples. This graph includes metabolites involved in amino acid metabolism, glycolysis and TCA cycle to help derive overall uptake of nutrients from the medium and cellular excretions over culture time.

3.5.2. Incorporation of ^{13}C from [U-^{13}C] Glucose in HuH7 cells

In order to study ^{13}C enrichment in specific carbon positions, high-resolution 2D ^{1}H-^{13}C HSQC spectra were obtained from polar intracellular extracts of HuH7 cells, from the same time points as in 3.4.1 (Figure 3. 12). The HSQC spectra permit evaluation of distribution of carbon fluxes by measuring signal intensities, ^{13}C-^{13}C coupling patterns, and identification of contributions of labelled precursors to diverse metabolic pathways [169–171]. Metabolite identification in the HSQC spectra was carried out using the MetaboLab[172] library based on the Human Metabolome Database (HMDB)[173] and Biological Magnetic Resonance Data Bank[174]. The ratio of relative ^{13}C-enrichment was obtained for all individual carbon atoms by comparing the signal intensity in labelled samples derived from [U-^{13}C] glucose with the signal intensity of control matched samples which reflect the ^{13}C natural abundance.

Figure 3. 13 shows how incubation of HuH7 cells with [U-^{13}C] glucose would label several downstream metabolic intermediates in biosynthetic reactions. Glucose is oxidised via glycolysis to produce pyruvate, which is transformed into lactate or alanine, depending on the energy and substrate needs of the cells. Moreover, the hepatocytes are further oxidising pyruvate into acetyl-CoA by the pyruvate dehydrogenase (PDH) complex to feed the TCA cycle. Doing this, cells are not only improving the energy metabolism yield but also providing intermediates of the cycle to serve as precursors for the production of amino acids, nucleotides and other key pathways.

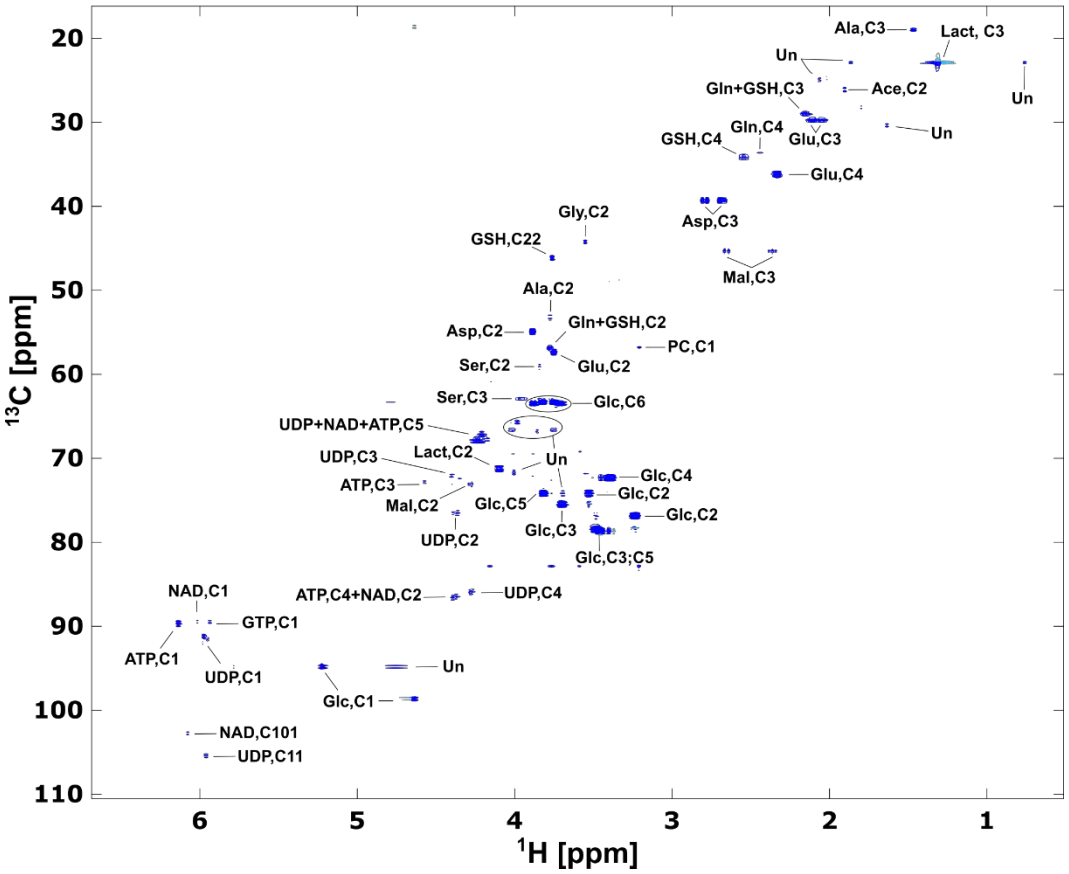

Figure 3. 12 – A representation of an ^{1}H-^{13}C HSQC spectrum of HuH7 polar cell extract after 9 hours labelling with [U-^{13}C] glucose. Several metabolites with ^{13}C fractional enrichments, such as amino acids, sugars and nucleotides are generated and have been assigned. Assignments are indicated as follows: three-letter code used for amino acids, Lact lactate, Ace acetate, Mal malate, ATP adenosine triphosphate, NAD nicotinamide adenine dinucleotide, PC phosphocholine, UDP uridine diphosphate, Un unassigned.

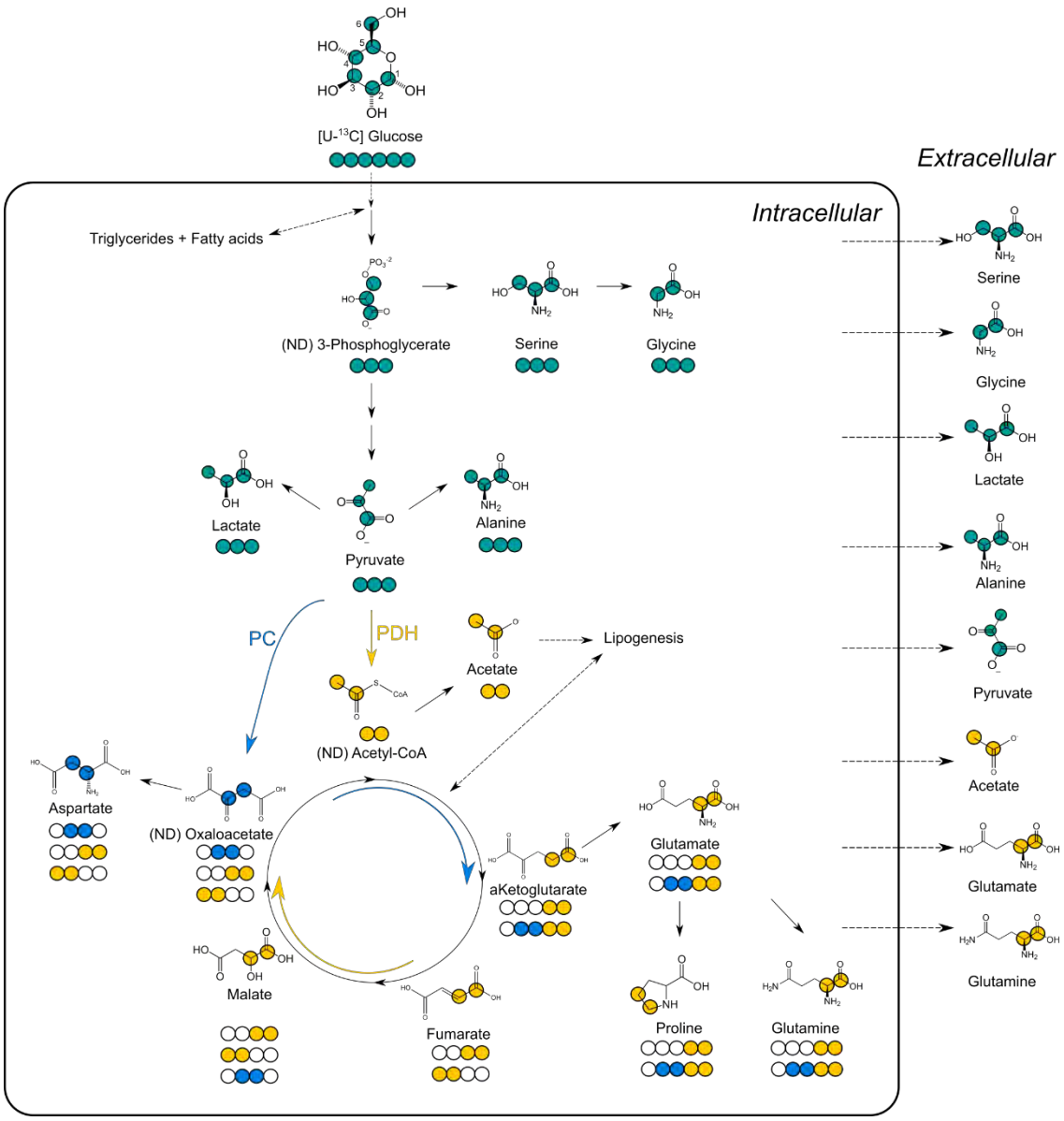

Figure 3. 13 – Graphical representation of label distribution in the main metabolic pathways when HuH7 cells are incubated with [U-^{13}C] glucose.

For each time point during culture, intracellular steady state ^{13}C-enrichment was calculated and the analysis of the distribution of labelled carbons in various intermediates was plotted as shown in Figure 3. 14. Taurine is shown as an example of an unlabelled metabolite when glucose is used as a precursor, demonstrating that when ratios are calculated from natural abundance the fold-change is indeed 1. Glucose was incorporated by the HuH7 cells and a gradual increase in ^{13}C-enrichment was observed for one carbon metabolism metabolites like glycine and serine. Also, the downstream glycolytic products lactate and alanine, are labelled in carbon 2 and 3, which indicates that [U-^{13}C] pyruvate is being produced. Pyruvate entry into the TCA cycle can occur either via pyruvate dehydrogenase producing [1,2-^{13}C] acetyl-CoA or via pyruvate carboxylase (PC) originating [2,3-^{13}C] oxaloacetate. TCA cycle intermediates are then produced via PDH/PC and label incorporation is visible in metabolites such as glutamate, glutathione, malate and aspartate.

At early time points, there was high incorporation of ^{13}C in carbon 4 of glutamate, reflecting the presence of isotopomer [4,5-^{13}C] glutamate and only later (over 3 hours) showed a higher ratio in carbon 2 and 3, revealing that the molecules underwent two passages through the TCA cycle and had a contribution from PC products to generate [2,3,4,5-^{13}C] glutamate. On the other hand, pyruvate carboxylase activity is reflected in labelling patterns in aspartate and malate [140], which are labelled in position 2 and 3 at higher levels than glutamate.

As a result of high glycolytic and TCA cycle fluxes, ATP seems to be incorporating ^{13}C at a consistent rate, as well as NAD^+. Although HuH7 cells don't seem to reach an isotopic steady state by the end of 12 hours, metabolic tracing can be achieved with a high label incorporation from 3 hours onwards. Ratios of at least 10-fold can be measured

in these cells for glycolysis, TCA cycle and serine biosynthesis in this short time-frame, providing a global picture of metabolic profile in a timely manner (Figure 3. 14).

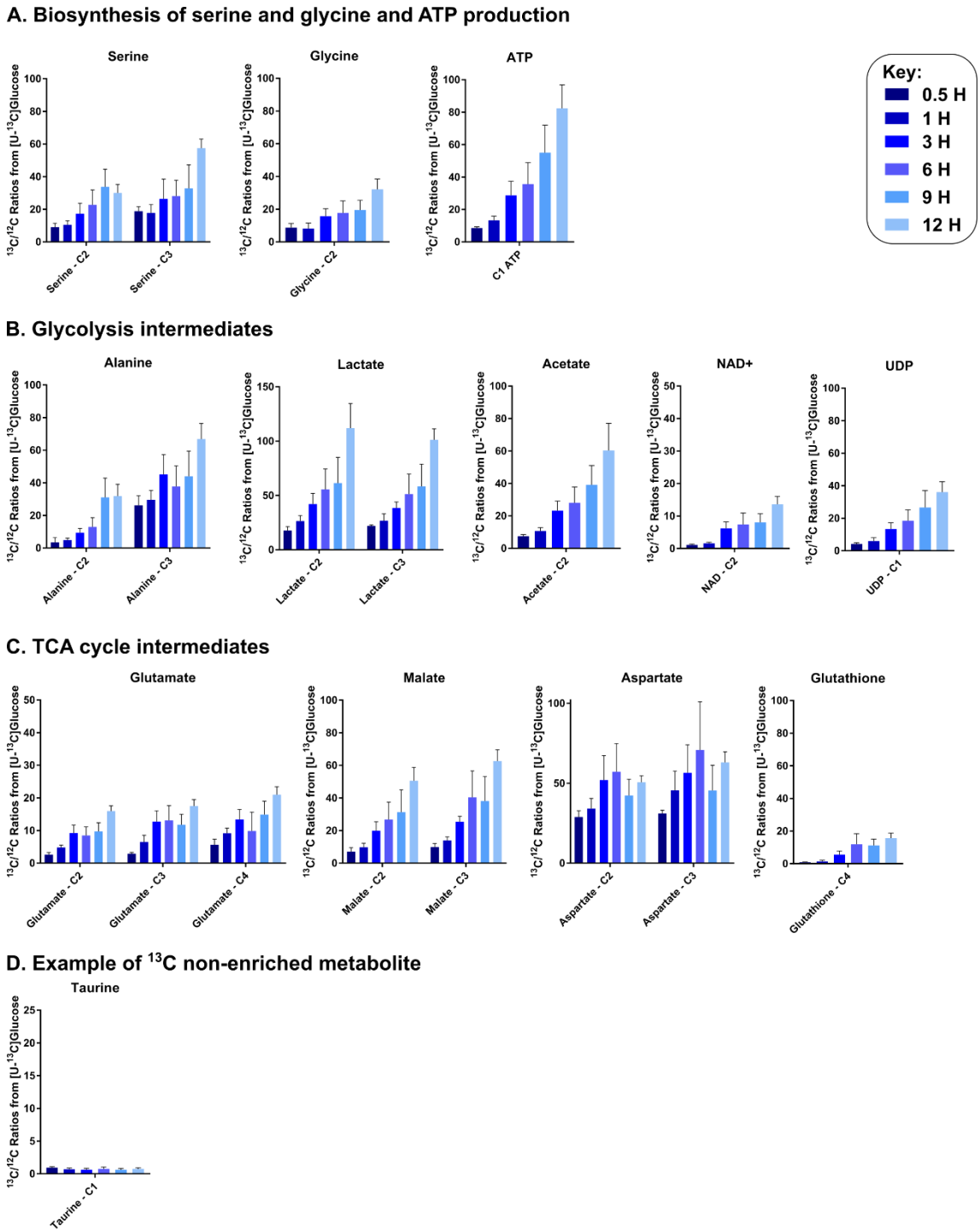

Figure 3. 14 – [U-^{13}C] glucose is incorporated in metabolites of several metabolic pathways in time. ^{13}C-incorporation was calculated as a ratio of ^{13}C/^{12}C using labelled and matched control samples (n=3). Ratios were expressed as means ± standard error of the mean.

3.5.3. The importance of choosing the right precursor

3.5.3.1. Cellular behaviour adapts to nutrient availability

Nowadays, non-alcoholic fatty liver disease is the most common chronic liver condition worldwide and this has been closely linked with the increase of fructose consumption [21,24,144]. Alteration in the homeostasis of carbohydrates, such as fructose and glucose, will lead to steatosis and inflammation in the liver. Although fructose and glucose share similar metabolic pathways, their entry into and regulation by cells is quite different. Hepatocellular expression of glucose and fructose transporters expression can change during the development of diseases, thereby altering carbohydrate regulation [2,175].

To investigate whether fructose is incorporated and metabolised by hepatic cells *in vitro* and how it performs relative to glucose, HuH7 cells were incubated for 3 different time-points in complete medium containing 20 mM ^{12}C- or [U-^{13}C] glucose or 20 mM ^{12}C- or [U-^{13}C] fructose. The ^{13}C-enrichments were calculated for metabolites participating in glycolysis, TCA cycle and one-carbon metabolism as represented in Figure 3. 15.

For the first 30 minutes, glucose seems to be incorporated and metabolised at a higher ratio than fructose, and label is expressed mainly in metabolites from glycolysis and aspartate, derived from pyruvate carboxylase activity. After 2 hours incubation, fructose incorporation occurs at a greater extent and shows ^{13}C-enrichment in the same metabolites as when glucose was used, albeit at a lower ratio than glucose. However, after 6 hours, there is a higher expression of labelled metabolites across all the analysed metabolic pathways with a slightly different trend between the precursors. While glucose derived metabolites are more pronounced in the glycolytic metabolites and TCA cycle intermediates there are some major changes when fructose is used. Although fructose can be metabolised and enter glycolysis at the level of the triose-phosphates, it can also

be directed to the production of lipids. In support of this, significant decreases can be seen at the level of acetate and lactate. Acetate can also be directed towards *de novo* lipogenesis, but further studies are needed to confirm the fate of the labelled carbons.

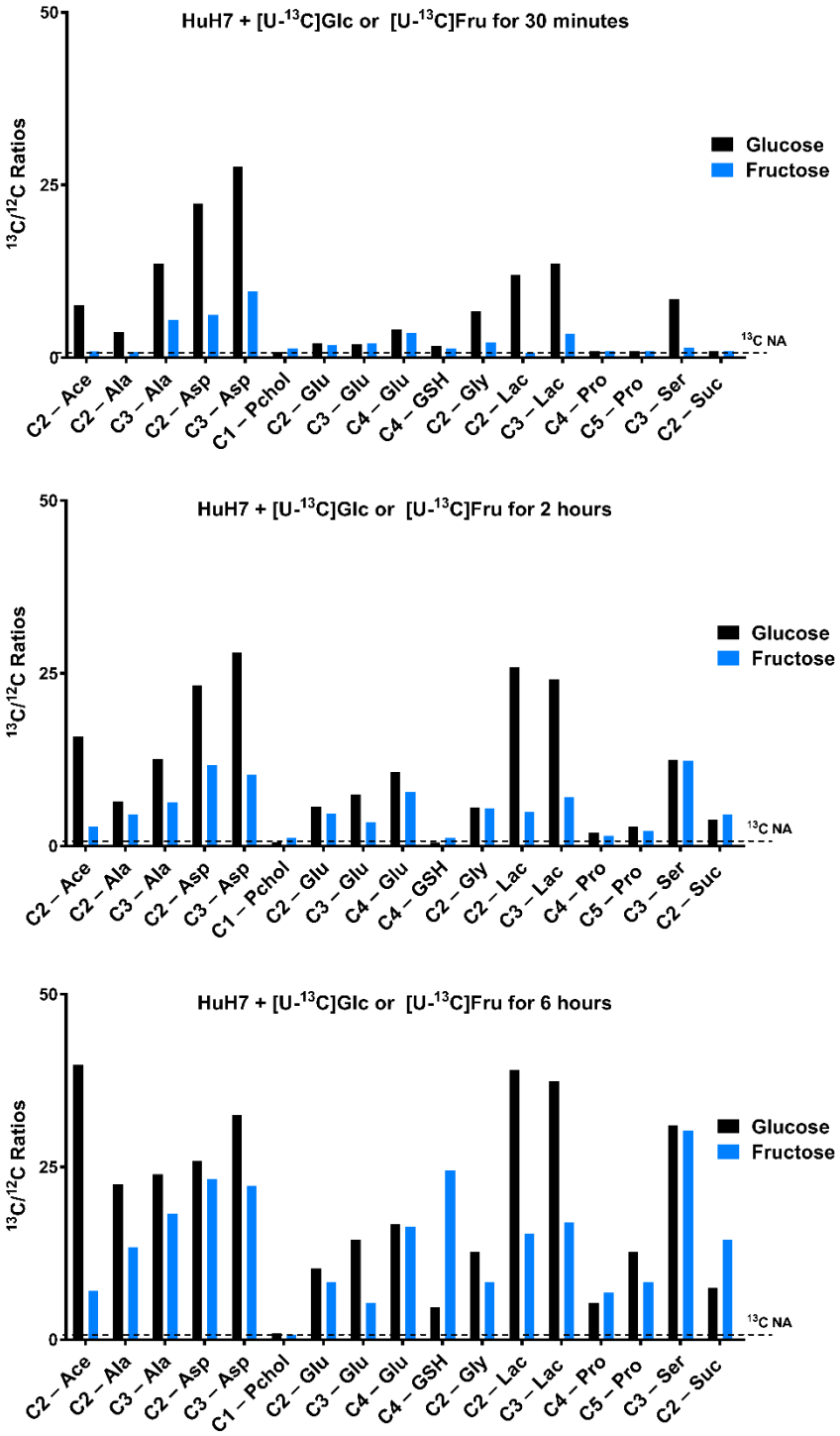

Figure 3. 15 – ^{13}C-enrichment in several key metabolites of HuH7 cells after exposure to [U-^{13}C] glucose or [U-^{13}C] fructose occurs at different rate depending on precursor used. Three distinct time points (30 minutes, 2 hours and 6 hours) were analysed by ^{1}H-^{13}C HSQC in comparison to unlabelled matched samples.

3.5.3.2. Challenges using human *ex vivo* liver for metabolic studies

Tracer-based metabolism in primary liver samples has great potential for diagnostic purposes in translational medicine, particularly in the context of understanding glucose and lipid metabolism in fatty liver disease. Therefore, there is a need to obtain a reliable model to track metabolic changes in human liver disease using ^{13}C precursors on human samples. Although the Birmingham Liver Group has access to fresh human tissue specimens, in my hands tracer studies have proven to be a challenge. Difficulties were related to delays between tissue collection from patient and availability in the research laboratory, sample preparation, difficult handling of small samples and even the method to deliver the ^{13}C-labelled precursor. However, below I show two distinct tested methods that allowed tracing of ^{13}C-enrichment in *ex vivo* samples, either by extracting and plating primary human hepatocytes or by *ex vivo* human liver tissue perfusions.

3.5.3.2.1. Extraction and plating of primary cells

Primary human hepatocytes were prepared from liver tissue, as previously described in 2.3.2. The hepatocytes were plated in collagen-coated T75 cm^2 Corning flasks, allowed to attach to the new surface and microscopically assessed for viability. In order to investigate if they were still metabolically active, these hepatocytes were exposed to [U-^{13}C] glucose for 4.5 hours. Label incorporations were observed for several metabolites, such as alanine, lactate, glutamate and glutathione, as demonstrated in Figure 3. 16. [U-^{13}C] glucose was incorporated within this time frame and was converted to metabolites from glycolysis and TCA cycle. Nevertheless, metabolic activity was still minimal considering the long incubation time with the [U-^{13}C] glucose, which is unsatisfactory considering that my main goal is looking for metabolic variations in disease. Therefore, a new method was tested, exploring the use of an intact liver wedge.

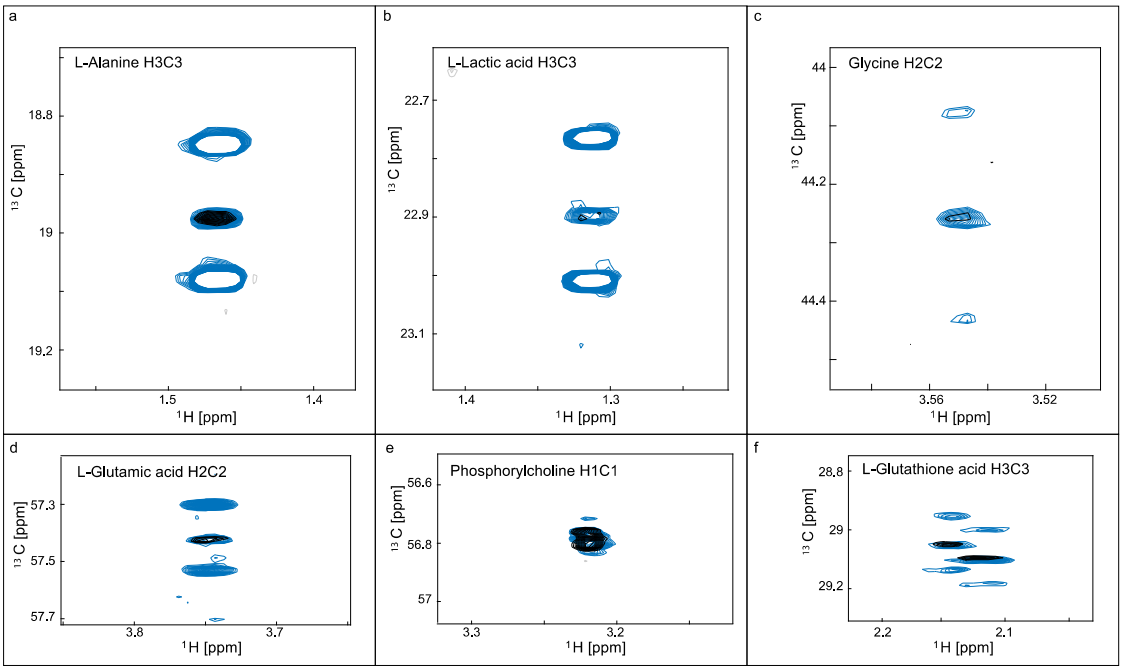

Figure 3. 16 – Feasibility of tracer-based analysis from donor liver samples represented by overlaid sections from ^{1}H-^{13}C HSQC of polar extracts from hepatocytes isolated from a donor liver sample. Black and blue resonances arise from samples exposed for 4.5h to media containing unlabelled glucose and [U-^{13}C] glucose, respectively. Panels show the spectral regions for L-Alanine C3 (a), L-Lactic acid C3 (b), L-Glycine C2 (c), L-Glutamic acid C2 (d), Phosphorylcholine C1 (e) and L-Glutathione C3 (f). Phosphorylcholine was not enriched and is included as a scaling reference but the other metabolites were enriched by [U-^{13}C] glucose.

This figure is published in [120], but it is my own work.

3.5.3.2.2. Perfusion of human livers *ex vivo*

Despite a reduction in metabolic rate, human *ex vivo* livers continue to be functional at least 24 hours, as demonstrated by several teams in the recent years [176–179]. Therefore, *ex vivo* liver perfusion was explored as a potential alternative for me to study real time metabolism.

I began using freshly harvested liver tissue wedges from a patient with primary biliary cholangitis (PBC) which were perfused with basal media containing 20mM of [U-^{13}C] glucose or fructose. Matched unlabelled controls from the same donor were also tested. In Figure 3. 17 we can see expansions of ^{1}H-^{13}C HSQC spectra from a representative control sample (blue), one labelled with [U-^{13}C] glucose (red) and another with [U-^{13}C] fructose (green), after 1 hour of perfusion. At this time-point I observed the incorporation of both labelled precursors by the liver as well as downstream ^{13}C-incorporation in several metabolites. In the glucose sample, I was able to see coupling patterns in glucose (precursor), lactate and alanine. However, although this experiment was carried on for longer than one hour, ^{13}C-incorporation was not seen in any other metabolites as time progressed. On the other hand, when the PBC liver wedge was perfused with labelled fructose, a higher number of metabolites were enriched in ^{13}C together with a high incorporation of fructose. Fructose was converted to lactate and alanine, similar to the glucose sample, but was also metabolised into sorbitol, glycerol and glycerol 3-phosphate that could enter *de novo* lipogenesis. With this I have shown that labelled precursors work in the context of human *ex vivo* liver perfusions, for real time assessment of metabolism.

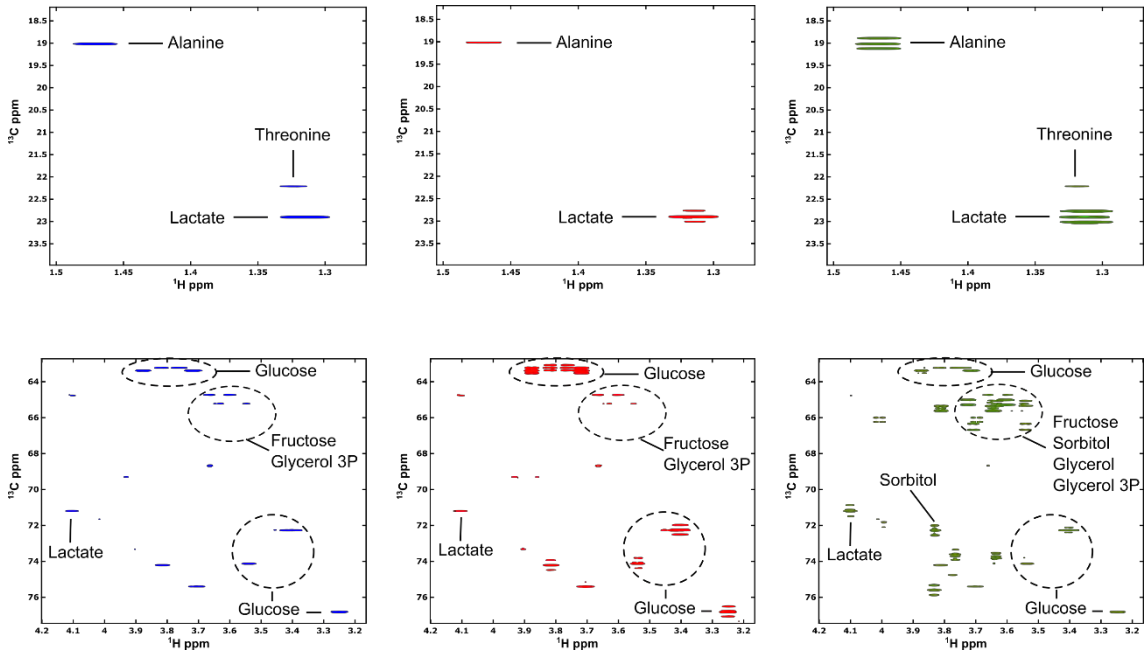

Figure 3. 17 – Tracer-based analysis of PBC liver sample, analysed by ^{1}H-^{13}C HSQC spectra. Comparing with the unlabelled matched control sample (in blue), the incorporation of [U-^{13}C] glucose (in red) or fructose (in green) is visible using a perfusion system. The labelled precursors are integrated and metabolised by the tissue, forming intermediates of glycolysis and fructolysis.

3.6. Discussion

3.6.1. Sample preparation and improvements in NMR technology

The assessment of the cellular metabolism and study of regulation of biological systems has been achieved with NMR-based metabolomics. This is important for the investigation of disease mechanisms, identification of new biomarkers and monitor therapeutic outcomes. Therefore, optimising sample preparation and data acquisition in a metabolomics workflow is crucial to obtain reliable and reproducible results [103,180].

In my thesis, an extraction procedure was optimised for the hepatocarcinoma cell line HuH7 as it was the chosen cell line for all *in vitro* studies. The growth characteristics of this cell line were assessed for 5 days and a growth curve was created. Cells were found to reach confluency 3 days after splitting them, reaching approximately 1 x 10^7 cells per flask, the optimal number for analysis by NMR spectroscopy [151]. Considering that I was interested in studying the metabolic variations in response to different proliferative stimuli, such as different carbohydrate sources or fat-overloading, cells should be studied while in the proliferation phase. This allow me to follow the metabolic activity of healthy cells providing information about cellular energy metabolism and biosynthetic pathways, which is also specific for each cell type and environment [181–183]. Thus, HuH7 cells metabolism was studied after 48 – 72 hours of plating them into a new flask.

Next, I evaluated the metabolite extraction method and compared the variations in specific metabolites caused by the polarity change in the quenching solvent mixture. The overall metabolic content was not significantly altered by the different volumes of chloroform used, however the concentration of several organic acids showed substantial differences. Bearing in mind that the polar fraction of the metabolome is of most interest for this thesis, using a final volume of 400 µl of chloroform provided optimal results for a wide range of metabolites of interest and different polarities [180,184]. This allowed me to

obtain higher concentrations of amino acids, carboxylic acids and choline containing compounds, whilst minimising the extraction of lipids and other macromolecular components.

Following the optimisation of sample preparation, I sought to evaluate the improvements in signal to noise in NMR spectra, enabled by the use of micro-cryoprobes, especially when analysing mass-limited samples. Here, two different samples were studied, including a sucrose solution (0.1M) and an intracellular polar extract from HuH7 cells. The result was similar for both samples, revealing that the use of cryogenic temperatures generates great sensitivity improvements, by a factor of 4 to 10 when compared with a room temperature probe, which is in agreement with Serber *et al* [119].

This signal to noise ratio was further enhanced when the 1.7 mm micro-cryoprobe was used, leading to a rise of at least 4 times comparing to the 5 mm cryoprobe. The use of these micro-cryoprobes in NMR-based metabolomics offers great advantage when only small sample amounts are available, for example when using primary cells, and high throughput rates are required. Moreover, the sensitivity increase obtained by using cryogenic probes improves efficiency of metabolite determination by NMR, especially when using ^{13}C-labelled substrates [117,118].

Determination of ^{13}C-incorporation in specific positions of metabolites requires acquisition of high resolution 2D NMR spectra, which is usually very time consuming [185]. Thus, the combination of a micro-cryoprobe for sensitivity enhancement and acquisition of non-uniform sampling (NUS) 2D HSQC spectra was assessed for metabolomics applications. My analysis has shown that a regular high-resolution HSQC acquired for 16 hours was virtually identic to the HSQC acquired with a 25% NUS

schedule for around 4.5 hours. Using non-uniform sampling, only a specific number of indirect data points was collected, which later needed to be reconstructed using algorithms to generate a spectrum [186]. As a result, the acquisition times were reduced and the resolution in the indirect dimension was maintained [185,187]. This is particularly important for my research as the NUS-HSQC spectra retained multiplicity information, providing highly resolved carbon multiplet patterns and allowing to determine the ^{13}C flux through the metabolic pathways and specific isotopomers.

3.6.2. Metabolism in hepatic cells

Investigation of cellular metabolism and its impact during cell growth and proliferation can provide information about metabolite fluxes, nutrient availability and metabolic energy state of cells [181,188,189].

For this study, adherent HuH7 cells were plated and were allowed to attach to the new growth surface to initiate proliferation. A time-point experiment was performed during the exponential growth of the cells, in which they spread over the surface until space becomes limiting, up until they passed to the stationary phase characterized by maintenance metabolism [188,189]. When mammalian cells are in the growth and proliferation phase, they need to increase their uptake of nutrients and reprogram glycolysis and TCA cycle towards the generation of building blocks for macromolecular synthesis, such as large proteins and DNA. When cells start entering the maintenance phase, signalling pathways are activated and metabolite concentrations start to stabilize [190,191].

When analysing intracellular polar extracts, it was possible to confirm that as time in culture increased there was consumption of glucose and branched chain amino acids, as previously reported [182,183,190]. Moreover, intermediates of glycolysis and TCA cycle such as lactate, alanine, acetate, glutamate and succinate were increased over culture time. These metabolites can supply other metabolic pathways in response to biosynthetic demand and energetic needs of the cells. This can either be towards lipid metabolism, protein synthesis and nucleotide formation, which increases biomass formation of proliferating cells [188,192].

On the other hand, when analysing medium samples, consumption of available nutrients to preserve the cellular energy metabolic needs was detected. Hence, uptake of glucose by the cells was reflected in the decreased levels of glucose in the medium, but

amino acids levels were barely altered. More importantly, increased cellular glycolytic flux was confirmed by the rising excretion of organic acids in the medium, including pyruvate, lactate, acetate and glutamate, which will ultimately alter medium pH, as reflected by the colour change in the media over time. These changes in pH can also alter intracellular activity, inhibiting enzymes such as phosphofructokinase, leading to a decrease in glucose consumption and an increase in glutamine utilisation [191,193,194]. This was confirmed in my cells, as they started consuming glutamine from the 9h time-point forward, reflected in the decreasing intracellular concentration as well as the glutamine levels in the medium.

Although the dynamic nature of the cell metabolome is perfectly traceable using NMR analysis, it is very dependent on sampling time. Thus, to follow metabolic interaction in HuH7 cells during cell growth at a steady metabolic rate and whilst avoiding cellular stress, my data would suggest that metabolism should be studied between 6 and 9h after the start of the growth phase.

To better understand glucose utilisation by HuH7 cells during anabolic metabolism, a tracer-based study was performed using [U-^{13}C] glucose. Using the same time points as the previous study, the incorporation of ^{13}C in specific metabolites led to further information regarding metabolic rates and regulation of metabolic pathways. My results have shown that [U-^{13}C] glucose is taken up by the cell, enters glycolysis to produce pyruvate and, according to cellular needs, it can further be transformed in lactate or alanine, or enter the TCA cycle via acetyl-CoA [1]. ^{13}C-enrichments were observed for TCA cycle intermediates such as glutamate, malate, aspartate and glutathione, which reflect pyruvate flux. One-carbon metabolism intermediates were also formed during this time course, with high levels of labelled serine and glycine being generated.

Hepatic metabolism involves all reactions related to carbohydrate oxidation, *de novo* lipogenesis, amino acid metabolism and TCA cycle activity. During the cellular growth phase, glucose is oxidised through glycolysis at a high rate, producing high levels of alanine, lactate and pyruvate. Next, pyruvate can enter the TCA cycle via two alternative routes to generate intermediates of lipogenesis, amino acid synthesis and to produce ATP [19,195]. Using [U-^{13}C] glucose, fully labelled isotopomers of pyruvate were produced at the end of glycolysis, which can either enter the TCA cycle via pyruvate dehydrogenase (PDH) to generate acetyl-CoA or via pyruvate carboxylase (PC) to produce oxaloacetate. When pyruvate enters the TCA cycle via PDH activity, isotopomers of [4,5-^{13}C] glutamate are formed, while PC activity originates [2,3-^{13}C] oxaloacetate. From this, gluconeogenic activity of the liver can be assessed by measuring the TCA cycle intermediates isotopomers that are produced via PDH/PC. In this study, higher rates of labelled malate and aspartate where detected than of glutamate and glutathione during the proliferative phase. Therefore, we show that enzymatic activity is regulated in response to metabolic needs as it could also change to replenish the TCA cycle when intermediates are shunted to other pathways [196,197].

Study of the TCA cycle activity in particular, provided significant information in the context of NAFLD, and this pathway has previously been related to disease progression [197–199]. Similarly, metabolic homeostasis is affected by the regulation of PDH/PC activity, which has also been shown to contribute to hepatic steatosis [200–202]. However, perhaps the most interesting set of data derives from my experiments using fructose exposed cells. Carbohydrate metabolism in HuH7 was studied comparing both [U-^{13}C] glucose and [U-^{13}C] fructose uptake and metabolism. Although both metabolites share similar metabolic routes, their regulation is quite different. Using HuH7 cells, the ratio of ^{13}C-incorporation revealed a faster glycolytic rate for glucose than fructose in the first 30 minutes, which

could be related to an initial faster uptake. By the end of 2 hours, these differences were not as substantial and some metabolic products were found to be incorporating the ^{13}C at the same rate, including TCA cycle intermediates glutamate, succinate and proline, as well as one carbon-metabolism intermediates serine and glycine. Interestingly, ^{13}C-incorporation ratios of alanine, lactate and acetate were lower than when glucose was used as the substrate, which demonstrates the differences in metabolic flexibility when using different carbohydrate sources [203]. At the end of the experiment (6 hours), the metabolic activity was enhanced, and ratios of ^{13}C-incorporation were quite similar for both substrates. Thus, my studies demonstrate the feasibility of employing both glucose and fructose as a ^{13}C-labelled precursor using hepatic cells, opening possibilities to study the effect of different precursor carbohydrates in the context of NAFLD. This concept is developed further in subsequent chapters.

3.6.3. Human *ex vivo* liver for metabolic studies

To test the feasibility of use of *ex vivo* human livers for metabolic studies using ^{13}C-labelled precursors, two different methods were considered. First, primary hepatocytes were extracted from the liver tissue as previously explored in our laboratory [148]. Using [U-^{13}C] glucose I was able to confirm that freshly isolated hepatocytes are still metabolically active following the extraction procedure. Furthermore, glucose was incorporated and metabolised within approximately 4 hours, which was visible in 2D HSQC spectra by the appearance of ^{13}C coupling patterns in glycine, glycolytic end products alanine and lactate, and in TCA cycle intermediates such as glutamate and glutathione. These results are in partial agreement with Winnike *et al* [204], who only detected ^{13}C-enrichment of the metabolites in rat primary hepatocytes, but not in human. Moreover, they only used 1D ^{1}H NMR spectra to detect the presence of satellite peaks, which is more difficult to accurately measure ^{13}C-isotopomers in complex mixtures.

Although these results show that this technique is feasible to study ^{13}C-incorporations in human tissue, the process used to obtain the intact primary hepatocytes is quite long (ca. 6-8 hours) and most of the cells isolated were not viable. In my hands, live cells constituting only 40% of the obtained hepatocytes, as reported previously [148]. Hence, I felt that an alternate methodology was required in order to obtain reliable results and that mimic the overall cellular interactions and metabolism in an intact liver.

Several studies demonstrate the benefit *ex vivo* perfusion for improving organ preservation, functionality and suitability for transplantation [176,205,206]. Therefore, using a perfusion method for studying metabolic alterations in response to external stimuli seemed a suitable alternative, and indeed this has been formerly explored by Bruinsma *et al* [207].

Metabolism of ^{13}C-labelled carbohydrates was assessed in an *ex vivo* liver perfusion setup using intact human liver wedges. In the first instance, similar weight liver tissue wedges were collected from a patient with PBC and perfused with basal media containing 20 mM of [U-^{13}C] glucose or fructose, or their matched unlabelled controls. Analysing the unlabelled control liver wedge, it was possible to detect metabolites that compose the main metabolic pathways involving glucose and fructose. When a ^{13}C-labelled substrate was used, their uptake was observed and the transfer of ^{13}C from glucose and fructose was observed in glycolytic metabolites, by displaying coupling patterns in the HSQC spectra. Both liver wedges were able to uptake the carbohydrate source and metabolise it to produce several metabolites.

The wedge perfused with labelled glucose only revealed ^{13}C-enrichments in lactate and alanine, even after one hour of perfusion, which is consistent with the reduction in metabolic rate and cellular function referred by Barbas *et al* [205]. However, when [U-^{13}C] fructose was the source substrate, it was further metabolised into sorbitol, glycerol and glycerol 3-phosphate. These differences may arise from the lack of regulation of fructose metabolism, while glucose is dependent on hormonal signalling and enzymatic regulation [26].

Nevertheless, this method allowed study of hepatic metabolism in human *ex vivo* tissue, and tracing the fate of ^{13}C-substrates in real time. Therefore, I selected this as my method of choice to work with intact human tissue rather than using extracted primary liver cells.

CHAPTER 4

METABOLIC CHANGES DURING THE PROGRESSION OF LIVER DISEASE

4. Metabolism in liver disease

4.1. Overview

Non-alcoholic fatty liver disease (NAFLD) affects a large number of the world population and its incidence and prevalence are increasing to epidemic proportions[61]. Assessment of the severity of liver disease progression or regression has limitations at present. Currently used techniques are based on serum and imaging tests, such as ultrasound and computed tomography, as well as the interpretation of liver specimens after a biopsy. Their variable diagnostic accuracy, limitations, invasive nature and lack of validation has led to significant advances in other techniques such as nuclear magnetic resonance (NMR) spectroscopy, magnetic resonance imaging (MRI) and elastography [65,87–89].

The application of metabolomics has significantly improved the field of disease phenotyping and the discovery of novel biomarkers. Therefore, finding biomarkers to aid with assessment of disease prognosis and diagnosis is essential since it will provide a better understanding of the multiple risk and pathogenic factors for NASH, a more serious form of NAFLD [61,86]. In particular, the generation of tests that can be use on less invasively collected samples or by imaging platforms, and which have good accuracy and predictive powered across the full spectrum of disease would be hugely significant.

This chapter describes characterization of metabolic and pathogenic alterations in NAFLD from simple steatosis and progression to non-alcoholic steatohepatitis (NASH). I began by studying the effect of oleic acid-induced steatosis on the intracellular metabolism of hepatocytes, in a quantifiable *in vitro* model. Next, human liver tissue was used to assess the severity and extent of the liver injury during NAFLD progression. Histological analysis of human samples was performed, followed by a metabolomics analysis using 1D ^{1}H NMR spectra of intracellular polar and organic extracts.

4.2. Induction of steatosis in controlled experiments

4.2.1. Quantification of lipid accumulation in HuH7 cells

Accumulation of lipids to form fatty droplets in hepatocytes is a pathological marker of non-alcoholic fatty liver disease that can progress to NASH. Livers are histologically defined as steatotic when there is a visible accumulation of lipid droplets in at least 5% of hepatocytes. When fat accumulates intracellularly, lipids form large droplets filling the cytoplasm (macro-steatosis) and/or form small vesicles in the cytoplasm (micro-steatosis) [208–210]. To explore the utility of the hepatoma cell line HuH7 as an *in vitro* model of hepatic steatosis, cells were treated in culture with oleic acid (OA). Oleic acid is an 18-carbon length monounsaturated fatty acid (C18:1) which is present in animal and vegetable oils [208].

HuH7 cells were treated with a high concentration of OA (2mM) for 24 and 48 hours and lipid accumulation was visualized in the form of lipid droplets. Lipid accumulation was observed in the form of macro- and micro-vesicular steatosis (see Figure 4. 1). In the first 24 hours, cells maintained a 80-90% viability with little cellular death, however, if they were exposed for a longer period, such as 48 hours, their viability rapidly decreased, with only 50-60 % of viable cells (data not shown, but in agreement with Gómez-Lechón *et al* [210]).

Overall, oleic acid at a concentration of 2 mM has induced steatosis in HuH7 cells, mimicking the effect of lipid accumulation in fatty liver disease.

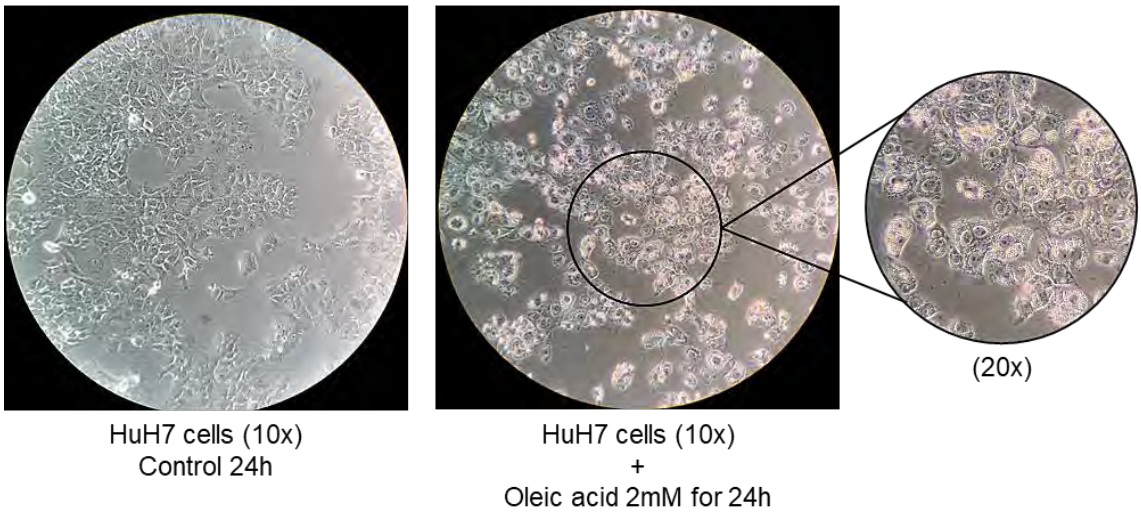

Figure 4. 1 – Fatty acid accumulation occurs in HuH7 cells when exposed to oleic acid for a period of 24 hours. HuH7 cells were exposed to 2mM of oleic acid for 24 hours and representative microscopic pictures from n=6 flasks were obtained. A comparison between cells under control conditions (left) demonstrates that cells exposed to oleic acid (right) are able to incorporate free fatty acids and form lipid droplets in the cytoplasm. A higher magnification (20x) allows to observe simple steatosis in the HuH7 cells which also increase in size.

4.2.2. Effects on the metabolome of hepatocytes assessed by 1D ^{1}H NMR spectroscopy of cellular polar extracts

Considering that 24 hours of treatment with oleic acid at 2 mM resulted in accumulation of lipids intracellularly with minimal cell death, I next assessed changes in cell metabolism. HuH7 cells were treated with oleic acid for 24 hours, and intracellular polar extracts were obtained for NMR analysis. Figure 4. 2 represents the metabolites identified in the 1D ^{1}H NMR spectra of both control and OA exposed samples that were used for quantification purposes. Approximately 30 metabolites were identified, including amino acids, organic acids, carbohydrates and choline-containing compounds, which are involved in the main biochemical processes of a cell.

The addition of oleic acid in the medium for 24 hours induced small changes in overall cellular metabolism (see Figure 4. 3). Although there were no significant alterations between both conditions, there was a trend for increased amino acid metabolism, reflected by the increase in branched chain amino acids (leucine, isoleucine and valine), as well as aromatic amino acids and serine. The decreased levels of fructose, the main carbon source in this experiment, and the slightly elevated levels of acetate and ATP could be indicators of higher glycolysis rate and energy metabolism. Nevertheless, the most noteworthy trend is the increase of both glycerophosphocholine (GPC) and the antioxidant taurine.

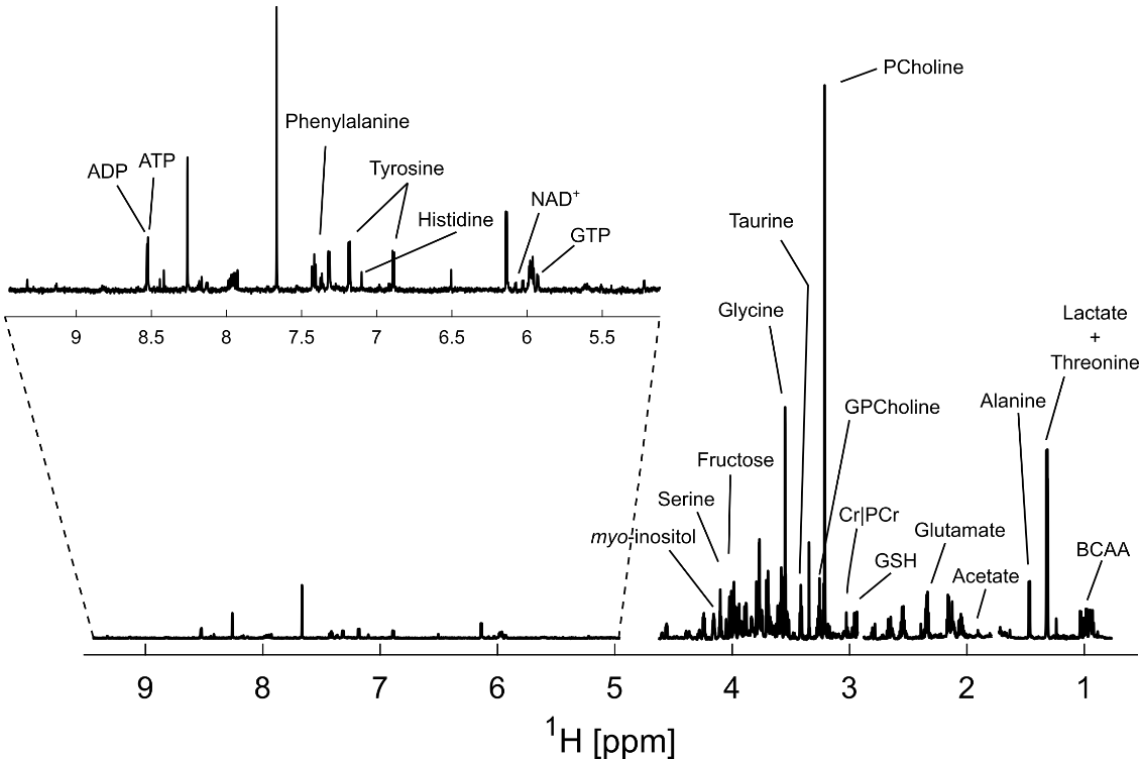

Figure 4. 2 – Representative 1D ^{1}H NMR spectrum of HuH7 cells cultured with glucose-free DMEM supplemented with fructose acquired in an 800 MHz spectrometer, 5mm cryoprobe (in Denmark Technical University). Metabolites used for integration and metabolic analysis are represented in the spectrum.

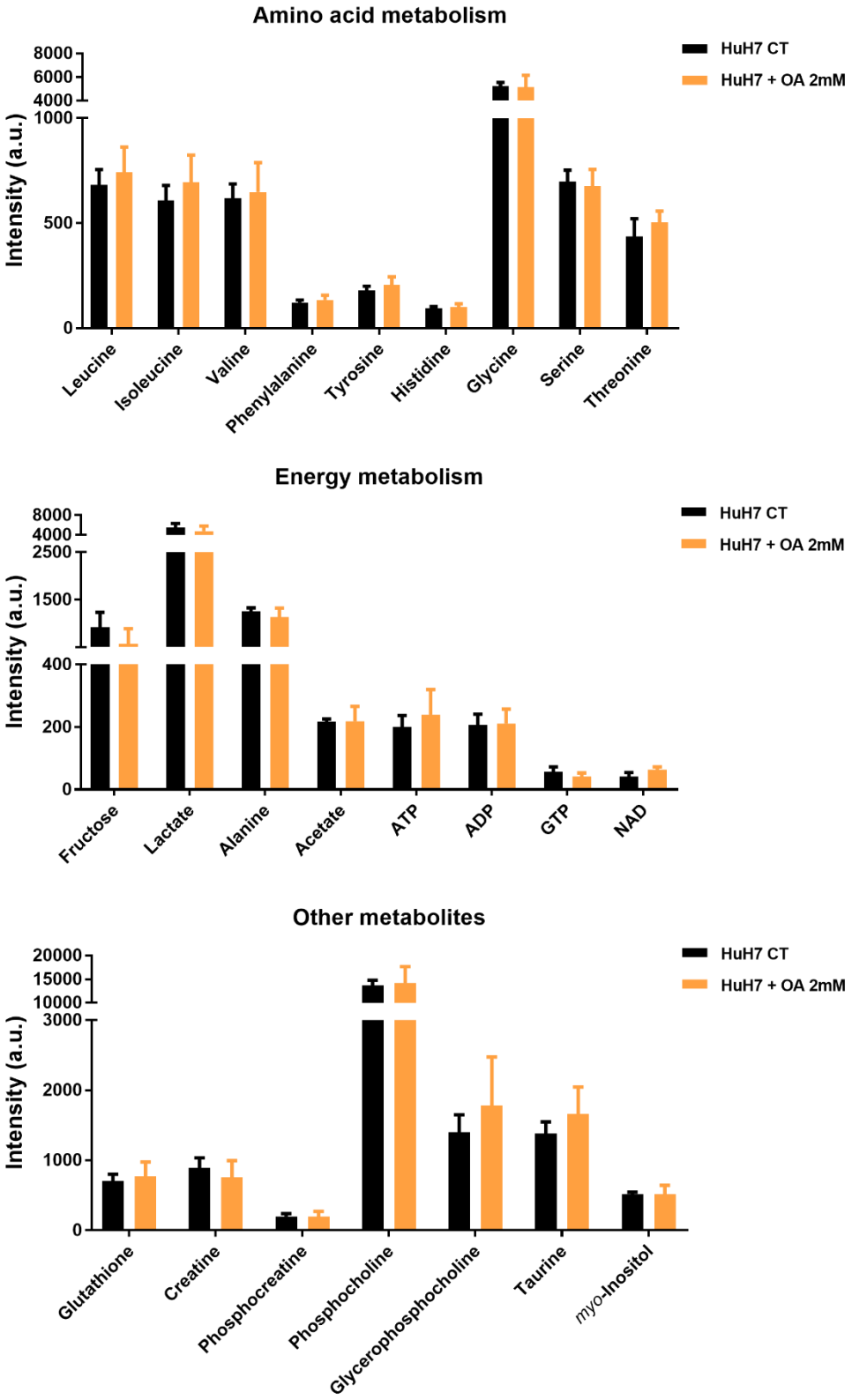

Figure 4. 3 – Induced *in vitro* steatosis in HuH7 cells did not significantly change the overall cellular metabolism. Bar graphs were obtained from the integration of metabolites from n=6 independent experiments. Error bars represent standard deviation.

4.3. Progression from steatosis to NASH

To investigate the changes that occur during the human progression of liver disease, metabolic characterization of explanted human liver tissue was performed. Human liver tissue is superior to use of single cells lines in culture as it retains appropriate liver structure, it contains all the cell types found *in vivo* and accounts for human variability [147,211].

4.3.1. Histological analysis of human liver disease

Histological staining of cells and tissues is an important technique that allows to study structures of cells and tissue characteristics under a microscope. One of the most used combinations of stain dyes for medical diagnosis are haematoxylin and eosin [212].

Haematoxylin and Eosin (H&E) stain contains two dyes which will act upon the pH of the tissue structures, giving important structural information about the condition of the tissue. Haematoxylin which is a basic dye, stains acidic or basophilic structures violet and dark blue such as nuclei of cells. On the other hand, eosin is an acidic dye and stains basic or eosinophilic structures in several shades of red and pink, such as cytoplasm and collagen [213,214].

Using H&E staining, I started by categorising the morphological appearance of normal and diseased tissue (normal, steatotic and NASH). As shown in Figure 4. 4, normal donor samples exhibited normal liver architecture with distinguishable lobes, liver cells arranged around the hepatic venules and small portal tracts (black arrows). At higher magnification, hepatic artery branches and bile ducts were visible as were branches of the portal vein, forming the portal triad (asterisk). This was surrounded by strands/sheets of hepatocytes. In contrast, fatty donor livers (steatotic) were structurally similar but showed the presence of macro- (red arrow) and micro-vesicular steatosis (blue

arrow). In NASH livers, significant structural change was evident. Some steatosis was visible (red arrow) alongside lobular inflammation (green arrow). Bridging and extensive fibrosis was also visible (yellow arrow).

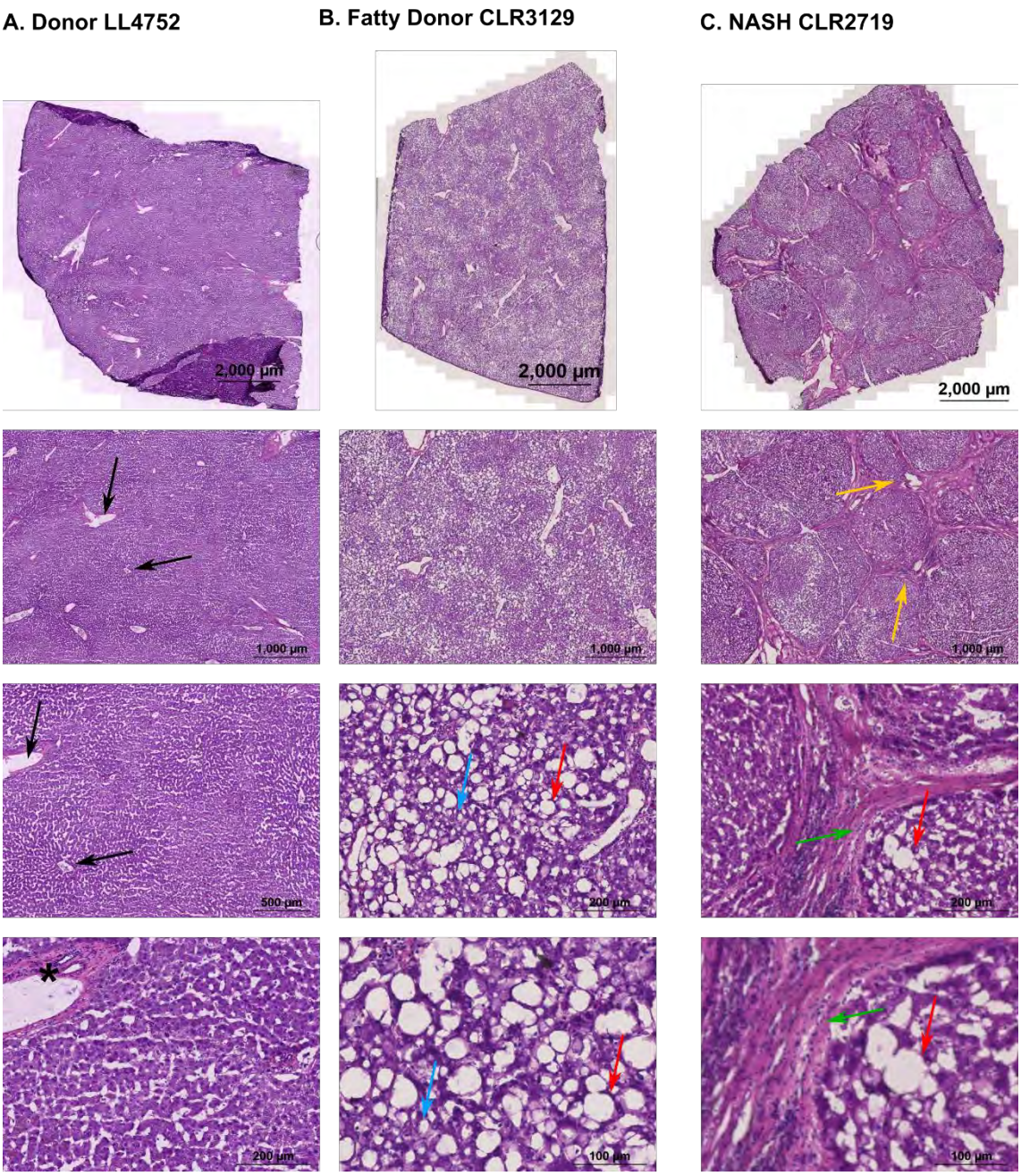

Figure 4. 4 – H&E staining of human livers over the progression of NAFLD. A) HE stained donor, B) fatty donor and C) NASH liver. Explanted livers were fixed and cryo-sectioned for H&E staining. Representative images are shown from n= 3-5 resected/donor and NASH livers at increasing magnifications. Arrows in black represent hepatic venules and central veins, black asterisk represents the portal triad, arrows in red macro-steatosis, arrows in blue micro-steatosis, arrows in yellow fibrosis and arrows in green inflammatory cells. Digital images of whole tissue were captured with the AxioScanZ.1 slide scanner.

4.3.2. NMR metabolomics of liver disease

Analysis of metabolomic data from different human liver specimens allows us to obtain information about the organ state and to measure its variations under different pathological processes. The ability to measure and quantify relative intensities of metabolites by NMR spectroscopy is important to obtain a comprehensive overview of the metabolome. Since I have shown the profound changes in pathological appearance of the liver as NAFLD progresses, metabolite extractions were performed as described in the previous chapter, in order to measure metabolite changes that accompany these processes. By obtaining two distinct fractions from each liver sample, one polar and one organic phase, it was possible to investigate the main metabolic pathways which can be disturbed following hepatocyte damage.

4.3.2.1. Polar extracts

Figure 4. 5 shows an example of average ^{1}H NMR spectra of polar extracts from donor (black), fatty donor (blue) and NASH (red) livers. A comparison between the three stages was performed using the integration of key metabolites from glycolysis, TCA cycle, amino acid metabolism and others, as represented in Figure 4. 6. This showed that while there were no single specific notorious difference between the samples, there were metabolic variations that reflect adaptation during NAFLD progression. For example, there was a trend for increase in amino acid metabolism and glycolytic ratio, as well as increased TCA cycle activity towards the more severe form of NAFLD.

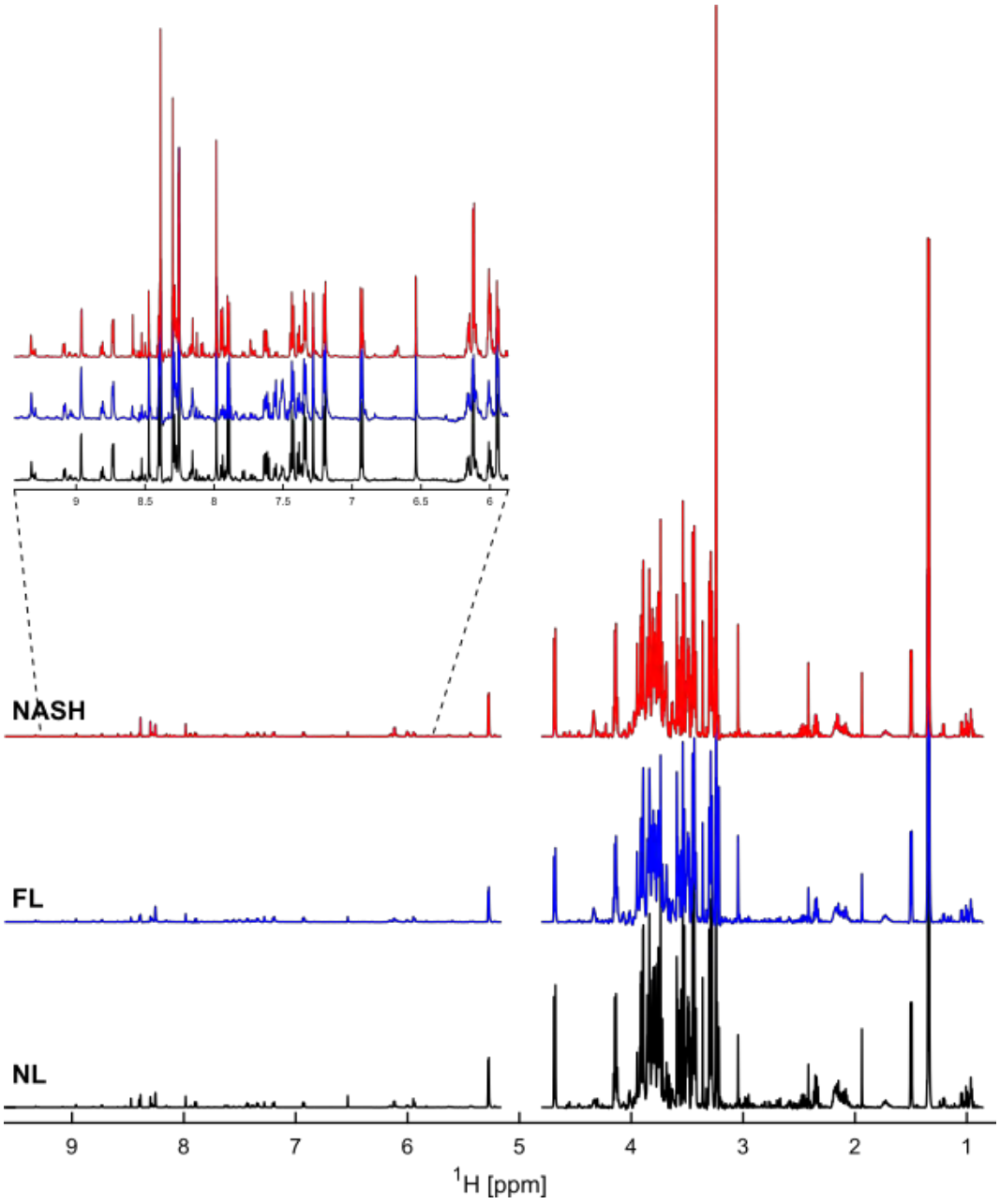

Figure 4. 5 – Representative 1D ^{1}H NMR spectra of intracellular polar extracts from donor livers (NL in black), fatty livers (FL in blue) and non-alcoholic steatohepatitis livers (NASH in red).

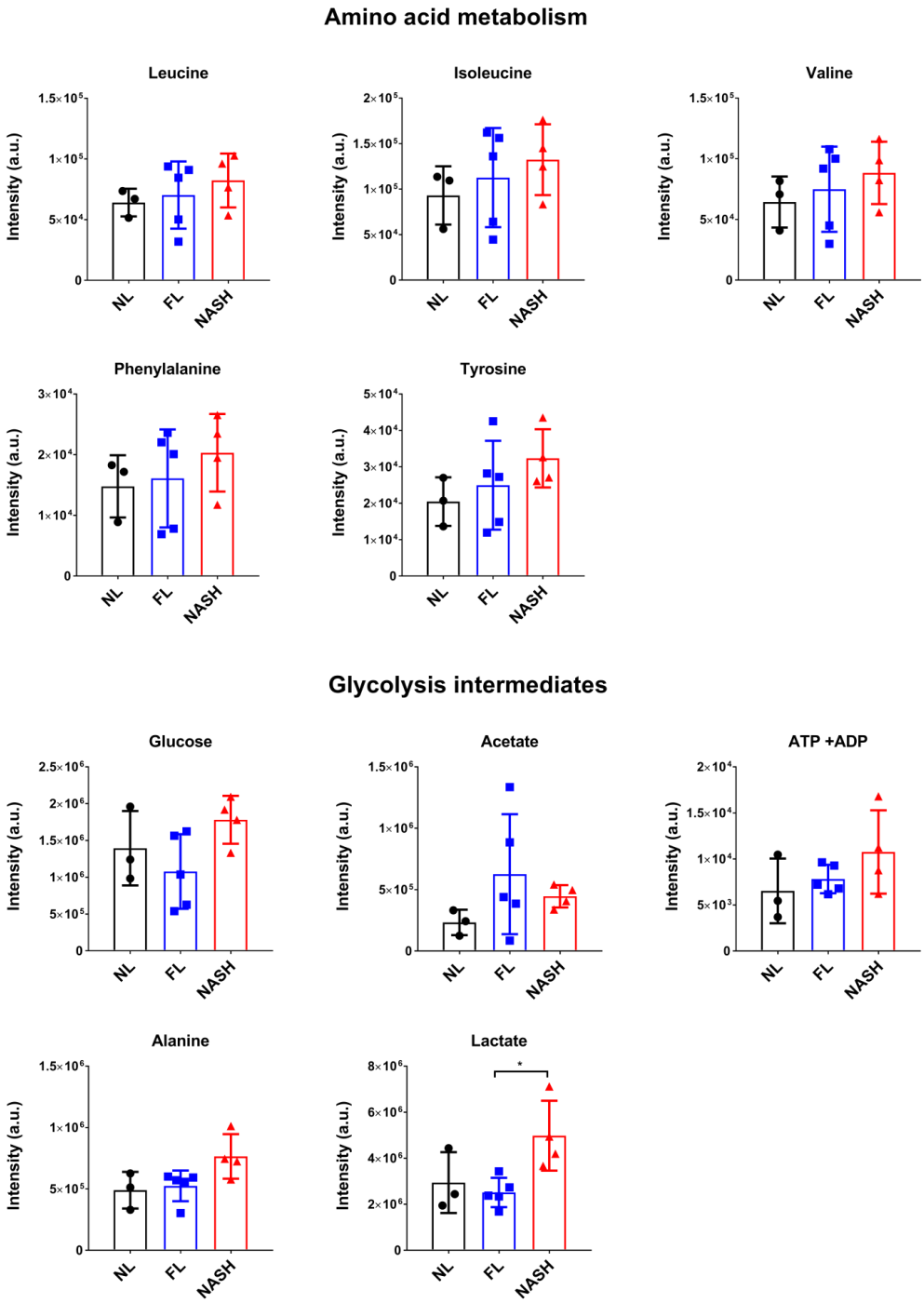

(continued in next page)

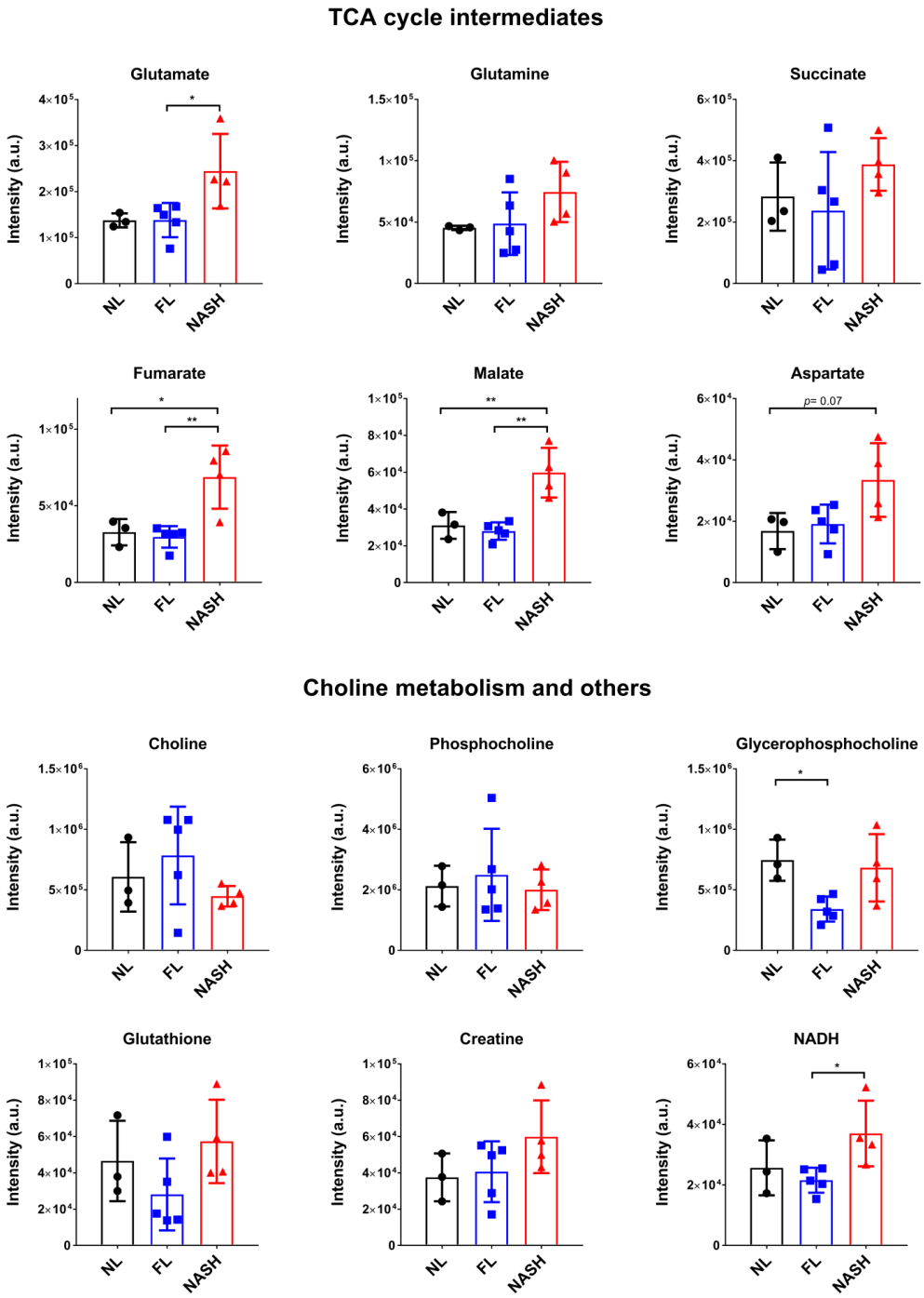

Figure 4. 6 – Comparison of individual intracellular polar metabolites from donor livers (NL in black), fatty livers (FL in blue) and non-alcoholic steatohepatitis livers (NASH in red) that participate in glycolysis, TCA cycle metabolism, amino acid metabolism, choline metabolism and other pathways. (n=3-5 independent samples. Error bars represent standard deviation and *p*-values as follows: *p<0.05, **p<0.01, ***p<0.001).

4.3.2.2. Lipid extracts

Next the lipid fraction of the metabolome of the donor, fatty and NASH livers was analysed by ^{1}H NMR spectroscopy. A representative spectrum from a donor liver is shown in Figure 4. 7, with typical peak assignments of lipid components in Table VIII based on [215]. Although the overall spectrum displays broad signals from various fatty acyl chain resonances with similar chemical shifts, the main lipid constituents in a cell were observed and quantifiable. These included the lipid components of the phospholipidic membrane, cholesterol and cholesterol esters, phosphatidylcholine (PTC) and phosphatidylethanolamine (PTE), as well as sphingomyelin (SM) and smaller amounts of neutral lipids.

A quantification of the main components of the lipid extract was carried out from the 1D ^{1}H spectra of all the human liver explants and it is represented in Figure 4. 8. No significant difference (* $p < 0.05$) was observed in the NMR-based analysis of the lipid profile except for the glycerophospholipid backbone between normal and cirrhotic livers (NASH). Nevertheless, the quantities of triglycerides, cholesterol, PTC, and fatty acyl chains show a small trend for the reduction of lipid content as disease progresses.

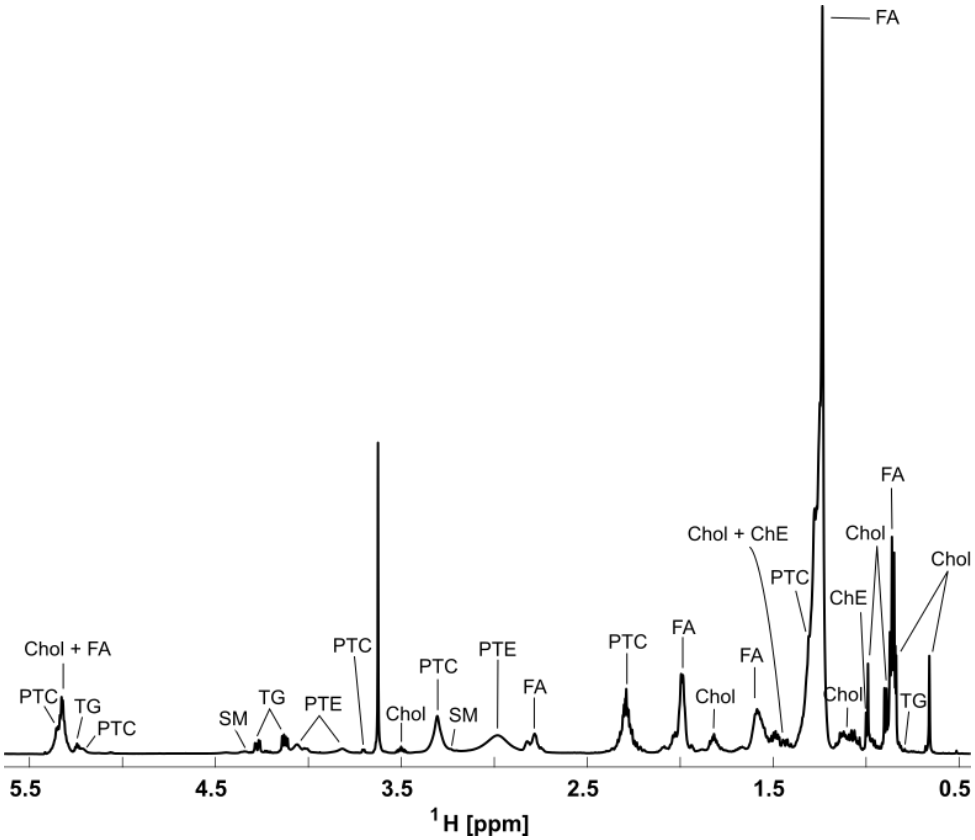

Figure 4. 7 – Representative 1D ^{1}H spectrum of the liver lipid extracts. Assignments are labelled as following: Chol – Cholesterol; ChE – Cholesterol ester; FA – Fatty acids/Fatty acyl chains; PTC – phosphatidylcholine; PTE – phosphatidylethanolamine; SM – Sphingomyelin; TG – Triglyceride.

Table VIII – Typical ^{1}H NMR spectroscopy based assignment of lipid components in the organic extract of cells.

Lipid components	Assigned Resonance protons	Chemical shift (ppm) in $CDCl_3$
Cholesterol (Chol)	- CH_3 (C18 methyl group)	0.66
Fatty acyl chain	- CH_3 $(CH_2)_n$	0.85
Free Cholesterol (FChol)	- CH_3 (C19 methyl group)	0.98
Fatty acyl chain (FA)	- $(CH_2)_n$	1.23
Phospholipid (PTE)	- CH2 – N (phosphatidylethanolamine)	3.10
Sphingomyelin (SM)	- $N(CH_3)_3$	3.32
Phospholipid (PTC)	- CH2 – N (phosphatidylcholine)	3.71
Triglyceride (TG)	- CH_2 (glycerol backbone)	4.13 & 4.26

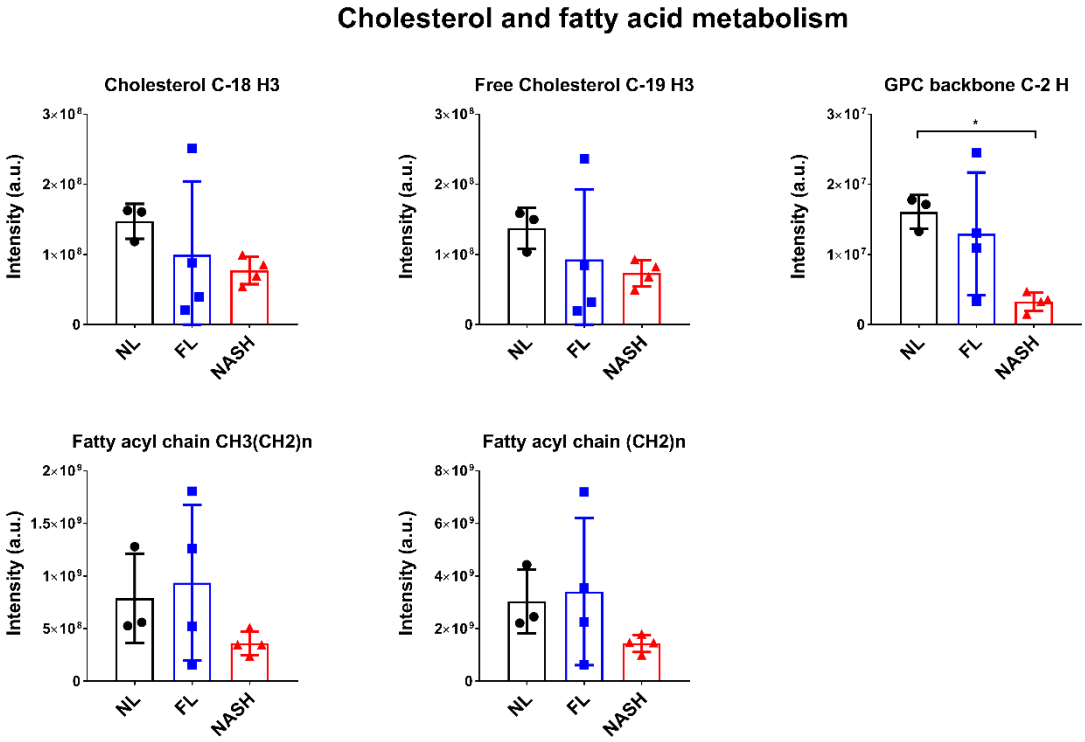

Figure 4. 8 – Comparison of individual intracellular organic metabolites from donor livers (NL in black), fatty livers (FL in blue) and non-alcoholic steatohepatitis livers (NASH in red) that participate in cholesterol and fatty acid metabolism.

4.4. Discussion

4.4.1. *In vitro* model

In vitro models of hepatic steatosis have been developed to investigate the adverse effects of excessive free fatty acids and its relationship with NAFLD pathology [147,210,216]. A fatty liver gets its classification when there is the accumulation of fat in over 5% of hepatocytes. Hence, exposing the hepatocarcinoma cell line (HuH7) to a high dose of oleic acid to induce fat-overloading and accumulation can provide evidence regarding the metabolic and cytotoxic effects of exposure to fat.

In our experiment, the exposure of HuH7 to a high dose of oleic acid has shown that lipid droplets are accumulated intracellularly in the form of macro- and micro-vesicular steatosis. Despite lipotoxicity was observed, cell viability was maintained over 80% for the first 24 hours of exposure to oleic acid. As cells continue to be metabolically active, intracellular polar extracts were obtained to analyse metabolic alterations by ^{1}H NMR spectroscopy. Overall cellular metabolism was not significantly altered; however, some trends were observed in terms of energy metabolism related with increased amino acid levels and glycolysis rate.

A trend for increased glycerophosphocholine (GPC) and adenosine triphosphate (ATP) was observed and both are closely associated with phospholipid metabolism in mammalian cells. GPC is the main component of the cell membrane and it's a catabolic product of the phosphatidylcholine, when fatty acids are removed. Therefore, when in the presence of oleic acid, cells seem to produce more GPC and a reduction of PC is seen. Cells can be incorporating fatty acids in the membrane in order to challenge the amount of oleic acid incorporated by the cells and maintain homeostasis [217,218].

Although some studies suggest that triglycerides accumulation due to the overflow of free fatty acids in hepatocytes can have a protective effect [219–221], cellular metabolism is still dependent on complex dynamic cellular-response networks and toxicity pathways. Additional stimuli, such as inflammation, are usually required to more closely resemble human NAFLD manifestation [64,220]. Therefore, *in vitro* models of NAFLD such as this one still have significant limitations in terms of reproducing metabolic changes that occur in an human steatotic liver [208,210].

4.4.2. *Ex vivo* specimens

To address the limitations of the *in vitro* model to study fatty liver metabolism, *ex vivo* human liver samples were used to investigate the metabolic adaptations that occur during NAFLD progression.

In the first instance, H&E staining was used to assess the morphological appearance of the normal and diseased tissue. Distinguishable characteristics were observed for each liver section of normal, fatty donors and NASH livers. While the normal livers have revealed a normal lobular architecture and lean cells, fatty donors and NASH livers were quite distinct. Fatty donors revealed a similar structure as the normal liver, but with the additional presence of vesicular steatosis. As disease progresses towards a more aggressive form (NASH), steatosis is less evident, and inflammation and fibrosis take place, as described in [222].

Next, samples from the same tissue blocks analysed by H&E were subjected to intracellular extraction of polar and organic metabolites. This allowed to have a better understanding of the characteristic metabolic profiles of the liver tissue during different NAFLD stages. Relative to polar metabolites, the most significant changes were observed when normal tissue was compared with NASH samples, while steatotic livers

had a similar profile to the normal samples. In NASH samples, key metabolites of glycolysis were changed with increases visible for alanine, lactate and ATP + ADP, together with increased levels of TCA cycle intermediates including glutamate, fumarate, malate and aspartate. Elevated hepatic TCA cycle activity has been previously reported for patients with NAFLD and NASH, which is related with impaired mitochondrial metabolism and inflammation [198,199]. Likewise, transition of a steatotic liver towards NASH has been associated with modifications in mitochondrial oxidative metabolism, which include alterations at the ATP synthesis level, reactive oxygen species generation and mediation of inflammatory responses [223,224].

Despite altered hepatic lipid homeostasis being used as an indicator of NAFLD, analysis of the organic fraction has revealed less impressive metabolic changes. Although numerous lipid species were identified by ^{1}H NMR spectroscopy, a high variability across human samples was observed which made it difficult to assess metabolic alterations accurately. Still, as the amount of steatosis reduces and fibrosis increases (NASH samples), the lipid content seems to be lower as well. In a NASH liver, hepatocyte viability is highly influenced by the interactions between fatty acids and pro-inflammatory signalling, which will ultimately affect their function and leads to fibrosis. The presence of less viable hepatocytes might be linked with the decreased overall levels of lipid constituents in the organic extract, however not directly indicating reduced lipid metabolism [225].

Numerous metabolic changes in lipid metabolism were also seen in a lipidomics study by Puri *et al* [226], however only the distribution of lipid species and ratios were related with liver disease progression. A review by Kawano *et al* [227] has focused on identifying the lipid species linked with the progression of NAFLD, but the mechanisms responsible for the lipid metabolic dysregulation in NASH patients is still not fully understood. More

recently, Chiappini *et al* [228] have reported the quantification of lipids in 61 liver biopsies by gas phase or liquid phase chromatography coupled to mass spectrometry (GC/LC-MS) together with machine learning approaches. Again, even though the complete lipidic profile allowed the discrimination between control and NASH patients, no specific lipid could be used as a unique biomarker. Hence, a better approach is necessary to study the metabolic alterations that occur during disease progression.

In order to understand the dysregulations of the main metabolic pathways involved in the appearance and progression of NAFLD, new approaches are necessary. Although our methods have been proven to work with both cellular and tissue samples, similar biochemical features in our models/approaches still require further testing. To do so, a new murine model of NASH was characterised in the next chapter to help reducing the knowledge gap regarding specific metabolic pathways alterations, biomarkers and liver pathology.

CHAPTER 5

IN VIVO MODEL OF NAFLD

5. How can mouse data be valuable to pre-clinical trials?

5.1. Overview

Use of conventional *in vitro* techniques may not be the best approach to understand metabolic alterations in NAFLD. Multiple processes contribute to fatty liver disease development and are related to fat synthesis and accumulation, reduction in fatty acid oxidation, mitochondrial dysfunction, inflammation and ultimately fibrosis [22,229,230]. Furthermore, multiple cell types contribute to disease pathogenesis and there is a clear interplay between other tissues such as the muscle and adipose tissue [231]. This plus the fact that mechanisms associated with the progression of the disease are not yet fully characterised, several animal models of NAFLD have been developed and reviewed [146].

Mouse and rat animal models have been frequently used to understand major pathophysiological mechanisms of NAFLD. Several studies have focused their attention towards the C57BL/6 mouse strain since good hepatic responses are usually obtained in terms of obesity, steatosis, insulin resistance and inflammation in response to dietary regimens [146,232–234]. Therefore, adjusting various factors such as dietary constituents and also external factors (cage environment and temperatures) will allow us to mimic the histopathology and pathogenesis of human NAFLD.

In this chapter, cohorts of C57BL/6J mice were used to study the implications of consumption of a high fat diet in the development of fatty liver disease. Two different cohorts were used to assess whether in a 10 week experiment it would be possible to observe hepatic steatosis and inflammation, or if a longer experimental time frame of over 20 weeks would be needed. The addition of fructose- or glucose-sweetened water on top of a HFD was also investigated in order to characterise the different metabolic profiles and responses in mice. For this, histological assessments of the liver were done, together with a multicolour flow cytometric analysis. Finally, to further understand

mechanistic alterations during liver disease progression, NMR metabolomics was used in combination with a gene profiler PCR array.

5.2. Fatty Liver model – 10 weeks

A cohort of thirty-two, six to eight-week old, C57BL/6J male mice were fed a low fat diet (LFD 4057 kcal) or high fat diet (HFD 4057 kcal) and given ad libitum access to regular water or water supplemented with 20% (w/v) fructose or glucose. At the end of a 10-week period, mice fed a LFD weighed 30.2 ± 2.7 g, whereas mice on HFD with regular water weighed 41.0 ± 4.4 g. When HFD was accompanied by water supplemented with sugars, mice showed significantly increased body weight. When glucose (HFD + 20% Glc) was used, mice weighed 43.2 ± 3.8 g on average, which was similar to when fructose (HFD + 20% Fru) was used (43.4 ± 3.6g, Figure 5. 1 and Table IX). The additional weight gain in these animals was associated increased liver weight, as the HFD + sugar mouse livers were larger than the control LFD and HFD alone. We also observed accumulation of body fat as the waist circumference of sugar exposed mice was much larger (Figure 5. 2).

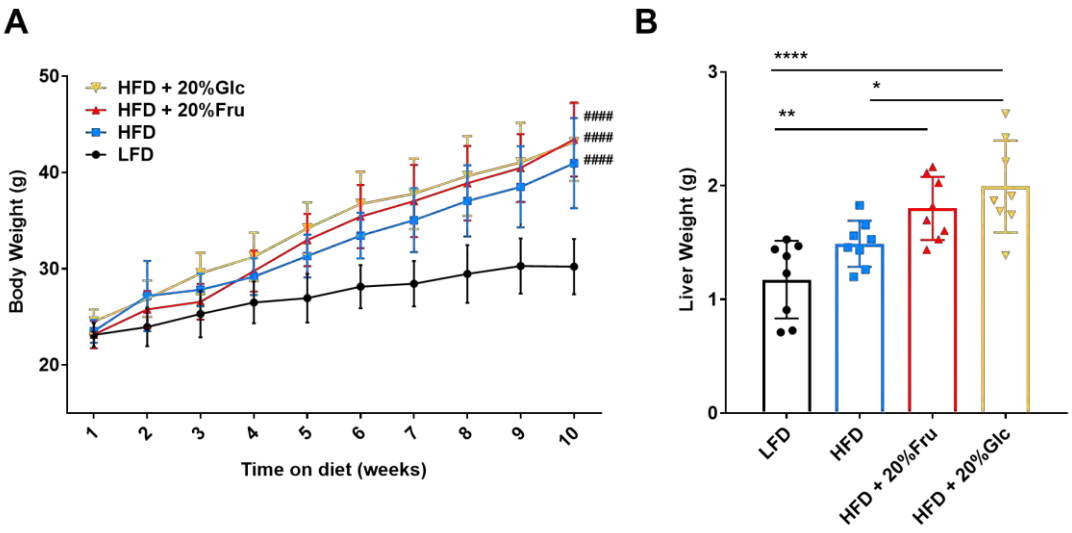

Figure 5. 1 – Body weight gain of mice on LFD or HFD, with either regular, 20% fructose, or glucose-sweetened water for 10 weeks. (B) Liver weights of the same mice at sacrifice. (n=8 mice per group, and bars represent mean ± standard deviation and *p*-values as follows: *$p<0.05$, **$p<0.01$, ***$p<0.001$). ####p<0.0001 when comparing with LFD in graph A.

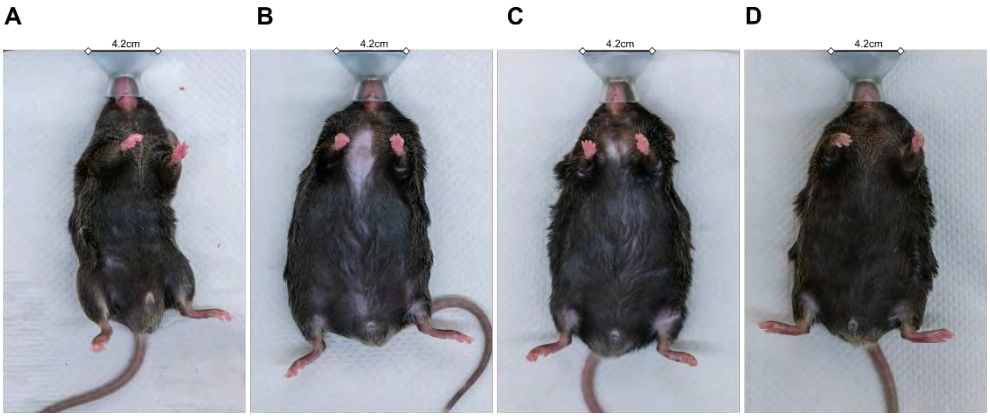

Figure 5. 2 – Visual representation of mice after feeding of low fat diet (A) or high fat diet, supplemented with either regular (B), 20% fructose (C), or 20% glucose(D)-sweetened water for 10 weeks. The panel shows a frontal view of representative animals under anaesthesia to highlight body proportions.

Table IX – Body and liver weight of mice on LFD or HFD, supplemented with either regular, 20% fructose, or glucose-sweetened water for 10 weeks.

	BODY WEIGHT (g)	LIVER WEIGHT (g)
LFD	30.2 ± 2.7	1.2 ± 0.3
HFD	41.0 ± 4.4	1.5 ± 0.2
HFD + 20% Fru	43.4 ± 3.6	1.8 ± 0.3
HFD + 20% Glc	43.2 ± 3.8	2.0 ± 0.4

Note 4 - n=8 mice per group and values represent mean ± standard deviation.

Liver morphology from mice after the 10-week feeding was assessed with haematoxylin and eosin (H&E) staining (Figure 5. 3). In LFD fed mice, the tissue has a normal liver morphology only displaying minimal fat deposition in some areas. This was variable between animals, as 4 of them revealed a normal healthy liver and the other 4 exhibited small areas of fatty hepatocytes. Normal hepatocytes are marked with black arrows denoting normal cellular organization in the tissue (Figure 5. 3).

In contrast, mice on a HFD showed severe morphological changes in the tissue. All HFD-fed animals had a significant amount of fat deposition in hepatocytes across the lobule, with areas of marked macro- (red arrows) and micro-steatosis (blue arrows). At this stage, no inflammatory cells were found in the tissue which suggest that the liver is still in the initial stages of NAFLD. Also, there was no evident difference between animals on HFD alone and animals on a HFD supplemented with sweetened water at this point. Similar to LFD animals, interindividual variability was observed in mice on a HFD alone and mice on a HFD + 20% fructose. Here, half of these cohorts had a quite normal liver and the other half were highly steatotic. An example of this variability across groups is shown in Figure 5. 4.

This analysis allowed me to confirm the accumulation of fat in the liver following 10 weeks of high fat diet, and also that the calorically matched low fat diet replicates the effects of chow diet which is normally used as a control diet.

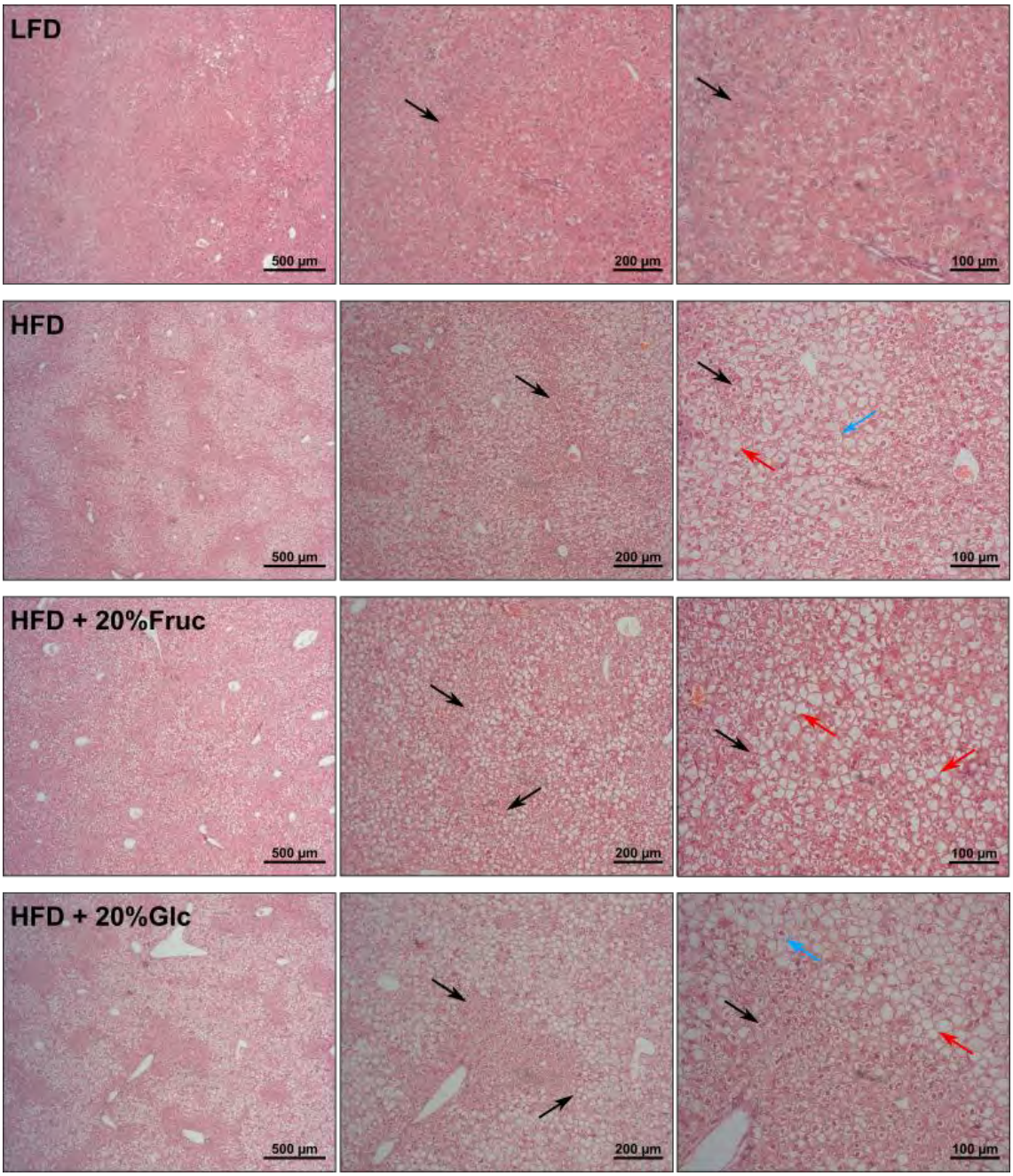

Figure 5. 3 – H&E staining of mouse livers on a low fat diet (LFD) and high fat diet (HFD), with either regular, 20% fructose, or 20% glucose-sweetened water for 10 weeks. At the time of collection, livers were fixed in paraffin and sectioned for H&E staining. Representative images are shown from n= 8 livers per group at increasing magnifications (5x, 10x and 20x). Arrows in black represent hepatocytes, arrows in red macro-steatosis, arrows in blue micro-steatosis.

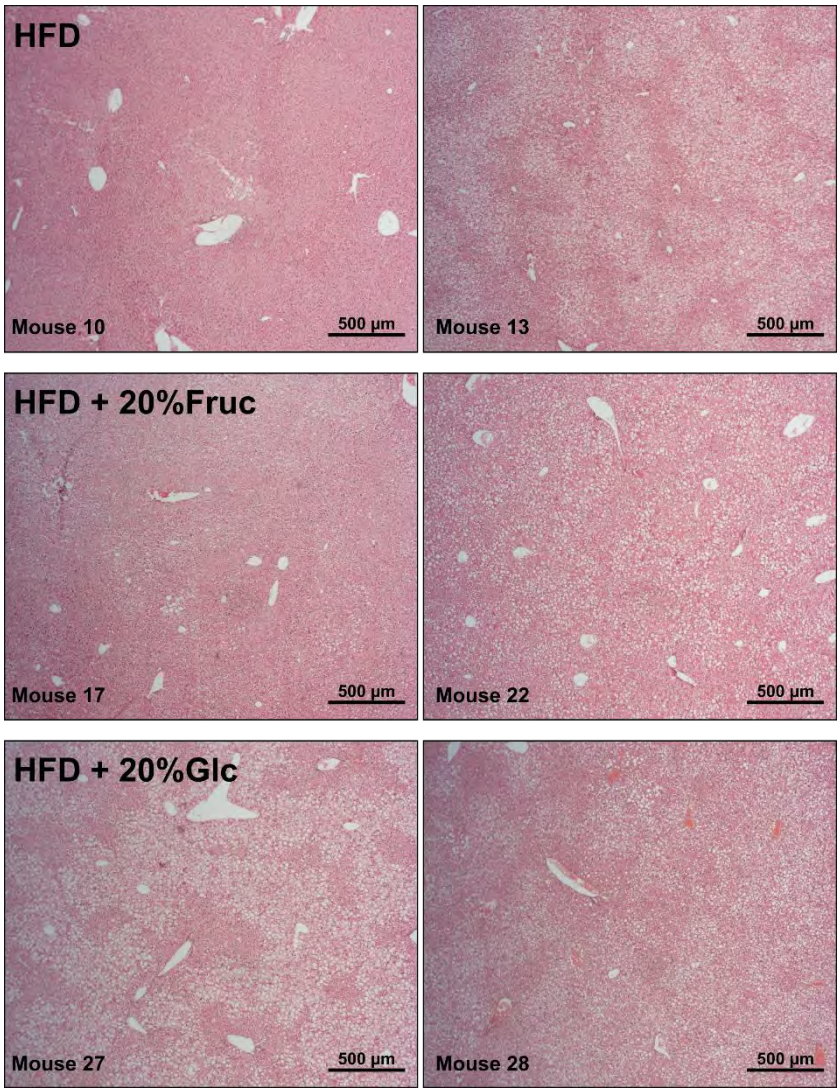

Figure 5. 4 – Variability in fat deposition in mice on a HFD and HFD+ 20% fructose, but not in HFD + 20% glucose. At the time of collection, livers were fixed in paraffin and sectioned for H&E staining. Representative images are shown at 5x original magnification.

5.2.1. Clinical biochemistry analysis of serum

Liver function tests and urea concentration were measured in serum samples from all mice at the end of the study (Table X). Even though the liver appearance and body weight composition in HFD animals was notoriously different from LFD mice, the liver function tests did not reveal any significant alteration. An exception was seen for alkaline phosphatase (ALP), which was increased in the LFD group. Enzyme activities of alanine transaminase (ALT) and aspartate transaminase (AST), were found to not significantly change between diets. One important detail is that, in agreement with our histological findings (Figure 5. 4), the biochemical data showed a big variability between samples within the same diet group. On the other hand, urea levels were quite different between dietary groups, being specially decreased in mice on a HFD + 20% glucose when compared with the others. LFD and HFD fed animals seem to have a similar serum concentration of urea, while HFD supplemented with sweetened-water induces a significant reduction of its levels (Figure 5. 5).

Table X – Serum parameters in liver function tests and urea levels in mice after 10 weeks on a LFD or HFD, supplemented with either regular, 20% fructose, or glucose-sweetened water.

GROUP	ALP U/l	ALT U/l	AST U/l	UREA mmol/l
LFD	133.0 ± 78.5	120.3 ± 100.9	243 ± 192.2	10.3 ± 1.7
HFD	63.3 ± 6.3	81.3 ± 61.5	152.8 ± 131.3	10.9 ± 1.6
HFD + 20% Fru	77.5 ± 19.8	56.0 ± 31.8	112.5 ± 45.9	8.6 ± 1.8
HFD + 20% Glc	72.5 ± 13.6	120.3 ± 62.3	143.5 ± 131.7	6.1 ± 0.8

Note 5 – n=8 mice per group and values represent mean ± standard deviation.

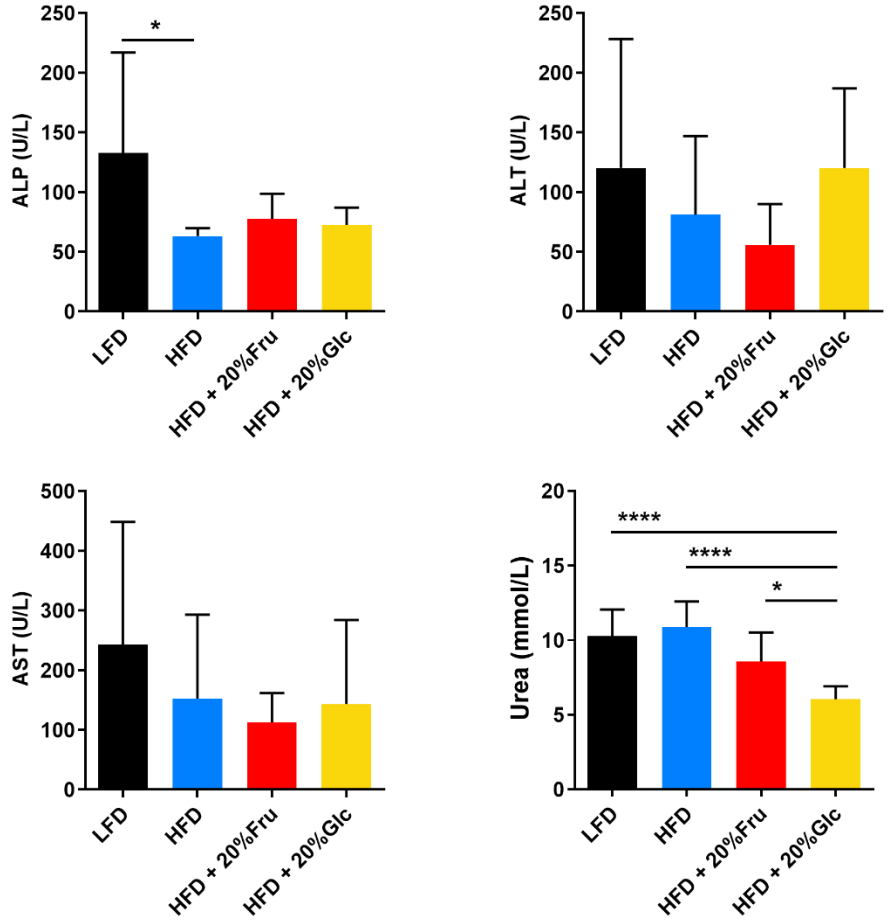

Figure 5. 5 – Serum biochemistry parameters for ALP, ALT and AST enzyme activities and urea levels in mice at week 10. The blood collection was done by cardiac puncture under anaesthesia. (n=8 mice per group, and bars represent mean ± standard deviation and *p*-values as follows: *$p<0.05$, **$p<0.01$, ***$p<0.001$)., ****$p<0.0001$)

5.2.2. Flow cytometry and NMR spectroscopy at 10 weeks

Upon culling, a proportion of the liver was digested in order to perform multicolour flow cytometric analysis of resident immune cells. However, at this timepoint no significant degree of inflammation was observed (not shown). The yield of inflammatory cells observed was low and as soon as we started selecting subpopulations according to lymphoid or myeloid gating strategies, the number of cells in each gate was extremely low or cells in that population were non-existent. This is consistent with observations made in the H&E analysis for these animals, where no inflammatory cells were observed in any of the livers across the different dietary groups.

The 1D ^{1}H NMR analysis did not reveal any significant metabolic differences as the overall metabolic response from all groups was very similar. No significant alterations between groups were observed regarding *ca*. 40 metabolites identified and analysed. Realistic conclusions about metabolic changes could not be drawn since there was a high variability observed between samples and this complicated the normalisation of NMR data.

Consequently, we decided to concentrate all our efforts in a more detailed analysis for the 21-week experimental group which displayed more promising metabolic alterations, higher levels of steatosis and inflammation and more significant injury.

5.3. NASH model – 21 weeks

A cohort of forty, six to eight-week old, C57BL/6J male mice were fed a low fat diet (LFD 4057 kcal) or high fat diet (HFD 4057 kcal) and given ad libitum access to regular water, or water supplemented with 20% (w/v) fructose or glucose. At the end of a 21-week period, there was a significant difference between mice fed a LFD weighing on average 35.9 ± 0.2 g, and mice fed a HFD diet, weighing around 50 g in all groups (Figure 5. 6 and Table XI). Mice on HFD with regular water weighed 50.3 ± 2.4 g, mice that had water supplemented with fructose weighed 51.7 ± 4.0g and mice with glucose 49.2± 2.8 g on average. Overall, HFD induced a greater weight gain than LFD, which was accompanied by increased liver weight. Livers from mice fed LFD weighed 1.7 ± 0.2 g whereas mice fed a HFD had larger and heavier livers. Mice on HFD alone had a liver weight of 2.5 ± 0.6 g, similar to mice on HFD + 20% glucose at 2.8 ± 0.6 g, whereas mice on a HFD + 20% fructose had livers weighing 3.2 ± 1.0 g.

In humans, clinical signs of non-alcoholic fatty liver disease (NAFLD) include overweight, high levels of subcutaneous fat, liver enlargement and discoloration. As shown in Figure 5. 7, body mass and proportions were very different when comparing LFD and HFD fed animals. Mice fed LFD had a standard appearance, a healthy red blushing liver and no visible subcutaneous fat in the abdominal area. Mice on a HFD however displayed a high body mass index and waist circumference, which is a known risk factor for NAFLD [61,95]. Also, livers look discoloured and contained fat deposits which were visible to the naked eye. Although all groups of animals on HFD demonstrated steatosis and high body weight, HFD animals which had water supplemented with fructose had a greater accumulation of subcutaneous fat in the abdominal area and an even paler liver. In order to confirm the degree of steatosis and liver injury, histology studies were performed.

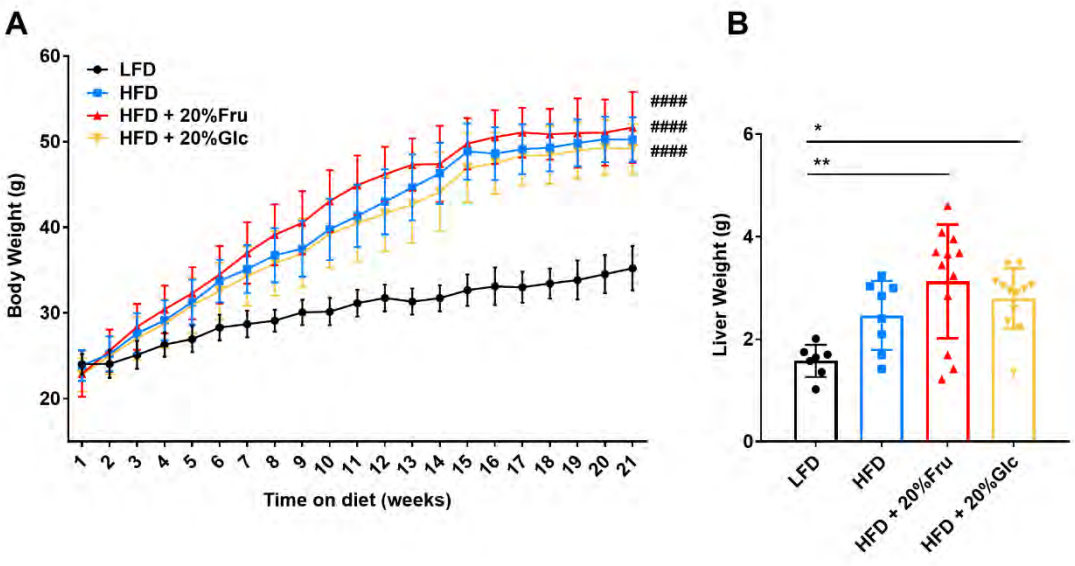

Figure 5. 6 – Fructose supplementation on HFD leads to higher weight gain and enlarged liver. On the left, weight gain of mice on low fat diet (LFD) and high fat diet (HFD) with either regular, 20% fructose, or 20% glucose-sweetened water for 21 weeks. On the right panel, liver weights of the same mice at sacrifice. (n= 7-12 mice per group, and bars represent mean ± standard deviation and *p*-values as follows: **p*<0.05, ***p*<0.01, ****p*<0.001,*****p*<0.0001, and ####p<0.0001 when comparing with LFD in graph A.

Table XI - Body and liver weight of mice on LFD or HFD, supplemented with either regular, 20% fructose, or glucose-sweetened water for 21 weeks.

GROUP	BODY WEIGHT (g)	LIVER WEIGHT (g)
LFD	35.9 ± 0.2	1.7 ± 0.2
HFD	50.3 ± 2.4	2.5 ± 0.6
HFD + 20% Fru	51.7 ± 4.0	3.2 ± 1.0
HFD + 20% Glc	49.2 ± 2.8	2.8 ± 0.6

Note 6 – n = 7-12 mice per group and values represent mean ± standard deviation.

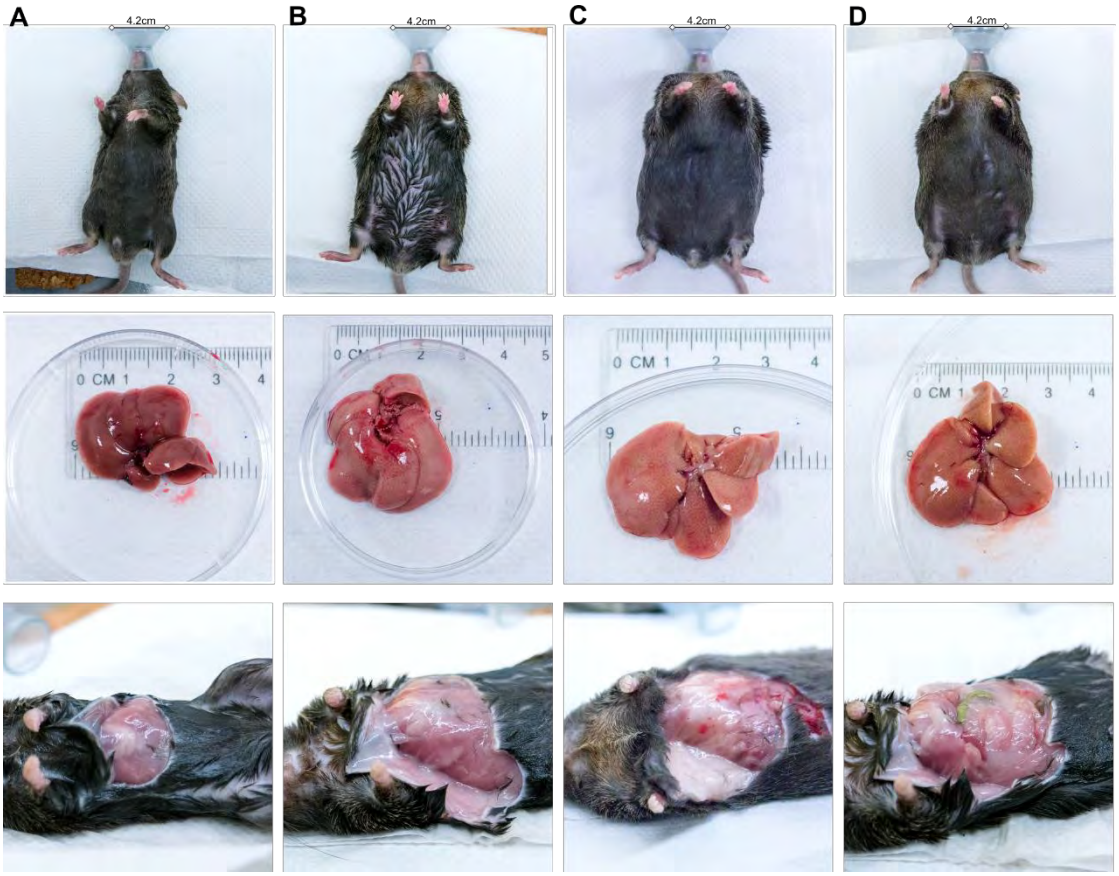

Figure 5. 7 – Visual representation of mice after feeding of low fat diet (A) or high fat diet with either regular (B), 20% fructose (C), or 20% glucose(D)-sweetened water for 21 weeks. The upper panel is a frontal view of animals under anaesthesia at the culling time showing body proportions. Middle panel is the macroscopic view of their livers after collection. Bottom panel is a close-up view of abdominal area and subcutaneous fat.

Sections of liver were stained with haematoxylin and eosin (H&E) to assess the general histological appearance of the liver (Figure 5. 8). In LFD fed mice, the tissue had a normal liver architecture displaying hepatic cells distributed around portal areas and central venules. At higher magnification, hepatocytes were arranged into cords and separated by sinusoids (black arrows) as expected. On the other hand, mice on a HFD showed very distinct characteristics. Both HFD alone and HFD with 20% fructose samples showed immense fat accumulation in the hepatocytes, presenting macro- (in red arrow) and micro-vesicular steatosis (in blue arrow). Importantly, in the samples from mice fed HFD with glucose-sweetened water, liver tissue revealed elevated levels of macro-steatosis but also a high degree of inflammatory cells around the portal areas (in green arrows). This analysis confirmed the accumulation of fat and inflammation in the liver following 21 weeks of high fat diet, whilst the low fat diet samples were histologically normal in appearance.

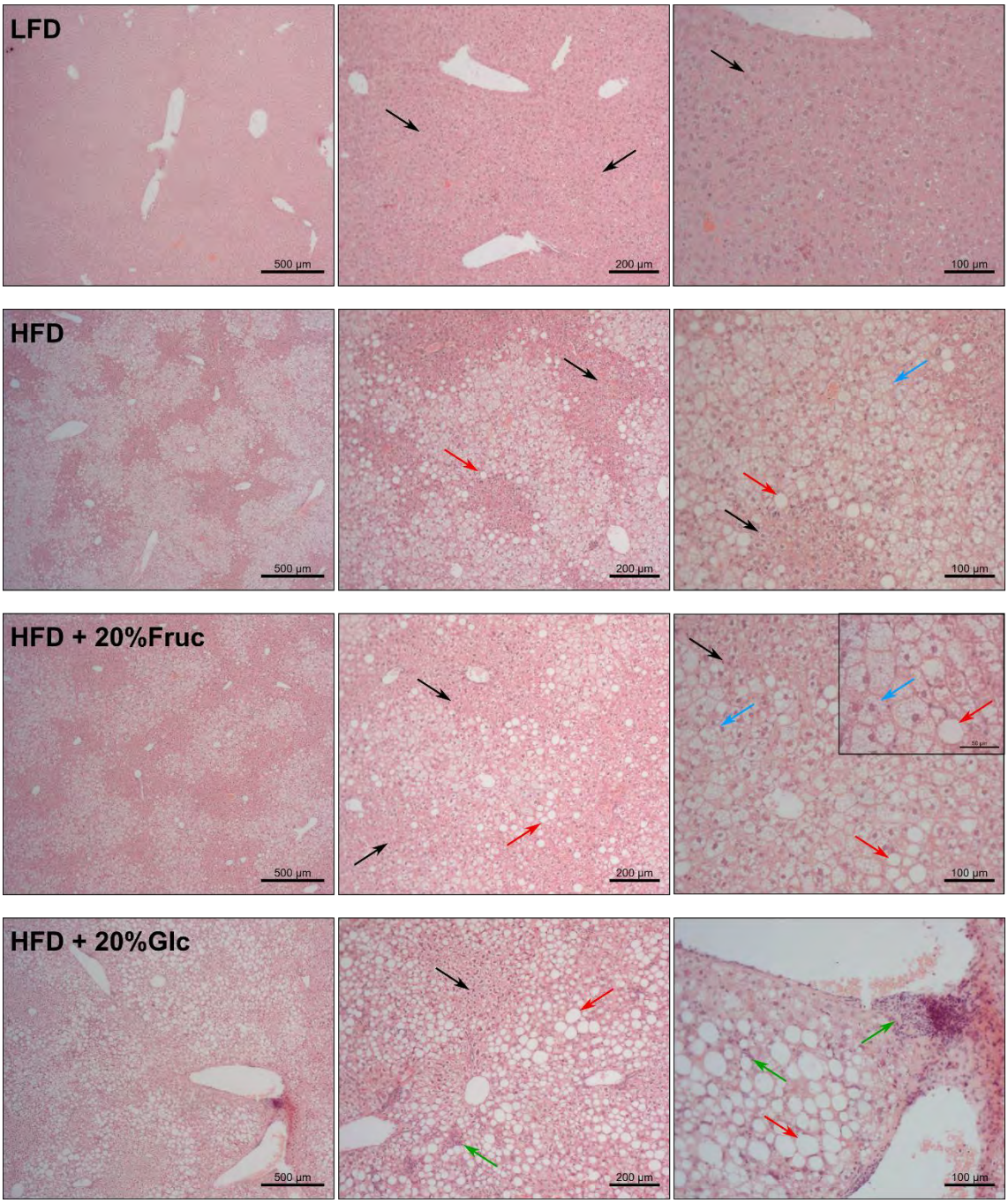

Figure 5. 8 – H&E staining of mouse livers on a low fat diet (LFD) and high fat diet (HFD), supplemented with either regular, 20% fructose, or 20% glucose-sweetened water for 21 weeks. At the time of collection, livers were fixed in paraffin and sectioned for H&E staining. Representative images are shown from n=7-8 livers per group at increasing magnifications (5x, 10x and 20x). Arrows in black represent hepatocytes, arrows in red macro-steatosis, arrows in blue micro-steatosis, and arrows in green inflammatory cells.

5.3.1. Clinical biochemistry analysis of serum

In order to obtain information about the state of the mouse liver, several liver function tests were performed during the progression of the study. Blood was collected at three different time points from the same animals, at weeks 4 and 13 via tail vein bleeding and at the end of the experiment via cardiac puncture under anaesthesia, at week 21 (Figure 5. 9, Figure 5. 10 and Table XII).

As alkaline phosphatase (ALP) is predominantly produced by the biliary cells, its elevation suggests biliary obstruction or epithelial damage. Although there were no significant intra- and inter- dietary group changes in ALP during the progression of the study, there was a trend for higher ALP in HFD fed animals with access to sweetened water (Table XII). Nevertheless, according to Triverdi *et al* [235], the predominant source of ALP in C57BL/6 strains is the skeletal tissue, being absent in liver and gut. Therefore, any ALP present in the circulation will not reflect liver-derived changes in this enzyme.

Regarding hepatocellular injury, both alanine transaminase (ALT) and aspartate transaminase (AST) are good markers, as they are released into the blood in greater amounts when hepatocytes are damaged. Dissimilarly to ALP, variations in ALT and AST between dietary groups were quite striking. ALT levels for LFD animals are maintained at a reasonably low level during the 21 weeks, whereas for mice on HFD ALT levels were abnormally high from 13 weeks onwards. This is especially the case for animals fed HFD + 20% fructose, where ALT values were found to be twice as high as any other group by week 21. A similar trend was observed for AST values, where again LFD animals showed lower enzymatic activity than HFD groups. Similarly, HFD + 20% glucose animals had extremely elevated serum enzymes which reflects the pronounced liver damage and inflammation observed in the H&E analysis.

Urea levels were also measured and were higher for the LFD group at 10.3 ± 1.2 mmol/l at the end of the experiment, but still within reference values [236]. HFD alone and HFD with 20% fructose samples revealed similar levels with 7.8 ± 0.6 mmol/l and 8.9 ± 1.0 mmol/l, respectively, being within the normal range as well. On the other hand, urea values for HFD fed animals with 20% glucose are quite low with a concentration of 5.0 ± 0.8 mmol/l, suggesting the presence of liver injury.

To further investigate the degree of the liver injury and the inflammatory state of the liver, flow cytometry analysis was then performed using cells extracted from the liver.

Table XII - Serum parameters in liver function tests and urea levels in mice after 21 weeks on a LFD or HFD, supplemented with either regular, 20% fructose, or glucose-sweetened water.

GROUP	ALP U/l	ALT U/l	AST U/l	UREA mmol/l
LFD	60.5 ± 3.2	38.5 ± 10.2	128.0 ± 70.6	10.3 ± 1.2
HFD	79.5 ± 15.7	141.8 ± 95.4	195.4 ± 117.3	7.8 ± 0.6
HFD + 20% Fru	117.0 ± 20.5	547.1 ± 352.0	458.6 ±179.3	8.9 ± 1.0
HFD + 20% Glc	135.0 ± 46.4	274.9 ± 96.9	215.1 ± 97.3	5.0 ± 0.8

Note 7 – n = 6-8 mice per group and values represent mean ± standard deviation (at week 21).

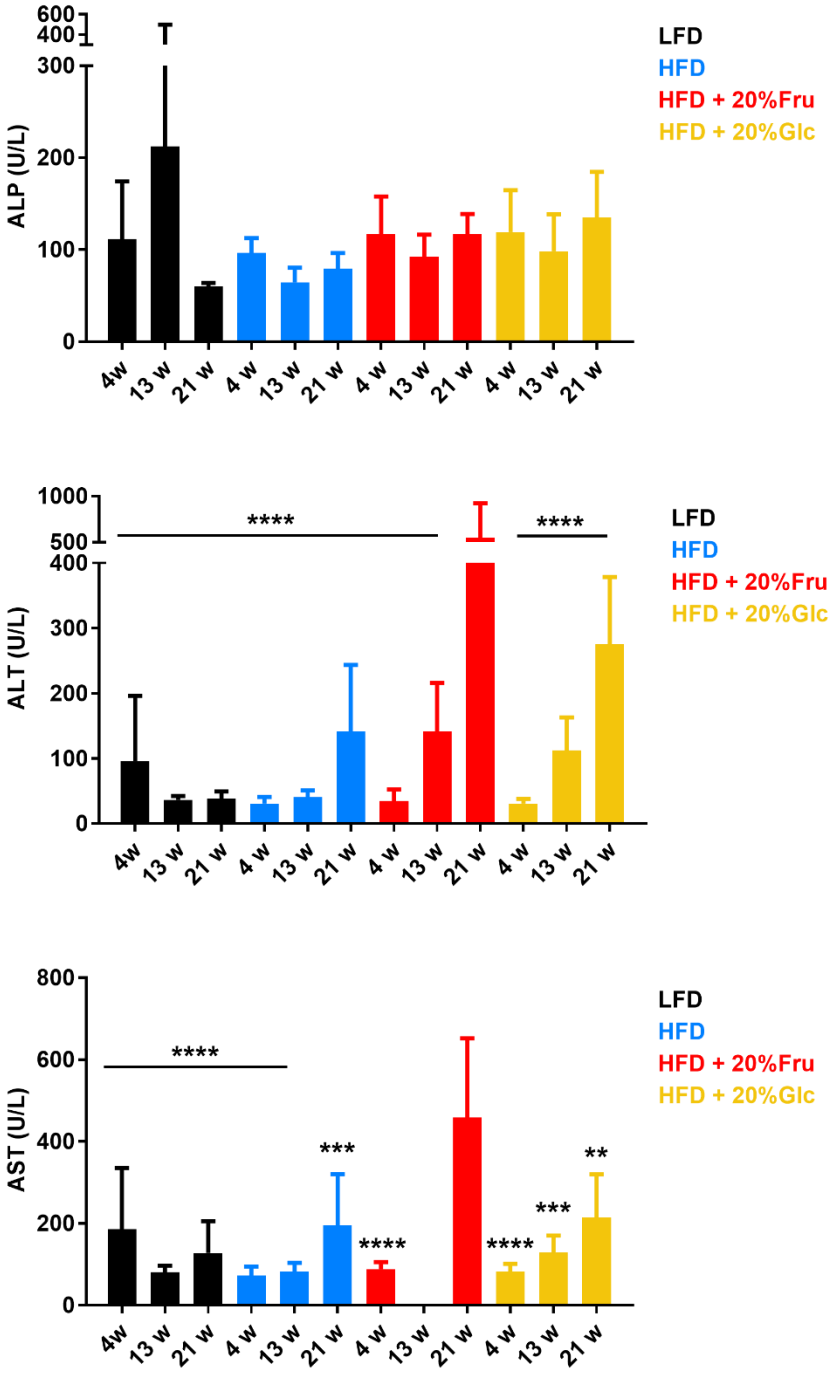

Figure 5. 9 – Serum biochemistry parameters for ALP, ALT and AST enzyme levels in mice at week 4, 13 and 21. The first two collections (week 4 and 13) were obtained by tail vein blood sampling and the last collection was done by cardiac puncture under anaesthesia. (n= 6-8 mice per group, and bars represent mean ± standard deviation and *p*-values as follows: **p*<0.05, ***p*<0.01, ****p*<0.001, *****p*<0.0001 in regard to HFD +20% fructose 21 weeks). Note: 13 weeks AST levels for HFD + 20% fructose group could not be measured due to haemolysis and serum contamination.

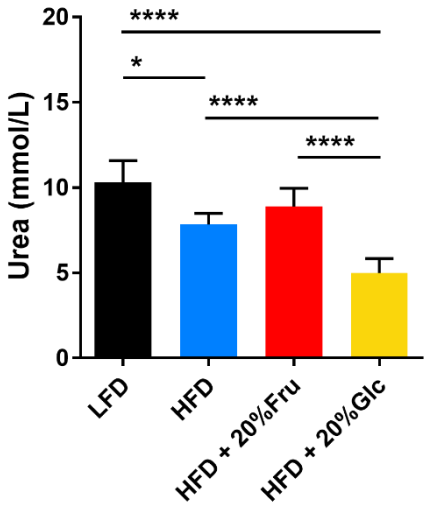

Figure 5. 10 – Serum biochemistry parameters for urea levels in mice at week 21. The blood collection was carried out by cardiac puncture under anaesthesia. (n=7-8 mice per group, and bars represent mean ± standard deviation and *p*-values as follows: *$p<0.05$, **$p<0.01$, ***$p<0.001$, ****$p<0.0001$).

5.3.2. Multicolour flow cytometry analysis of mouse livers at 21 weeks

To investigate immunological responses to liver injury, multicolour flow cytometric analysis was used. The simultaneous detection of multiple parameters was used to detect the phenotype of the immune cells in the liver either at baseline or during an inflammatory response, retrieving information about the immune status of the tissue [237–239].

Intrahepatic immune cells were freshly isolated from the liver through mechanical disruption into a single cell suspension. Then, the immune cells were isolated with an Optiprep™ Density Gradient Medium, eliminating cellular debris. Lastly, lymphoid and a myeloid lineage panels were used to identify the major populations of both innate and adaptive immune cells including B, T and natural killer (NK) T cells, as well as macrophages and granulocytes.

In order to identify the different subsets of the cellular populations, the lymphoid panel was analysed as demonstrated in Figure 5. 11. An initial gating strategy was used to firstly identify lymphoid cells and to exclude dead cells and doublets. To identify specific lymphocytes, live cells were then gated with NK1.1 to investigate NK T cell subsets or gated using the expression of $CD45^+$ cells to identify T-cells. T-cells were then further sub-grouped into $CD4^+$ and $CD8^+$ T-cells.

Analysis of intrahepatic lymphocytes has revealed a difference in most cell populations between the LFD and the HFD, especially when sweetened water was used (Figure 5. 12). Starting by gating on live cells, CD45 was used to identify immune cells as it is expressed on all leucocytes. When comparing with LFD, HFD diet alone did not show any significant differences in $CD45^+$ cell frequency. However, $CD45^+$ cell population was significantly increased in the HFD + 20% fructose and glucose groups. To further phenotype T cells, antibodies for $CD4^+$ and $CD8^+$, were used as markers for

helper and cytotoxic T cells, respectively. $CD4^+$ population was lower than $CD8^+$ for LFD animals. Regarding HFD fed animals, they had a higher frequency of $CD8^+$ cells than $CD4^+$, in agreement with the $CD45^+$ expression. This suggests the presence of more pro-inflammatory cells in the HFD tissue.

NK T cells are able to modulate immune response through cytokine signalling when danger signals are released. Detection of NK T cells in LFD mice is quite low, confirming the low level of inflammation, but for HFD groups NK T levels were elevated. Even though there was no significant difference between fructose and glucose samples, it becomes quite clear that these sugars induced a worse outcome in terms of inflammation than HFD alone.

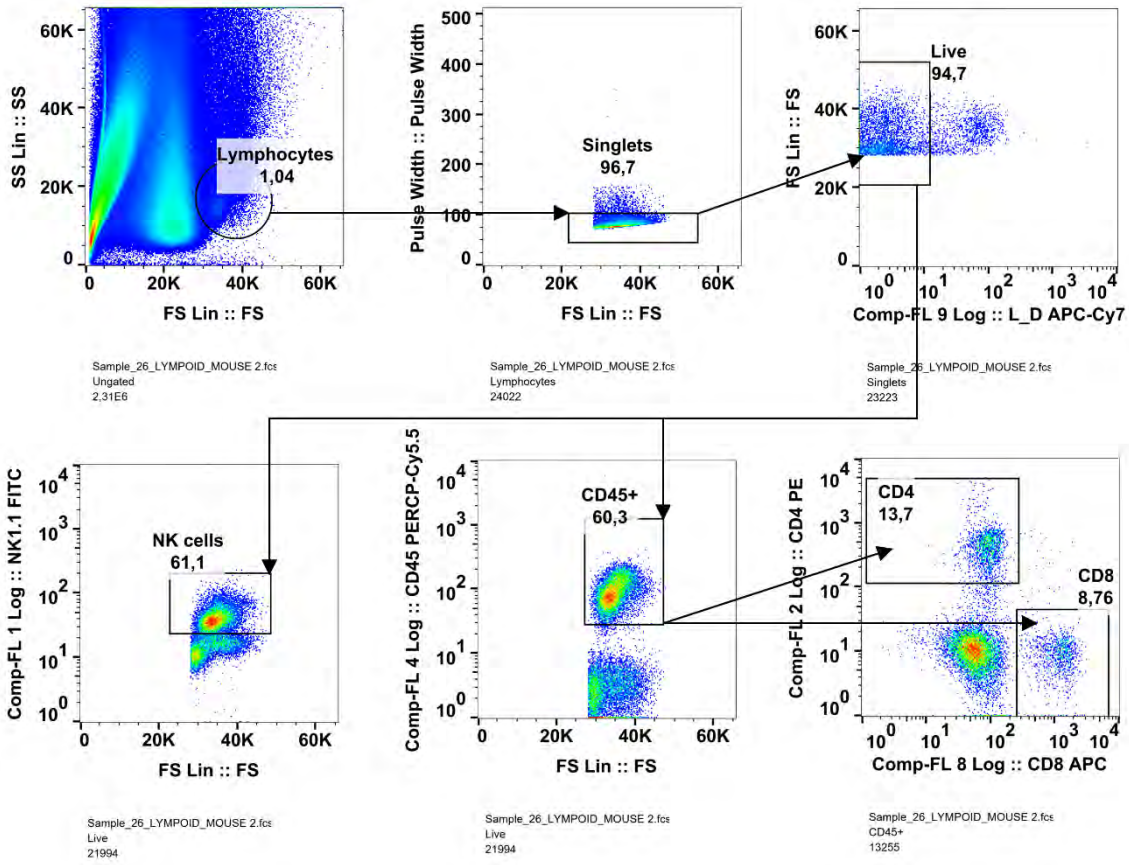

Figure 5. 11 – Representative flow cytometry plots demonstrating the gating strategy of lymphoid panel for T-cell characterisation. Lymphocytes were gated on live single cells, then separated in two sub-populations between NK cells expressing NK1.1 and $CD45^+$ cells. The remaining T cell population from $CD45^+$ cells was split into two populations based on $CD4^+$ and $CD8^+$ cells.

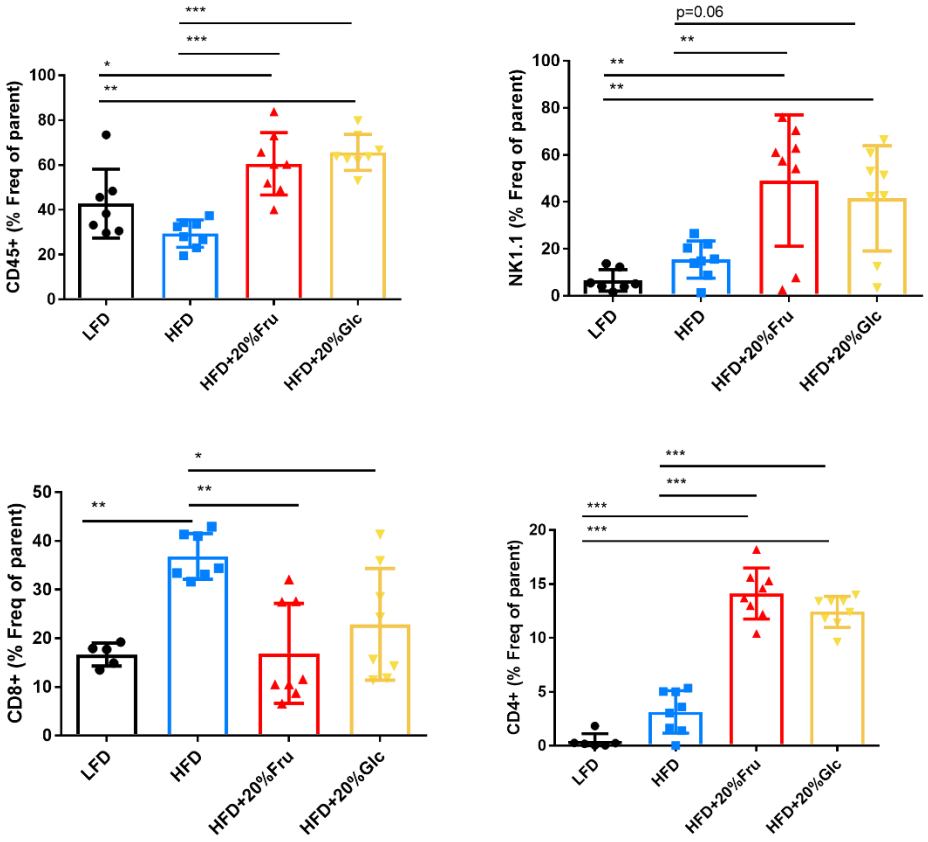

Figure 5. 12 – Increased T-cell populations were detected when mice are fed a high fat diet, especially when complemented with sweetened water for 21 weeks. (n=5-8 mice per group, and bars represent mean ± standard deviation and *p*-values as follows: **p*<0.05, ***p*<0.01, ****p*<0.001, *****p*<0.0001)

Infiltration of myeloid cells was analysed according to the gating strategy shown in Figure 5. 13. This strategy was used to firstly identify myeloid cells, gating according to size and singularity, as well as viability.

Myeloid cells (monocytes, macrophages, dendritic cells and granulocytes) were identified from the live cell population gating on the $CD45^{+}$ and $CD3^{-}$ cells. Figure 5. 14, shows an increase of myeloid cells population in mice fed an HFD, which is significantly altered for HFD + 20% fructose or glucose groups when compared with the LFD. Using the combination of the antibodies CD11b and F4/80, the populations of macrophages, monocytes and granulocytes can be obtained. Again, these populations showed an altered immune response in HFD fed animals with sweetened water in comparison with the LFD ones. To further understand the effective immune response, anti-Gr-1 antibody (the combination of anti-Ly6C and anti-Ly6G antibodies) was used identify granulocytes and macrophages. I observed no significant alterations in these populations across the diet spectrum.

In summary, my flow cytometric analysis revealed some differences in the immune status of the mouse liver when animals are fed a low or high fat diet. A more pronounced hepatic inflammation occurs when mice are fed a HFD, which was further aggravated when water was supplemented with sugar. Here, fructose and glucose seemed to trigger a very similar response with enhanced recruitment of both lymphoid and myeloid cell populations.

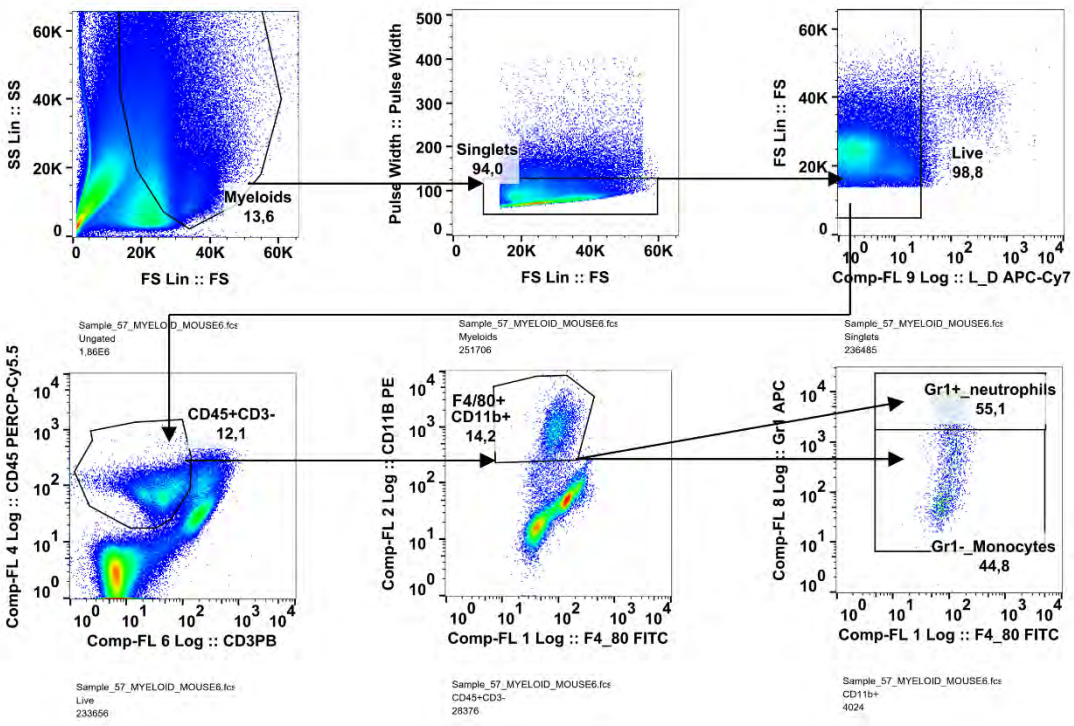

Figure 5. 13 – Representative flow cytometry plots demonstrating the gating strategy of myeloid panel for myeloid cell characterisation. Myeloid cells were identified from the live single cell population and then gated on the $CD45^{+}$ and $CD3^{-}$ population. Next, the combination of the antibodies CD11b and F4/80 allowed to obtain the macrophage, monocytes and granulocytes populations, which were further split into neutrophils and monocytes based on Gr1 expression – $Gr1^{+}$ and $Gr1^{-}$ cells.

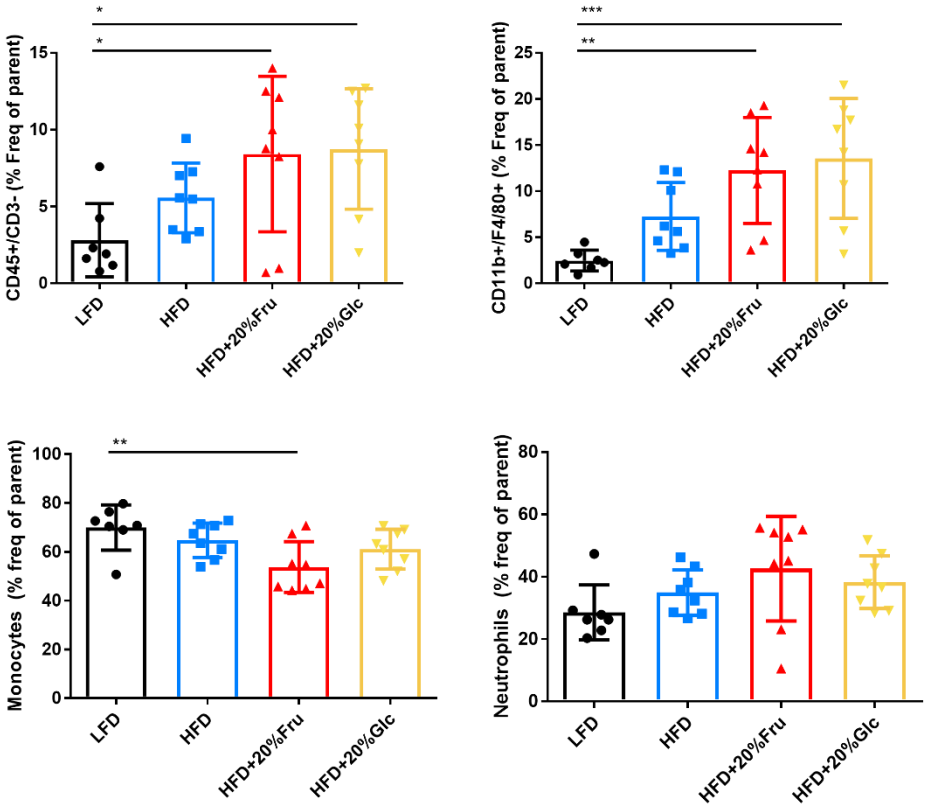

Figure 5. 14 – Hepatic macrophage number increases when mice are fed a high fat diet supplemented with sweetened water for 21 weeks. (n=5-8 mice per group, and bars represent mean ± standard deviation and *p*-values as follows: *p<0.05, **p<0.01, ***p<0.001)

5.3.3. NMR metabolomic analysis of hepatic cells at 21 weeks

Cell metabolism refers to the substrate consumption and production in the metabolic pathways and processes within a living cell. Therefore, the metabolic composition of cells under different conditions may help to assess the cells' pathophysiological status and their response to different stimuli [99,103,120]. Hence, to understand the disease-associated metabolic changes driven by the high fat diet, NMR spectroscopy was used.

5.3.3.1. 1D analysis of control samples

Intracellular hepatic metabolic profiles were obtained from 1D ^{1}H NMR spectra of aqueous cell extracts and are represented in Figure 5. 15. Mouse livers have a complex metabolic composition, and over 30 compounds were unambiguously identified including amino acids (leucine, isoleucine, valine, alanine, glycine, phenylalanine), organic acids (lactate, acetate, succinate) and nucleotides (UMP, IMP, ATP, GTP, NAD^{+}). Additional intracellular metabolites were detected, including glutathione, taurine, glucose, and choline containing compounds.

To investigate the metabolic alterations induced in mice by the different diets, a quantification of hepatic metabolites was carried out (Figure 5. 16). Amino acid metabolism was shown to be variable across all groups, with altered patterns of changes depending on the amino acids measured. However, on balance there was no significant change seen with a particular diet. Still, other metabolic pathways seemed to show trends for change. Of note, there was a trend for higher production of TCA cycle intermediates in mice fed a HFD + sugars, which was more distinct for glucose than fructose. The opposite trend was seen at the level of nucleotide production, where LFD and HFD alone displayed higher levels of UMP, IMP, AMP and GTP, for example. Among the measured metabolites, the most intriguing changes were related with energy production metabolic

pathways and intermediates, as well as the phospholipid-precursor phosphocholine (Figure 5. 17).

The high fat diet alone seemed to induce similar variations to the low fat diet, while the sugar supplementation led to the opposite response. Hepatic glucose levels were higher in the first two groups and are significantly decreased in the HFD + sugar diets. This had an impact towards the further end of glycolysis, which is seen at the level of enzymatic substrates, such as adenosine mono-, di- and tri-phosphate (AMP, ADP and ATP) and guanosine triphosphate (GTP), as well as in some substrates of the TCA cycle (fumarate and malate). Here, TCA cycle intermediates are significantly increased in the HFD + sugars, with particular increase in the glucose supplementation. Furthermore, the adenosine phosphates are significantly reduced in HFD + sugar when compared with the LFD and HFD alone. At the GTP levels, the trend is similar, however only comparison with the glucose supplementation seems to be significant.

Another significant change was seen at the level of the phospholipid precursors, especially for the metabolite phosphocholine. This metabolite behaves similarly in the LFD and the HFD + 20% glucose, where both are significantly decreased when compared with the other two. No difference was observed though between HFD alone and when fructose was added to the water.

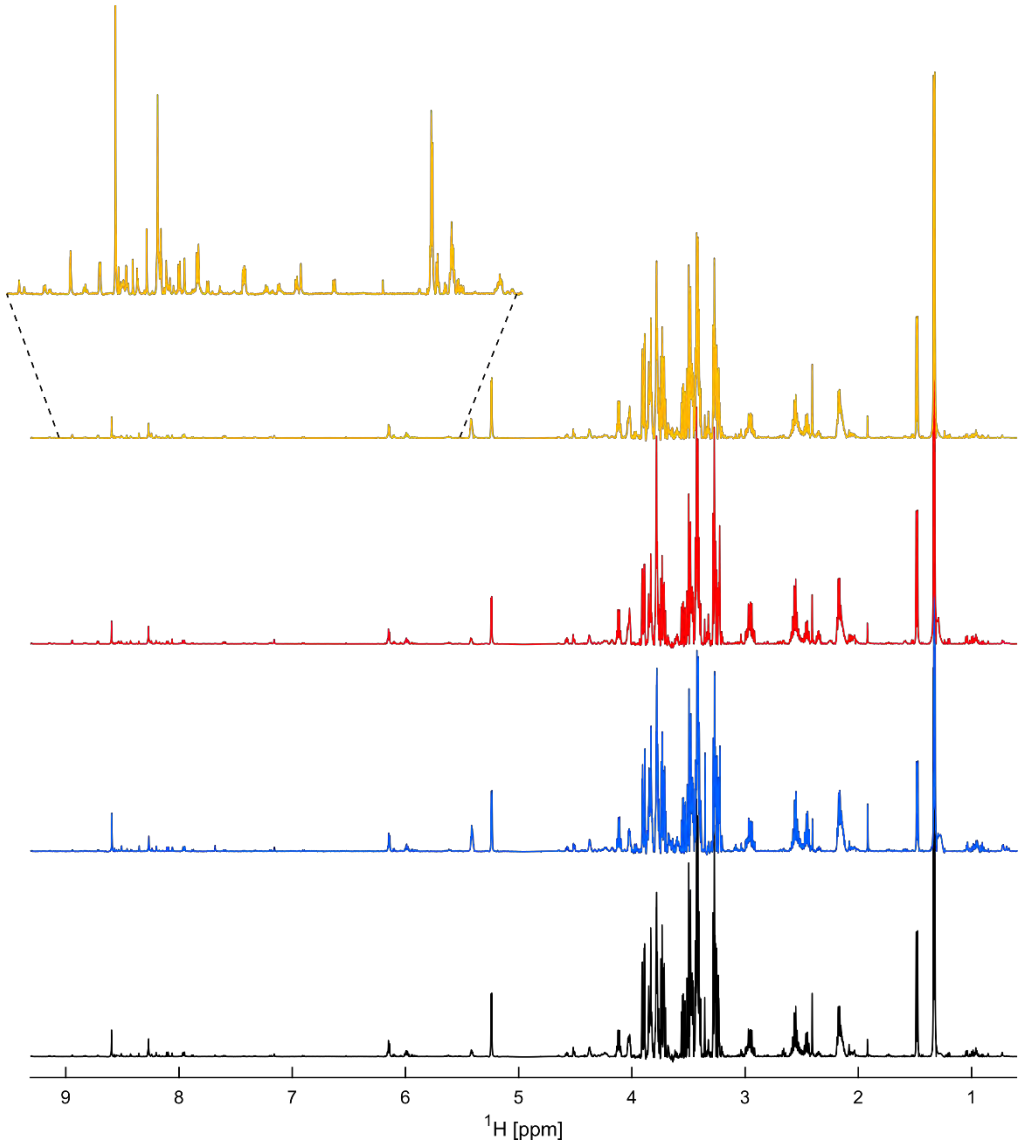

Figure 5. 15 – Representative 1D ^{1}H spectra of all dietary groups. Colour coded as: LFD in black, HFD in blue, HFD + 20% fructose in red, HFD + 20% glucose in yellow.

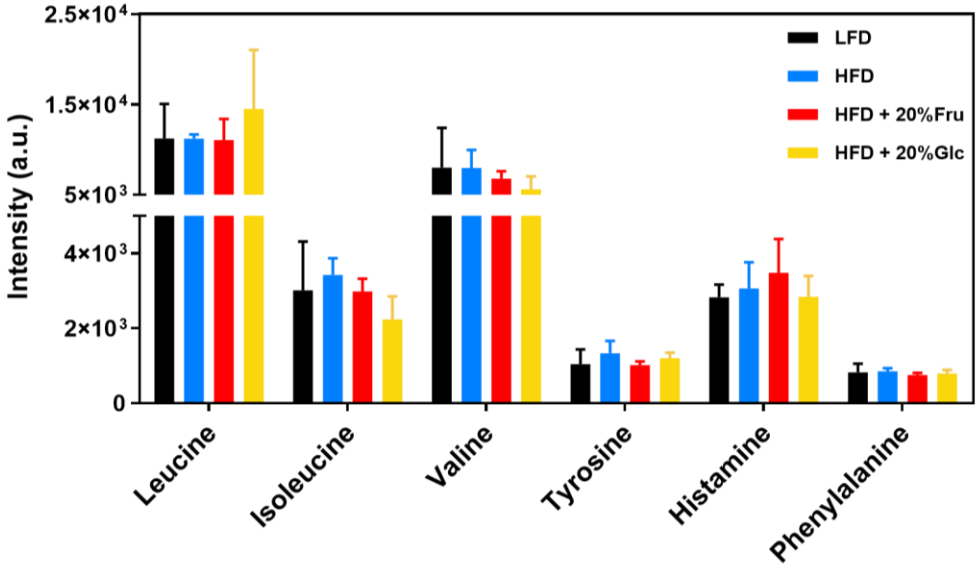

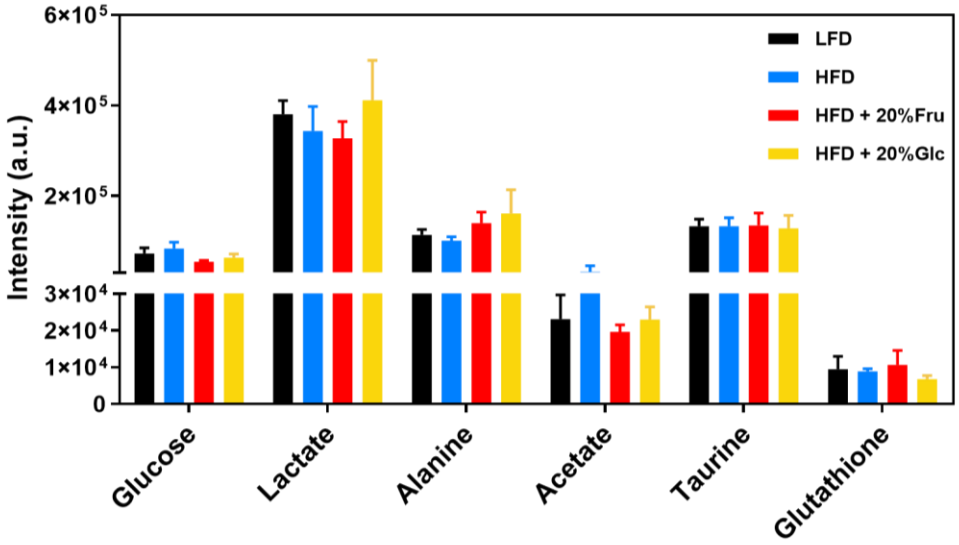

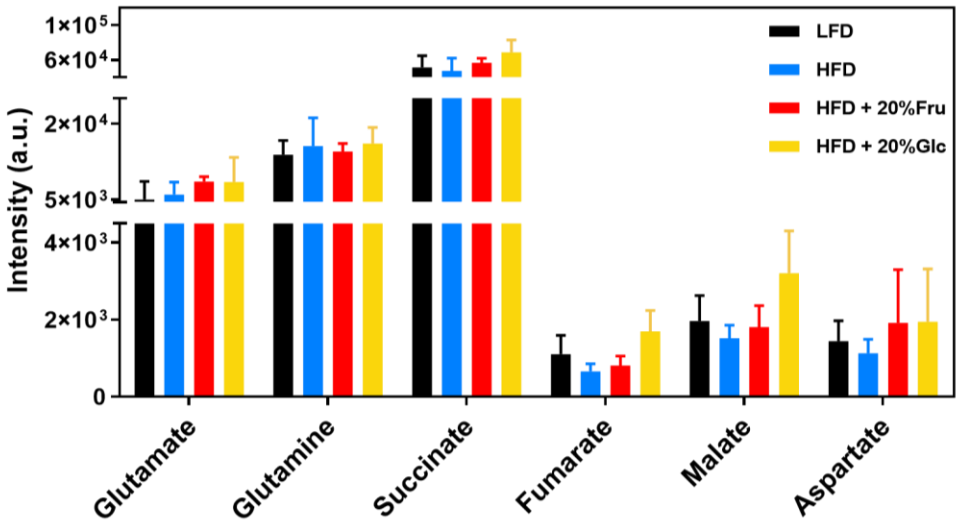

(continued in next page)

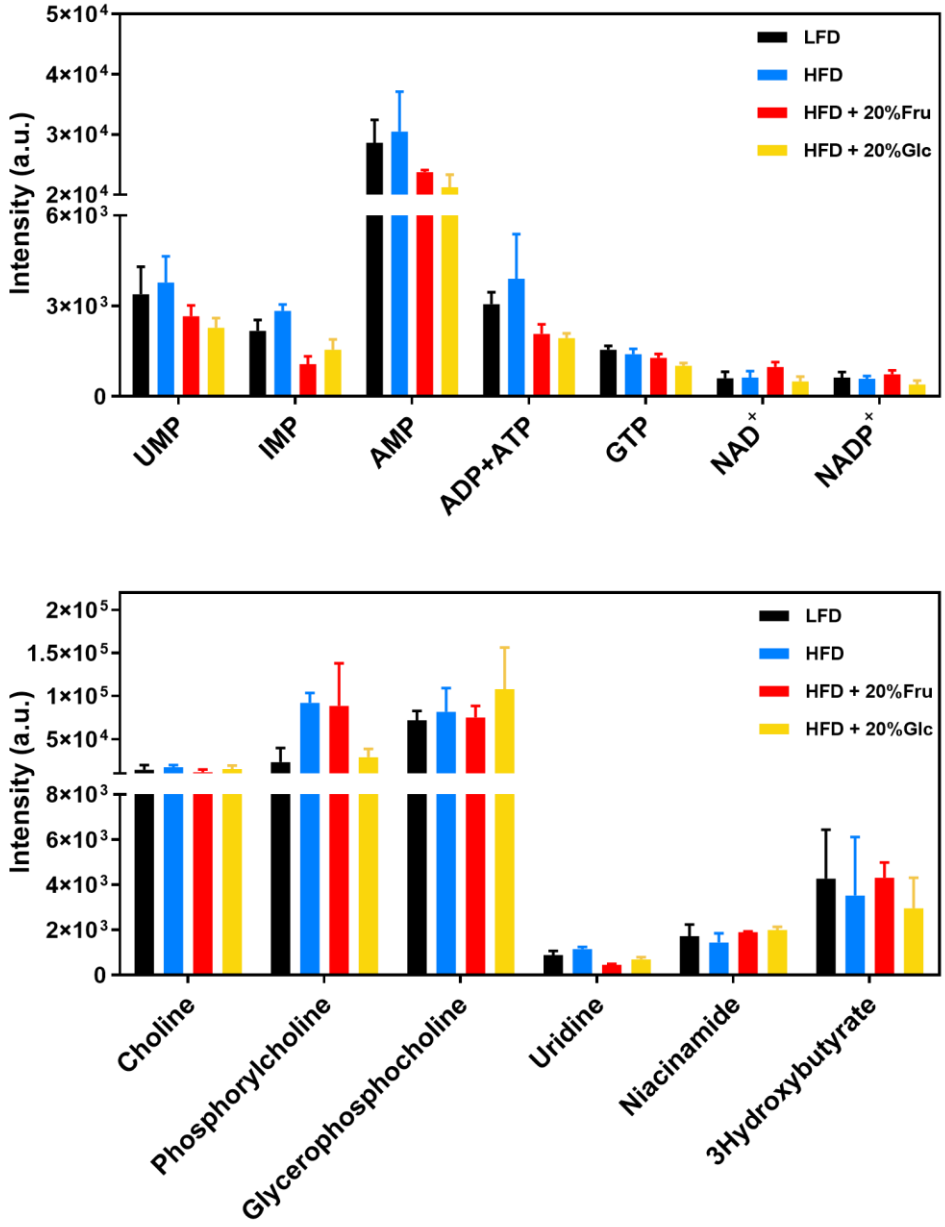

Figure 5. 16 – Hepatic intracellular variations induced by diet are surprisingly small considering how different the source of nutrients is in a LFD versus a HFD. (n= 4 mice per group, and bars represent mean ± standard deviation).

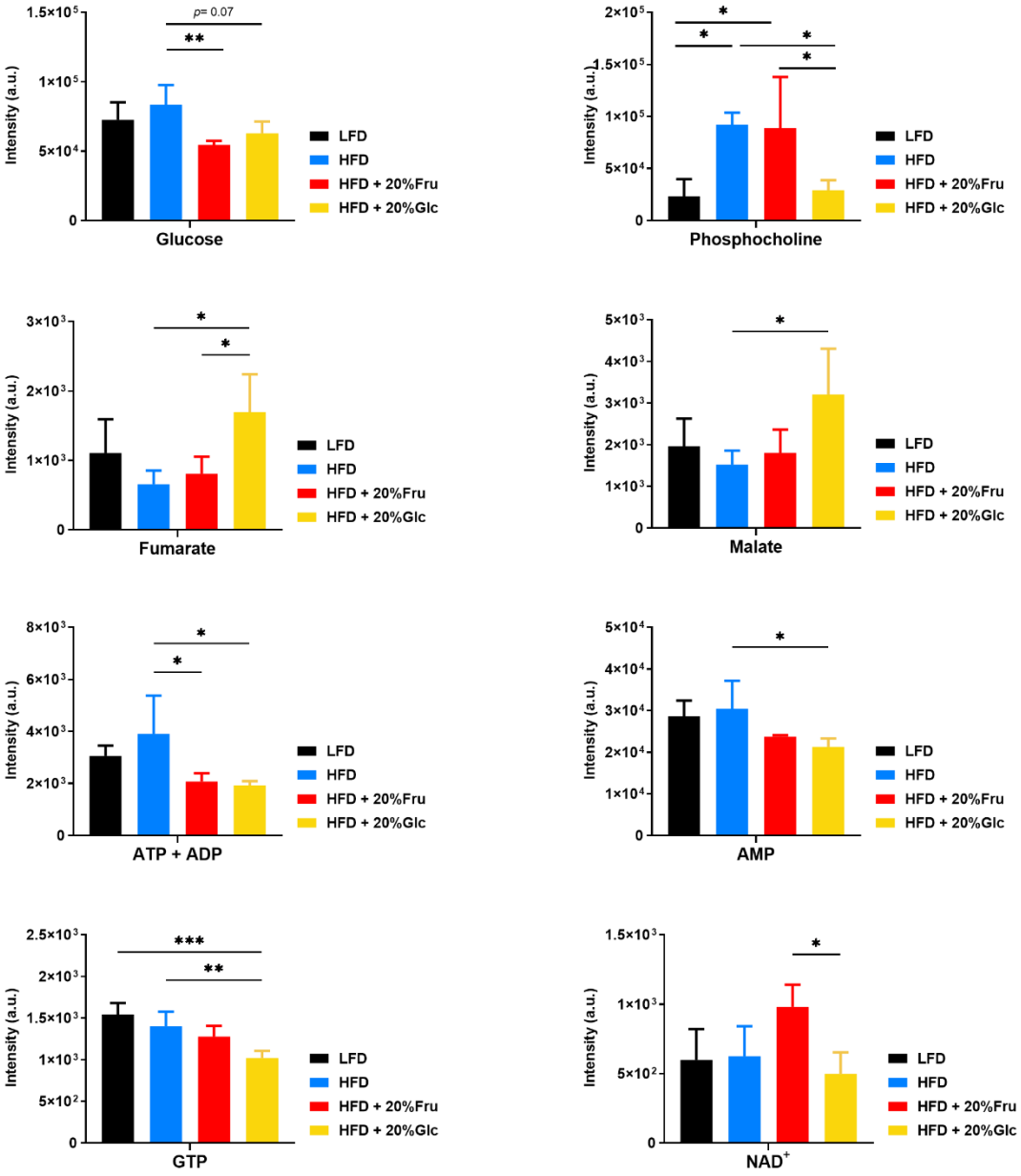

Figure 5. 17 – Using a high fat diet for 21 weeks has only induced significant variations in a few metabolites, mainly associated with energy metabolism. (n= 4 mice per group, and bars represent mean ± standard deviation and *p*-values as follows: **p*<0.05, ***p*<0.01, ****p*<0.001).

5.3.3.2. 2D analysis of control and ^{13}C-labelled samples

As 1D metabolomics only offers an instant, static measurement of the physiology of a living organism, a tracer-based analysis was performed using this animal model. Using ^{13}C-labelled precursors, one can determine metabolic products and their contribution to multiple pathways [120,140,171]. Mice were given an intraperitoneal injection of 1M [U-^{13}C] fructose 30 minutes before culling allowing me to trace fructose metabolism *in vivo*. Next, the liver was collected and immediately immersed in liquid nitrogen to stop metabolism, followed by a metabolite extraction.

2D ^{1}H-^{13}C- HSQC spectra were used for this study as they provide information about directly linked protons (^{1}H) and carbons (^{13}C). Hence, signal intensities in HSQC spectra allowed quantification of site-specific label incorporation ratios in metabolites. The level of label incorporation was obtained by comparing signal intensities in the labelled and natural abundance reference spectra, i.e., between animals that received an injection of [U-^{13}C] fructose and the control animals.

Observing representative HSQC spectra for all groups in Figure 5. 18, it becomes evident that once fructose had entered the circulatory system it was further metabolised in the liver. Comparing control livers (top panel) and livers from animals that received an injection of labelled fructose (lower panel), it is possible to observe J_{cc} couplings for alanine, glucose and glycerate, which occurs when neighbouring carbons have ^{13}C-incorporation. These metabolites display ^{13}C-incorporation in several carbons which can only occur if they were produced from the given [U-^{13}C] fructose, and this is also visible for glutamate, glutamine and succinate (Figure 5. 19).

Signal intensities were obtained from matched spectra (control and labelled), ratios of ^{13}C-incorporation were calculated and are represented in Figure 5. 19. Interestingly, it seemed that in 30 minutes after fructose has entered the organism it was completely

cleared. Therefore, parent fructose signals were very weak or even absent in the HSQC spectra collected at 30 minutes. As fructose enters the cell, it can enter glycolysis producing glycerate, alanine and lactate, and move towards the TCA cycle, giving rise to glutamate, glutamine and succinate. If there is enough energy available, fructose can also enter gluconeogenesis and produce glucose and sorbitol.

It might be expected that animals on diets with different nutrient sources would metabolise fructose at different ratios depending on demand, however this does not seem to be the case with these mice. Nevertheless, there was a trend for higher production of glucose in animals fed HFD + 20% fructose compared with the other groups. The opposing trend is observed for alanine and lactate, exhibiting a small reduction in its levels, as well as TCA cycle intermediates. Another minor trend was also visible at the level of glycerate production as this seems to be produced at a higher ratio when animals were given sugars in the water with HFD, particularly glucose.

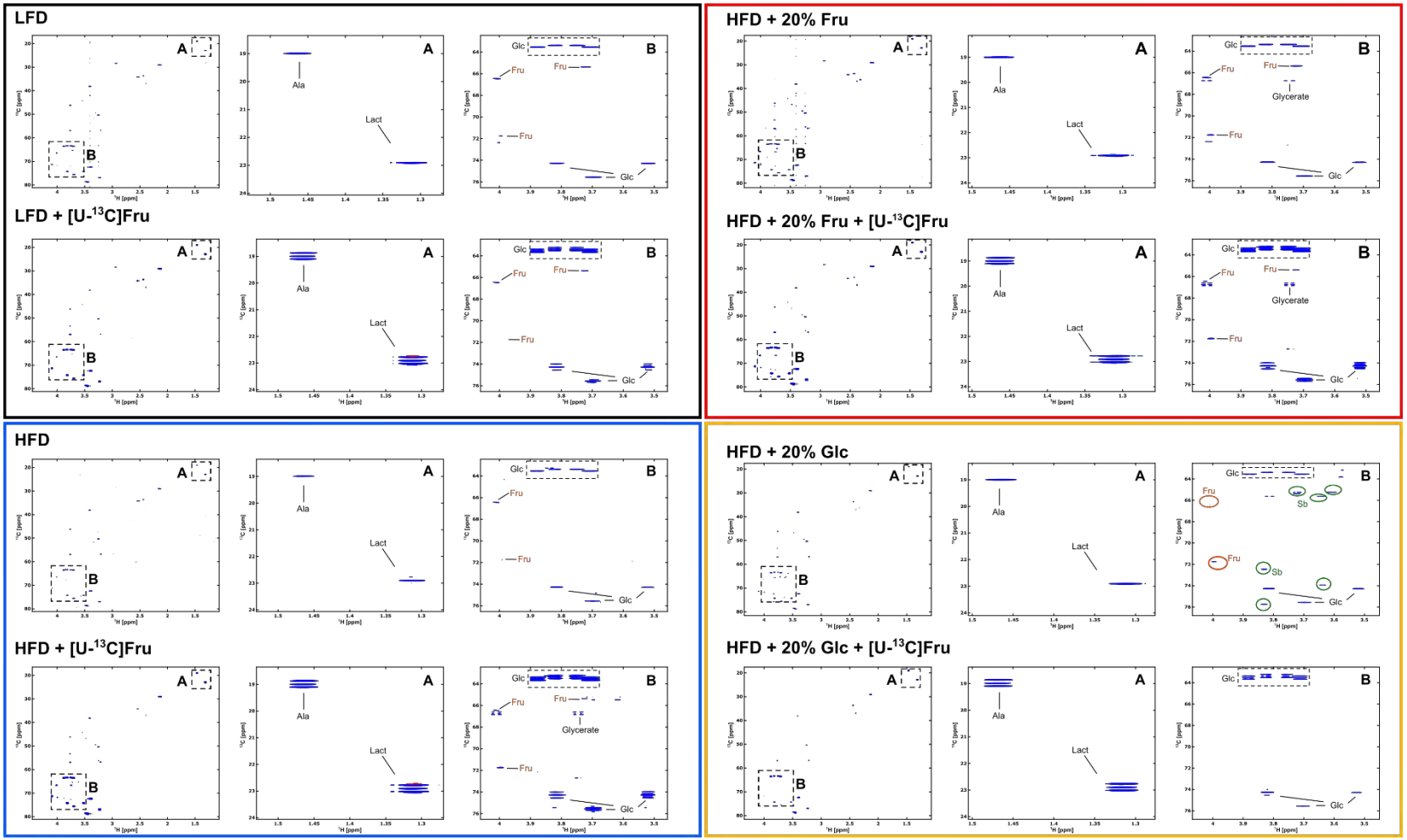

Figure 5. 18 – Representative HSQC spectra for all groups: LFD, HFD, HFD + 20% fructose, HFD + 20% glucose in control mice vs [U-^{13}C] fructose injected mice at culling time. Designations of metabolites are: Fru fructose, Glc glucose, Ala alanine, Lact lactate, Sb sorbitol. (n= 4 independent samples from mice livers per group).

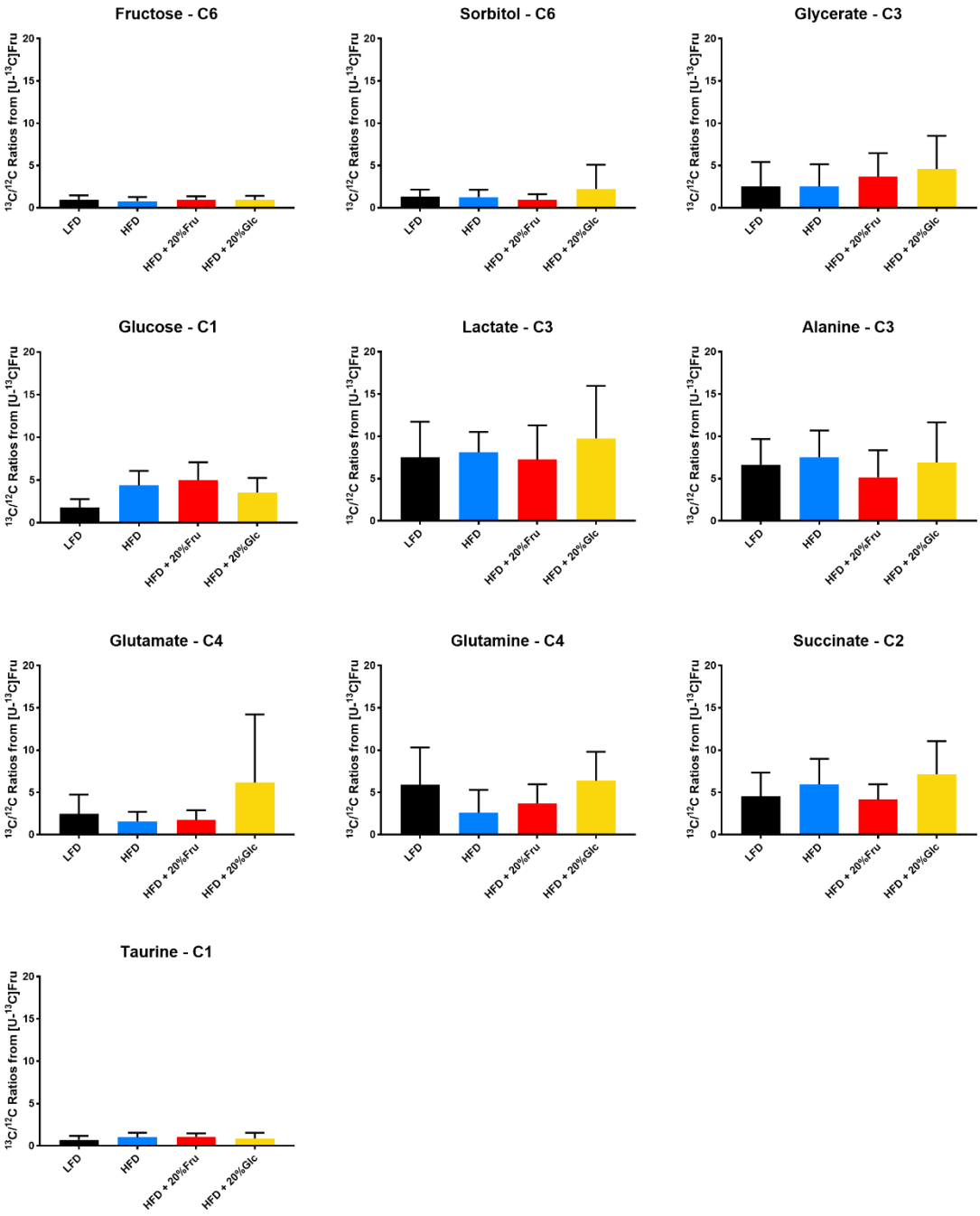

Figure 5. 19 – Ratios of ^{13}C-incorporation in fructolysis intermediates from [U-^{13}C] fructose in mouse livers. (n= 4 mice per group, and bars represent mean ± standard error of the mean).

5.3.4. Gene expression profiling using qPCR array

The combination of different biochemical approaches offers great advantages to investigate the potential molecular mechanisms involved in the development and progression of NAFLD [240]. Therefore, in addition to NMR-based metabolomics analysis, hepatic gene expression was also quantified using a RT^2 profiler PCR array focused on the main pathways involved in fatty liver disease, including insulin and adipokine signalling, carbohydrate and lipid metabolism, inflammatory response and apoptosis. Using this array to investigate a total of 84 genes simultaneously allowed me to obtain a complete profile of pertinent genetic expression changes in mouse livers following a HFD and sugar supplementation. The data from these studies is represented in Figure 5. 20.

Using the hepatic gene expression of LFD-fed animals as a control group, HFD-fed animals showed increased expression of genes involved in lipid metabolism and transport, insulin signalling and decreased carbohydrate metabolism. These are exemplified by epidermal fatty acid-binding protein (*Fabp5*), glucose 6-phosphate 1-dehydrogenase (*G6pdx*), insulin-like growth factor-binding protein (*Igfbp1*), interleukin-1 beta (*Il1b*) and sterol regulatory element-binding protein 1 (*Srebf1*), which were all downregulated in HFD-fed animals, along with increased in CD36 antigen (*Cd36*) expression..

Addition of fructose or glucose to HFD induced further changes in apoptosis and inflammatory response genes, adipokine signalling and other lipid metabolism and transport. However, fructose induced more changes in genes related with fatty acids, triglyceride and cholesterol metabolism while glucose affected genes involved in glycolysis and gluconeogenesis, inositol-related metabolites and saturation of acyl-CoAs.

In the HFD + 20% fructose, the main significant changes in gene expression were for acetyl-CoA carboxylase 1 (*Acaca*), hepatic fatty acid-binding protein (*Fabp1*), lipoprotein lipase (*Lpl*), serine/threonine protein kinases (*Mapk8* and *Mtor*), phosphatidylinositol 3-kinase regulatory subunit alpha (*Pik3r1*), inorganic phosphatase (*Ppa1*) and solute carrier family 2, facilitate glucose transporter member 1 (*Slc2a1*). There was also a down-regulation of epidermal fatty acid-binding protein (*Fabp5*). On the other hand, using a HFD + 20% glucose induced down-regulation of peroxisomal acyl-CoA oxidase 1 (*Acox1*), CCAAT/enhancer-binding protein beta (*Cebpb*), epidermal fatty acid-binding protein (*Fabp5*), glucose 6-phosphatase (*G6pc*) and glucose 6-phosphate 1-dehydrogenage (*G6pdx*), and over-expression of oxysterols receptor LXR-beta (*Nr1h2*), phosphatidylinositol 4,5-biphosphate 3-kinase catalytic subunit alpha isoform (*Pik3ca*) and pyruvate kinase PKLR (*Pklr*).

Taking advantage of heatmaps allowed me to discern broad patterns in the global gene expression in the liver and notable variations, although not all changes were statistically different. Increased expression of genes involved in insulin signalling pathways was observed when using a HFD, with the greatest impact observed for HFD + 20% glucose animals. For example, insulin-like growth factor 1 was over expressed in HFD alone and fructose supplemented animals, and its expression was decreased for the glucose group. In contrast, genes involved in carbohydrate metabolism were mainly down-regulated when using a HFD, but when glucose was added, upregulation of phosphoenolpyruvate carboxykinase (*Pck2*) and glycerol kinase was detected (*Gk*). The most important variation was seen in carbohydrate-responsive element-binding protein - ChREBP (*Mlxipl*), and pyruvate kinase (*Pklr*) which were only upregulated when sugar supplementation was used and not by the HFD alone.

Regarding cholesterol metabolism and transport, a similar pattern was observed between HFD alone and HFD + 20% fructose and not glucose. Here, apolipoprotein related genes were upregulated (*Apob, Apoc3, Apoe*) in HFD and HFD + 20% fructose, while nuclear receptors of subfamily 1(*Nr1h-*) and peroxisome proliferative activated receptors (*Ppar-*) were upregulated similarly across all groups. Interestingly, upregulation of genes involved in beta-oxidation, lipid metabolism and transport, and oxidative phosphorylation was observed in all groups, but in particular for sugar supplemented animals. Overall, hepatic gene expression was affected by the HFD feeding and most evident changes were observed for animals with sugar supplementation.

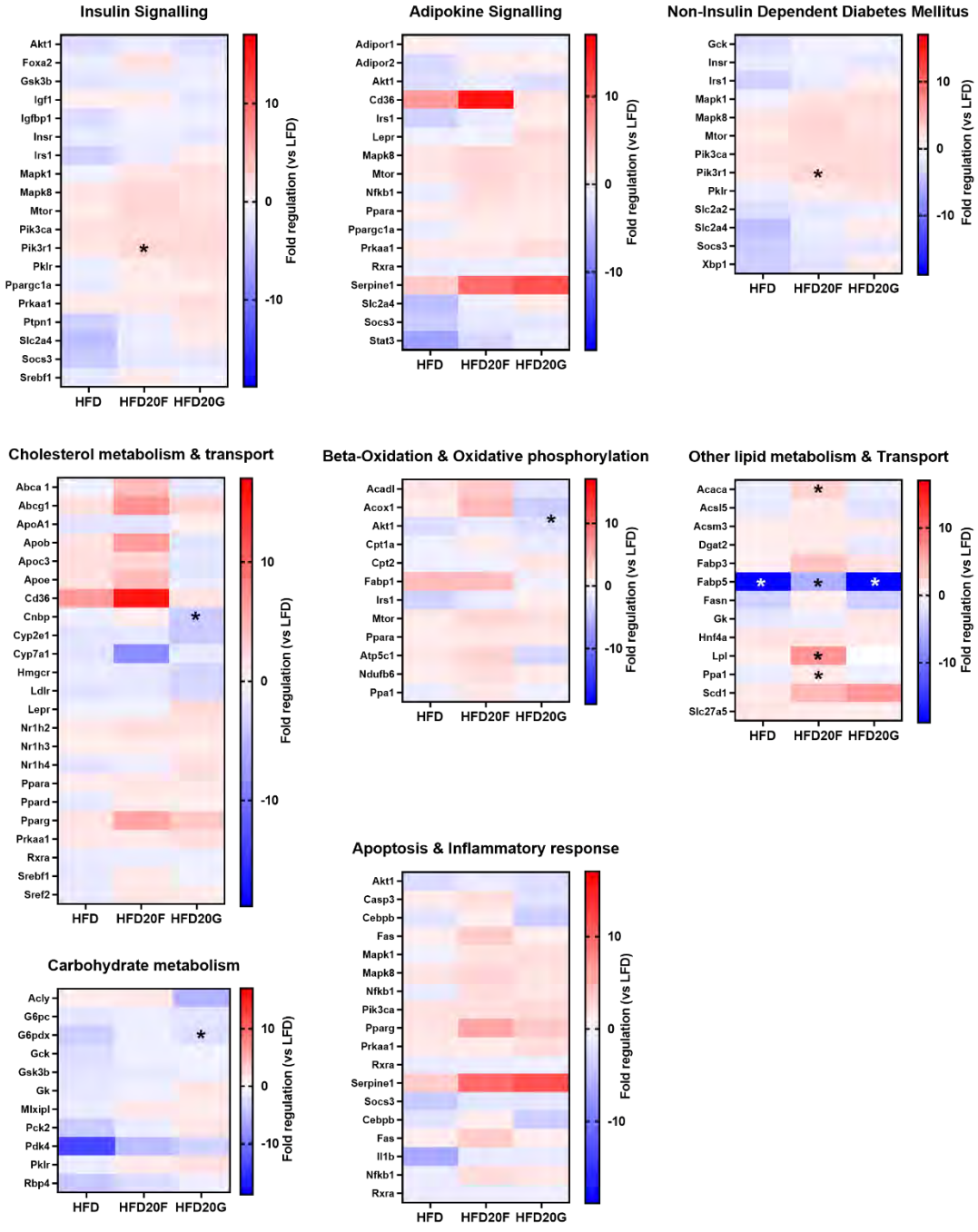

Figure 5. 20 – Hepatic gene expression is affected by the consumption of a high fat diet and sugar metabolism. Heatmaps represent fold regulation of gene expression obtained by qPCR and compared with the LFD group as a control. n= 3-4 animals per group and *p-value <0.05.

5.4. Discussion

5.4.1.1. The influence of diet on liver inflammation and disease

Animal models of NAFLD and NASH have been developed in order to investigate the relationship between metabolic abnormalities and disease progression. A high fat diet (HFD) will lead to excess supply of free fatty acids, which will accumulate in the liver inducing insulin resistance, decreased fatty acid oxidation, and *de novo* lipogenesis all culminating in steatosis. This is similar to the effect seen when I exposed hepatocyte cell lines to free fatty acids in my culture experiments in Chapter 4. Therefore, mice will gain weight and develop hepatic steatosis on HFD-feeding [94,241,242]. These effects are seen during human NAFLD progression, which is characterised by obesity, hepatic steatosis and inflammation, insulin resistance and dyslipidaemia [145,146].

As we were also trying to investigate the contribution of glucose and fructose to the development of NASH, it was very important to understand the dietary components and their sources as this will directly affect metabolism and behaviour. Therefore, using a matched control diet with similar total daily intake of calories (kcal) and nutrient source to the HFD was of utmost importance [149]. We have chosen to use a low fat diet as a control diet instead of a traditional chow diet, to minimise the metabolic variables and control for calorific intake. This way, both dietary groups had access to matched caloric intake with the same purified ingredients, including fibre type, source of carbohydrates and fats [243].

In our animal model, the low fat diet has proven to be a good control as the mice displayed a normal liver morphology and no hepatic lipid accumulation, even though it contained 7% sucrose to match the high fat diet content. On the other hand, animals on a high fat diet had elevated weight gains and fat accumulated subcutaneously, as previously described [72,145,232,244,245].

Mice on a HFD had a substantial liver enlargement and histopathological examination revealed high levels of steatosis. While all mice on a HFD developed macro- and micro-vesicular steatosis within hepatocytes, only mice on a HFD + 20% fructose or glucose featured inflammatory cell infiltration in the H&E analysis. The combination of sugars and fat has resulted in a higher hepatic steatosis and inflammation, thus caused disease progression from simple steatosis towards NASH. As previously described, the immune system contributes to NASH progression by secretion of cytokines from the cross-talk of $CD8^+$ T cells, NKT cells and hepatocytes, as well as increase in oxidative stress and collagen deposition. As transition from simple steatosis to NASH in humans is characterised by inflammation and fibrosis leading to a worse outcome in patients, this model using HFD + sugars offers advantages over a simple HFD alone which only causes simple steatosis [55,244,246].

One limitation of this study was the difficulty to determine whether the addition of the sugar acted synergistically with the high fat content from the diet or if the effects observed are only due to the higher caloric intake compared to HFD alone. A possible solution to determine the influence of the added caloric intake by the sugar supplementation would be to have a separate group of LFD animals with fructose- or glucose-supplemented water in this study. However, a recent study by Softic *et al* [247] has demonstrated that mice on a chow diet supplemented with sugars did not induce any major physiological difference.

Another constraint in metabolic studies is the social interaction that occurs within cages. Behavioural dominance among male mice was also observed, which will ultimately influence the eating routine of some animals [248]. As a result, some greedier mice would eat more than others in the first few weeks while establishing dominance, resulting in a higher interindividual and intraindividual variation. These were assumed

to contribute to the observed variability of response at the first ten-week experiment, where several animals within the same group displayed such different phenotypes.

Even though the effects of both fructose and glucose have the same caloric value and were similar in hepatic lipid deposition (H&E) and weight gain, fructose has induced an overall poorer outcome. Fructose supplementation has led to a greater accumulation of abdominal fat, higher liver enlargement and higher transaminase levels, as previously reported [72,249].

5.4.1.2. Blood biochemistry analysis

Assessment of biochemical liver function tests in mice allowed me to screen the status of the liver during the disease model progression. According to a publication by Otto *et al* [236] stating refence intervals for C57BL/6J mice, normal alkaline phosphatase (ALP) values for male mice should be between 80-100 U/l. Although there were inconsistent values for animals on a LFD in the first weeks, all other mice have shown to have very consistent levels of ALP throughout the experimental time, being just slightly elevated when compared with the described normal values reported by Otto *et al*. Nevertheless, there was no significant alteration induced by the high fat diet and variations, which seems to reflect normal biliary function, without sign of cholestasis [40,81].

As both alanine transaminase (ALT) and aspartate transaminase (AST) are used as markers of hepatocellular injury, these variations are the most significant for our study. Even though both enzymes are present in a wide variety of tissues, ALT is considered to be the most liver specific of the two as it is mostly found in the liver. Nevertheless, AST levels are considered more sensitive markers of liver disease [81,236,250].

To be considered within normal and healthy values, ALT should be below 40 U/l. This was observed in animals fed LFD until the end of the experiment but was quite different for the remaining groups. Mice on a HFD alone seemed to have normal levels until week 13, however by the end of the 21st week these values were significantly increased. As shown in several studies [146,232,251], progression of simple steatosis to NASH occurs from week 12 onwards, which seems to be compatible with our serological and histological observations. On the other hand, when fructose and glucose are used to supplement the water, an increase of ALT was observed much earlier. Our results have shown that by week 13, mice have elevated transaminase levels which are only observed by week 21 when HFD only is used. The effects are enhanced during the remaining time

of the experiment. By the end of the 21 weeks, these ALT values seem to rise steeply for animals with fructose supplementation, reaching on average 547 U/l, whereas animals with glucose supplementation didn't increase as steeply, reaching only around 275 U/l on average. This is a good indicator that fructose is causing a more significant liver injury and inflammation than glucose.

Finally, the normal range for AST is usually 40-60 U/l for C57BL/6J mice, which is somewhat lower than the levels observed for the LFD animals. Normal levels were maintained in the HFD alone mice until week 13, but were slightly increased by the end of 21 weeks. Similar to the ALT elevations, animals with access to sweetened water had an earlier increase of AST levels, being abnormal by the end of 13 weeks. Again, mice with HFD + 20% fructose revealed a more significant increase by the end of the experiment. All these alterations in transaminase levels are in agreement with the observations made macroscopically regarding body weight and abdominal fat accumulation, where animals on a HFD + 20% fructose had a worse outcome.

Human NAFLD patients at increased risk for steatohepatitis feature multiple factors associated with insulin resistance, carbohydrate excess and metabolic diseases, including obesity, dyslipidaemia, sugar consumption and sedentary lifestyle [143,252]. Hence, my model of mice on a HFD + sugar confirms that these metabolic factors are closely associated with NAFLD progression, and more importantly confirms the utility of this system as a preclinical model of human disease.

Initial diagnosis of human NAFLD and assessment of its severity is usually achieved through the analysis of plasma concentration of liver enzymes, bilirubin and albumin. More specifically, AST and ALT are the commonly the only indicators for hepatic alteration. Disease progression using AST/ALT ratio is particularly useful in distinguishing alcoholic liver disease (ALD) and NAFLD. An elevated AST/ALT ratio

usually is associated with long term pathologies such as fibrosis and cirrhosis, where a ratio greater than 2 usually is attributed to alcoholic hepatitis. Regarding steatosis, both enzymes are normally elevated, but it is more likely that ALT will be higher in the first instance. Only when steatosis starts to progress towards NASH, will AST/ALT levels consequently increase allowing a good prediction of NAFLD stage [253–256].

Overall, our findings describe a model where NAFLD is occurring and progressing towards NASH and that is consistent with previous studies; Liu *et al* have described that increased serum ALT is directly correlated with liver cell steatosis and apoptosis [251]. Fraulob *et al* have also demonstrated that C57BL/6 mice fed a high fat diet (60% fat) have increased levels of transaminases when compared with mice on a standard chow diet [257]. More recently, Gallego-Duran *et al* also verified that ALT and AST levels in HFD-fed C57BL/6 mice are related to liver damage, where AST levels are higher than controls at earlier time points.

In this study, urea levels were also measured at the latest time point, after 21 weeks on diet. Urea is a waste product synthesised in the liver when combining nitrogen with metabolites that result from the breakdown of proteins and amino acids. Urea is released into the bloodstream and carried to the kidneys where it can be filtered and excreted in the urine. Although elevated urea is usually used as a marker for acute renal disease, when urea levels are low this could reflect severe liver damage [41,84]. In LFD and HFD groups, urea levels are within the normal range, however when the water was supplemented with sugars and a HFD, mice reveal a decrease in urea levels. Furthermore, HFD + 20% glucose seems to be inducing a higher effect.

Lower levels of blood urea nitrogen are usually associated with inadequate protein intake, reduced urea synthesis and abnormal excretion of urea. Our mice had a similar

protein intake across the dietary groups, so it is highly unlikely that the reduction observed for urea levels in HFD + sugar mice is related with protein intake. Also, there are studies showing that when metabolic liver function is compromised, urea synthesis capacity can be noticeably decreased [258,259]. To confirm this, it would have been optimal to obtain urea concentration at the beginning and during the experimental time and evaluate how it changes with progression of liver disease.

Moreover, patients with NAFLD have demonstrated a higher risk of developing renal function impairment, sharing common risk factors such as type 2 diabetes and obesity [83,260,261]. Therefore, lower levels of urea can also be related with the decline in kidney function, but further testing would be necessary.

5.4.1.3. Flow cytometric analysis

To assess whether the high fat diet and sugar supplementation would cause liver inflammation, a functional characterization of the adaptive and innate immune cells was carried out using flow cytometry analysis.

My analysis has revealed that damage arising from exposure to long term HFD led to liver inflammation when compared with a LFD group. This was especially stimulated when sweetened water was used in addition to the HFD, as seen with the increased frequency in the expression of $CD45^+$ cells. To further phenotype T cells, they were subdivided in different subsets regarding their physiological functions. Subsets were organized as T helper subsets ($CD4^+$), cytotoxic T cells ($CD8^+$), and lastly natural killer cells ($NK1.1^+$).

Although livers from animals on a LFD showed little histological evidence of immune infiltration, we did see some evidence of resident lymphocytes and $CD4^+$ proportions were lower than $CD8^+$. Whilst this reflects previous T cell ratios seen in normal uninjured livers [262], a better approach in future would be the use of counting beads in the acquisition setup, so a total number of cells could be obtained in relation to the mass of liver used for the digestion. Of note however, HFD fed animals also had a higher proportion of $CD8^+$ cells than $CD4^+$, in agreement with the $CD45^+$ expression, with greater cell frequency for sugar supplemented groups. This suggests the presence of more pro-inflammatory cells in the HFD tissue, which is consistent with the observations made in the H&E analysis. This data agrees with the observations made in human pathology, as the activation of several T cell subsets is recognised as a driver of NAFLD progression [9]. Similar to our study, progression from steatosis to NASH has been described to shown increased levels of $CD4^+$ and $CD8^+$ in humans [48,263,264].

NK T cells are highly abundant in the liver and are involved in liver injury regeneration and fibrotic responses. They also contribute to NAFLD pathogenesis acting as proinflammatory cells [265]. While in the LFD group the quantity of this subset was quite low, the combination of a HFD and sugars led to increased abundance of NK T cells. It is noteworthy that a HFD alone is insufficient to induce substantial inflammation, yet no significant differences were found between the effects of added fructose and glucose.

Some NK T cells are able to recognise glycolipids together with CD1d, so NK T cells can be rapidly activated in the presence of lipids. Following the continued exposure to a HFD, altered lipid metabolism and hepatic steatosis can therefore modulate antigen presentation to hepatic T cells leading to hepatic inflammation [49]. In humans, NK T cells have been reported to contribute to the pathogenesis of NAFLD as the cytotoxic cells increase in number according to disease progression. NASH patients reveal increased number of hepatic NK T cells than patients with simple steatosis, which is influenced by the fibrosis severity [9,49,265]. Thus again, our murine model is recreating human pathophysiology.

When the liver enters an inflammatory state, the first responses activate key players of the innate immune system, particularly myeloid cells which were also analysed by flow cytometry. Our study has shown that similar to the lymphoid populations, these cells increased in number in the HFD livers when compared with the LFD, and this change was significant when sugar was added to the water. Here there was a proportional increase in the myeloid $CD45^+/CD3^-$ and $CD11b^+/F4/80^+$ subsets within injured livers. Whilst the total myeloid population was clearly increased in HFD animals + sugar, when subsets of neutrophils, monocytes and macrophages were split according to $Gr1^+/Gr1^-$ expression. While $CD11b^+/Gr1^+$ cells include monocytes, neutrophils and eosinophils, $CD11b^+/Gr1^-$ will include monocytes, but there was no significant difference between

groups. This may be due to the large variation between individuals and the fact that my data is expressed as proportion of cells rather than absolute number. Thus, in a liver of increasing size it would be possible to have a significant increase in total number of inflammatory cells whilst the proportion of each subset within the total remains unchanged. Again, as noted for our lymphoid populations it would be worth using counting beads to determine absolute cell counts.

In an effort to maintain the tissue immune homeostasis, macrophage infiltration occurs, and neutrophils are recruited when pro-inflammatory cytokines and chemokines are released. In healthy conditions, the main function of macrophages is to induce a regenerative response by detecting and destroying pathogenic products, as well as cellular debris from the hepatic circulation. Neutrophils, on the other hand, are the first line of defence regarding infection response and play an important role in controlling gut bacterial translocation [52,55]. When the liver is continuously exposed to sources of inflammation, such as hepatic steatosis and lipotoxicity, hepatocyte damage is recurrent and lobular inflammation will be promoted [209,266]. This was observed in our HFD + sugar animals, which showed increased lymphoid and myeloid populations as shown in previous studies with increased number of $F4/80^{+}$ macrophages [244,267,268]. Several studies report that the intestinal immune responses are also implicated in NAFLD pathology, which ultimately influence hepatic neutrophils and monocyte recruitment and function. This is due to the release of cytokines and exposure to pathogenic molecules as a consequence of gut permeability changes [269–271]. Although bacterial products can be detrimental (cytokine release), they can also be beneficial for liver regeneration and play a role in neutrophil accumulation [272,273]. Thus, although our data supports the idea that increased lymphoid and myeloid cell number in the liver is a hallmark of NAFLD, I

would need to do further functional studies to determine whether this balance is beneficial or detrimental in the murine model.

Hence, for further comprehension of the immune state, flow cytometric analysis using functional markers could also be helpful. Identifying different subsets of macrophages, such as the polarisation markers for M1 and M2 populations, and their function state, analysing the secretion of proinflammatory cytokines such as IL-6 and TNFα, or cytokine drivers of T cell differentiation like the Th1, Th17 and Th22 subsets, would help understand the cellular responses. These approaches have previously been used to phenotype both human and animal samples to obtain a better mechanistic understanding of the immune response during NAFLD progression, as reviewed in [9,48].

An alternative technique that could be used to expand our findings, would be immunohistochemistry. Here, immune cell distribution across the liver tissue could be further assessed in order to gain insight as to which cells are interacting with hepatic immune components [274].

In summary, we were able to detect macrophage infiltration along with lymphocytes involved in NAFLD pathogenesis, which activation is facilitated by the consumption of a HFD with sweetened water supplementation. Notably, both adaptive and innate immune systems are involved during the progression of liver disease. Thus, we can conclude that fructose and glucose supplementation do accelerate the progression of NAFLD by increasing inflammation and triggering immune response. Still, specific mechanisms that drive this progression are not yet fully characterised and cellular exchanges between the liver, gut and adipose tissue should be also considered.

5.4.1.4. Metabolic alterations studied by NMR spectroscopy and genetic expression

NMR spectroscopy metabolomics has been widely used to measure the physiological state of biological systems, mechanisms of toxicity and metabolic interactions between different organs. Moreover, it helps understanding the metabolic disturbances that occur during disease progression which is important for improved disease therapies and biomarker discovery [104,105,275]. Furthermore, the identification of key genes in NAFLD is also useful for the discovery of pathophysiological alterations during disease progression. In the past this analysis was carried out based on bioinformatic and meta-analysis, GeneChip microarrays and real-time PCR using liver biopsy samples [240,276–279].

The analysis of liver-specific metabolic profiles by NMR spectroscopy and hepatic gene expression by qPCR has provided an overview of the impact of the low and high fat diet in liver disease progression. Although the results in the preceding sections have demonstrated a clear physiological effect of the diet in liver steatosis and inflammation, metabolomic analysis has shown only a few significant metabolite level alterations, even with the progression of NAFLD. Intracellular variations of polar metabolites indicate that a HFD alone has a similar metabolic profile to the LFD-fed animals, whereas the sugar supplementation has led to a more pronounced effect in the liver metabolism. Significant differences were observed in key metabolites of the glycolytic pathway and nucleotides, as well as in the level of choline-containing compound phosphocholine.

When comparing intrahepatic glucose levels between the dietary groups, LFD and HFD groups are quite similar, while the HFD + sugar animals demonstrate a clear reduction. Glucose regulation in the liver occurs in response to blood sugar levels and it is regulated by insulin and glucagon. As most of these animals were continuously exposed to a HFD supplemented with sugars, they developed a fatty liver and insulin

resistance, a common effect of NAFLD [257,280,281]. This fits with my gene expression analysis, as insulin-like growth factor 1 (*Igf1*) was over expressed in HFD alone and fructose-supplemented animals, and its expression was decreased for the glucose group.

Important unique variations in the glucose group included increased insulin receptor substrate 1 (*Irs1*), and solute carrier family 2 member 4 (*Slc2a4*), as well as genes involved in glycolysis. These involved the up-regulation of phosphoenolpyruvate carboxykinase (*Pck2*) and glycerol kinase (*Gk*), which lead to an increase in glucose transport and metabolism, as well as insulin resistance. When using the fructose supplementation, a more specific response was seen with an over-expression of genes related with triglyceride metabolism (*Lpl*), fatty acid metabolism (*Acaca, Fabp1* and *Fasn*) and cholesterol metabolism (apolipoproteins). This could explain why mice on this diet had a higher subcutaneous fat accumulation and a fat and heavier liver. Commonly altered genes in both sugar supplementations and that are associated with the metabolic phenotype analysed by NMR, are related with carbohydrate-responsive element-binding protein – ChREBP (*Mlxipl*), and pyruvate kinase (*Pklr*) which were only upregulated when sugar supplementation was used and not by the HFD alone. This was previously described by Softic *et al* [71,247] and directly related with liver fat content accumulation in human fatty liver disease [278].

Another interesting variation visible for all groups was the down-regulation of epidermal fatty acid-binding protein (*Fabp5*). Fabp5 is a fatty acid-binding protein isoform co-expressed in adipocytes and macrophages responsible for enhancing free fatty acids solubility and transport to the endoplasmic reticulum [282]. Therefore, down-regulation of this protein can be a compensatory mechanism to stop net lipid accumulation in cells that are related with hepatic fatty acid infiltration [283].

As lipid synthesis is promoted, metabolic state transitions occur towards a higher energy availability for other tissues. In agreement with this are the levels of TCA cycle intermediates fumarate and malate, which demonstrate a trend towards higher production, especially for glucose fed mice. Sun *et al* [284] have reported that an HFD intake stimulated glycolysis and overall energy metabolism, including TCA cycle intermediates fumarate and aspartate (produced from malate), which is consistent with our results. Increased TCA cycle activity and hepatic mitochondrial metabolism have been reported for mice [198,223,285] and humans [199,286], contributing to NAFLD pathology. Moreover, the balance between ATP+ADP and AMP seem to be dysregulated. Alterations in adenosine phosphates homeostasis, as well as GTP, are related with fundamental metabolic processes that control metabolic pathways [287]. The loss of hepatic ATP has been associated with compromised mitochondrial respiratory chain activity, as previously reported for a rodent model of NASH [288] and NASH patients [289], but further understanding of the metabolic implications is still needed.

Lastly, significant changes in the phospholipid content was also observed for the phosphocholine. Both Dumas *et al* [290] and Chao and co-workers [291] have reported increased phospholipid content in urine and serum when using a HFD when compared with the control group, and linked this to the relationship between gut and liver metabolism. Choline can be either phosphorylated to generate phosphocholine or be converted to methylamine by the gut microbiota, therefore alterations in these metabolite levels can reflect the interactions between the mammalian pathways and gut microbiota. As mentioned by Jian *et al* [292], availability of choline and its intermediates is also related with apolipoprotein-B secretion, which will ultimately affect LDL receptors and can lead to accumulation of triglycerides in the liver.

Analysis of 1D ^{1}H NMR profiles only provides a static picture of metabolism, not reflecting cellular biochemical regulation over time. To investigate whether fructose metabolism would be altered following a prolonged high fat diet and sugar consumption, a stable isotope tracer-based analysis was performed. The injection of [U-^{13}C] fructose in mice 30 minutes before culling allowed exploration of the usage of fructose *in vivo* and its accumulation into downstream metabolic products.

The complete consumption of fructose after a single i.p. injection was observed for all dietary groups as no labelled fructose signals were detected in the 2D ^{1}H-^{13}C HSQC spectra after 30 minutes. Moreover, fructose was directed towards glycolysis generating glycerate, alanine and lactate, and it was further metabolised in the TCA cycle producing glutamine, glutamate and succinate. The conversion of fructose to sorbitol was also observed, as well as the production of glucose via gluconeogenesis, which was similar across all dietary groups.

Previous studies have demonstrated the fate of labelled precursors *in vivo* following a HFD, in order to study the contribution of specific metabolites in the main biosynthetic pathways and was reviewed by Sun and Empie in [293]. Here, even though different labelling schemes were employed, sugar oxidation was observed generating ^{13}C isotopomers of glucose, lactate, glycerol, lipids, glycogen and ATP + CO_2, in agreement with my observations.

The conversion of fructose to glucose has been observed in several human studies [294–296], and was dependent on exercise, gender and health status. In agreement with this, we found a trend for increased glucose production in HFD alone and HFD + 20% fructose animals, whereas HFD + 20% glucose was not so high when compared to LFD-fed animals. This may occur due to differences in carbohydrate regulation, as fructose is able to avoid rate limiting steps in glycolysis and gluconeogenesis. Moreover, the continuous

exposure to fructose may alter the expression of specific GLUTs and lead to increased absorption of sugars, as it was demonstrated by Karim *et al* in the context of human liver disease [2]. Furthermore, the production of intermediates of glycolysis included higher levels of glycerate, alanine and lactate, which can later enter the TCA cycle.

Using fructose as our initial substrate, we have shown that glutamate, glutamine and succinate are being produced. Although quite variable, there is a trend for increased TCA cycle activity when mice are fed a HFD, especially when supplemented with glucose. Satapati *et al* [198] has also demonstrated that *in vivo* hepatic TCA cycle activity is enhanced following a HFD, with higher oxidative fluxes at 16 weeks and persisting until week 32. Increased CO_2 and fatty acid oxidation were also confirmed for mice with fatty livers; however, their analysis was performed using blood samples and different labelled precursors which could explain the difference observed between their results and our study in terms of metabolic impact.

The use of ^{13}C-labelled fructose in metabolic studies is still limited, but recently Jang *et al* [297] have described the fate of dietary fructose using both ^{13}C-labelled glucose and fructose. The contribution of liver, kidney, pancreas and small intestine were evaluated in fructose metabolism, suggesting that the small intestine is the main location for fructose absorption and metabolism. In a case where a high dose of dietary fructose is given to mice, fructose is transported to portal circulation and enters the liver where it can be further converted to other metabolites. Similar to our study, they also demonstrate that the liver is able to synthesise glucose via gluconeogenesis, be converted to glycolysis and TCA cycle intermediates and also glycerate. Interestingly, glycerate can be produced from fructose but not glucose, which can eventually induce liver toxicity by activating lipogenesis. Supporting this, Tran *et al* [298] also demonstrated that a high dose of fructose

given to adults was able to increase glycerol levels as well as VLDL palmitate levels, which reflects increases in DNL.

While our results fit with the picture seen in human studies, analysis of serum samples and other contributing organs to fructose metabolism would be extremely valuable to understand the specific mechanisms involved in NAFLD progression. Also, a different method of fructose delivery and time-frame should be tested in order to understand how the absorption process would affect availability of substrates. Hence, in the next chapter [U-^{13}C] fructose was delivered to *ex* vivo human samples to compare metabolic routes and products generated according to the system used. Lastly, a ketohexokinase inhibitor was tested to investigate its impact in hepatic metabolism when fructose cannot be regularly metabolised.

CHAPTER 6

THERAPEUTIC INTERVENTION WITH KETOHEXOKINASE INHIBITOR – THE GAME CHANGER

6. Therapeutic intervention using a KHK inhibitor

6.1. Overview

Over the last few years, the prevalence rates for NAFLD and NASH have been associated with the increasing intake of dietary fructose [27]. Fructose enters the liver through the hepatic circulation and is initially phosphorylated by the ketohexokinase (KHK, also known as fructokinase) hepatic enzyme in carbon 1. Since fructose metabolism is not dependent on insulin signalling, fructose 1-phosphate is rapidly cleaved by aldolase B to form D-glyceraldehyde and dihydroxyacetone phosphate. By bypassing the main rate limiting steps in glycolysis, fructose can provide a relatively unregulated source of carbon precursors to drive lipid production and glycolytic intermediates [21,299–301] (See Figure 6. 1 for more details).

Some recent studies in mice with a KHK knockdown have demonstrated that the inhibition of ketohexokinase can protect from diet-induced hepatic steatosis, insulin resistance and obesity [302–304]. Therefore, KHK inhibition could be clinically relevant in protecting human liver steatosis, inflammation and profibrotic activity. However little human data exists to support the potential mode of action.

In this chapter, human liver tissue was subjected to immunohistochemistry analysis and western blot to assess the expression of total KHK and its two isoforms, A and C, and how this varies with disease. Next, to evaluate the efficacy of KHK inhibition under steatogenic conditions, a perfusion system centred on viable human liver tissue wedges was used. Using ^{13}C-labelled fructose, the mechanisms by which the KHK inhibitor alters hepatic lipid accumulation and the glycolytic pathway were studied. Lastly, ^{13}C-fructose clearance *in vivo* was studied using the mouse *in vivo* model of NAFLD described in the previous chapter. This was done by assessing the ^{13}C-enrichment in intermediates of fructolysis, glycolytic end products and TCA cycle intermediates in mice livers.

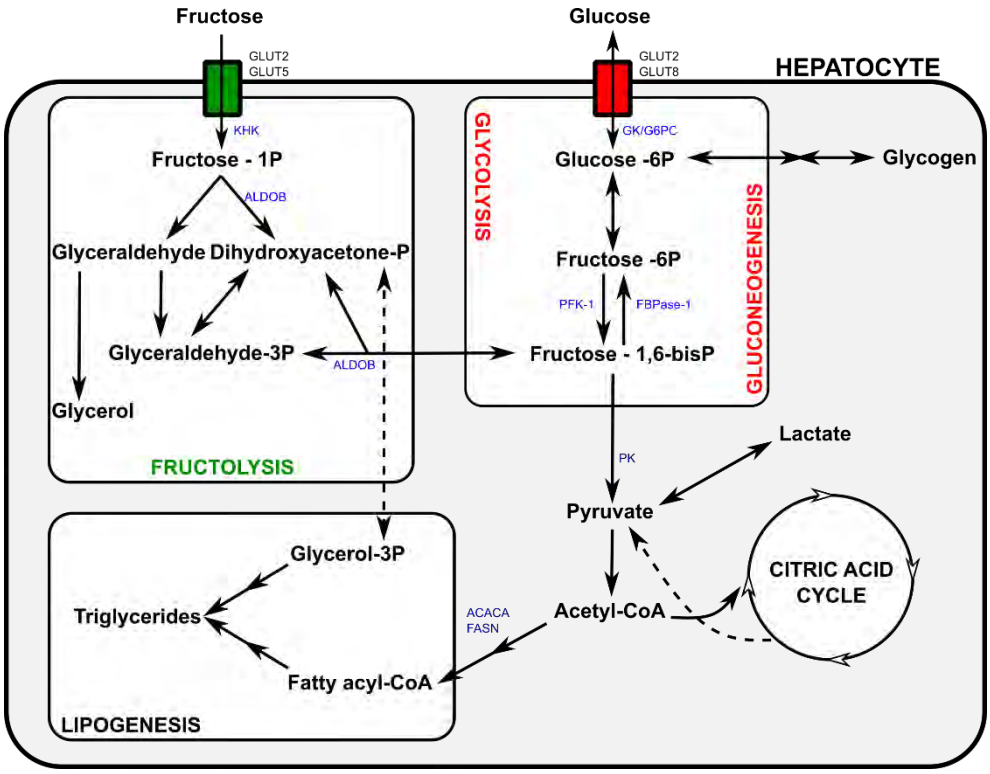

Figure 6. 1 – Main pathways for fructose and glucose metabolism within hepatocytes. In Fructolysis, initial phosphorylation of fructose occurs via ketohexokinase (KHK) activity. In Glycolysis, glucose is initially phosphorylated by glucokinase (GK). A critical regulatory step in glycolysis is mediated by phosphofructokinase 1 (PFK-1) which catalyses the conversion of fructose 6-phosphate and ATP to fructose 1,6-bisphosphate and ADP. Another important reaction is mediated by pyruvate kinase (PK), the enzyme responsible for the final step of glycolysis, in which phosphoenolpyruvate is converted to pyruvate with the production of ATP. Common to both pathways is the formation of the trioses dihydroxyacetone phosphate and glyceraldehyde 3-phosphate, catalysed by aldolase B (ALDOB). Enzymes involved in *de novo* lipogenesis are also represented, including acetyl-CoA carboxylase alpha (ACACA) and fatty acid synthase (FASN).

6.2. Expression of KHK in the human liver

The ketohexokinase enzyme is mostly abundant in liver, renal cortex and small intestine, but it can also be present in other tissues such as brain, lung, muscle and optic nerve [305,306]. KHK exists in two isoforms generated by alternative splicing in exon 3, consisting of KHK-A and KHK-C. While both isoforms are able to metabolise fructose, their kinetic properties and expression in tissue differs. KHK-A is expressed at low levels in a wide range of tissues and has a high Michaelis constant (K_m) for fructose, suggesting that it is unlikely that KHK-A plays a significant role in metabolism of dietary fructose. On the other hand, KHK-C is expressed primarily in the liver, kidney and intestine, has a greater affinity and lower K_m for fructose, therefore being considered to be the primary enzyme involved in fructose metabolism [302,305–307].

To investigate the human expression of KHK in the liver, qPCR analysis was performed (with support from Dr. Emma Shepherd). In Figure 6. 2A it is possible to observe a similar expression of total KHK RNA in normal and NASH livers. There is also a comparable expression with livers from patients with other chronic liver diseases where cirrhosis is derived from autoimmune cholangiopathies, such as PSC and PBC. When using cultured primary liver cells (Figure 6. 2B), hepatocytes revealed a predominant KHK expression, whereas fibroblasts (aLMF) and epithelial (BEC) populations demonstrate a lower expression of the KHK.

To support these findings, the histological localisation of KHK in diseased and normal human liver specimens was determined using a pan KHK antibody for immunohistochemical staining (Figure 6. 3). In a normal liver (Figure 6. 3A), staining was uniformly observed across the lobule, where both the nuclei and cytoplasm of hepatocytes expressed the KHK. Still, hepatocytes were found to be more intensely immunolabelled near macro-vesicular steatotic areas, in peripheric hepatocytes. Nuclear

staining for KHK was also shown by Diggle *et al* [305] in normal liver, however with a high variability as not all nuclei intensely immunolabelled were positive. Therefore, immunohistochemistry data for this protein should be interpreted carefully.

In cirrhotic NASH livers (Figure 6. 3B), expression was also concentrated in hepatocytes within regenerative nodules, but intensity of expression within hepatocytes was similar between normal and fatty donor liver specimens. Also, some KHK positive staining was found at the level of biliary epithelial cells of bile ducts.

To determine which isoforms of KHK (KHK-A and KHK-C), are expressed under normal and cirrhotic liver conditions, a western blot analysis was carried out (Figure 6. 4 – by Dr. Emma Shepherd). A decrease in the total expression of KHK was observed for cirrhotic livers, both ALD and NASH, when compared with normal donors (NL). Also, KHK-C was shown to be the most abundant expressed isoform in the liver.

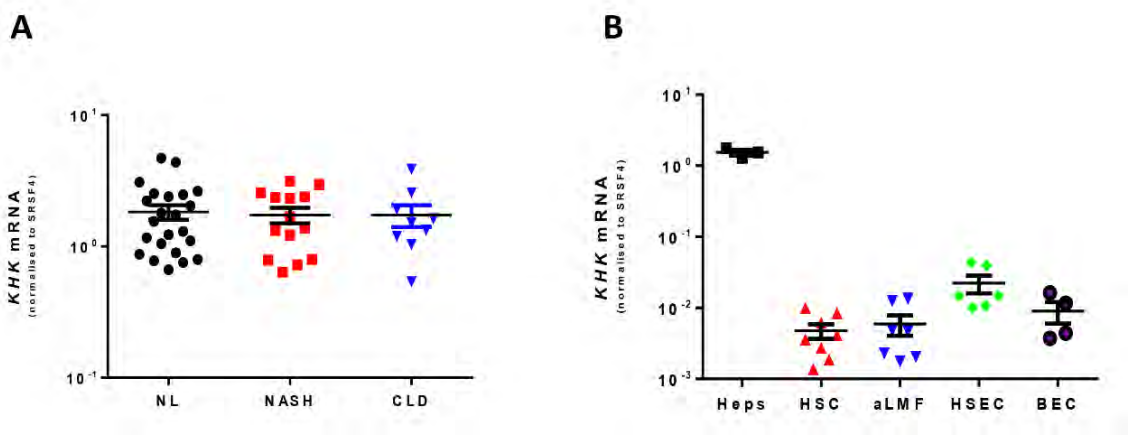

Figure 6. 2 - Quantification of total KHK mRNA in whole human liver (A) or isolated primary human liver cells (B) by qPCR. Data represents individual values and mean ± SEM expression compared to SRSF4 housekeeping gene in (A) whole liver: normal (NL), non-alcoholic steatohepatitis (NASH) and chronic liver disease (CLD); or (B) primary liver cells: hepatocytes (Heps), hepatic stellate cells (HSC), activated liver myofibroblasts (aLMF) or biliary epithelial cells (BEC). Data acquired by Emma Shepherd and used with consent.

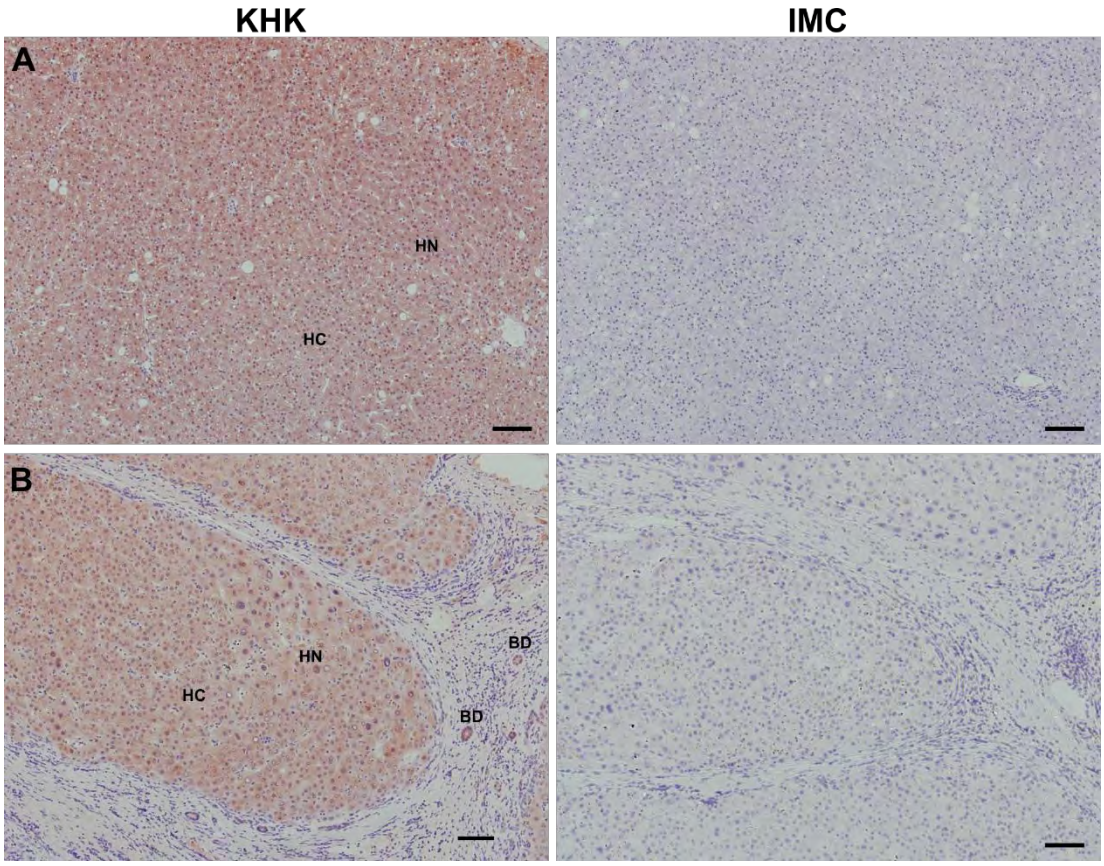

Figure 6. 3 -Immunohistochemical localisation of KHK in normal human liver tissue (A) and NASH liver (B) using a pan-KHK primary antibody. KHK positive staining is observed in hepatocyte nuclei (HN), hepatocyte cytoplasm (HC) and biliary epithelial cells of bile ducts (BD). (Data is representative of n≥10 livers, scale bar 100 μm). IMC – isotype matched control.

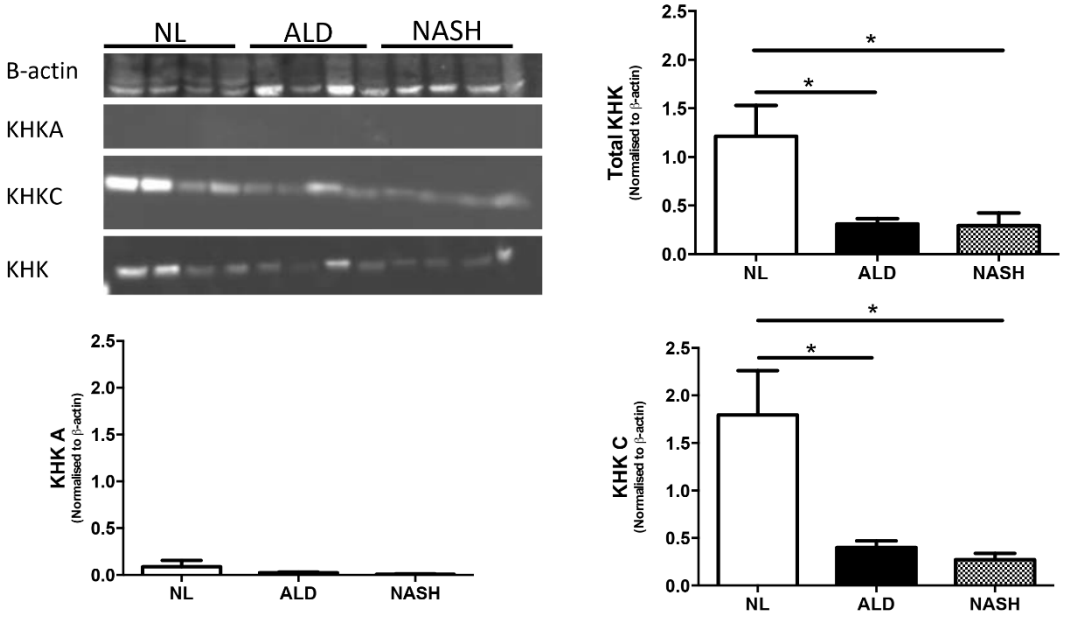

Figure 6. 4 – Comparison of protein expression of total KHK and isoforms A and C in human liver from normal donors (NL), alcoholic liver disease (ALD) and non-alcoholic steatohepatitis (NASH) by western blotting. Top right panel shows the representative blot, whilst the graphs show quantification from n=4 samples in each category. Data is shown as mean ± SD expression normalised to β-actin. Paired *t*-test indicated significant reduction vs NL livers *p< 0.05. Data acquired by Emma Shepherd and used with consent.

6.3. Does targeted KHK inhibition alter fructose metabolism in human liver?

6.3.1. Ex vivo human perfusion system

In order to address the efficacy of the ketohexokinase (KHK) inhibitor from TAKEDA pharmaceuticals in *ex vivo* human livers, a perfusion system delivering [U-^{13}C] fructose was used. In this experiment, paired small wedges of *ex vivo* livers were perfused with glucose-free DMEM to remove blood. Then, samples were perfused with media alone or with KHK inhibitor (10 μM), in glucose-free DMEM containing unlabelled fructose for 30 minutes. Afterwards, the wedges were perfused with glucose-free DMEM containing 20mM [U-^{13}C] fructose for a period of 3 hours. Tissue samples were collected during the period of perfusion, at 0.5, 1, 2 and 3 hours, as snap-frozen sections for NMR analysis or in paraffin for histological assessment.

Figure 6. 5 shows that the liver wedges maintained good integrity throughout the perfusion period as the H&E tissue morphology at the beginning of the experiment is similar to that after 3 hours. Additionally, analysis of tissue samples by NMR spectroscopy allowed me to confirm that the liver remains metabolically active and capable of incorporating and metabolising fructose throughout the experimental time frame. Figure 6. 6 shows a representative ^{1}H-^{13}C-HSQC spectrum of a control sample after 1-hour exposure to [U-^{13}C] fructose, revealing the presence of the labelled precursor as well as other metabolites that participate in specific pathways of fructose and glucose hepatic metabolism. Some metabolites such as glycerol, glycerol 3-phosphate, sorbitol, glucose, alanine and lactate display ^{13}C-labelling patterns, reflecting the flux of ^{13}C-carbons from fructose in the liver, and can be seen in the augmented spectral regions A and B.

To follow these ^{13}C-enrichments in a more precise way, high resolution ^{1}H-^{13}C-HSQC spectra were obtained and compared for each time-point and condition (Figure 6. 7). In the first 30 minutes of perfusion with [U-^{13}C] fructose, there is an accumulation of fructose in the liver and the formation of sorbitol in both conditions. After 1-hour of perfusion, the control liver starts to produce metabolites needed for lipid metabolism, including glycerol and glycerol 3-phosphate, but also metabolites from the last stages of glycolysis such as alanine and lactate. However, when KHK was inhibited, metabolism of fructose was severely slowed down, reflected by higher levels of fructose and sorbitol.

HSQC spectra bear considerable information in coupling patterns arising from scalar couplings between chemically bonded ^{13}C-labelled carbon atoms. As [U-^{13}C] fructose was used, couplings can be seen in metabolic products downstream. Unlabelled metabolites are represented as a central signal of usually lower intensity (arising from 1.1% natural abundance ^{13}C), while ^{13}C-enriched metabolites display coupling patterns. An example of this phenomena can be seen in Figure 6. 8, where the alanine peak in control samples displays a coupling pattern with high intensity peaks, whereas peaks in KHK inhibited samples are much weaker.

At the end of 3-hours of perfusion, the control sample shows the increasing production of glycerol intermediates from fructose, which may suggest that fructose overload can stimulate *de novo* lipogenesis. A similar trend is observed in glycolytic intermediates, where alanine and lactate demonstrate high levels of ^{13}C-incorporation. On the other hand, in KHK inhibited samples, where the usual pathway of fructose is blocked, the accumulation of fructose inside the cell is observed as well as the build-up of sorbitol. These findings confirm that a single dose of the KHK inhibitor can impair fructose metabolism by slowing it down considerably.

To aid interpretation, peak intensities were obtained from metabolites identified in the HSQC spectra and are shown in a diagrammatic representation of the major fructose metabolism pathway in Figure 6. 9. Over the experimental time course (0.5 to 3 hours), we can see the variation in peak intensities in control (blue) or KHK-inhibited (red) livers.

Worthy of note, as the fructose concentration used in the perfusion system is quite elevated and not all substrate is needed to produce energy, the liver was able to activate the gluconeogenic pathway in the control liver wedge. This is confirmed by the coupling pattern observed in glucose carbon-4 but not carbon-1 (Figure 6. 10). For this to happen, glucose can only be formed via ^{13}C-labelled trioses such as glyceraldehyde and dihydroxyacetone phosphate and not via the polyol pathway [308]. Interestingly, this pattern is not observed in the KHK-inhibited samples, which suggests its higher need of glucose for downstream products of glycolysis.

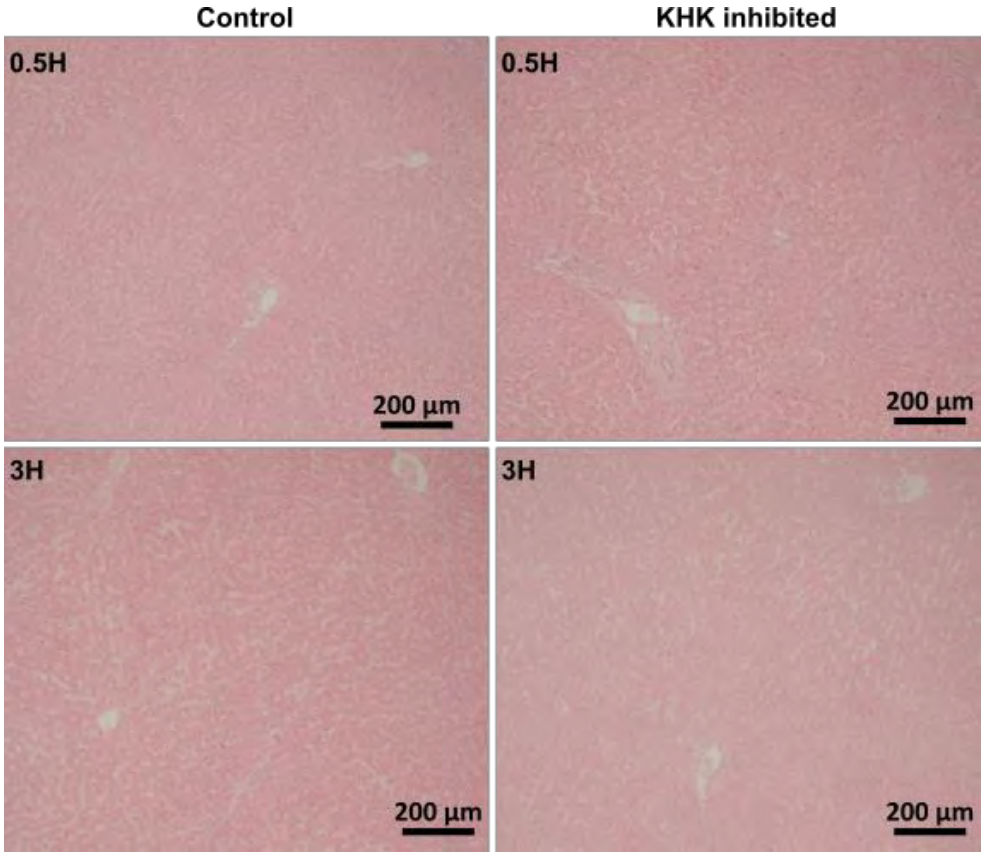

Figure 6. 5 -Human liver wedges maintain structural integrity during perfusion. Sections of liver were collected at each time point of the *ex vivo* human perfusion, fixed in paraffin and sectioned for H&E staining. Representative images were obtained and are shown from the beginning and end of perfusion time (magnification of 5x).

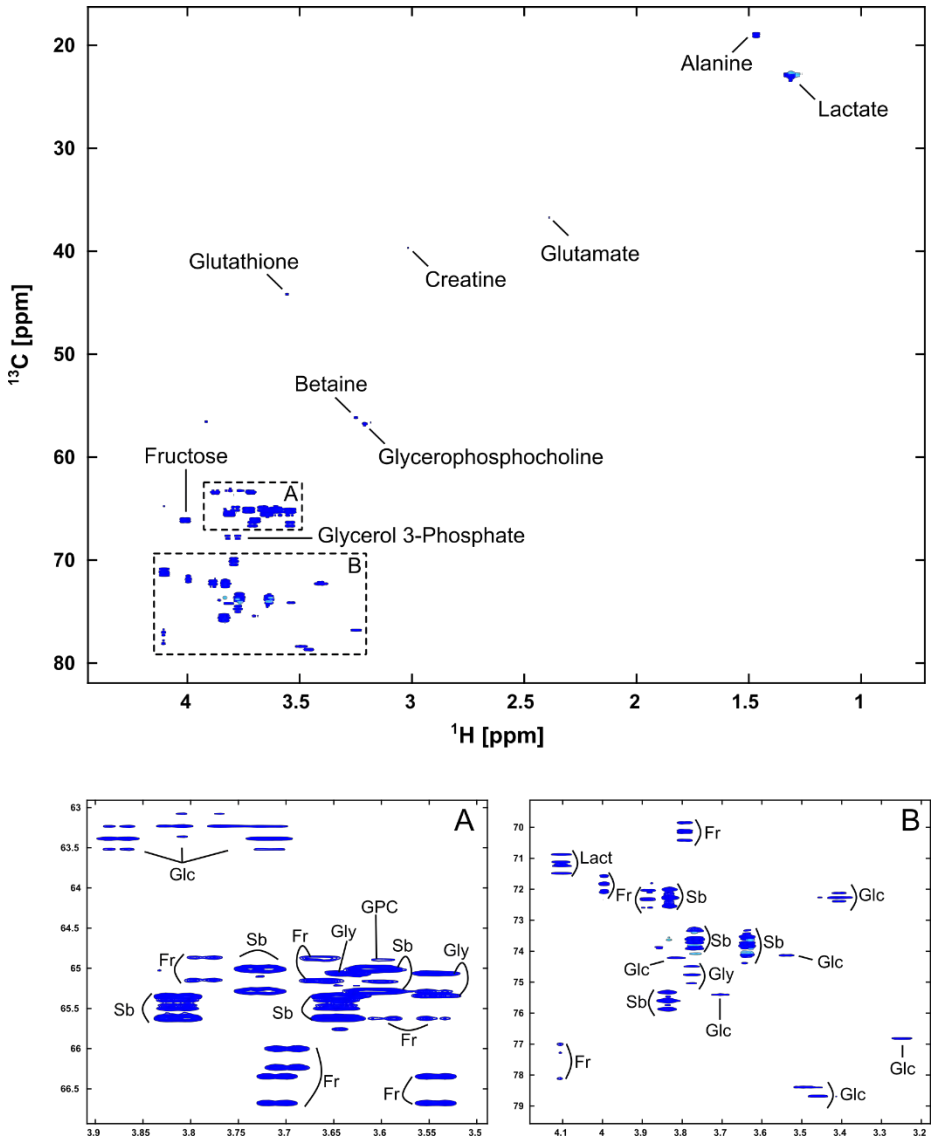

Figure 6. 6 – Representative ^{1}H-^{13}C-HSQC spectrum of a control ALD liver perfused with [U-^{13}C] fructose for one hour. A and B are augmented spectral regions from the spectrum on top. The abbreviations indicate Glc Glucose, GPC Glycerophosphocholine, Fr Fructose, Sb Sorbitol, Gly Glycerol and Lact Lactate.

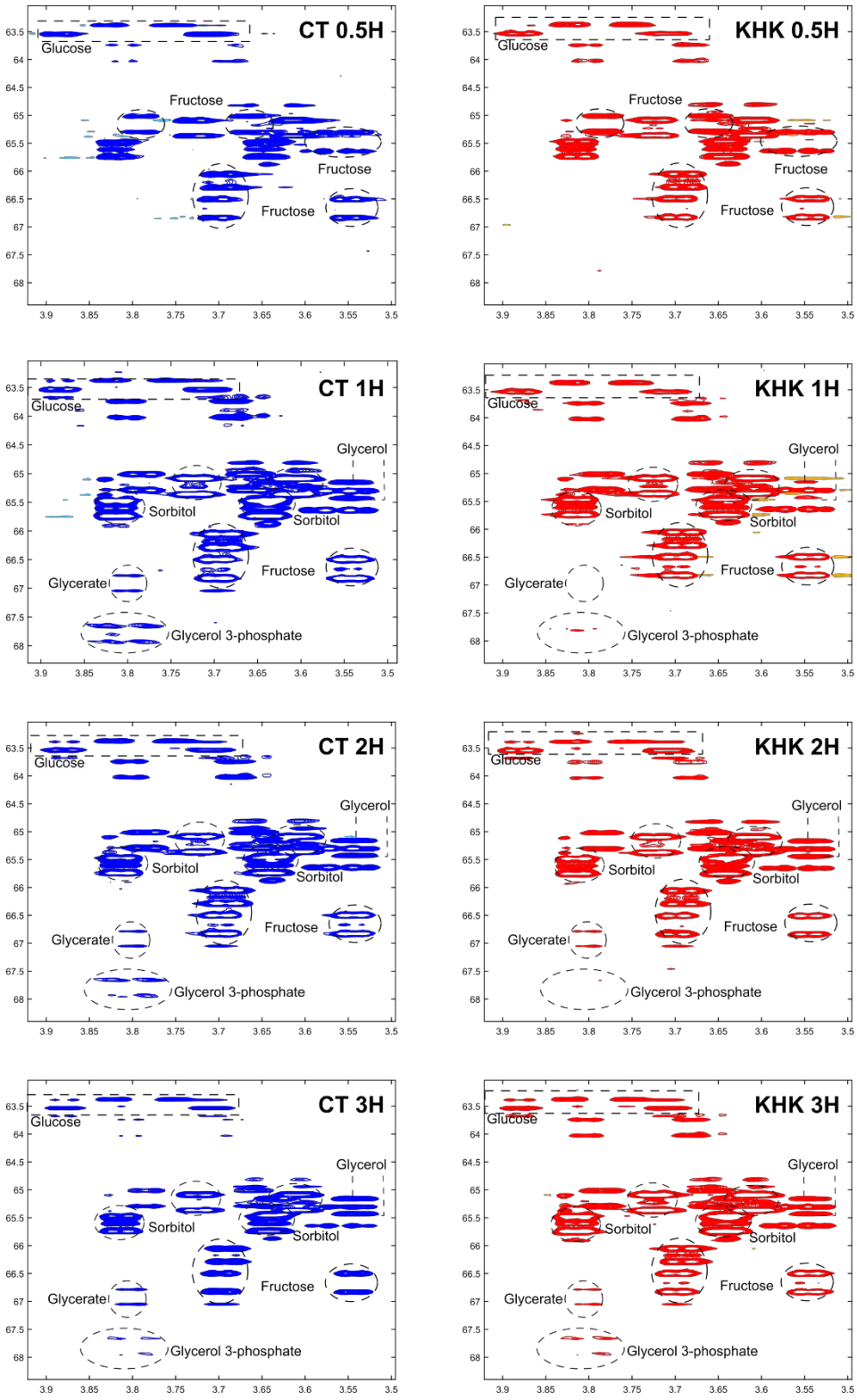

Figure 6. 7 – ^{1}H-^{13}C-HSQC spectra from control (CT) and KHK-inhibited (KHK) human liver wedges for the indicated periods (0.5 to 3 hours). Peak assignments are indicated by hashed lines and circles.

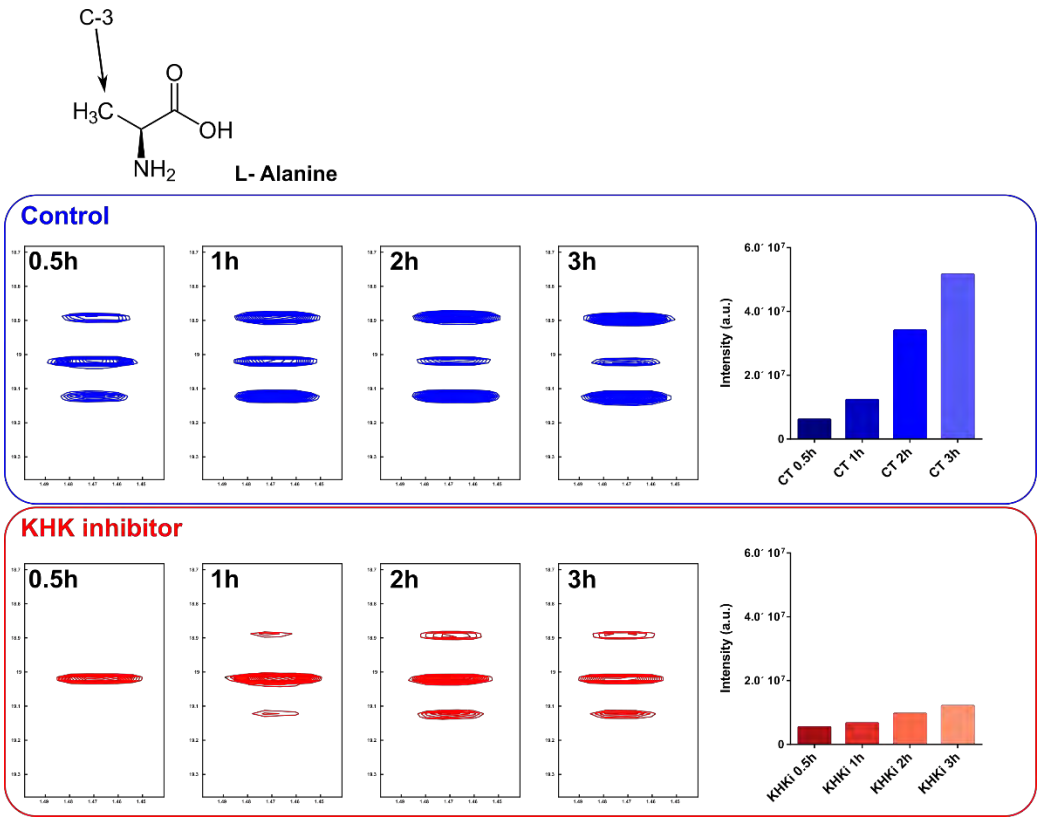

Figure 6. 8 – ^{1}H-^{13}C-HSQC spectral region of alanine carbon-3 in control samples (blue) and in KHK inhibited samples (red). Bar graphs depict the peaks intensities at all time-points. In an ^{1}H-^{13}C-HSQC spectrum, the central peak represents the natural abundance of ^{13}C in alanine carbon-3, while the outer peaks arise from the coupling to the adjacent ^{13}C in carbon-3 and carbon-2, transferred from carbons of ^{13}C-labelled fructose.

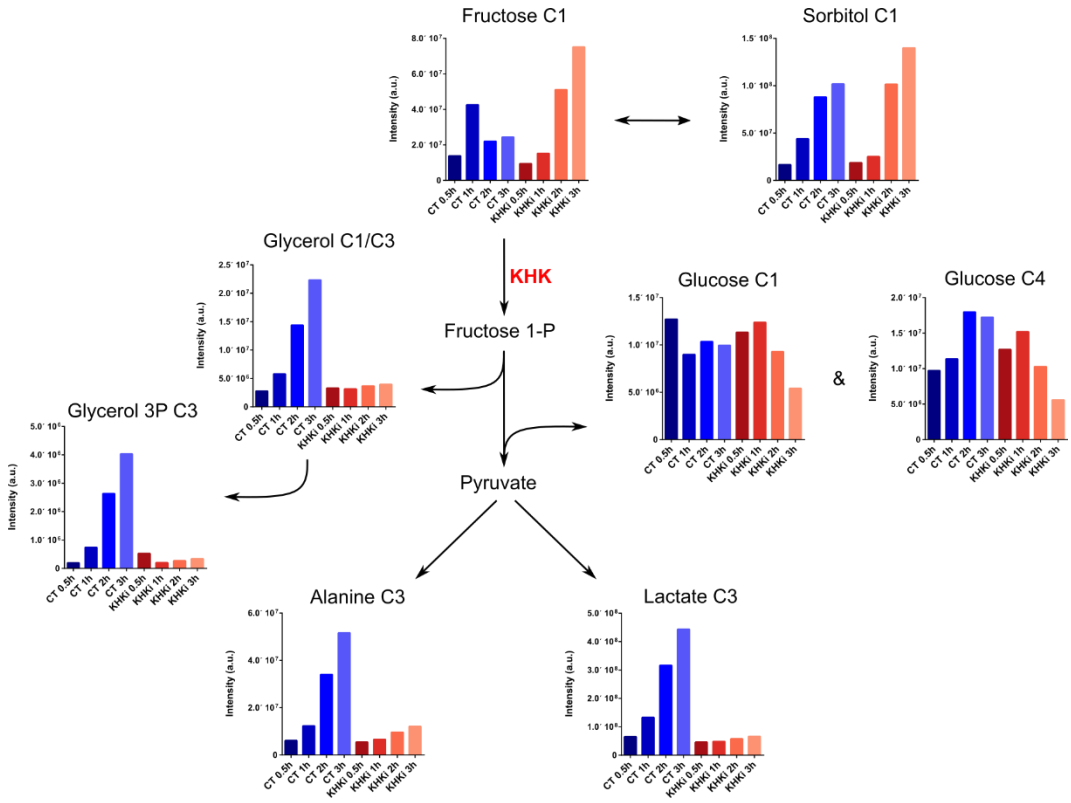

Figure 6. 9 – Diagrammatic representation of the major fructose metabolic pathway overlaid with peak intensities obtained from the integration of HSQC peaks for indicated metabolites in an ALD liver. Bar graphs represent control (blue) or KHK-treated (red) liver wedges over the experimental time course (0.5 to 3 hours).

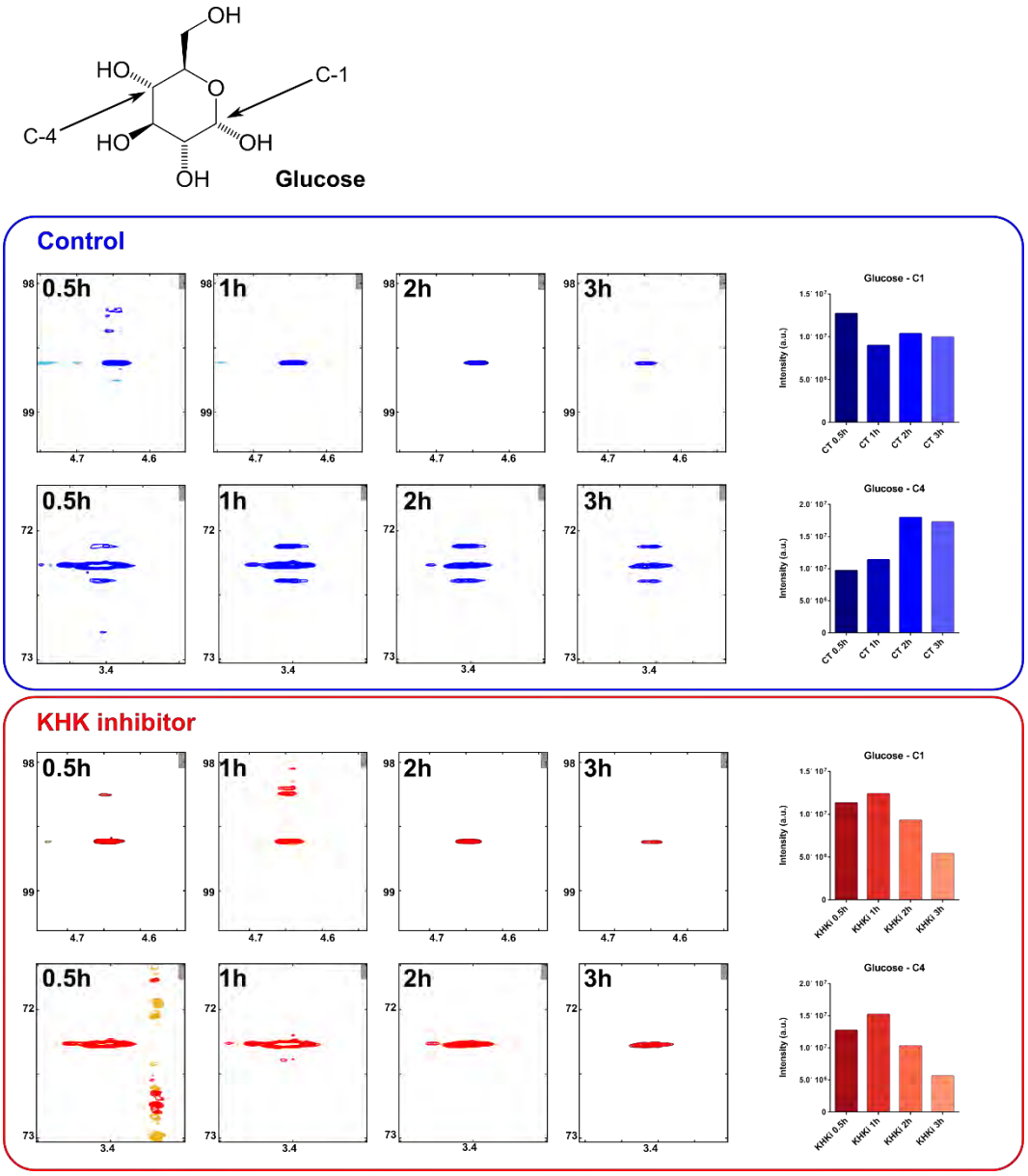

Figure 6. 10 – ^{1}H-^{13}C-HSQC spectral region of glucose carbon-1 (C1) and carbon-4 (C4) in control samples (blue) and in KHK inhibited samples (red). Bar graphs depict the peaks intensities at all time-points. The coupling patterns resulting from ^{13}C-incorporationin in neighbour carbons are only visible in control samples carbon-4, reflecting gluconeogenic activity.

To investigate the efficacy of the KHK inhibitor at different stages of NAFLD, the perfusion system was also tested using two fatty donor samples and a NASH liver. The experiments were carried out using the same protocol where the concentration of KHK inhibitor, time-points and liver wedges sizes were standardised (Figure 6. 11 to Figure 6. 13). Analysing the HSQC spectra (not shown) from these three livers for the duration of the time-course under control and KHK-treated samples, I observed that the effects were similar to the ALD liver results for most time points.

[U-^{13}C] fructose was incorporated by all liver wedges but is metabolised faster in control samples than in KHK inhibited samples. Similar to the ALD liver (Figure 6. 9), fructose levels in the KHK-inhibited wedges reflect increase in peak intensity along the time course. Similarly, increases in sorbitol levels are observed across all samples and support the idea that the KHK inhibition activates the polyol pathway to clear fructose intracellular levels thereby generating sorbitol as a metabolic product.

Relative to glycolytic substrates (alanine and lactate), ^{13}C-incorporation is observed for all samples under control conditions, with increasing rates throughout the experimental time. In the KHK-treated samples, even though the KHK inhibition did not stop fructose metabolism completely, rates of ^{13}C-incorporation in these metabolites are clearly reduced. Metabolism of fructose is then compromised, and less substrate is used for glycolysis.

In the fructolysis pathway branch that generates glycerol and glycerol 3-phosphate, the variation between samples is quite different. While in the first fatty donor liver the production of these metabolites is almost completely inhibited (Figure 6. 11), as in the ALD liver (Figure 6. 9), for the other two samples this is not as linear. The second fatty donor liver (Figure 6. 12) displays a good inhibition of glycerol production, when comparing with the control sample for the duration of the experiment, however the

glycerol 3-phosphate intensities are irregular. In the NASH liver (Figure 6. 13), the KHK inhibitor only seems to be effective for the first two hours. While glycerol levels seem to be low when compared with the control condition, suggesting a good inhibitory efficacy at all time-points, glycerol 3-phosphate levels at the 3rd hour of perfusion increases rapidly. Even so, it continues to be lower than levels in control livers without the KHK inhibitor.

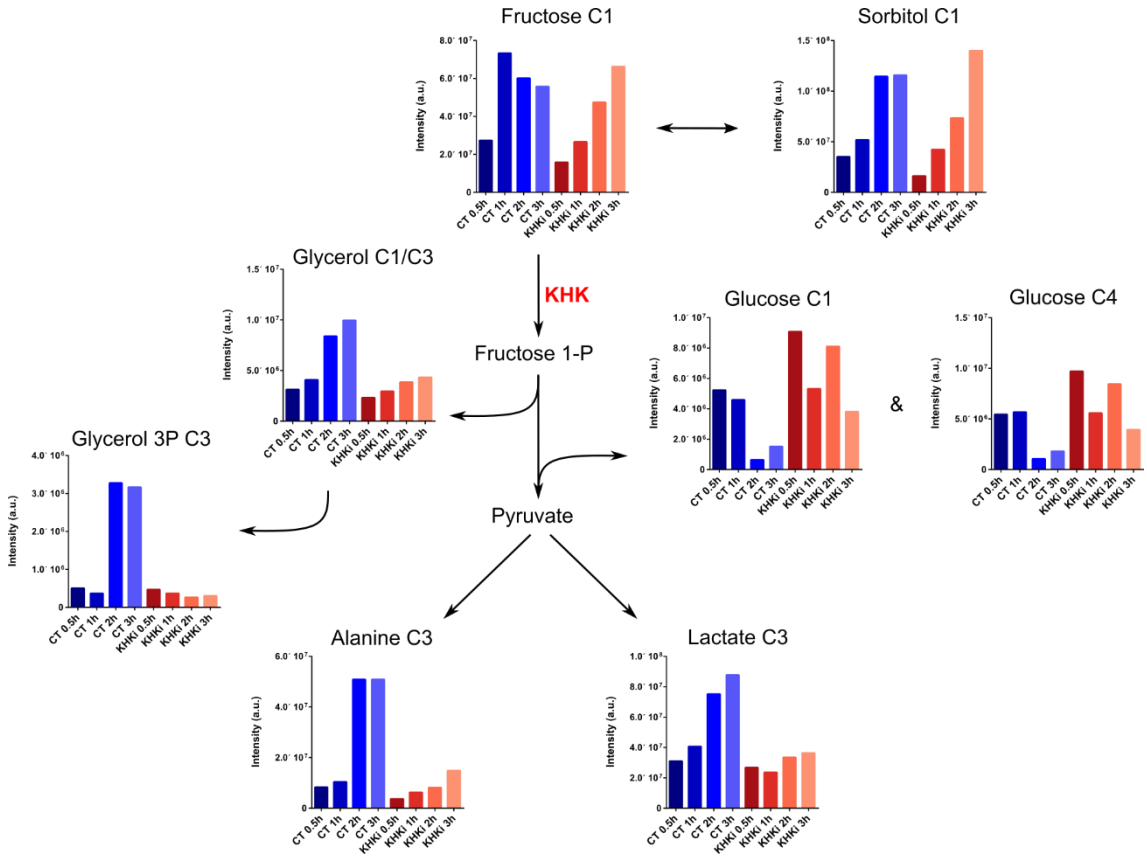

Figure 6. 11 – Diagrammatic representation of the major fructose metabolic pathway overlaid with peak intensities obtained from the integration of HSQC peaks for indicated metabolites in a fatty donor liver. Bar graphs represent control (blue) or KHK-treated (red) liver wedges over the experimental time course (30min to 3hours).

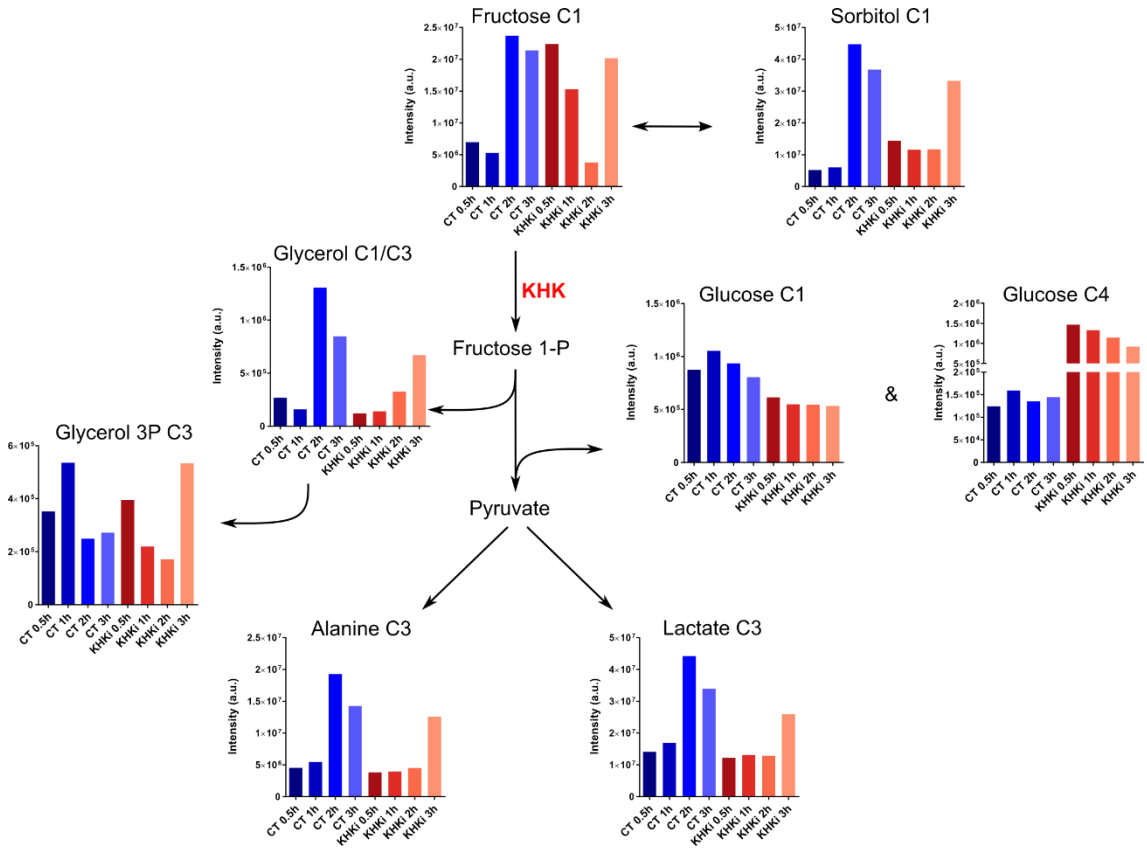

Figure 6. 12 – Diagrammatic representation of the major fructose metabolic pathway overlaid with peak intensities obtained from the integration of HSQC peaks for indicated metabolites in a fatty donor liver. Bar graphs represent control (blue) or KHK-treated (red) liver wedges over the experimental time course (30min to 3hours).

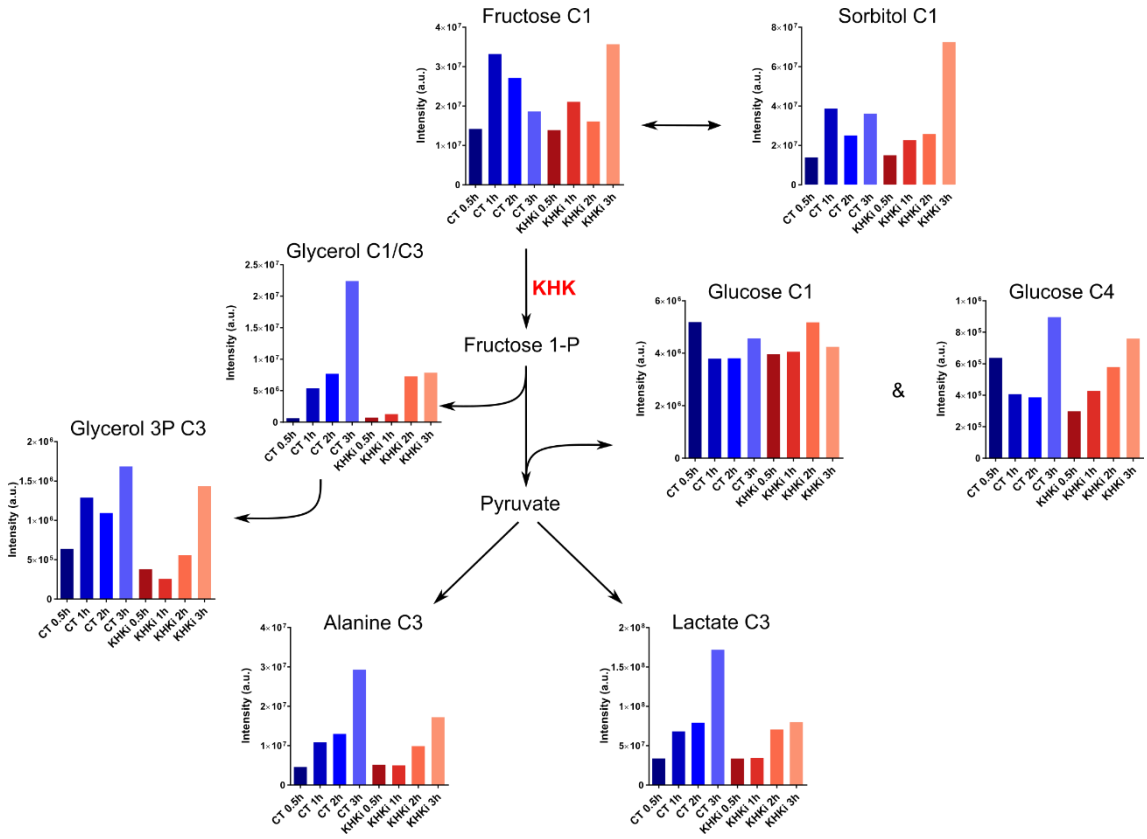

Figure 6. 13 – Diagrammatic representation of the major fructose metabolic pathway overlaid with peak intensities obtained from the integration of HSQC peaks for indicated metabolites in a NASH liver. Bar graphs represent control (blue) or KHK-treated (red) liver wedges over the experimental time course (30min to 3hours).

6.4. How does KHK inhibition impact fructose metabolism in the mouse model of NAFLD?

6.4.1. Overview

Following the positive outcomes from the perfusion system using human *ex vivo* livers to explore fructose metabolism and KHK inhibition, a murine *in vivo* approach was explored. The human liver model does not account for the whole complexity of NAFLD *in vivo*, especially regarding metabolic interactions with other organs. Therefore, a model that closely resembles the human disease was needed to evaluate the impact of KHK inhibition.

In this thesis, the mouse model of NAFLD developed and characterised in the previous chapter was used. Similar to the human model, ^{13}C-labelled fructose was used to determine how fructose is delivered to the tissue and how the KHK treatment would alter metabolism. For this, mice on a high fat diet for 21 weeks were weighed and dosed with KHK inhibitor at 15 mg/kg, 4 hours prior to culling. 1M [U-^{13}C] fructose was injected into the mice 30 minutes before they were euthanised, giving enough time for fructose to be absorbed, delivered and metabolised in the liver. Finally, while mice were under terminal anaesthesia, blood was collected to further determine liver enzymes levels.

6.4.2. Liver enzymes levels are reduced when KHK is inhibited

As liver enzymes are widely used as biomarkers of liver injury, their levels were measured at the end of the experiment. Only animals on a high fat diet with water supplemented with sugars were given a KHK inhibitor injection, as these had the most significant liver pathology. Even though the injection of the KHK inhibitor was only given four hours before culling the animals, a clear reduction in serum alkaline phosphatase (ALP) and transaminase (ALT and AST) levels was observed (Figure 6. 14 and Table XIII) after administration of inhibitor.

ALP levels were reduced in both groups when KHK inhibitor was given, however only the group with glucose sweetened water had a significant decrease (p <0.05). On the other hand, transaminase levels were significantly more affected by the KHK inhibition in the fructose group than in the glucose one. Enzyme activity of alanine transaminase (ALT) and aspartate transaminase (AST) were found to significantly decrease in the HFD + 20% fructose group (p <0.05 and p <0.01, respectively). In the glucose group, although a slight reduction was observed, it was not significant (Figure 6. 14).

Table XIII – Serum parameters in liver function tests in mice after 21 weeks on a HFD supplemented with 20% fructose or glucose-sweetened water, either with or without injection of the KHK inhibitor (KHKi) before culling.

GROUP	ALP U/L	ALT U/L	AST U/L
HFD + 20% Fru	117.0 ± 20.5	547.1 ± 352.0	458.69 ± 179.3
HFD + 20% Fru + KHKi	70.5 ± 17.8	128.3 ± 44.2	147.0 ± 57.5
HFD + 20% Glc	135.0 ± 46.4	274.9 ± 96.9	215.1 ± 97.3
HFD + 20% Glc + KHKi	68.3 ± 13.5	201.75 ± 37.2	160.5 ± 42.5

Note 8 – n = 4 mice per group and values represent mean ± standard deviation.

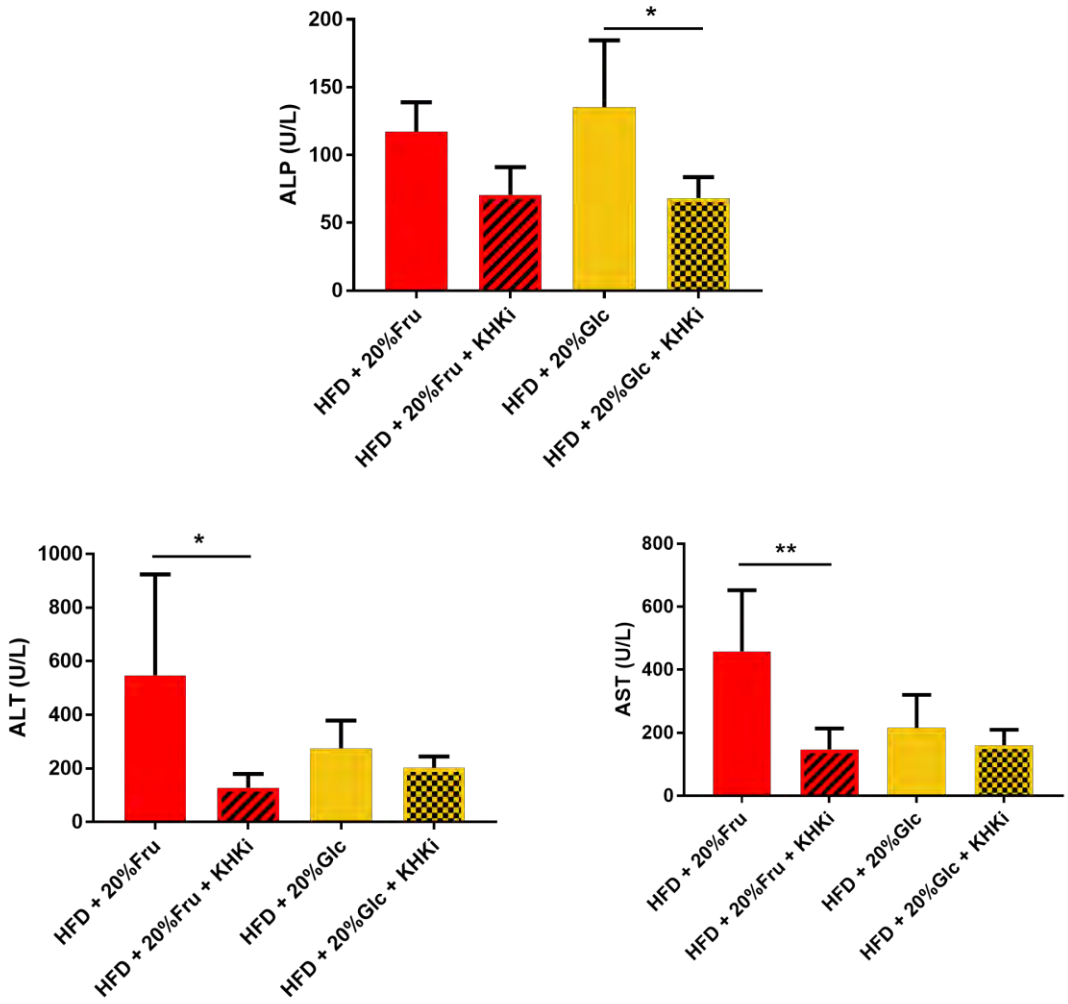

Figure 6. 14 – Blood biochemistry reveals a reduction in liver enzymes of mice on a high fat diet for 21 weeks, when they receive an i.p. injection of KHK inhibitor four hours before culling. (n=4-8 mice per group, and bars represent mean ± standard deviation and *p*-values as follows: *$p<0.05$, **$p<0.01$, ***$p<0.001$).

6.4.3. KHK-treated animals have reduced fructose metabolism

To replicate the pharmacological inhibition of KHK in the human experiments, mice fed a high fat diet for 21 weeks were given a single dose of KHK inhibitor via intra-peritoneal injection. Also, additional injection of [U-^{13}C] fructose has permitted the study of metabolic changes based on ^{13}C labelling patterns in response to KHK inhibition. Using 2D ^{1}H-^{13}C-HSQC NMR spectra, we were able to identify ^{13}C-enrichments in intermediates of glycolysis such as glucose, alanine and lactate, TCA cycle intermediates succinate, glutamate and glutamine, as well as fructolysis intermediates glycerate and sorbitol.

In Figure 6. 15, we can see that mice on a HFD + 20% fructose sweetened water that received an injection of [U-^{13}C] fructose display ^{13}C-labelled intermediates in the liver as shown in the previous chapter. More importantly, when mice were treated with the KHK inhibitor, we can see the appearance of signals from labelled fructose and sorbitol, which under normal conditions were not present, as well as the loss of the glycerate peaks. A similar trend was observed for mice on a HFD + 20% glucose, where there is a recovery of fructose peaks and accumulation of sorbitol, as shown in Figure 6. 16.

Figure 6. 17 shows the quantification of the signal intensities obtained from the HSQC spectra for both groups and corresponding ratios of ^{13}C-incorporation. A noteworthy increase in the fructose signal was observed for animals treated with the KHK inhibitor, especially for animals with fructose supplementation (p <0.01). Although not statistically different, sorbitol peaks also display a rise in intensity when compared to untreated animals in both diets. All the remaining labelled metabolites identified in the HSQC spectra were quantified and revealed a reduction in ^{13}C-incorporation when KHK was inhibited. The most interesting decrease is seen at the glycerate level, where KHK inhibition caused a four-fold reduction in the incorporation of ^{13}C. This final ratio is equal

to 1, which is usually obtained from natural abundant metabolites. This means that the remaining glycerate in these samples may derive from the basal liver metabolism in HFD-fed mice and not from metabolism of the labelled fructose. Glycolysis and TCA cycle intermediates have revealed less impressive reductions at the level of ^{13}C-enrichments, however the trend for metabolic decline is reflected in glucose, lactate, alanine, glutamate, glutamine and succinate levels.

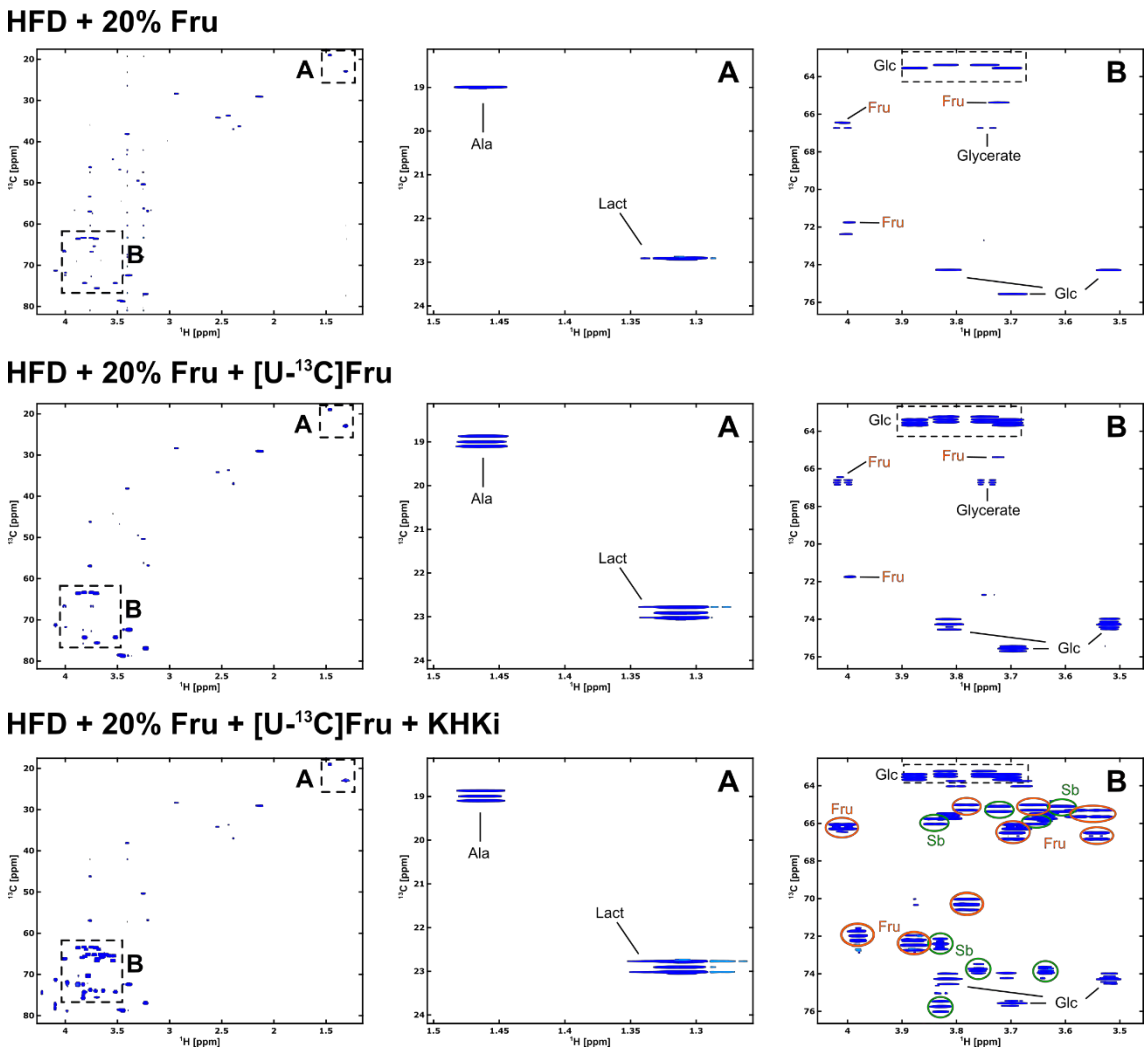

Figure 6. 15 – Representative HSQC spectra of HFD + 20% fructose fed animals, either in control conditions or when given an injection of 1M [U-^{13}C] fructose. Mice that received ^{13}C-labelled fructose were also divided into two groups, with half of them being given an injection of the KHK inhibitor. Designations of metabolites are: Fru fructose, Glc glucose, Ala alanine, Lact lactate, Sb sorbitol. (n= 4 independent samples from mice livers per group).

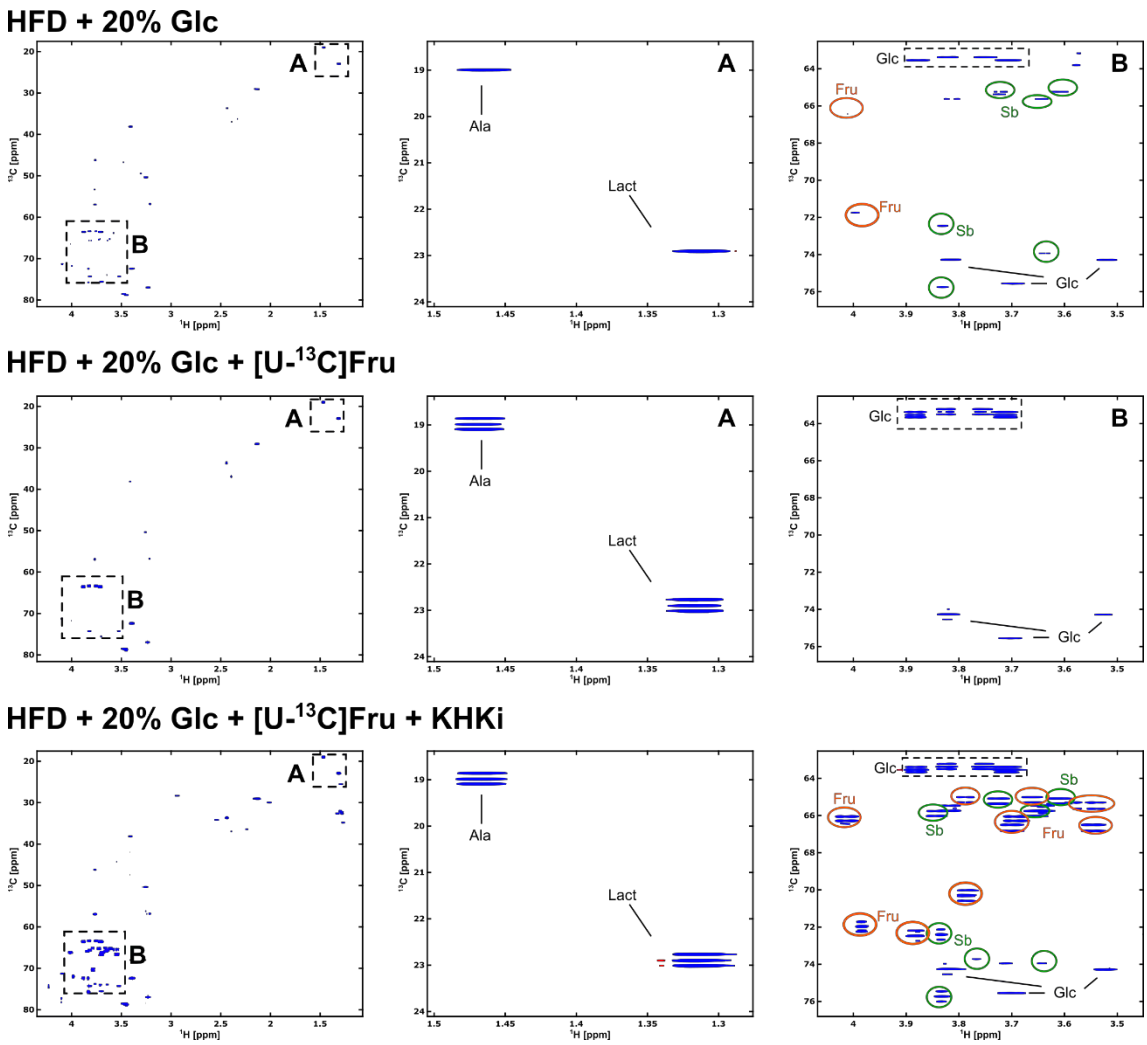

Figure 6. 16 – Representative HSQC spectra of HFD + 20% glucose fed animals, either in control conditions or when given an injection of 1M [U-^{13}C] fructose. Mice that received ^{13}C-labelled fructose were also divided into two groups, with half of them being given an injection of the KHK inhibitor. Designations of metabolites are: Fru fructose, Glc glucose, Ala alanine, Lact lactate, Sb sorbitol. (n= 4 independent samples from mice livers per group).

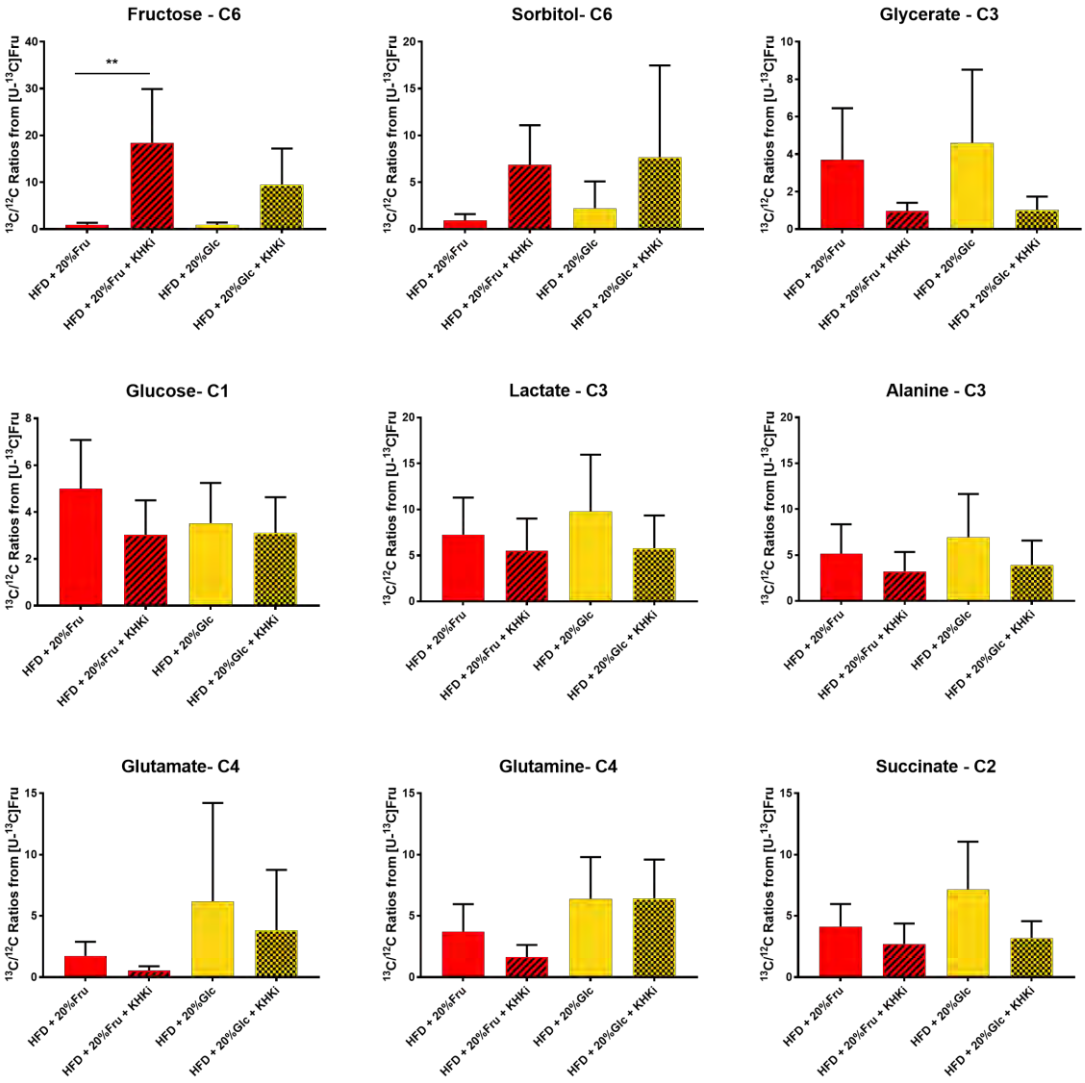

Figure 6. 17 – Ratios of ^{13}C-incorporation in fructolysis intermediates from [U-^{13}C] fructose in mouse livers with or without injection of KHK inhibitor *in vivo*. (n = 4 independent samples from mice livers per group. Bars represent mean ± standard error of the mean and *p*-values as follows: *p<0.05, **p<0.01).

6.1.Discussion

6.1.1. KHK hepatic expression

Fructose has been considered a driver of obesity, metabolic syndrome and fatty liver disease. This could correlate with the reported upregulated expression of the major fructose transporter GLUT-5 in disease, namely in alcoholic liver disease (ALD) and non-alcoholic steatohepatitis (NASH) [2,24]. Once transported into the cell, KHK is the main enzyme responsible for the metabolism of fructose. We were able to provide evidence that the ketohexokinase is abundantly expressed in liver cells, mostly in the cytoplasm of hepatocytes. Moreover, the predominant expression of the KHK-C isoform in the liver was confirmed in livers with simple steatosis, but also ALD and NASH [302,305]. Li *et al* [307] have also shown the expression of KHK in NASH patients, especially the KHK-C isoform. However, they also reported a shift occurring between isoform C to A in hepatocytes, which was usually seen in severe NASH patients developing HCC. This fits with our expression as highest prevalence of the C isoform was seen in fatty donor material rather than end stage NASH samples. In agreement with this, Lanaspa *et al* [303] used fructose-sensitive mice to show that tissues expressing the KHK-C isoform and not A are able to confer protection against impaired fructose metabolism. Thus our samples from fatty donor livers may have increased KHK-C to deal with dietary circulating fructose.

Inversely to what Ouyang *et al* [301] has shown, the expression of KHK was not directly correlated with the progression of NAFLD. In our study, patients with simple steatosis (NL) display higher total protein expression than cirrhotic patients (ALD and NASH). However, the reduction in total KHK protein in cirrhotic patients may simply relate to decrease in hepatocyte viability as well frequency due to the presence of fibrotic areas in the liver. Thus, the proportional area of hepatocytes decreases. In diseased livers, tissue

injury triggers inflammation and hepatocellular death, which will play a role in the exacerbation of impaired liver function. Cell death in hepatocytes contributes to fibrogenesis and carcinogenesis [309]. Therefore, depletion of total KHK in NASH livers when compared with simple steatosis might be a mere indication of hepatocyte death rather than quantitative protein expression per cell and this would fit with our RNA and staining data.

6.1.2. Human liver perfusion

The development of a new human liver perfusion assay has permitted detailed study of metabolic processes. This system yielded important mechanistic information regarding the consequences of fructose overload in non-alcoholic fatty liver disease. I was also able to provide valuable proof-of concept pre-clinical data to support use of KHK inhibition as a strategy in NAFLD patients.

By adding ^{13}C-labelled fructose into media perfused through intact human *ex vivo* liver wedges, I was able to confirm that fructose accumulates intracellularly and that it activates both glycolytic and lipogenic pathways. While fructose accumulation led to the enhancement of glycolysis seen by the production of alanine and lactate, *de novo* lipogenesis (DNL) was enabled by the unregulated generation of glycerol and its derivatives.

Increased consumption of dietary fructose goes hand in hand with NAFLD incidence, and several studies have demonstrated that fructose uptake is able to induce a higher expression of enzymes linked to the first steps of fructose metabolism; these include KHK and aldolase B, as well as glycolytic enzymes phosphofructokinase 1 and pyruvate kinase [26,74,310]. In control conditions, alanine and lactate levels rise following fructose exposure of my tissue samples, which is in agreement with a ^{1}H MR spectroscopy study in patients with NAFLD [311]. Here, assessment of hepatocellular metabolism of alanine and lactate has revealed potential for biochemical discrimination between simple steatosis and NASH, especially when combined with triglyceride concentrations.

High fructose accumulation in hepatocytes also leads to excessive production of acetyl-CoA in mitochondria, which enters the TCA cycle to form citrate and then it can be released in the cytosol to induce DNL [312]. *De novo* lipogenesis stimulated by carbohydrates such as fructose, is mainly mediated by ChREBP and SREBP-1c, and

these transcription factors regulate the expression of several lipogenic enzymes in the liver. According to some recent studies [74,247,313], fructose can induce hepatic expression of these factors in patients with fatty liver disease, leading to the upregulation of lipid synthetic and storage enzymes which contribute to lipogenesis. Moreover, high TCA cycle activity was detected in NAFLD patients [198,199], leading to increased oxidative stress in mitochondria and contributing to the inflammation during disease progression [314].

In order to investigate the potential of targeting fructose metabolism to modify hepatic steatosis and improve fatty liver disease outcome, ketohexokinase activity was pharmacologically inhibited. I was able to demonstrate that fructose metabolism in the liver was severely affected when KHK was inhibited. As expected [26], reduced levels of alanine, lactate and glycerol were seen in the KHK-treated samples. Moreover, when KHK is inhibited and fructose metabolism is impaired, intracellular levels of fructose were elevated and the polyol pathway was activated. Thus, sorbitol levels have risen in these samples suggesting that KHK inhibition may serve as a useful target for fatty liver disease treatment.

Interestingly, the analysis of HSQC spectra from all perfused livers revealed that the KHK inhibition was equally effective for all liver disease stages. Even though the donor livers with simple steatosis had higher levels of KHK protein expression than cirrhotic livers, the impact of KHK inhibition on fructose metabolism was comparable across all tested samples. This could be relevant for clinical therapy as my data suggests that KHK inhibition could be employed even in the most progressive stages of liver disease, without reducing its efficacy.

However, some odd exceptions were seen in this study, namely the 2-hour time-point of the donor liver in Figure 6. 12 for fructose. This could be explained by normalisation errors of HSQC peak intensities. As explained in chapter 2 (materials and methods), 1D NOESY total spectra area values are used to normalise signal intensities from HSQCs to account for variability in the metabolite pools from each tissue sample, but if variations are too great then this method is no longer the best approach. Furthermore, even though metabolite levels of glycerol seem to be lower in KHK-inhibited samples at all time points, glycerol 3-phosphate levels seem to increase after 3 hours for both the donor and NASH livers (Figure 6. 12 and Figure 6. 13). Even though these levels are still lower than the matched control samples, this information is vital when considering the time course of inhibitory action and efficacy. The concentration of KHK inhibitor was maintained throughout all experiments, but drug efficiency was dependent on liver wedge weight and healthy/damaged hepatocyte ratio. Therefore, when translating these findings into human patient studies, the dose and concentration of KHK inhibitor should be adapted according to the level of steatosis and fibrosis of the liver tissue, reflecting the extent of healthy hepatocytes in the liver. Also, multiple dosing schemes should be considered to deliver the correct concentration and preserve efficiency of KHK inhibition at various time frames. This would form part of the Phase 1 and 2 studies required to secure approval for use of these therapeutics.

In summary, my NMR-based metabolomic analysis highlighted the hepatic metabolic consequences of fructose administration in an intact human tissue setup for the first time. I have shown that pharmacological inhibition of KHK can be useful to modify fructose metabolism, reducing hepatic lipogenesis in patients with NAFLD. Nevertheless, analysis of a larger number of samples is needed to confirm these findings, together with an improved optimisation of inhibitor concentration for specific liver disease stages.

6.1.3. *In vivo* inhibition of KHK

Using an *in vivo* model of NAFLD and the pharmacological inhibition of KHK, I was able to demonstrate that KHK activity has a great impact on systemic metabolism. As demonstrated in the previous chapter, animals on a high fat diet with access to water supplemented with sugar reveal severe transaminitis and steatosis at the end of a 21-week experiment. By giving an injection of KHK inhibitor prior to culling the mice, an impressive decrease in transaminase levels was observed. KHK inhibition was more effective for animals with fructose supplementation than glucose, which reflects the different metabolic disturbances triggered by these carbohydrates [26,315].

Alanine transaminase (ALT) and aspartate transaminase (AST) are present in high concentration in liver cells and act to catalyse the transfer of an amino group from alanine and aspartate, respectively, to a α-keto group. These reaction products are glutamate and either pyruvate or oxaloacetate, which are intermediates in major metabolic pathways important to maintain energy homeostasis. ALT and AST are usually elevated in serum in response to hepatocyte injury, but since they have diverse physiological functions aside from amino acid metabolism, decreases observed following KHK inhibition should be carefully interpreted [39,81].

Serological ALT and AST levels reflect the level of these liver enzymes that are spilled into the blood stream. Therefore, this rapid change could be related to the downregulation of liver enzymes or even an indicator of the improvement of hepatocyte status. Healthier cells will leak less enzymes into the serum, which will ultimately alter the level of circulating liver enzymes [81,82]. In this study, histological assessment of the liver tissue has revealed that animals treated with KHK inhibitor had a similar morphology as the control samples. The degree of necrotic hepatic cells found in control samples was comparable with KHK inhibited samples, which indicates that detected

changes are due to metabolic alterations rather than a consequence of dramatic reduction in hepatocyte necrosis. To support this, from a single dose of KHK inhibitor, liver levels of alanine and TCA cycle intermediates were effectively reduced, as confirmed in the 2D NMR analysis. Thus, even in a short period of time (4 hours), ALT and AST reactions could be regulated and detected according to fructose and glucose metabolic product availability.

Nonetheless, the ease by which liver function tests results can be altered without evident amelioration of hepatic inflammation and steatosis is interesting. As previously described [245,303,316], KHK knockdown animals demonstrate lower levels of transaminases, which is usually accompanied by reductions in inflammation and steatosis. The effectiveness achieved with the pharmacological inhibition of KHK in just a few hours is quite promising in terms of liver enzyme amelioration, but information regarding systemic metabolism would be tremendously helpful. Metabolic analysis of the serum would provide a better understanding of the underlying metabolic mechanisms responsible for these alterations, and identification of substrates and products following KHK inhibition in the serum would allow us to confirm why transaminases respond so fast.

To further investigate the metabolic fate of [U-^{13}C] fructose when KHK is inhibited, NMR analysis was carried out. My results have shown that intermediates of glycolysis and fructolysis are reduced in KHK-treated mice, demonstrating that a single dose of KHK inhibitor is able to induce an overall reduction of fructose metabolism *in vivo*. Despite the significant impact of KHK inhibition in fructose and sorbitol levels, intermediates from glycolysis and the TCA cycle were not as substantial.

Interestingly, some studies have demonstrated that the consumption of carbohydrates and polyols can promote the growth of bifidobacteria and alter the microflora in healthy individuals [317–319]. Following pharmacological KHK inhibition, the production and accumulation of sorbitol can become relevant for NAFLD patients. The shift in the microbiome towards the production of beneficial prebiotics could help resolve inflammation that typically arises from the gut-liver axis interaction. Although this would not be the case in the time frame of our murine experiments.

Since other regulatory mechanisms are involved in the production of alanine and lactate, as well as TCA cycle intermediates, it is not a surprise to see a less significant decrease in these metabolites when KHK was inhibited. Considering that other substrates can feed glycolysis and enter the TCA cycle, additional contributions from alternative pathways should not be overlooked. Glucose can be generated from several sources including dietary components and glycogen storage, amino acids can be obtained through the breakdown of proteins and lipids can also enter different pathways depending on energy requirements [26,293,320]. Therefore, although an isotope tracer was used to follow fructose metabolism, in steatotic conditions there is a dysregulation in metabolic pathways that contribute to this energetic imbalance, as it was verified in the previous chapter.

As I only analysed metabolites in the liver, there is also the possibility that I am not accurately accounting for the total amount of ^{13}C-labelled metabolic products. Some studies have also shown the importance of the kidney and intestine in metabolising circulating fructose [297,304,321,322]. For example, Jang *et al* [297] demonstrated that the intestine plays a significant role in the clearance of fructose, converting fructose to glucose and other circulating metabolites before reaching the liver. This shielding capacity can be interrupted following a high dose of fructose, impacting hepatic function.

In another study, Miller *et al* [304] have shown that even when KHK is knocked down in mice, residual metabolism of fructose in these animals can be observed. Nevertheless, KHK KO animals had reduced liver weight and triglyceride levels even when they had a dietary fructose challenge. Hence, these studies together with our results provide further confirmation that KHK manages sugar and lipid metabolism in a tissue-specific manner.

In conclusion, I have demonstrated how fructose administration affects hepatic metabolism using NMR-based metabolomics. Also, human and murine models have been used to support the benefit of inhibiting ketohexokinase activity in order to attenuate diet-induced hepatic steatosis and protect against fructose toxicity in patients with NAFLD.

CHAPTER 7

CONCLUSIONS AND FUTURE WORK

7. Conclusions and future work

7.1. Summary of main findings

Non-alcoholic fatty liver disease affects a large portion of the world population and its incidence and prevalence are increasing to epidemic proportions. However, methods for accurate diagnosis and prediction of disease progression are still not optimal. Hence, the main goal of this thesis was to determine the hepatic metabolic fingerprint at different stages of NAFLD, since a better understanding of underlying mechanism will accelerate pre-clinical discovery.

At first, the best method for NMR metabolic profiling based on *in vitro* and *ex vivo* samples was optimised, and sample preparation and improvements in NMR technology were tested. Analysis of both mammalian cell line (HuH7) and human hepatic tissue revealed that metabolite extraction methods and tracer-based fluxes should be adapted according to the specific type of cell in a study [120]. To obtain the maximum number of metabolites from a proliferative cell, metabolism was stopped between 48 and 72 hours after plating, which provided the best time frame to study metabolic adaptations that occur during disease progression. Additionally, the feasibility of using ^{13}C-glucose and ^{13}C-fructose was assessed for tracer-based studies using both biological systems (cells and tissue), demonstrating that both are easily incorporated and metabolised in the hepatocytes.

Furthermore, developments in NMR technology were assessed and the use of cryoprobes led to improvements of at least 4 to 10 fold in signal to noise ratio in NMR spectra of sucrose and hepatocytes, and these were further increased when a smaller probe (1.7 mm cryoprobe) was used. Also, the use of non-uniform sampling schedules to acquire faster 2D HSQC spectra confirmed that acquisition times can be significantly reduced without compromising the resolution in the indirect dimension.

Next, the optimised methodology was validated using an *in vitro* model of steatosis, where HuH7 cells were exposed to a high concentration of oleic acid (2 mM) to mimic the effect of lipid accumulation in fatty liver disease. In the first 24 hours a good cell viability was maintained (80-90 %) and macro- and micro-steatosis was observed. My optimised 1D ^{1}H NMR spectroscopy workflows were applicable to these samples, but interestingly it didn't show gross alterations. This shows how liver cells can accommodate short term changes in metabolic loading by increasing carbohydrate and lipid consumption and export to maintain homeostasis. Hence, these studies did also show that there were acute changes related to energy metabolism (higher ATP), and trends for increased amino acid levels and glycolysis rate in cells supplied with excess oleic acid.

Nevertheless, the use of a single layer hepatocyte culture does not provide the best model to study the changes that occur during the human progression of human disease since it does not account for interactions with other cells and 3D structure that exist in a liver. Thus, *ex vivo* samples were analysed to understand how whole liver metabolism adapts during NAFLD progression and how this compared to standard *in vitro* models. Here, after an H&E analysis to confirm the morphological appearance and class identification of these specimens, NMR analysis of both polar and lipid layers was performed. Metabolic profiles of the liver tissue were obtained for different NAFLD stages and, while normal livers resembled steatotic liver metabolism with only a few changes, NASH samples had the most significant alterations. Key metabolites of glycolysis were increased in the context of NASH, especially alanine, lactate and ATP, together with increases in TCA cycle intermediates, glutamate, fumarate, malate and aspartate. Regarding the lipid metabolism, the organic phase fraction did not show significant alterations, although a high number of species were identified.

As these models were still limiting to understand the precise metabolic mechanisms involved in NAFLD progression over time in the same individual, an *in vivo* murine model was used to investigate physiological, metabolic and gene expression alterations that occur during weight gain, hepatic steatosis and inflammation after prolonged exposure to HFD with and sugar supplementation. Using numerous techniques, including flow cytometry, qPCR and NMR spectroscopy, my main findings highlighted the inter-related changes in liver enzyme levels and metabolic changes in carbohydrate and lipid metabolism. The animal model was representative of the human disease as I was able to demonstrate increased hepatic steatosis in mice after HFD consumption, accompanied by transaminitis, obesity and accumulation of subcutaneous fat. The addition of sugars to the HFD led to an aggravated phenotype, especially when fructose was used. Importantly, a resultant inflammatory response to this hepatocellular stress was activated in these animals, as shown by inflammatory cell infiltration in the H&E analysis, and flow cytometry data which revealed an increase in hepatic lymphocyte and myeloid populations as injury progressed.

Mice with access to the sweetened-water also displayed a selective enhancement of the glycolytic pathway and TCA cycle, as well as increases in nucleotides. Tracer-based studies using [U-^{13}C] fructose allowed me to follow its fate *in vivo*, and production of glycerol intermediates needed for de novo lipogenesis was observed for these obese mice. This was also accompanied by changes in gene expression for genes involved in cholesterol and lipid metabolism. Thus, my accumulated data from the fructose fed animals highlights the utility of this models as a tool for preclinical biomarker discovery and testing of novel therapeutic interventions that may be useful in the context of human medicine.

Finally, to support the preclinical value of this model I tested use of a ketohexokinase inhibitor as a potential therapeutic strategy in NAFLD patients. Here both the human *ex vivo* perfusion system and the *in vivo* model of NAFLD were applied. Key metabolic benefit of using a ketohexokinase inhibitor was documented for both systems, as fructose metabolism was proven to be significantly reduced, with decreases seen in both glycolytic and lipogenic intermediates, as well as lower transaminases levels in serum. Hence, in an environment where increased rates of NAFLD in the human population are attributable at least in part to increased fructose content in food, I have not only been able to describe the mechanisms by which this leads to steatohepatitis, but have also shown the potential of targeting this pathway therapeutically.

In summary, NMR-based metabolomics approaches were proven to be relevant for the study of metabolic adaptations during disease progression, improving understanding of molecular mechanisms involved in steatosis and inflammation. Application of metabolomics, together with biological methods such as H&E analysis, qPCR and flow cytometry, can be very useful for the diagnosis and staging of liver disease, and help identifying new biomarkers and therapeutic strategies.

7.2. Future work

Even though I have accomplished several specific aims of this project, many questions still remain to be answered. As I believe a good project is never really finished, a natural progression of this work would be to expand the *in vivo* model and the *ex vivo* perfusion system, to allow me to test the long term efficacy of targeting ketohexokinase in established disease. Here, for example, several weeks-long treatments with the inhibitor could be considered in a weekly basis, given at the end of the dietary feeding protocol to see if long term physiological and pathological improvement in disease scores are achievable. This would be more directly applicable to the likely human presentation and treatment of disease.

For the mouse model of NAFLD, further experiments using serum or analysing kidney, intestine and pancreas tissues could shed more light on the relative contribution of specific and multiple extra-hepatic organs to fructose absorption and metabolism. This could be achieved by performing NMR-based metabolomics, to obtain a more complete picture of the mouse metabolome during disease progression. The use of labelled tracers would also allow tracing of the build-up of ^{13}C-enriched metabolic products and their fate *in vivo* by observing flux rates within the different organs.

To validate the application of the *ex vivo* perfusion system in pre-clinical studies, research should be carried out in additional livers, involving a broader range of liver diseases. For example, assessment of metabolic profiles, and response to pharmacological inhibition in different liver diseases/stages would be an important part of the preclinical work up for securing FDA approval for a new drug. Information on how a drug works in a diseased *vs* normal liver is normally generated using mammalian models and there are clear incidences where such testing has failed to predict efficacy (or detrimental effects) in subsequent human trials. In my example, the application of

this system to establish the optimal concentration for ketohexokinase inhibitor while avoiding toxicity would be of great help when trying to translate these findings to human clinical studies. Further research could also be conducted to determine the length of effectiveness of the inhibitor, as well as multiple dosing strategies to establish the ideal therapeutic intervention and efficiency. Additionally, the application of ^{13}C-labelled precursors *in vivo* is safe, and ^{13}C MRI is a functional medical imaging technique that could be applied to investigate cellular metabolism *in vivo* in a non-invasive manner.

7.3. Final remark

Increased prevalence of non-alcoholic fatty liver disease is a major problem worldwide, yet, advances in non-invasive approaches for disease detection and follow-up, as well as to establish proper therapeutic interventions are still lacking. Using a NMR-based technique I have developed new methodologies and added new mechanistic knowledge to increase understanding of NAFLD pathogenesis, providing mechanistic information about steatosis and inflammation, as well as carbohydrate and lipid metabolism. My work has also had direct clinical impact since I have also highlighted the clinical significance of a ketohexokinase inhibitor (see list of outputs) which may eventually be used in human patients.

Briefly, I believe my findings have important implications for future practice in the field of fatty liver disease and will contribute towards the study and development of effective therapeutics to treat NAFLD.

8. REFERENCES

(1) Liangyou, R. Energy Metabolism in the Liver. In *Comprehensive Physiology*; John Wiley & Sons, Inc.: Hoboken, NJ, USA, 2014; Vol. 4, pp 177–197.

(2) Karim, S.; Liaskou, E.; Fear, J.; Garg, A.; Reynolds, G.; Claridge, L.; Adams, D. H.; Newsome, P. N.; Lalor, P. F. Dysregulated Hepatic Expression of Glucose Transporters in Chronic Disease: Contribution of Semicarbazide-Sensitive Amine Oxidase to Hepatic Glucose Uptake. *Am. J. Physiol. Gastrointest. Liver Physiol.* **2014**, *307* (12), G1180-90.

(3) Rodes, J.; Benhamou, J.-P.; Blei, A.; Reichen, J.; Rizzetto, M. *The Textbook of Hepatology: From Basic Science to Clinical Practice*; Blackwell, 2008.

(4) Taub, R. Liver Regeneration: From Myth to Mechanism. *Nat. Rev. Mol. Cell Biol.* **2004**, *5* (10), 836–847.

(5) Ebrahimkhani, M. R.; Neiman, J. A. S.; Raredon, M. S. B.; Hughes, D. J.; Griffith, L. G. Bioreactor Technologies to Support Liver Function in Vitro. *Adv. Drug Deliv. Rev.* **2014**, *69–70*, 132–157.

(6) Bilzer, M.; Roggel, F.; Gerbes, A. L. Role of Kupffer Cells in Host Defense and Liver Disease. *Liver Int.* **2006**, *26* (10), 1175–1186.

(7) Racanelli, V.; Rehermann, B. The Liver as an Immunological Organ. *Hepatology* **2006**, *43* (S1), S54–S62.

(8) Lalor, P. F.; Shields, P.; Grant, A. J.; Adams, D. H. Recruitment of Lymphocytes to the Human Liver. *Immunol. Cell Biol.* **2002**, *80* (1), 52–64.

(9) Van Herck, M. A.; Weyler, J.; Kwanten, W. J.; Dirinck, E. L.; De Winter, B. Y.; Francque, S. M.; Vonghia, L. The Differential Roles of T Cells in Non-Alcoholic Fatty Liver Disease and Obesity. *Front. Immunol.* **2019**, *10*, 82.

(10) Senoo, H. Structure and Function of Hepatic Stellate Cells. *Med. Electron Microsc.*

2004, *37* (1), 3–15.

(11) Kordes, C.; Sawitza, I.; Häussinger, D. Hepatic and Pancreatic Stellate Cells in Focus. *Biol. Chem.* **2009**, *390* (10), 1003–1012.

(12) 3.0, S. M. A. by S. is licensed under a C. C. A. SMART - Servier Medical ART - 3000 free medical images https://smart.servier.com/ (accessed May 25, 2019).

(13) Titchenell, P. M.; Quinn, W. J.; Lu, M.; Chu, Q.; Lu, W.; Li, C.; Chen, H.; Monks, B. R.; Chen, J.; Rabinowitz, J. D.; et al. Direct Hepatocyte Insulin Signaling Is Required for Lipogenesis but Is Dispensable for the Suppression of Glucose Production. *Cell Metab.* **2016**, *23* (6), 1154–1166.

(14) Röder, P. V; Wu, B.; Liu, Y.; Han, W. Pancreatic Regulation of Glucose Homeostasis. *Exp. Mol. Med.* **2016**, *48* (3), e219.

(15) Raddatz, D.; Ramadori, G. Carbohydrate Metabolism and the Liver: Actual Aspects from Physiology and Disease. *Z. Gastroenterol.* **2007**, *45* (1), 51–62.

(16) Agius, L. Glucokinase and Molecular Aspects of Liver Glycogen Metabolism. *Biochem. J.* **2008**, *414* (1), 1–18.

(17) Karim, S.; Adams, D. H.; Lalor, P. F. Hepatic Expression and Cellular Distribution of the Glucose Transporter Family. *World J. Gastroenterol.* **2012**, *18* (46), 6771–6781.

(18) Postic, C.; Dentin, R.; Girard, J. Role of the Liver in the Control of Carbohydrate and Lipid Homeostasis. *Diabetes Metab.* **2004**, *30* (5), 398–408.

(19) Gyamfi, D.; Danquah, K. O. Nutrients and Liver Metabolism. In *Molecular Aspects of Alcohol and Nutrition*; Elsevier, 2016; pp 3–15.

(20) Lehninger, A. L.; Nelson, D. L. (David L.; Cox, M. M. *Principles of Biochemistry*; W.H. Freeman, 2005.

(21) Bray, G. A.; Nielsen, S. J.; Popkin, B. M. Consumption of High-Fructose Corn

Syrup in Beverages May Play a Role in the Epidemic of Obesity. *Am. J. Clin. Nutr.* **2004**, *79* (4), 537–543.

(22) Hannou, S. A.; Haslam, D. E.; McKeown, N. M.; Herman, M. A. Fructose Metabolism and Metabolic Disease. *J. Clin. Invest.* **2018**, *128* (2), 545–555.

(23) Mueckler, M.; Thorens, B. The SLC2 (GLUT) Family of Membrane Transporters. *Mol. Aspects Med.* **2013**, *34* (2–3), 121–138.

(24) Douard, V.; Ferraris, R. P. The Role of Fructose Transporters in Diseases Linked to Excessive Fructose Intake. *J. Physiol.* **2013**, *591* (2), 401–414.

(25) Barone, S.; Fussell, S. L.; Singh, A. K.; Lucas, F.; Xu, J.; Kim, C.; Wu, X.; Yu, Y.; Amial, H.; Seidler, U.; et al. Slc2a5 (Glut5) Is Essential for the Absorption of Fructose in the Intestine and Generation of Fructose-Induced Hypertension. *J. Biol. Chem.* **2009**, *284* (8), 5056–5066.

(26) Geidl-Flueck, B.; Gerber, P. A. Insights into the Hexose Liver Metabolism—Glucose versus Fructose. *Nutrients* **2017**, *9* (9), 1026.

(27) Jensen, T.; Abdelmalek, M. F.; Sullivan, S.; Nadeau, K. J.; Green, M.; Roncal, C.; Nakagawa, T.; Kuwabara, M.; Sato, Y.; Kang, D. H.; et al. Fructose and Sugar: A Major Mediator of Non-Alcoholic Fatty Liver Disease. *J. Hepatol.* **2018**, *68* (5), 1063–1075.

(28) Herman, M. A.; Samuel, V. T. The Sweet Path to Metabolic Demise: Fructose and Lipid Synthesis. *Trends Endocrinol. Metab.* **2016**, *27* (10), 719–730.

(29) Bechmann, L. P.; Hannivoort, R. A.; Gerken, G.; Hotamisligil, G. S.; Trauner, M.; Canbay, A. The Interaction of Hepatic Lipid and Glucose Metabolism in Liver Diseases. *J. Hepatol.* **2012**, *56* (4), 952–964.

(30) Jiang, J.; Nilsson-Ehle, P.; Xu, N. Influence of Liver Cancer on Lipid and Lipoprotein Metabolism. *Lipids Health Dis.* **2006**, *5* (1), 4.

(31) Nguyen, P.; Leray, V.; Diez, M.; Serisier, S.; Bloc'h, J. Le; Siliart, B.; Dumon, H. Liver Lipid Metabolism. *J. Anim. Physiol. Anim. Nutr. (Berl).* **2008**, *92* (3), 272–283.

(32) Houten, S. M.; Wanders, R. J. A. A General Introduction to the Biochemistry of Mitochondrial Fatty Acid β-Oxidation. *J. Inherit. Metab. Dis.* **2010**, *33* (5), 469–477.

(33) Khan, B. V.; Fungwe, T. V.; Wilcox, H. G.; Heimberg, M. Cholesterol Is Required for the Secretion of the Very-Low-Density Lipoprotein: In Vivo Studies. *Biochim. Biophys. Acta* **1990**, *1044* (3), 297–304.

(34) Vairappan, B. Cholesterol Regulation by Leptin in Alcoholic Liver Disease. In *Molecular Aspects of Alcohol and Nutrition*; Elsevier, 2016; pp 187–200.

(35) Gonzalez, F. J.; Tukey, R. H. *Goodman and Gilman's Manual of Pharmacology and Therapeutics - Chapter 3*; McGraw Hill Professional, 2007.

(36) Holeček, M. Branched-Chain Amino Acids in Health and Disease: Metabolism, Alterations in Blood Plasma, and as Supplements. *Nutr. Metab.* **2018**, *15* (1), 33.

(37) Fernando, H.; Wiktorowicz, J. E.; Soman, K. V; Kaphalia, B. S.; Khan, M. F.; Shakeel Ansari, G. A. Liver Proteomics in Progressive Alcoholic Steatosis. *Toxicol. Appl. Pharmacol.* **2013**, *266* (3), 470–480.

(38) Frayn KN. *Metabolic Regulation: A Human Perspective*; Wiley-Blackwell Pub, 2010.

(39) McGill, M. R. The Past and Present of Serum Aminotransferases and the Future of Liver Injury Biomarkers. *EXCLI J.* **2016**, *15*, 817–828.

(40) Burke, M. D. Liver Function: Test Selection and Interpretation of Results. *Clin. Lab. Med.* **2002**, *22* (2), 377–390.

(41) Hosten, A. O. BUN and Creatinine. In *Clinical Methods: The History, Physical,*

and Laboratory Examinations; Butterworths, 1990.

(42) Bogdanos, D. P.; Gao, B.; Gershwin, M. E. Liver Immunology. *Compr. Physiol.* **2013**, *3* (2), 567–598.

(43) Tarasenko, T. N.; McGuire, P. J. The Liver Is a Metabolic and Immunologic Organ: A Reconsideration of Metabolic Decompensation Due to Infection in Inborn Errors of Metabolism (IEM). *Mol. Genet. Metab.* **2017**, *121* (4), 283–288.

(44) Horst, A. K.; Neumann, K.; Diehl, L.; Tiegs, G. Modulation of Liver Tolerance by Conventional and Nonconventional Antigen-Presenting Cells and Regulatory Immune Cells. *Cell. Mol. Immunol.* **2016**, *13* (3), 277–292.

(45) Shuai, Z.; Leung, M. W. Y.; He, X.; Zhang, W.; Yang, G.; Leung, P. S.; Eric Gershwin, M. Adaptive Immunity in the Liver. *Cell. Mol. Immunol.* **2016**, *13* (3), 354–368.

(46) Robinson, M. W.; Harmon, C.; O'Farrelly, C. Liver Immunology and Its Role in Inflammation and Homeostasis. *Cell. Mol. Immunol.* **2016**, *13* (3), 267–276.

(47) Golubovskaya, V.; Wu, L. Different Subsets of T Cells, Memory, Effector Functions, and CAR-T Immunotherapy. *Cancers (Basel).* **2016**, *8* (3).

(48) Narayanan, S.; Surette, F. A.; Hahn, Y. S. The Immune Landscape in Nonalcoholic Steatohepatitis. *Immune Netw.* **2016**, *16* (3), 147.

(49) Tajiri, K.; Shimizu, Y. Role of NKT Cells in the Pathogenesis of NAFLD. *Int. J. Hepatol.* **2012**, *2012*, 1–6.

(50) Deng, Z. Bin; Liu, Y.; Liu, C.; Xiang, X.; Wang, J.; Cheng, Z.; Shah, S. V; Zhang, S.; Zhang, L.; Zhuang, X.; et al. Immature Myeloid Cells Induced by a High-Fat Diet Contribute to Liver Inflammation. *Hepatology* **2009**, *50* (5), 1412–1420.

(51) Williams, C. D.; Jaeschke, H. Role of Innate and Adaptive Immunity during Drug-Induced Liver Injury. *Toxicol. Res. (Camb).* **2012**, *1* (3), 161.

(52) Kazankov, K.; Jørgensen, S. M. D.; Thomsen, K. L.; Møller, H. J.; Vilstrup, H.; George, J.; Schuppan, D.; Grønbæk, H. The Role of Macrophages in Nonalcoholic Fatty Liver Disease and Nonalcoholic Steatohepatitis. *Nat. Rev. Gastroenterol. Hepatol.* **2019**, *16* (3), 145–159.

(53) Chung, E. Y.; Liu, J.; Homma, Y.; Zhang, Y.; Brendolan, A.; Saggese, M.; Han, J.; Silverstein, R.; Selleri, L.; Ma, X. Interleukin-10 Expression in Macrophages during Phagocytosis of Apoptotic Cells Is Mediated by Homeodomain Proteins Pbx1 and Prep-1. *Immunity* **2007**, *27* (6), 952–964.

(54) Duque, G. A.; Descoteaux, A. Macrophage Cytokines: Involvement in Immunity and Infectious Diseases. *Front. Immunol.* **2014**, *5* (OCT), 491.

(55) Gao, B.; Tsukamoto, H. Inflammation in Alcoholic and Nonalcoholic Fatty Liver Disease: Friend or Foe? *Gastroenterology* **2016**, *150* (8), 1704–1709.

(56) Prame Kumar, K.; Nicholls, A. J.; Wong, C. H. Y. Partners in Crime: Neutrophils and Monocytes/Macrophages in Inflammation and Disease. *Cell Tissue Res.* **2018**, *371* (3), 551–565.

(57) Inzaugarat, M. E.; Ferreyra Solari, N. E.; Billordo, L. A.; Abecasis, R.; Gadano, A. C.; Cherñavsky, A. C. Altered Phenotype and Functionality of Circulating Immune Cells Characterize Adult Patients with Nonalcoholic Steatohepatitis. *J. Clin. Immunol.* **2011**, *31* (6), 1120–1130.

(58) Tirosh, O. *Liver Metabolism and Fatty Liver Disease*; Tirosh, O., Ed.; Oxidative Stress and Disease; CRC Press, 2014.

(59) Michelotti, G. A.; Machado, M. V; Diehl, A. M. NAFLD, NASH and Liver Cancer. *Nat. Rev. Gastroenterol. Hepatol.* **2013**, *10* (11), 656–665.

(60) Petta, S.; Valenti, L.; Bugianesi, E.; Targher, G.; Bellentani, S.; Bonino, F. A "Systems Medicine" Approach to the Study of Non-Alcoholic Fatty Liver Disease.

Dig. Liver Dis. **2016**, *48* (3), 333–342.

(61) European Association for the Study of the Liver, (EASL); European Association for the Study of Obesity, (EASO); European Association for the Study of Diabetes, (EASD). EASL–EASD–EASO Clinical Practice Guidelines for the Management of Non-Alcoholic Fatty Liver Disease. *J. Hepatol.* **2016**, *64* (6), 1388–1402.

(62) Asrani, S. K.; Devarbhavi, H.; Eaton, J.; Kamath, P. S. Burden of Liver Diseases in the World. *J. Hepatol.* **2019**, *70* (1), 151–171.

(63) Polyzos, S. A.; Kountouras, J.; Mantzoros, C. S. Obesity and Nonalcoholic Fatty Liver Disease: From Pathophysiology to Therapeutics. *Metabolism.* **2019**, *92*, 82–97.

(64) Day, C. P.; James, O. F. Steatohepatitis: A Tale of Two"hits"? *Gastroenterology* **1998**, *114* (4), 842–845.

(65) Imajo, K.; Kessoku, T.; Honda, Y.; Tomeno, W.; Ogawa, Y.; Mawatari, H.; Fujita, K.; Yoneda, M.; Taguri, M.; Hyogo, H.; et al. Magnetic Resonance Imaging More Accurately Classifies Steatosis and Fibrosis in Patients with Nonalcoholic Fatty Liver Disease Than Transient Elastography. *Gastroenterology* **2016**, *150* (3), 626-637.e7.

(66) Browning, J. D.; Horton, J. D.; Neuschwander-Tetri, B.; Caldwell, S.; Clark, J.; Brancati, F.; Diehl, A.; Angulo, P.; Marchesini, G.; Day, C.; et al. Molecular Mediators of Hepatic Steatosis and Liver Injury. *J. Clin. Invest.* **2004**, *114* (2), 147–152.

(67) Dietrich, P.; Hellerbrand, C. Non-Alcoholic Fatty Liver Disease, Obesity and the Metabolic Syndrome. *Best Pract. Res. Clin. Gastroenterol.* **2014**, *28* (4), 637–653.

(68) Lim, J. S.; Mietus-Snyder, M.; Valente, A.; Schwarz, J. M.; Lustig, R. H. The Role of Fructose in the Pathogenesis of NAFLD and the Metabolic Syndrome. *Nat. Rev.*

Gastroenterol. Hepatol. **2010**, *7* (5), 251–264.

(69) Stanhope, K. L.; Schwarz, J. M.; Keim, N. L.; Griffen, S. C.; Bremer, A. A.; Graham, J. L.; Hatcher, B.; Cox, C. L.; Dyachenko, A.; Zhang, W.; et al. Consuming Fructose-Sweetened, Not Glucose-Sweetened, Beverages Increases Visceral Adiposity and Lipids and Decreases Insulin Sensitivity in Overweight/Obese Humans. *J. Clin. Invest.* **2009**, *119* (5), 1322–1334.

(70) Varma, V.; Boros, L. G.; Nolen, G. T.; Chang, C. W.; Wabitsch, M.; Beger, R. D.; Kaput, J. Metabolic Fate of Fructose in Human Adipocytes: A Targeted 13C Tracer Fate Association Study. *Metabolomics* **2015**, *11* (3), 529–544.

(71) Softic, S.; Gupta, M. K.; Wang, G. X.; Fujisaka, S.; O'Neill, B. T.; Rao, T. N.; Willoughby, J.; Harbison, C.; Fitzgerald, K.; Ilkayeva, O.; et al. Divergent Effects of Glucose and Fructose on Hepatic Lipogenesis and Insulin Signaling. *J. Clin. Invest.* **2017**, *127* (11), 4059–4074.

(72) Jürgens, H.; Haass, W.; Castañeda, T. R.; Schürmann, A.; Koebnick, C.; Dombrowski, F.; Otto, B.; Nawrocki, A. R.; Scherer, P. E.; Spranger, J.; et al. Consuming Fructose-Sweetened Beverages Increases Body Adiposity in Mice. *Obes. Res.* **2008**, *13* (7), 1146–1156.

(73) Ouyang, X.; Cirillo, P.; Sautin, Y.; McCall, S.; Bruchette, J. L.; Diehl, A. M.; Johnson, R. J.; Abdelmalek, M. F. Fructose Consumption as a Risk Factor for Non-Alcoholic Fatty Liver Disease. *J. Hepatol.* **2008**, *48* (6), 993–999.

(74) Kim, M.-S.; Krawczyk, S. A.; Doridot, L.; Fowler, A. J.; Wang, J. X.; Trauger, S. A.; Noh, H.-L.; Kang, H. J.; Meissen, J. K.; Blatnik, M.; et al. ChREBP Regulates Fructose-Induced Glucose Production Independently of Insulin Signaling. *J. Clin. Invest.* **2016**, *126* (11), 4372–4386.

(75) Mock, K.; Lateef, S.; Benedito, V. A.; Tou, J. C. High-Fructose Corn Syrup-55

Consumption Alters Hepatic Lipid Metabolism and Promotes Triglyceride Accumulation. *J. Nutr. Biochem.* **2017**, *39*, 32–39.

(76) Dinicolantonio, J. J.; Subramonian, A. M.; O'Keefe, J. H. Added Fructose as a Principal Driver of Non-Alcoholic Fatty Liver Disease: A Public Health Crisis. *Open Hear.* **2017**, *4* (2), e000631.

(77) Abdelmalek, M. F.; Suzuki, A.; Guy, C.; Unalp-Arida, A.; Colvin, R.; Johnson, R. J.; Diehl, A. M. Increased Fructose Consumption Is Associated with Fibrosis Severity in Patients with Nonalcoholic Fatty Liver Disease. *Hepatology* **2010**, *51* (6), 1961–1971.

(78) Abdelmalek, M. F.; Lazo, M.; Horska, A.; Bonekamp, S.; Lipkin, E. W.; Balasubramanyam, A.; Bantle, J. P.; Johnson, R. J.; Diehl, A. M.; Clark, J. M. Higher Dietary Fructose Is Associated with Impaired Hepatic Adenosine Triphosphate Homeostasis in Obese Individuals with Type 2 Diabetes. *Hepatology* **2012**, *56* (3), 952–960.

(79) Hochuli, M.; Aeberli, I.; Weiss, A.; Hersberger, M.; Troxler, H.; Gerber, P. A.; Spinas, G. A.; Berneis, K. Sugar-Sweetened Beverages with Moderate Amounts of Fructose, but Not Sucrose, Induce Fatty Acid Synthesis in Healthy Young Men: A Randomized Crossover Study. *J. Clin. Endocrinol. Metab.* **2014**, *99* (6), 2164–2172.

(80) Than, N. N.; Newsome, P. N. A Concise Review of Non-Alcoholic Fatty Liver Disease. *Atherosclerosis* **2015**, *239* (1), 192–202.

(81) Newsome, P. N.; Cramb, R.; Davison, S. M.; DIllon, J. F.; Foulerton, M.; Godfrey, E. M.; Hall, R.; Harrower, U.; Hudson, M.; Langford, A.; et al. Guidelines on the Management of Abnormal Liver Blood Tests. *Gut* **2018**, *67* (1), 6–19.

(82) Kim, W. R.; Flamm, S. L.; Di Bisceglie, A. M.; Bodenheimer, H. C. Serum

Activity of Alanine Aminotransferase (ALT) as an Indicator of Health and Disease. *Hepatology* **2008**, *47* (4), 1363–1370.

(83) Pais, R.; Bourron, O. Fatty Liver and Renal Function Impairment – Time for Awareness? *J. Hepatol.* **2018**, *68* (1), 13–15.

(84) Zachariah, S.; Kumar, K.; Lee, S. W. H.; Choon, W. Y.; Naeem, S.; Leong, C. Interpretation of Laboratory Data and General Physical Examination by Pharmacists. In *Clinical Pharmacy Education, Practice and Research*; Elsevier, 2019; pp 91–108.

(85) Friedman, S. L.; Neuschwander-Tetri, B. A.; Rinella, M.; Sanyal, A. J. Mechanisms of NAFLD Development and Therapeutic Strategies. *Nat. Med.* **2018**, *24* (7), 908–922.

(86) Yeh, M. M.; Brunt, E. M. Pathological Features of Fatty Liver Disease. *Gastroenterology* **2014**, *147* (4), 754–764.

(87) Nalbantoglu, I. L. K.; Brunt, E. M. Role of Liver Biopsy in Nonalcoholic Fatty Liver Disease. *World J. Gastroenterol.* **2014**, *20* (27), 9026–9037.

(88) Dulai, P. S.; Sirlin, C. B.; Loomba, R. MRI and MRE for Non-Invasive Quantitative Assessment of Hepatic Steatosis and Fibrosis in NAFLD and NASH: Clinical Trials to Clinical Practice. *J. Hepatol.* **2016**, *65* (5), 1006–1016.

(89) Amathieu, R. Nuclear Magnetic Resonance Based Metabolomics and Liver Diseases: Recent Advances and Future Clinical Applications. *World J. Gastroenterol.* **2016**, *22* (1), 417.

(90) Younossi, Z. M.; Loomba, R.; Rinella, M. E.; Bugianesi, E.; Marchesini, G.; Neuschwander-Tetri, B. A.; Serfaty, L.; Negro, F.; Caldwell, S. H.; Ratziu, V.; et al. Current and Future Therapeutic Regimens for Nonalcoholic Fatty Liver Disease and Nonalcoholic Steatohepatitis. *Hepatology* **2018**, *68* (1), 361–371.

(91) Promrat, K.; Kleiner, D. E.; Niemeier, H. M.; Jackvony, E.; Kearns, M.; Wands, J. R.; Fava, J. L.; Wing, R. R. Randomized Controlled Trial Testing the Effects of Weight Loss on Nonalcoholic Steatohepatitis. *Hepatology* **2010**, *51* (1), 121–129.

(92) Vilar-Gomez, E.; Yasells-Garcia, A.; Martinez-Perez, Y.; Calzadilla-Bertot, L.; Torres-Gonzalez, A.; Gra-Oramas, B.; Gonzalez-Fabian, L.; Villa-Jimenez, O.; Friedman, S. L.; Diago, M.; et al. Development and Validation of a Noninvasive Prediction Model for Nonalcoholic Steatohepatitis Resolution after Lifestyle Intervention. *Hepatology* **2016**, *63* (6), 1875–1887.

(93) Ahmed, I. A.; Mikail, M. A.; Mustafa, M. R.; Ibrahim, M.; Othman, R. Lifestyle Interventions for Non-Alcoholic Fatty Liver Disease. *Saudi J. Biol. Sci.* **2019**.

(94) Wiernsperger, N. Hepatic Function and the Cardiometabolic Syndrome. *Diabetes, Metab. Syndr. Obes. Targets Ther.* **2013**, *6*, 379–388.

(95) Friedman, S. L.; Neuschwander-Tetri, B. A.; Rinella, M.; Sanyal, A. J. Mechanisms of NAFLD Development and Therapeutic Strategies. *Nat. Med.* **2018**, *24* (7), 908–922.

(96) Holmes, E.; Wilson, I. D.; Nicholson, J. K. Metabolic Phenotyping in Health and Disease. *Cell* **2008**, *134* (5), 714–717.

(97) Schofield, Z.; Reed, M. A.; Newsome, P. N.; Adams, D. H.; Günther, U. L.; Lalor, P. F. Changes in Human Hepatic Metabolism in Steatosis and Cirrhosis. *World J. Gastroenterol.* **2017**, *23* (15), 2685.

(98) Nicholson, J. K.; Connelly, J.; Lindon, J. C.; Holmes, E. Metabonomics: A Platform for Studying Drug Toxicity and Gene Function. *Nat. Rev. Drug Discov.* **2002**, *1* (2), 153–161.

(99) Emwas, A. M.; Merzaban, J. S.; Serrai, H. *Theory and Applications of NMR-Based Metabolomics in Human Disease Diagnosis*, First Edit.; Elsevier Ltd., 2015; Vol.

1.

(100) Nielsen, J. Systems Biology of Metabolism. *Annu. Rev. Biochem.* **2017**, *86* (1), 245–275.

(101) Dumas, M.; Kinross, J.; Nicholson, J. K. Metabolic Phenotyping and Systems Biology Approaches to Understanding Metabolic Syndrome and Fatty Liver Disease. *Gastroenterology* **2014**, *146* (1), 46–62.

(102) Klassen, A.; Faccio, A. T.; Canuto, G. A. B.; da Cruz, P. L. R.; Ribeiro, H. C.; Tavares, M. F. M.; Sussulini, A. Metabolomics: Definitions and Significance in Systems Biology. In *Advances in Experimental Medicine and Biology*; 2017; Vol. 965, pp 3–17.

(103) Duarte, I. F. Following Dynamic Biological Processes through NMR-Based Metabonomics: A New Tool in Nanomedicine? *J. Control. Release* **2011**, *153* (1), 34–39.

(104) Nagana Gowda, G. A.; Raftery, D. Can NMR Solve Some Significant Challenges in Metabolomics? *J. Magn. Reson.* **2015**, *260*, 144–160.

(105) Markley, J. L.; Brüschweiler, R.; Edison, A. S.; Eghbalnia, H. R.; Powers, R.; Raftery, D.; Wishart, D. S. The Future of NMR-Based Metabolomics. *Curr. Opin. Biotechnol.* **2017**, *43*, 34–40.

(106) Levitt, M. H. *Spin Dynamics : Basics of Nuclear Magnetic Resonance*; John Wiley & Sons, 2008.

(107) Slichter, C. P. Elements of Resonance; 1978; pp 1–10.

(108) Villas-Boas, S. G.; Nielsen, J.; Smedsgaard, J.; Hansen, M. A. E.; Roessner-Tunali, U. *Metabolome Analysis: An Introduction*; John Wiley & Sons, 2007.

(109) Keeler, J. *Understanding NMR Spectroscopy*; John Wiley and Sons, 2010.

(110) Lindon, J. C.; Nicholson, J. K.; Holmes, E. *The Handbook of Metabonomics and*

Metabolomics; Elsevier, 2011.

(111) Tycko, R. NMR at Low and Ultralow Temperatures. *Acc. Chem. Res.* **2013**, *46* (9), 1923–1932.

(112) Günther, U. L. Dynamic Nuclear Hyperpolarization in Liquids. In *TripleC*; 2011; Vol. 11, pp 23–69.

(113) Balci, M. *Basic 1H- and 13C-NMR Spectroscopy*; 2005.

(114) Kelly, A. E.; Ou, H. D.; Withers, R.; Dötsch, V. Low-Conductivity Buffers for High-Sensitivity NMR Measurements. *J. Am. Chem. Soc.* **2002**, *124* (40), 12013–12019.

(115) Styles, P.; Soffe, N. F. A High-Resolution NMR Probe in Which the Coil and Preamplifier Are Cooled with Liquid Helium. *J. Magn. Reson.* **1984**, *60*, 397–404.

(116) Dixon, W. T. The Relation of Signal/Noise to Magnetic Field Strength and Sample Size in Magic-Angle-Spinning Solids Experiments. *J. Magn. Reson.* **1984**, *57* (2), 289–293.

(117) Hilton, B. D.; Martin, G. E. Investigation of the Experimental Limits of Small-Sample Heteronuclear 2D NMR. *J. Nat. Prod.* **2010**, *73* (9), 1465–1469.

(118) Kovacs, H.; Moskau, D.; Spraul, M. Cryogenically Cooled Probes—a Leap in NMR Technology. *Prog. Nucl. Magn. Reson. Spectrosc.* **2005**, *46* (2–3), 131–155.

(119) Serber, Z.; Richter, C.; Dötsch, V. Carbon-Detected NMR Experiments to Investigate Structure and Dynamics of Biological Macromolecules. *ChemBioChem* **2001**, *2* (4), 247–251.

(120) Saborano, R.; Eraslan, Z.; Roberts, J.; Khanim, F. L.; Lalor, P. F.; Reed, M. A. C.; Günther, U. L. A Framework for Tracer-Based Metabolism in Mammalian Cells by NMR. *Sci. Rep.* **2019**, *9* (1), 2520.

(121) Takeda, M.; Hallenga, K.; Shigezane, M.; Waelchli, M.; Löhr, F.; Markley, J. L.;

Kainosho, M. Construction and Performance of an NMR Tube with a Sample Cavity Formed within Magnetic Susceptibility-Matched Glass. *J. Magn. Reson.* **2011**, *209* (2), 167–173.

(122) Abragam, a; Goldman, M. Principles of Dynamic Nuclear Polarisation. *Reports Prog. Phys.* **1978**, *41* (3), 395–467.

(123) Ardenkjaer-Larsen, J. H.; Fridlund, B.; Gram, A.; Hansson, G.; Hansson, L.; Lerche, M. H.; Servin, R.; Thaning, M.; Golman, K. Increase in Signal-to-Noise Ratio of over 10,000 Times in Liquid-State NMR. *Proc. Natl. Acad. Sci.* **2003**, *100* (18), 10158–10163.

(124) Le Belle, J. E.; Harris, N. G.; Williams, S. R.; Bhakoo, K. K. A Comparison of Cell and Tissue Extraction Techniques Using High-Resolution 1H-NMR Spectroscopy. *NMR Biomed.* **2002**, *15* (1), 37–44.

(125) Martineau, E.; Tea, I.; Loaëc, G.; Giraudeau, P.; Akoka, S. Strategy for Choosing Extraction Procedures for NMR-Based Metabolomic Analysis of Mammalian Cells. *Anal. Bioanal. Chem.* **2011**, *401* (7), 2133–2142.

(126) McKay, R. T. How the 1D-NOESY Suppresses Solvent Signal in Metabonomics NMR Spectroscopy: An Examination of the Pulse Sequence Components and Evolution. *Concepts Magn. Reson. Part A Bridg. Educ. Res.* **2011**, *38 A* (5), 197–220.

(127) de la Vega-Hernández, K.; Antuch, M. The Heteronuclear Single-Quantum Correlation (HSQC) Experiment: Vectors versus Product Operators. *J. Chem. Educ.* **2015**, *92* (3), 482–487.

(128) Golman, K.; Zandt, R. I.; Lerche, M.; Pehrson, R.; Ardenkjaer-Larsen, J. H. Metabolic Imaging by Hyperpolarized 13C Magnetic Resonance Imaging for In Vivo Tumor Diagnosis. *Cancer Res.* **2006**, *66* (22), 10855–10860.

(129) Wilson, D. M.; Hurd, R. E.; Keshari, K.; Van Criekinge, M.; Chen, A. P.; Nelson, S. J.; Vigneron, D. B.; Kurhanewicz, J. Generation of Hyperpolarized Substrates by Secondary Labeling with [1,1-13C] Acetic Anhydride. *Proc. Natl. Acad. Sci.* **2009**, *106* (14), 5503–5507.

(130) Dona, A. C.; Kyriakides, M.; Scott, F.; Shephard, E. A.; Varshavi, D.; Veselkov, K.; Everett, J. R. A Guide to the Identification of Metabolites in NMR-Based Metabonomics/Metabolomics Experiments. *Comput. Struct. Biotechnol. J.* **2016**, *14*, 135–153.

(131) Kostidis, S.; Addie, R. D.; Morreau, H.; Mayboroda, O. A.; Giera, M. Quantitative NMR Analysis of Intra- and Extracellular Metabolism of Mammalian Cells: A Tutorial. *Anal. Chim. Acta* **2017**, *980*, 1–24.

(132) Giraudeau, P.; Silvestre, V.; Akoka, S. Optimizing Water Suppression for Quantitative NMR-Based Metabolomics: A Tutorial Review. *Metabolomics* **2015**, *11* (5), 1041–1055.

(133) Haasnoot, C. A. G.; Hilbers, C. W. Effective Water Resonance Suppression in 1D- and 2D-FT–1H-nmr Spectroscopy of Biopolymers in Aqueous Solution. *Biopolymers* **1983**, *22* (5), 1259–1266.

(134) Piotto, M.; Saudek, V.; Sklenář, V. Gradient-Tailored Excitation for Single-Quantum NMR Spectroscopy of Aqueous Solutions. *J. Biomol. NMR* **1992**, *2* (6), 661–665.

(135) Khera, S.; Grillo, M.; Schnier, P.; Hollis, S. Application of Diffusion-Edited NMR Spectroscopy for the Structural Characterization of Drug Metabolites in Mixtures. *J. Pharm. Biomed. Anal.* **2010**, *51* (1), 164–169.

(136) Wright, B.; Greatbanks, D.; Taberner, J.; Wilson, I. D. Comparison of Three Methods for Water Suppression in Biofluid NMR: Advantages of

NOESYPRESAT. *Pharm. Pharmacol. Commun.* **1995**, *1* (4), 197–199.

(137) Beckonert, O.; Keun, H. C.; Ebbels, T. M. D.; Bundy, J.; Holmes, E.; Lindon, J. C.; Nicholson, J. K. Metabolic Profiling, Metabolomic and Metabonomic Procedures for NMR Spectroscopy of Urine, Plasma, Serum and Tissue Extracts. *Nat. Protoc.* **2007**, *2* (11), 2692–2703.

(138) Bruker User Library | Bruker https://www.bruker.com/service/information-communication/nmr-pulse-program-lib/bruker-user-library.html (accessed Jun 9, 2019).

(139) Fan, T. W.-M.; Lane, A. N. Structure-Based Profiling of Metabolites and Isotopomers by NMR. *Prog. Nucl. Magn. Reson. Spectrosc.* **2008**, *52* (2–3), 69–117.

(140) Carrigan, J. B.; Reed, M. A. C.; Ludwig, C.; Khanim, F. L.; Bunce, C. M.; Günther, U. L. Tracer-Based Metabolic NMR-Based Flux Analysis in a Leukaemia Cell Line. *Chempluschem* **2016**, *81* (5), 453–459.

(141) Heude, C.; Nath, J.; Carrigan, J. B.; Ludwig, C. Nuclear Magnetic Resonance Strategies for Metabolic Analysis; Springer, Cham, 2017; pp 45–76.

(142) Mandal, P. K.; Majumdar, A. A Comprehensive Discussion of HSQC and HMQC Pulse Sequences. *Concepts Magn. Reson. Part A Bridg. Educ. Res.* **2004**, *20* (1), 1–23.

(143) Younossi, Z. M.; Marchesini, G.; Pinto-Cortez, H.; Petta, S. Epidemiology of Nonalcoholic Fatty Liver Disease and Nonalcoholic Steatohepatitis: Implications for Liver Transplantation. *Transplantation* **2019**, *103* (1), 22–27.

(144) Lyssiotis, C. A.; Cantley, L. C. Metabolic Syndrome: F Stands for Fructose and Fat. *Nature* **2013**, *502* (7470), 181–182.

(145) Stephenson, K.; Kennedy, L.; Hargrove, L.; Demieville, J.; Thomson, J.; Alpini,

G.; Francis, H. Updates on Dietary Models of Nonalcoholic Fatty Liver Disease: Current Studies and Insights. *Gene Expr.* **2018**, *18* (1), 5–17.

(146) Van Herck, M. A.; Vonghia, L.; Francque, S. M. Animal Models of Nonalcoholic Fatty Liver Disease—a Starter's Guide. *Nutrients* **2017**, *9* (10), 1072.

(147) Chavez-Tapia, N. C.; Rosso, N.; Tiribelli, C. In Vitro Models for the Study of Non-Alcoholic Fatty Liver Disease. *Curr. Med. Chem.* **2011**, *18* (7), 1079–1084.

(148) Bhogal, R. H.; Hodson, J.; Bartlett, D. C.; Weston, C. J.; Curbishley, S. M.; Haughton, E.; Williams, K. T.; Reynolds, G. M.; Newsome, P. N.; Adams, D. H.; et al. Isolation of Primary Human Hepatocytes from Normal and Diseased Liver Tissue: A One Hundred Liver Experience. *PLoS One* **2011**, *6* (3), e18222.

(149) Pellizzon, M. A.; Ricci, M. R. The Common Use of Improper Control Diets in Diet-Induced Metabolic Disease Research Confounds Data Interpretation: The Fiber Factor. *Nutr. Metab. (Lond).* **2018**, *15* (1), 3.

(150) Diehl, K.-H.; Hull, R.; Morton, D.; Pfister, R.; Rabemampianina, Y.; Smith, D.; Vidal, J.-M.; Vorstenbosch, C. Van De. A Good Practice Guide to the Administration of Substances and Removal of Blood, Including Routes and Volumes. *J. Appl. Toxicol.* **2001**, *21* (1), 15–23.

(151) Teng, Q.; Huang, W.; Collette, T. W.; Ekman, D. R.; Tan, C. A Direct Cell Quenching Method for Cell-Culture Based Metabolomics. *Metabolomics* **2009**, *5* (2), 199–208.

(152) Ludwig, C.; Günther, U. L. MetaboLab - Advanced NMR Data Processing and Analysis for Metabolomics. *BMC Bioinformatics* **2011**, *12:366* (1).

(153) Savorani, F.; Tomasi, G.; Engelsen, S. B. Icoshift: A Versatile Tool for the Rapid Alignment of 1D NMR Spectra. *J. Magn. Reson.* **2010**, *202* (2), 190–202.

(154) Wishart, D. S.; Jewison, T.; Guo, A. C.; Wilson, M.; Knox, C.; Liu, Y.; Djoumbou,

Y.; Mandal, R.; Aziat, F.; Dong, E.; et al. HMDB 3.0--The Human Metabolome Database in 2013. *Nucleic Acids Res.* **2013**, *41* (D1), D801–D807.

(155) Delaglio, F.; Grzesiek, S.; Vuister, G.; Zhu, G.; Pfeifer, J.; Bax, A. NMRPipe: A Multidimensional Spectral Processing System Based on UNIX Pipes. *J. Biomol. NMR* **1995**, *6* (3), 277–293.

(156) Hyberts, S. G.; Milbradt, A. G.; Wagner, A. B.; Arthanari, H.; Wagner, G. Application of Iterative Soft Thresholding for Fast Reconstruction of NMR Data Non-Uniformly Sampled with Multidimensional Poisson Gap Scheduling. *J. Biomol. NMR* **2012**, *52* (4), 315–327.

(157) Hu, K.; Westler, W. M.; Markley, J. L. Simultaneous Quantification and Identification of Individual Chemicals in Metabolite Mixtures by Two-Dimensional Extrapolated Time-Zero 1 H− 13 C HSQC (HSQC 0). *J. Am. Chem. Soc.* **2011**, *133* (6), 1662–1665.

(158) Fardus-Reid, F.; Warren, J.; Le Gresley, A. Validating Heteronuclear 2D Quantitative NMR. *Anal. Methods* **2016**, *8* (9), 2013–2019.

(159) Lewis, I. A.; Schommer, S. C.; Hodis, B.; Robb, K. A.; Tonelli, M.; Westler, W. M.; Sussman, M. R.; Markley, J. L. Method for Determining Molar Concentrations of Metabolites in Complex Solutions from Two-Dimensional 1 H− 13 C NMR Spectra. *Anal. Chem.* **2007**, *79* (24), 9385–9390.

(160) Zhang, B.; Xie, M.; Bruschweiler-Li, L.; Bingol, K.; Brüschweiler, R. Use of Charged Nanoparticles in NMR-Based Metabolomics for Spectral Simplification and Improved Metabolite Identification. *Anal. Chem.* **2015**, *87* (14), 7211–7217.

(161) Müller, E.; Berger, R.; Blass, E.; Sluyts, D. Liquid – Liquid Extraction. *Ullmann's Encycl. Ind. Chem.* **2005**, 54.

(162) Sana, T.; Fischer, S. Maximizing Metabolite Extraction for Comprehensive

Metabolomics Studies of Erythrocytes. *Agilent Technologies*. 2007, pp 5989-7407EN.

(163) Dettmer, K.; Nürnberger, N.; Kaspar, H.; Gruber, M. A.; Almstetter, M. F.; Oefner, P. J. Metabolite Extraction from Adherently Growing Mammalian Cells for Metabolomics Studies: Optimization of Harvesting and Extraction Protocols. *Anal. Bioanal. Chem.* **2011**, *399* (3), 1127–1139.

(164) Fan, T. W.-M.; Lane, A. N. Applications of NMR Spectroscopy to Systems Biochemistry. *Prog. Nucl. Magn. Reson. Spectrosc.* **2016**, *92–93*, 18–53.

(165) Dai, Z.; Locasale, J. W. Understanding Metabolism with Flux Analysis: From Theory to Application. *Metab. Eng.* **2017**, *43*, 94–102.

(166) Szyperski, T. Biosynthetically Directed Fractional 13C-Labeling of Proteinogenic Amino Acids. An Efficient Analytical Tool to Investigate Intermediary Metabolism. *Eur. J. Biochem.* **1995**, *232* (2), 433–448.

(167) Young, J.; Duckwall, C.; Murphy, T. Mapping Cancer Cell Metabolism with 13 C Flux Analysis: Recent Progress and Future Challenges. *J. Carcinog.* **2013**, *12* (1), 13.

(168) Metallo, C. M.; Walther, J. L.; Stephanopoulos, G. Evaluation of 13C Isotopic Tracers for Metabolic Flux Analysis in Mammalian Cells. *J. Biotechnol.* **2009**, *144* (3), 167–174.

(169) Carvalho, R. A.; Jarak, I. Mitochondrial Bioenergetics by 13C–NMR Isotopomer Analysis; Humana Press, New York, NY, 2018; pp 229–247.

(170) Jin, E. S.; Jones, J. G.; Merritt, M.; Burgess, S. C.; Malloy, C. R.; Sherry, A. D. Glucose Production, Gluconeogenesis, and Hepatic Tricarboxylic Acid Cycle Fluxes Measured by Nuclear Magnetic Resonance Analysis of a Single Glucose Derivative. *Anal. Biochem.* **2004**, *327* (2), 149–155.

(171) Smith, T. B.; Patel, K.; Munford, H.; Peet, A.; Tennant, D. A.; Jeeves, M.; Ludwig, C. High-Speed Tracer Analysis of Metabolism (HS-TrAM). *Wellcome Open Res.* **2018**, *3*, 5.

(172) Christian, L.; Ulrich, G. MetaboLab-Advanced NMR Data Processing and Analysis for Metabolomics. *BMC Bioinformatics* **2011**, *12* (1), 366.

(173) Wishart, D. S.; Feunang, Y. D.; Marcu, A.; Guo, A. C.; Liang, K.; Vázquez-Fresno, R.; Sajed, T.; Johnson, D.; Li, C.; Karu, N.; et al. HMDB 4.0: The Human Metabolome Database for 2018. *Nucleic Acids Res.* **2018**, *46* (D1), D608–D617.

(174) Ulrich, E. L.; Akutsu, H.; Doreleijers, J. F.; Harano, Y.; Ioannidis, Y. E.; Lin, J.; Livny, M.; Mading, S.; Maziuk, D.; Miller, Z.; et al. BioMagResBank. *Nucleic Acids Res.* **2007**, *36* (Database), D402–D408.

(175) Younossi, Z.; Anstee, Q. M.; Marietti, M.; Hardy, T.; Henry, L.; Eslam, M.; George, J.; Bugianesi, E. Global Burden of NAFLD and NASH: Trends, Predictions, Risk Factors and Prevention. *Nat. Rev. Gastroenterol. Hepatol.* **2017**, *15* (1), 11–20.

(176) Boteon, Y. L.; Afford, S. C.; Mergental, H. Pushing the Limits: Machine Preservation of the Liver as a Tool to Recondition High-Risk Grafts. *Curr. Transplant. Reports* **2018**, *5* (2), 113–120.

(177) Ravikumar, R.; Jassem, W.; Mergental, H.; Heaton, N.; Mirza, D.; Perera, M. T. P. R.; Quaglia, A.; Holroyd, D.; Vogel, T.; Coussios, C. C.; et al. Liver Transplantation After Ex Vivo Normothermic Machine Preservation: A Phase 1 (First-in-Man) Clinical Trial. *Am. J. Transplant.* **2016**, *16* (6), 1779–1787.

(178) Morovat, A.; Vogel, T.; Friend, P. J.; Jassem, W.; Brockmann, J. G.; Coussios, C. C.; Quaglia, A.; Heaton, N. D. The 24-Hour Normothermic Machine Perfusion of Discarded Human Liver Grafts. *Liver Transplant.* **2017**, *23* (2), 207–220.

(179) Wiggins, B. G.; Stamataki, Z.; Lalor, P. F. Using Ex Vivo Liver Organ Cultures to Measure Lymphocyte Trafficking; 2017; pp 177–194.

(180) Fan, T. W. M. Considerations of Sample Preparation for Metabolomics Investigation. *Methods Pharmacol. Toxicol.* **2012**, *17*, 7–27.

(181) Metallo, C. M.; Vander Heiden, M. G. Understanding Metabolic Regulation and Its Influence on Cell Physiology. *Mol. Cell* **2013**, *49* (3), 388–398.

(182) Hosios, A. M.; Hecht, V. C.; Danai, L. V.; Johnson, M. O.; Rathmell, J. C.; Steinhauser, M. L.; Manalis, S. R.; Vander Heiden, M. G. Amino Acids Rather than Glucose Account for the Majority of Cell Mass in Proliferating Mammalian Cells. *Dev. Cell* **2016**, *36* (5), 540–549.

(183) DeBerardinis, R. J.; Lum, J. J.; Hatzivassiliou, G.; Thompson, C. B. The Biology of Cancer: Metabolic Reprogramming Fuels Cell Growth and Proliferation. *Cell Metab.* **2008**, *7* (1), 11–20.

(184) Luo, B.; Groenke, K.; Takors, R.; Wandrey, C.; Oldiges, M. Simultaneous Determination of Multiple Intracellular Metabolites in Glycolysis, Pentose Phosphate Pathway and Tricarboxylic Acid Cycle by Liquid Chromatography-Mass Spectrometry. *J. Chromatogr. A* **2007**, *1147* (2), 153–164.

(185) Schlippenbach, T. von; Oefner, P. J.; Gronwald, W. Systematic Evaluation of Non-Uniform Sampling Parameters in the Targeted Analysis of Urine Metabolites by 1H,1H 2D NMR Spectroscopy. *Sci. Rep.* **2018**, *8* (1), 4249.

(186) Hyberts, S. G.; Robson, S. A.; Wagner, G. Interpolating and Extrapolating with HmsIST: Seeking a t Max for Optimal Sensitivity, Resolution and Frequency Accuracy. *J. Biomol. NMR* **2017**, *68* (2), 139–154.

(187) Lee, S.; Wen, H.; An, Y. J.; Cha, J. W.; Ko, Y.-J.; Hyberts, S. G.; Park, S. Carbon Isotopomer Analysis with Non-Unifom Sampling HSQC NMR for Cell Extract

and Live Cell Metabolomics Studies. *Anal. Chem.* **2016**, *89* (2), 1078–1085.

(188) Palm, W.; Thompson, C. B. Nutrient Acquisition Strategies of Mammalian Cells. *Nature* **2017**, *546* (7657), 234–242.

(189) Rehberg, M.; Ritter, J. B.; Genzel, Y.; Flockerzi, D.; Reichl, U. The Relation between Growth Phases, Cell Volume Changes and Metabolism of Adherent Cells during Cultivation. *J. Biotechnol.* **2013**, *164* (4), 489–499.

(190) Ward, P. S.; Thompson, C. B. Signaling in Control of Cell Growth and Metabolism. *Cold Spring Harb. Perspect. Biol.* **2012**, *4* (7), a006783–a006783.

(191) Rath, A. G.; Rehberg, M.; Janke, R.; Genzel, Y.; Scholz, S.; Noll, T.; Rose, T.; Sandig, V.; Reichl, U. The Influence of Cell Growth and Enzyme Activity Changes on Intracellular Metabolite Dynamics in AGE1.HN.AAT Cells. *J. Biotechnol.* **2014**, *178*, 43–53.

(192) Reznik, E.; Mehta, P.; Segrè, D. Flux Imbalance Analysis and the Sensitivity of Cellular Growth to Changes in Metabolite Pools. *PLoS Comput. Biol.* **2013**, *9* (8), e1003195.

(193) Lara, A. R.; Galindo, E.; Ramírez, O. T.; Palomares, L. A. Living With Heterogeneities in Bioreactors: Understanding the Effects of Environmental Gradients on Cells. *Mol. Biotechnol.* **2006**, *34* (3), 355–382.

(194) Granucci, N.; Pinu, F. R.; Han, T.-L.; Villas-Boas, S. G. Can We Predict the Intracellular Metabolic State of a Cell Based on Extracellular Metabolite Data? *Mol. Biosyst.* **2015**, *11* (12), 3297–3304.

(195) Klover, P. J.; Mooney, R. A. Hepatocytes: Critical for Glucose Homeostasis. *Int. J. Biochem. Cell Biol.* **2004**, *36* (5), 753–758.

(196) Merritt, M. E.; Harrison, C.; Sherry, A. D.; Malloy, C. R.; Burgess, S. C. Flux through Hepatic Pyruvate Carboxylase and Phosphoenolpyruvate Carboxykinase

Detected by Hyperpolarized 13C Magnetic Resonance. *Proc. Natl. Acad. Sci.* **2011**, *108* (47), 19084–19089.

(197) Cappel, D. A.; Deja, S.; Duarte, J. A. G.; Kucejova, B.; Iñigo, M.; Fletcher, J. A.; Fu, X.; Berglund, E. D.; Liu, T.; Elmquist, J. K.; et al. Pyruvate-Carboxylase-Mediated Anaplerosis Promotes Antioxidant Capacity by Sustaining TCA Cycle and Redox Metabolism in Liver. *Cell Metab.* **2019**.

(198) Satapati, S.; Sunny, N. E.; Kucejova, B.; Fu, X.; He, T. T.; Méndez-Lucas, A.; Shelton, J. M.; Perales, J. C.; Browning, J. D.; Burgess, S. C. Elevated TCA Cycle Function in the Pathology of Diet-Induced Hepatic Insulin Resistance and Fatty Liver. *J. Lipid Res.* **2012**, *53* (6), 1080–1092.

(199) Sunny, N. E.; Parks, E. J.; Browning, J. D.; Burgess, S. C. Excessive Hepatic Mitochondrial TCA Cycle and Gluconeogenesis in Humans with Nonalcoholic Fatty Liver Disease. *Cell Metab.* **2011**, *14* (6), 804–810.

(200) Sugden, M. C.; Holness, M. J. Mechanisms Underlying Regulation of the Expression and Activities of the Mammalian Pyruvate Dehydrogenase Kinases. *Arch. Physiol. Biochem.* **2006**, *112* (3), 139–149.

(201) Go, Y.; Jeong, J. Y.; Jeoung, N. H.; Jeon, J. H.; Park, B. Y.; Kang, H. J.; Ha, C. M.; Choi, Y. K.; Lee, S. J.; Ham, H. J.; et al. Inhibition of Pyruvate Dehydrogenase Kinase 2 Protects against Hepatic Steatosis through Modulation of Tricarboxylic Acid Cycle Anaplerosis and Ketogenesis. *Diabetes* **2016**, *65* (10), 2876–2887.

(202) Wu, C. Y.; Tso, S. C.; Chuang, J. L.; Gui, W. J.; Lou, M.; Sharma, G.; Khemtong, C.; Qi, X.; Wynn, R. M.; Chuang, D. T. Targeting Hepatic Pyruvate Dehydrogenase Kinases Restores Insulin Signaling and Mitigates ChREBP-Mediated Lipogenesis in Diet-Induced Obese Mice. *Mol. Metab.* **2018**, *12*, 12–24.

(203) Goodpaster, B. H.; Sparks, L. M. Metabolic Flexibility in Health and Disease. *Cell*

Metab. **2017**, *25* (5), 1027–1036.

(204) Winnike, J. H.; Pediaditakis, P.; Wolak, J. E.; McClelland, R. E.; Watkins, P. B.; Macdonald, J. M. Stable Isotope Resolved Metabolomics of Primary Human Hepatocytes Reveals a Stressed Phenotype. *Metabolomics* **2012**, *8* (1), 34–49.

(205) Barbas, A. S.; Goldaracena, N.; Dib, M. J.; Selzner, M. Ex-Vivo Liver Perfusion for Organ Preservation: Recent Advances in the Field. *Transplant. Rev.* **2016**, *30* (3), 154–160.

(206) Kegel, V.; Deharde, D.; Pfeiffer, E.; Zeilinger, K.; Seehofer, D.; Damm, G. Protocol for Isolation of Primary Human Hepatocytes and Corresponding Major Populations of Non-Parenchymal Liver Cells. *J. Vis. Exp.* **2016**, No. 109, 1–10.

(207) Bruinsma, B. G.; Sridharan, G. V.; Weeder, P. D.; Avruch, J. H.; Saeidi, N.; Özer, S.; Geerts, S.; Porte, R. J.; Heger, M.; Van Gulik, T. M.; et al. Metabolic Profiling during Ex Vivo Machine Perfusion of the Human Liver. *Sci. Rep.* **2016**, *6* (1), 22415.

(208) Juárez-Hernández, E.; Chávez-Tapia, N. C.; Uribe, M.; Barbero-Becerra, V. J. Role of Bioactive Fatty Acids in Nonalcoholic Fatty Liver Disease. *Nutr. J.* **2015**, *15* (1), 72.

(209) Neuschwander-Tetri, B. A. Nontriglyceride Hepatic Lipotoxicity: The New Paradigm for the Pathogenesis of NASH. *Curr. Gastroenterol. Rep.* **2010**, *12* (1), 49–56.

(210) Gómez-Lechón, M. J.; Donato, M. T.; Martínez-Romero, A.; Jiménez, N.; Castell, J. V.; O'Connor, J. E. A Human Hepatocellular in Vitro Model to Investigate Steatosis. *Chem. Biol. Interact.* **2007**, *165* (2), 106–116.

(211) Soldatow, V. Y.; Lecluyse, E. L.; Griffith, L. G.; Rusyn, I. In Vitro Models for Liver Toxicity Testing. *Toxicol. Res. (Camb).* **2013**, *2* (1), 23–39.

(212) Alturkistani, H. A.; Tashkandi, F. M.; Mohammedsaleh, Z. M. Histological Stains: A Literature Review and Case Study. *Glob. J. Health Sci.* **2015**, *8* (3), 72.

(213) Fischer, A. H.; Jacobson, K. A.; Rose, J.; Zeller, R. Hematoxylin and Eosin Staining of Tissueand Cell Sections. *Cold Spring Harb. Protoc.* **2008**, *3* (5), pdb.prot4986.

(214) Junqueira, L. C. U.; Carneiro, J. *Basic Histology : Text & Atlas*; Lange Medical Books, McGraw-Hill, Medical Pub. Division, 2005.

(215) Subramanian, A.; Joshi, B. S.; Roy, A. D.; Roy, R.; Gupta, V.; Dang, R. S. NMR Spectroscopic Identification of Cholesterol Esters, Plasmalogen and Phenolic Glycolipids as Fingerprint Markers of Human Intracranial Tuberculomas. *NMR Biomed.* **2008**, *21* (3), 272–288.

(216) Neuschwander-Tetri, B. A. Nontriglyceride Hepatic Lipotoxicity: The New Paradigm for the Pathogenesis of NASH. *Curr. Gastroenterol. Rep.* **2010**, *12* (1), 49–56.

(217) Fernández-Murray, J. P.; McMaster, C. R. Glycerophosphocholine Catabolism as a New Route for Choline Formation for Phosphatidylcholine Synthesis by the Kennedy Pathway. *J. Biol. Chem.* **2005**, *280* (46), 38290–38296.

(218) Richter, K.; Mathes, V.; Fronius, M.; Althaus, M.; Hecker, A.; Krasteva-Christ, G.; Padberg, W.; Hone, A. J.; McIntosh, J. M.; Zakrzewicz, A.; et al. Phosphocholine-an Agonist of Metabotropic but Not of Ionotropic Functions of A9-Containing Nicotinic Acetylcholine Receptors. *Sci. Rep.* **2016**, *6* (1), 28660.

(219) Nassir, F.; Rector, R. S.; Hammoud, G. M.; Ibdah, J. A. Pathogenesis and Prevention of Hepatic Steatosis. *Gastroenterol. Hepatol.* **2015**, *11* (3), 167–175.

(220) Tilg, H.; Moschen, A. R. Evolution of Inflammation in Nonalcoholic Fatty Liver Disease: The Multiple Parallel Hits Hypothesis. *Hepatology* **2010**, *52* (5), 1836–

1846.

(221) Yamaguchi, K.; Yang, L.; McCall, S.; Huang, J.; Xing, X. Y.; Pandey, S. K.; Bhanot, S.; Monia, B. P.; Li, Y. X.; Diehl, A. M. Inhibiting Triglyceride Synthesis Improves Hepatic Steatosis but Exacerbates Liver Damage and Fibrosis in Obese Mice with Nonalcoholic Steatohepatitis. *Hepatology* **2007**, *45* (6), 1366–1374.

(222) O'Neil, M.; Damjanov, I.; Taylor, R. M. *Liver Pathology for Clinicians*; Springer International Publishing: Cham, 2015.

(223) Patterson, R. E.; Kalavalapalli, S.; Williams, C. M.; Nautiyal, M.; Mathew, J. T.; Martinez, J.; Reinhard, M. K.; McDougall, D. J.; Rocca, J. R.; Yost, R. A.; et al. Lipotoxicity in Steatohepatitis Occurs despite an Increase in Tricarboxylic Acid Cycle Activity. *Am. J. Physiol. Metab.* **2016**, *310* (7), E484–E494.

(224) Zhang, S.; Nagana Gowda, G. A.; Asiago, V.; Shanaiah, N.; Barbas, C.; Raftery, D. Correlative and Quantitative 1H NMR-Based Metabolomics Reveals Specific Metabolic Pathway Disturbances in Diabetic Rats. *Anal. Biochem.* **2008**, *383* (1), 76–84.

(225) Akazawa, Y.; Nakao, K. To Die or Not to Die: Death Signaling in Nonalcoholic Fatty Liver Disease. *J. Gastroenterol.* **2018**, *53* (8), 893–906.

(226) Puri, P.; Baillie, R. A.; Wiest, M. M.; Mirshahi, F.; Choudhury, J.; Cheung, O.; Sargeant, C.; Contos, M. J.; Sanyal, A. J. A Lipidomic Analysis of Nonalcoholic Fatty Liver Disease. *Hepatology* **2007**, *46* (4), 1081–1090.

(227) Kawano, Y.; Nishiumi, S.; Saito, M.; Yano, Y.; Azuma, T.; Yoshida, M. Identification of Lipid Species Linked to the Progression of Non-Alcoholic Fatty Liver Disease. *Curr. Drug Targets* **2015**, *16* (12), 1293–1300.

(228) Chiappini, F.; Coilly, A.; Kadar, H.; Gual, P.; Tran, A.; Desterke, C.; Samuel, D.; Duclos-Vallée, J. C.; Touboul, D.; Bertrand-Michel, J.; et al. Metabolism

Dysregulation Induces a Specific Lipid Signature of Nonalcoholic Steatohepatitis in Patients. *Sci. Rep.* **2017**, *7* (1), 46658.

(229) Pierantonelli, I.; Svegliati-Baroni, G. Nonalcoholic Fatty Liver Disease: Basic Pathogenetic Mechanisms in the Progression from NAFLD to NASH. *Transplantation* **2019**, *103* (1), E1–E13.

(230) Reddy, J. K.; Rao, M. S. Lipid Metabolism and Liver Inflammation. II. Fatty Liver Disease and Fatty Acid Oxidation. *Am. J. Physiol. Gastrointest. Liver Physiol.* **2006**, *290* (5), G852-8.

(231) Donnelly, K. L.; Smith, C. I.; Schwarzenberg, S. J.; Jessurun, J.; Boldt, M. D.; Parks, E. J. Sources of Fatty Acids Stored in Liver and Secreted via Lipoproteins in Patients with Nonalcoholic Fatty Liver Disease. *J. Clin. Invest.* **2005**, *115* (5), 1343–1351.

(232) Fengler, V. H. I.; Macheiner, T.; Kessler, S. M.; Czepukojc, B.; Gemperlein, K.; Müller, R.; Kiemer, A. K.; Magnes, C.; Haybaeck, J.; Lackner, C.; et al. Susceptibility of Different Mouse Wild Type Strains to Develop Diet-Induced Nafld/Afld-Associated Liver Disease. *PLoS One* **2016**, *11* (5), e0155163.

(233) Shpyleva, S.; Pogribna, M.; Cozart, C.; Bryant, M. S.; Muskhelishvili, L.; Tryndyak, V. P.; Ross, S. A.; Beland, F. A.; Pogribny, I. P. Interstrain Differences in the Progression of Nonalcoholic Steatohepatitis to Fibrosis in Mice Are Associated with Altered Hepatic Iron Metabolism. *J. Nutr. Biochem.* **2014**, *25* (12), 1235–1242.

(234) Tryndyak, V.; De Conti, A.; Kobets, T.; Kutanzi, K.; Koturbash, I.; Han, T.; Fuscoe, J. C.; Latendresse, J. R.; Melnyk, S.; Shymonyak, S.; et al. Interstrain Differences in the Severity of Liver Injury Induced by a Choline- and Folate-Deficient Diet in Mice Are Associated with Dysregulation of Genes Involved in

Lipid Metabolism. *FASEB J.* **2012**, *26* (11), 4592–4602.

(235) Trivedi, P. J.; Weston, C. J.; Webb, G. J.; Newsome, P. N.; Hirschfield, G. M.; Adams, D. H. Serum Alkaline Phosphatase in Multidrug Resistance 2 (Mdr2-/-) Knockout Mice Is Strain Specific. *Hepatology* **2016**, *63* (1), 346.

(236) Otto, G. P.; Rathkolb, B.; Oestereicher, M. A.; Lengger, C. J.; Moerth, C.; Micklich, K.; Fuchs, H.; Gailus-Durner, V.; Wolf, E.; Hrabě de Angelis, M. Clinical Chemistry Reference Intervals for C57BL/6J, C57BL/6N, and C3HeB/FeJ Mice (Mus Musculus). *J. Am. Assoc. Lab. Anim. Sci.* **2016**, *55* (4), 375–386.

(237) Rossi, A. G.; Rossi, F. Flow Cytometric Techniques for Isolating and Analysing Leucocytes. *J. Inflamm.* **2015**, *12* (Suppl 1), O9.

(238) Oo, Y. H.; Weston, C. J.; Lalor, P. F.; Curbishley, S. M.; Withers, D. R.; Reynolds, G. M.; Shetty, S.; Harki, J.; Shaw, J. C.; Eksteen, B.; et al. Distinct Roles for CCR4 and CXCR3 in the Recruitment and Positioning of Regulatory T Cells in the Inflamed Human Liver. *J. Immunol.* **2010**, *184* (6), 2886–2898.

(239) Yu, Y. R. A.; O'Koren, E. G.; Hotten, D. F.; Kan, M. J.; Kopin, D.; Nelson, E. R.; Que, L.; Gunn, M. D. A Protocol for the Comprehensive Flow Cytometric Analysis of Immune Cells in Normal and Inflamed Murine Non-Lymphoid Tissues. *PLoS One* **2016**, *11* (3), e0150606.

(240) Badtke, M. P.; Cao, F.; Tavis, J. E. Combining Genetic and Biochemical Approaches to Identify Functional Molecular Contact Points. *Biol. Proced. Online* **2006**, *8* (1), 77–86.

(241) Lau, J. K. C.; Zhang, X.; Yu, J. Animal Models of Non-Alcoholic Fatty Liver Disease: Current Perspectives and Recent Advances. *J. Pathol.* **2017**, *241* (1), 36–44.

(242) Ito, M.; Suzuki, J.; Tsujioka, S.; Sasaki, M.; Gomori, A.; Shirakura, T.; Hirose, H.;

Ito, M.; Ishihara, A.; Iwaasa, H.; et al. Longitudinal Analysis of Murine Steatohepatitis Model Induced by Chronic Exposure to High-Fat Diet. *Hepatol. Res.* **2007**, *37* (1), 50–57.

(243) Research Diets. Diet Induced Obesity Diets https://researchdiets.com/opensource-diets/dio-series-diets (accessed May 8, 2019).

(244) Wolf, M. J.; Adili, A.; Piotrowitz, K.; Abdullah, Z.; Boege, Y.; Stemmer, K.; Ringelhan, M.; Simonavicius, N.; Egger, M.; Wohlleber, D.; et al. Metabolic Activation of Intrahepatic CD8+ T Cells and NKT Cells Causes Nonalcoholic Steatohepatitis and Liver Cancer via Cross-Talk with Hepatocytes. *Cancer Cell* **2014**, *26* (4), 549–564.

(245) Ishimoto, T.; Lanaspa, M. A.; Rivard, C. J.; Roncal-Jimenez, C. A.; Orlicky, D. J.; Cicerchi, C.; Mcmahan, R. H.; Abdelmalek, M. F.; Rosen, H. R.; Jackman, M. R.; et al. High-Fat and High-Sucrose (Western) Diet Induces Steatohepatitis That Is Dependent on Fructokinase. *Hepatology* **2013**, *58* (5), 1632–1643.

(246) Asrih, M.; Jornayvaz, F. R. Inflammation as a Potential Link between Nonalcoholic Fatty Liver Disease and Insulin Resistance. *J. Endocrinol.* **2013**, *218* (3), R25–R36.

(247) Softic, S.; Cohen, D. E.; Kahn, C. R. Role of Dietary Fructose and Hepatic De Novo Lipogenesis in Fatty Liver Disease. *Dig. Dis. Sci.* **2016**, *61* (5), 1282–1293.

(248) Kunkel, T.; Wang, H. Socially Dominant Mice in C57BL6 Background Show Increased Social Motivation. *Behav. Brain Res.* **2018**, *336*, 173–176.

(249) Patel, C.; Sugimoto, K.; Douard, V.; Shah, A.; Inui, H.; Yamanouchi, T.; Ferraris, R. P. Effect of Dietary Fructose on Portal and Systemic Serum Fructose Levels in Rats and in KHK −/− and GLUT5 −/− Mice. *Am. J. Physiol. Liver Physiol.* **2015**, *309* (9), G779–G790.

(250) Kew, M. C. Serum Aminotransferase Concentration as Evidence of Hepatocellular Damage. *Lancet* **2000**, *355* (9204), 591–592.

(251) Liu, R.; Pan, X.; Whitington, P. F. Increased Hepatic Expression Is a Major Determinant of Serum Alanine Aminotransferase Elevation in Mice with Nonalcoholic Steatohepatitis. *Liver Int.* **2009**, *29* (3), 337–343.

(252) Puri, P.; Sanyal, A. J. Nonalcoholic Fatty Liver Disease: Definitions, Risk Factors, and Workup. *Clin. Liver Dis.* **2012**, *1* (4), 99–103.

(253) Sattar, N.; Forrest, E.; Preiss, D. Non-Alcoholic Fatty Liver Disease. *BMJ* **2014**, *349* (sep19 15), g4596–g4596.

(254) Dyson, J. K.; Anstee, Q. M.; McPherson, S. Non-Alcoholic Fatty Liver Disease: A Practical Approach to Diagnosis and Staging. *Frontline Gastroenterol.* **2014**, *5* (3), 211–218.

(255) M. Brunt, E.; G. Tiniakos, D. Fatty Liver Disease. In *Surgical Pathology of the GI Tract, Liver, Biliary Tract, and Pancreas*; Elsevier, 2009; Vol. 20, pp 1087–1114.

(256) Botros, M.; Sikaris, K. A. The De Ritis Ratio: The Test of Time. *Clin. Biochem. Rev.* **2013**, *34* (3), 117–130.

(257) Fraulob, J. C.; Ogg-Diamantino, R.; Fernandes-Santos, C.; Aguila, M. B.; Mandarim-de-Lacerda, C. A. A Mouse Model of Metabolic Syndrome: Insulin Resistance, Fatty Liver and Non-Alcoholic Fatty Pancreas Disease (NAFPD) in C57BL/6 Mice Fed a High Fat Diet. *J. Clin. Biochem. Nutr.* **2010**, *46* (3), 212–223.

(258) Glavind, E.; Aagaard, N. K.; Grønbæk, H.; Møller, H. J.; Orntoft, N. W.; Vilstrup, H.; Thomsen, K. L. Alcoholic Hepatitis Markedly Decreases the Capacity for Urea Synthesis. *PLoS One* **2016**, *11* (7), e0158388.

(259) Sandahl, T. D.; Aagaard, N. K.; Thomsen, K. L.; Grøfte, T.; Greisen, J.;

Christiansen, J. S.; Vilstrup, H. Effects of Insulin-like Growth Factor-I Administration on in Vivo Regulation of Urea Synthesis in Normal Subjects and Patients with Cirrhosis. *Liver Int.* **2011**, *31* (1), 132–137.

(260) Jang, H. R.; Kang, D.; Sinn, D. H.; Gu, S.; Cho, S. J.; Lee, J. E.; Huh, W.; Paik, S. W.; Ryu, S.; Chang, Y.; et al. Nonalcoholic Fatty Liver Disease Accelerates Kidney Function Decline in Patients with Chronic Kidney Disease: A Cohort Study. *Sci. Rep.* **2018**, *8* (1), 4718.

(261) Musso, G.; Cassader, M.; Cohney, S.; Michieli, F. De; Pinach, S.; Saba, F.; Gambino, R. Fatty Liver and Chronic Kidney Disease: Novel Mechanistic Insights and Therapeutic Opportunities. *Diabetes Care* **2016**, *39* (10), 1830–1845.

(262) Norris, S.; Collins, C.; Doherty, D. G.; Smith, F.; McEntee, G.; Traynor, O.; Nolan, N.; Hegarty, J.; O'Farrelly, C. Resident Human Hepatic Lymphocytes Are Phenotypically Different from Circulating Lymphocytes. *J. Hepatol.* **1998**, *28* (1), 84–90.

(263) Rau, M.; Schilling, A.-K.; Meertens, J.; Hering, I.; Weiss, J.; Jurowich, C.; Kudlich, T.; Hermanns, H. M.; Bantel, H.; Beyersdorf, N.; et al. Progression from Nonalcoholic Fatty Liver to Nonalcoholic Steatohepatitis Is Marked by a Higher Frequency of Th17 Cells in the Liver and an Increased Th17/Resting Regulatory T Cell Ratio in Peripheral Blood and in the Liver. *J. Immunol.* **2016**, *196* (1), 97–105.

(264) Ferreyra Solari, N. E.; Inzaugarat, M. E.; Baz, P.; De Matteo, E.; Lezama, C.; Galoppo, M.; Galoppo, C.; Cherñavsky, A. C. The Role of Innate Cells Is Coupled to a Th1-Polarized Immune Response in Pediatric Nonalcoholic Steatohepatitis. *J. Clin. Immunol.* **2012**, *32* (3), 611–621.

(265) Amer, J.; Salhab, A.; Noureddin, M.; Doron, S.; Abu-Tair, L.; Ghantous, R.;

Mahamid, M.; Safadi, R. Insulin Signaling as a Potential Natural Killer Cell Checkpoint in Fatty Liver Disease. *Hepatol. Commun.* **2018**, *2* (3), 285–298.

(266) Ogawa, Y.; Imajo, K.; Honda, Y.; Kessoku, T.; Tomeno, W.; Kato, S.; Fujita, K.; Yoneda, M.; Saito, S.; Saigusa, Y.; et al. Palmitate-Induced Lipotoxicity Is Crucial for the Pathogenesis of Nonalcoholic Fatty Liver Disease in Cooperation with Gut-Derived Endotoxin. *Sci. Rep.* **2018**, *8* (1), 11365.

(267) Zhang, X.; Fan, L.; Wu, J.; Xu, H.; Leung, W. Y.; Fu, K.; Wu, J.; Liu, K.; Man, K.; Yang, X.; et al. Macrophage P38α Promotes Nutritional Steatohepatitis through M1 Polarization. *J. Hepatol.* **2019**, *0* (0).

(268) Nakashima, H.; Nakashima, M.; Kinoshita, M.; Ikarashi, M.; Miyazaki, H.; Hanaka, H.; Imaki, J.; Seki, S. Activation and Increase of Radio-Sensitive CD11b+ Recruited Kupffer Cells/Macrophages in Diet-Induced Steatohepatitis in FGF5 Deficient Mice. *Sci. Rep.* **2016**, *6* (1), 34466.

(269) Saltzman, E. T.; Palacios, T.; Thomsen, M.; Vitetta, L. Intestinal Microbiome Shifts, Dysbiosis, Inflammation, and Non-Alcoholic Fatty Liver Disease. *Front. Microbiol.* **2018**, *9*, 61.

(270) Kolodziejczyk, A. A.; Zheng, D.; Shibolet, O.; Elinav, E. The Role of the Microbiome in NAFLD and NASH. *EMBO Mol. Med.* **2019**, *11* (2), e9302.

(271) Wiest, R.; Albillos, A.; Trauner, M.; Bajaj, J. S.; Jalan, R. Targeting the Gut-Liver Axis in Liver Disease. *J. Hepatol.* **2017**, *67* (5), 1084–1103.

(272) Konturek, P.; Harsch, I.; Konturek, K.; Schink, M.; Konturek, T.; Neurath, M.; Zopf, Y. Gut–Liver Axis: How Do Gut Bacteria Influence the Liver? *Med. Sci.* **2018**, *6* (3), 79.

(273) Holub, M.; Cheng, C.-W.; Mott, S.; Wintermeyer, P.; van Rooijen, N.; Gregory, S. H. Neutrophils Sequestered in the Liver Suppress the Proinflammatory Response

of Kupffer Cells to Systemic Bacterial Infection. *J. Immunol.* **2009**, *183* (5), 3309–3316.

(274) Clark, I.; Torbenson, M. S. Immunohistochemistry and Special Stains in Medical Liver Pathology. *Adv. Anat. Pathol.* **2017**, *24* (2), 99–109.

(275) Nicholson, J. K.; Lindon, J. C.; Holmes, E. "Metabonomics": Understanding the Metabolic Responses of Living Systems to Pathophysiological Stimuli via Multivariate Statistical Analysis of Biological NMR Spectroscopic Data. *Xenobiotica.* **1999**, *29* (11), 1181–1189.

(276) Ryaboshapkina, M.; Hammar, M. Human Hepatic Gene Expression Signature of Non-Alcoholic Fatty Liver Disease Progression, a Meta-Analysis. *Sci. Rep.* **2017**, *7* (1), 12361.

(277) Li, L.; Liu, H.; Hu, X.; Huang, Y.; Wang, Y.; He, Y.; Lei, Q. Identification of Key Genes in Non-Alcoholic Fatty Liver Disease Progression Based on Bioinformatics Analysis. *Mol. Med. Rep.* **2018**, *17* (6), 7708–7720.

(278) Greco, D.; Kotronen, A.; Westerbacka, J.; Puig, O.; Arkkila, P.; Kiviluoto, T.; Laitinen, S.; Kolak, M.; Fisher, R. M.; Hamsten, A.; et al. Gene Expression in Human NAFLD. *Am. J. Physiol. Liver Physiol.* **2008**, *294* (5), G1281–G1287.

(279) Nakamuta, M.; Kohjima, M.; Morizono, S.; Kotoh, K.; Yoshimoto, T.; Miyagi, I.; Enjoji, M. Evaluation of Fatty Acid Metabolism-Related Gene Expression in Nonalcoholic Fatty Liver Disease. *Int. J. Mol. Med.* **2005**, *16* (4), 631–635.

(280) Lu, M.; Wan, M.; Leavens, K. F.; Chu, Q.; Monks, B. R.; Fernandez, S.; Ahima, R. S.; Ueki, K.; Kahn, C. R.; Birnbaum, M. J. Insulin Regulates Liver Metabolism in Vivo in the Absence of Hepatic Akt and Foxo1. *Nat. Med.* **2012**, *18* (3), 388–395.

(281) Titchenell, P. M.; Quinn, W. J.; Lu, M.; Chu, Q.; Lu, W.; Li, C.; Chen, H.; Monks,

B. R.; Chen, J.; Rabinowitz, J. D.; et al. Direct Hepatocyte Insulin Signaling Is Required for Lipogenesis but Is Dispensable for the Suppression of Glucose Production. *Cell Metab.* **2016**, *23* (6), 1154–1166.

(282) Berlanga, A.; Guiu-Jurado, E.; Porras, J. A.; Auguet, T. Molecular Pathways in Non-Alcoholic Fatty Liver Disease. *Clin. Exp. Gastroenterol.* **2014**, *7* (1), 221–239.

(283) Westerbacka, J.; Kolak, M.; Kiviluoto, T.; Arkkila, P.; Sirén, J.; Hamsten, A.; Fisher, R. M.; Yki-Järvinen, H. Genes Involved in Fatty Acid Partitioning and Binding, Lipolysis, Monocyte/Macrophage Recruitment, and Inflammation Are Overexpressed in the Human Fatty Liver of Insulin-Resistant Subjects. *Diabetes* **2007**, *56* (11), 2759–2765.

(284) Sun, Q.; Li, M.; Yang, X.; Xu, X.; Wang, J.; Zhang, J. Dietary Salecan Reverts Partially the Metabolic Gene Expressions and NMR-Based Metabolomic Profiles from High-Fat-Diet-Induced Obese Rats. *J. Nutr. Biochem.* **2017**, *47*, 53–62.

(285) Nakata, R.; Hyodo, F.; Murata, M.; Eto, H.; Nakaji, T.; Kawano, T.; Narahara, S.; Yasukawa, K.; Akahoshi, T.; Tomikawa, M.; et al. In Vivo Redox Metabolic Imaging of Mitochondria Assesses Disease Progression in Non-Alcoholic Steatohepatitis. *Sci. Rep.* **2017**, *7* (1), 17170.

(286) Sunny, N. E.; Bril, F.; Cusi, K. Mitochondrial Adaptation in Nonalcoholic Fatty Liver Disease: Novel Mechanisms and Treatment Strategies. *Trends Endocrinol. Metab.* **2017**, *28* (4), 250–260.

(287) Rogne, P.; Rosselin, M.; Grundström, C.; Hedberg, C.; Sauer, U. H.; Wolf-Watz, M. Molecular Mechanism of ATP versus GTP Selectivity of Adenylate Kinase. *Proc. Natl. Acad. Sci.* **2018**, *115* (12), 3012–3017.

(288) Serviddio, G.; Bellanti, F.; Tamborra, R.; Rollo, T.; Romano, A. D.; Giudetti, A.

M.; Capitanio, N.; Petrella, A.; Vendemiale, G.; Altomare, E. Alterations of Hepatic ATP Homeostasis and Respiratory Chain during Development of Non-Alcoholic Steatohepatitis in a Rodent Model. *Eur. J. Clin. Invest.* **2008**, *38* (4), 245–252.

(289) Cortez-Pinto, H.; Chatham, J.; Chacko, V. P.; Arnold, C.; Rashid, A.; Diehl, A. M. Alterations in Liver ATP Homeostasis in Human Nonalcoholic Steatohepatitis: A Pilot Study. *JAMA* **1999**, *282* (17), 1659–1664.

(290) Dumas, M.-E.; Barton, R. H.; Toye, A.; Cloarec, O.; Blancher, C.; Rothwell, A.; Fearnside, J.; Tatoud, R.; Blanc, V.; Lindon, J. C.; et al. Metabolic Profiling Reveals a Contribution of Gut Microbiota to Fatty Liver Phenotype in Insulin-Resistant Mice. *Proc. Natl. Acad. Sci.* **2006**, *103* (33), 12511–12516.

(291) Chao, J.; Huo, T.-I.; Cheng, H.-Y.; Tsai, J.-C.; Liao, J.-W.; Lee, M.-S.; Qin, X.-M.; Hsieh, M.-T.; Pao, L.-H.; Peng, W.-H. Gallic Acid Ameliorated Impaired Glucose and Lipid Homeostasis in High Fat Diet-Induced NAFLD Mice. *PLoS One* **2014**, *9* (6), e96969.

(292) Jiang, X. C.; Li, Z.; Liu, R.; Yang, X. P.; Pan, M.; Lagrost, L.; Fisher, E. A.; Williams, K. J. Phospholipid Transfer Protein Deficiency Impairs Apolipoprotein-B Secretion from Hepatocytes by Stimulating a Proteolytic Pathway through a Relative Deficiency of Vitamin E and an Increase in Intracellular Oxidants. *J. Biol. Chem.* **2005**, *280* (18), 18336–18340.

(293) Sun, S. Z.; Empie, M. W. Fructose Metabolism in Humans – What Isotopic Tracer Studies Tell Us. *Nutr. Metab. (Lond).* **2012**, *9* (1), 89.

(294) Paquot, N.; Schneiter, P.; Jéquier, E.; Gaillard, R.; Lefèbvre, P. J.; Scheen, A.; Tappy, L. Effects of Ingested Fructose and Infused Glucagon on Endogenous Glucose Production in Obese NIDDM Patients, Obese Non-Diabetic Subjects, and

Healthy Subjects. *Diabetologia* **1996**, *39* (5), 580–586.

(295) Lecoultre, V.; Benoit, R.; Carrel, G.; Schutz, Y.; Millet, G. P.; Tappy, L.; Schneiter, P. Fructose and Glucose Co-Ingestion during Prolonged Exercise Increases Lactate and Glucose Fluxes and Oxidation Compared with an Equimolar Intake of Glucose. *Am. J. Clin. Nutr.* **2010**, *92* (5), 1071–1079.

(296) Delarue, J.; Normand, S.; Pachiaudi, C.; Beylot, M.; Lamisse, F.; Riou, J. P. The Contribution of Naturally Labelled 13C Fructose to Glucose Appearance in Humans. *Diabetologia* **1993**, *36* (4), 338–345.

(297) Jang, C.; Hui, S.; Lu, W.; Cowan, A. J.; Morscher, R. J.; Lee, G.; Liu, W.; Tesz, G. J.; Birnbaum, M. J.; Rabinowitz, J. D. The Small Intestine Converts Dietary Fructose into Glucose and Organic Acids. *Cell Metab.* **2018**, *27* (2), 351-361.e3.

(298) Tran, C.; Jacot-Descombes, D.; Lecoultre, V.; Fielding, B. A.; Carrel, G.; Lê, K.-A.; Schneiter, P.; Bortolotti, M.; Frayn, K. N.; Tappy, L. Sex Differences in Lipid and Glucose Kinetics after Ingestion of an Acute Oral Fructose Load. *Br. J. Nutr.* **2010**, *104* (8), 1139–1147.

(299) Elliott, S. S.; Keim, N. L.; Stern, J. S.; Teff, K.; Havel, P. J. Fructose, Weight Gain, and the Insulin Resistance Syndrome. *Am. J. Clin. Nutr.* **2002**, *76* (5), 911–922.

(300) Stanhope, K. L. Sugar Consumption, Metabolic Disease and Obesity: The State of the Controversy. *Crit. Rev. Clin. Lab. Sci.* **2016**, *53* (1), 52–67.

(301) Ouyang, X.; Cirillo, P.; Sautin, Y.; McCall, S.; Bruchette, J. L.; Diehl, A. M.; Johnson, R. J.; Abdelmalek, M. F. Fructose Consumption as a Risk Factor for Non-Alcoholic Fatty Liver Disease. *J. Hepatol.* **2008**, *48* (6), 993–999.

(302) Ishimoto, T.; Lanaspa, M. A.; Le, M. T.; Garcia, G. E.; Diggle, C. P.; MacLean, P. S.; Jackman, M. R.; Asipu, A.; Roncal-Jimenez, C. A.; Kosugi, T.; et al. Opposing Effects of Fructokinase C and A Isoforms on Fructose-Induced Metabolic

Syndrome in Mice. *Proc. Natl. Acad. Sci.* **2012**, *109* (11), 4320–4325.

(303) Lanaspa, M. A.; Andres-Hernando, A.; Orlicky, D. J.; Cicerchi, C.; Jang, C.; Li, N.; Milagres, T.; Kuwabara, M.; Wempe, M. F.; Rabinowitz, J. D.; et al. Ketohexokinase C Blockade Ameliorates Fructose-Induced Metabolic Dysfunction in Fructose-Sensitive Mice. *J. Clin. Invest.* **2018**, *128* (6), 2226–2238.

(304) Miller, C. O.; Yang, X.; Lu, K.; Cao, J.; Herath, K.; Rosahl, T. W.; Askew, R.; Pavlovic, G.; Zhou, G.; Li, C.; et al. Ketohexokinase Knockout Mice, a Model for Essential Fructosuria, Exhibit Altered Fructose Metabolism and Are Protected from Diet-Induced Metabolic Defects. *Am. J. Physiol. Metab.* **2018**, *315* (3), E386–E393.

(305) Diggle, C. P.; Shires, M.; Leitch, D.; Brooke, D.; Carr, I. M.; Markham, A. F.; Hayward, B. E.; Asipu, A.; Bonthron, D. T. Ketohexokinase: Expression and Localization of the Principal Fructose-Metabolizing Enzyme. *J. Histochem. Cytochem.* **2009**, *57* (8), 763–774.

(306) Hayward, B. E.; Bonthron, D. T. Structure and Alternative Splicing of the Ketohexokinase Gene. *Eur. J. Biochem.* **1998**, *257* (1), 85–91.

(307) Li, X.; Qian, X.; Peng, L. X.; Jiang, Y.; Hawke, D. H.; Zheng, Y.; Xia, Y.; Lee, J. H.; Cote, G.; Wang, H.; et al. A Splicing Switch from Ketohexokinase-C to Ketohexokinase-A Drives Hepatocellular Carcinoma Formation. *Nat. Cell Biol.* **2016**, *18* (5), 561–571.

(308) DiTullio, N. W.; Berkoff, C. E.; Blank, B.; Kostos, V.; Stack, E. J.; Saunders, H. L. 3-Mercaptopicolinic Acid, an Inhibitor of Gluconeogenesis. *Biochem. J.* **2015**, *138* (3), 387–394.

(309) Luedde, T.; Kaplowitz, N.; Schwabe, R. F. Cell Death and Cell Death Responses in Liver Disease: Mechanisms and Clinical Relevance. *Gastroenterology* **2014**,

147 (4), 765-783.e4.

(310) Koo, H. Y.; Wallig, M. A.; Chung, B. H.; Nara, T. Y.; Cho, B. H. H. S.; Nakamura, M. T. Dietary Fructose Induces a Wide Range of Genes with Distinct Shift in Carbohydrate and Lipid Metabolism in Fed and Fasted Rat Liver. *Biochim. Biophys. Acta - Mol. Basis Dis.* **2008**, *1782* (5), 341–348.

(311) Kim, T. H.; Jun, H. Y.; Kim, K. J.; Lee, Y. H.; Lee, M. S.; Choi, K. H.; Yun, K. J.; Jeong, Y. Y.; Jun, C. H.; Cho, E. Y.; et al. Hepatic Alanine Differentiates Nonalcoholic Steatohepatitis From Simple Steatosis in Humans and Mice: A Proton MR Spectroscopy Study With Long Echo Time. *J. Magn. Reson. Imaging* **2017**, *46* (5), 1298–1310.

(312) Park, O. J.; Cesar, D.; Faix, D.; Wu, K.; Shackleton, C. H. L.; Hellerstein, M. K. Mechanisms of Fructose-Induced Hypertriglyceridaemia in the Rat. Activation of Hepatic Pyruvate Dehydrogenase through Inhibition of Pyruvate Dehydrogenase Kinase. *Biochem. J.* **2015**, *282* (3), 753–757.

(313) Jois, T.; Chen, W.; Howard, V.; Harvey, R.; Youngs, K.; Thalmann, C.; Saha, P.; Chan, L.; Cowley, M. A.; Sleeman, M. W. Deletion of Hepatic Carbohydrate Response Element Binding Protein (ChREBP) Impairs Glucose Homeostasis and Hepatic Insulin Sensitivity in Mice. *Mol. Metab.* **2017**, *6* (11), 1381–1394.

(314) Satapati, S.; Kucejova, B.; Duarte, J. A. G.; Fletcher, J. A.; Reynolds, L.; Sunny, N. E.; He, T.; Nair, L. A.; Livingston, K.; Fu, X.; et al. Mitochondrial Metabolism Mediates Oxidative Stress and Inflammation in Fatty Liver. *J. Clin. Invest.* **2015**, *125* (12), 4447–4462.

(315) Basarnoglu, M.; Basarnoglu, G.; Bugianesi, E. Carbohydrate Intake and Nonalcoholic Fatty Liver Disease: Fructose as a Weapon of Mass Destruction. *HepatoBiliary Surg Nutr* **2015**, *4* (2), 109–116.

(316) Lanaspa, M. A.; Ishimoto, T.; Li, N.; Cicerchi, C.; Orlicky, D. J.; Ruzycki, P.; Rivard, C.; Inaba, S.; Roncal-Jimenez, C. A.; Bales, E. S.; et al. Endogenous Fructose Production and Metabolism in the Liver Contributes to the Development of Metabolic Syndrome. *Nat. Commun.* **2013**, *4* (1), 1–8.

(317) Gostner, A.; Blaut, M.; Schäffer, V.; Kozianowski, G.; Theis, S.; Klingeberg, M.; Dombrowski, Y.; Martin, D.; Ehrhardt, S.; Taras, D.; et al. Effect of Isomalt Consumption on Faecal Microflora and Colonic Metabolism in Healthy Volunteers. *Br. J. Nutr.* **2006**, *95* (1), 40–50.

(318) Bouhnik, Y.; Flourié, B.; Riottot, M.; Bisetti, N.; Gailing, M. F.; Guibert, A.; Bornet, F.; Rambaud, J. C. Effects of Fructo-Oligosaccharides Ingestion on Fecal Bifidobacteria and Selected Metabolic Indexes of Colon Carcinogenesis in Healthy Humans. *Nutr. Cancer* **1996**, *26* (1), 21–29.

(319) Lenhart, A.; D Chey, W. A Systematic Review of the Effects of Polyols on Gastrointestinal Health and Irritable Bowel Syndrome. *Adv. Nutr.* **2017**, *8* (4), 587–596.

(320) Zamboni, N.; Saghatelian, A.; Patti, G. J. Defining the Metabolome: Size, Flux, and Regulation. *Mol. Cell* **2015**, *58* (4), 699–706.

(321) Andres-Hernando, A.; Li, N.; Cicerchi, C.; Inaba, S.; Chen, W.; Roncal-Jimenez, C.; Le, M. T.; Wempe, M. F.; Milagres, T.; Ishimoto, T.; et al. Protective Role of Fructokinase Blockade in the Pathogenesis of Acute Kidney Injury in Mice. *Nat. Commun.* **2017**, *8*, 14181.

(322) Johnson, R. J.; Rivard, C.; Lanaspa, M. A.; Otabachian-Smith, S.; Ishimoto, T.; Cicerchi, C.; Cheeke, P. R.; McIntosh, B.; Hess, T. Fructokinase, Fructans, Intestinal Permeability, and Metabolic Syndrome: An Equine Connection? *J. Equine Vet. Sci.* **2013**, *33* (2), 120–126.